Spatially resolved stellar mass buildup and quenching of star formation in massive disk galaxies over the last 10 Gyrs

著者	Abdurrouf
学位授与機関	Tohoku University
学位授与番号	11301甲第18262号
URL	http://hdl.handle.net/10097/00124047

PhD Thesis

Spatially resolved stellar mass buildup and quenching of star formation in massive disk galaxies over the last 10 Gyrs

(過去100億年の大質量円盤銀河の
内部での星の集積と星形成の終焉)

A DISSERTATION SUBMITTED TO
TOHOKU UNIVERSITY
IN PARTIAL FULFILLMENT OF REQUIREMENTS FOR
THE DEGREE OF DOCTOR OF SCIENCE

Abdurrouf

ASTRONOMICAL INSTITUTE
GRADUATE SCHOOL OF SCIENCE
TOHOKU UNIVERSITY

SEPTEMBER 2018

Abstract

It has been established that star formation activities in the universe were in their maximum rate about 10 Gyrs ago ($z \sim 2$; an epoch commonly called as the cosmic noon) after which most galaxies undergoing quenching of star formation activity. Despite the decreasing global average of star formation activity over the last 10 Gyrs, stellar mass buildup in the universe were still progressing. About 50% of the current stellar mass density in the universe is built over the last ~ 8.7 Gyrs ago. How galaxies quench their star formation activities and build their stellar masses during the cosmic afternoon epoch (i.e. an epoch after the cosmic noon) is still unclear. In order to understand that and furthermore study the spatially resolved quenching process and stellar mass buildup in galaxies, information on the spatially resolved star formation rate (SFR) and stellar mass (M_*) of galaxies over wide redshift range is needed. In this thesis, we study the spatially resolved distributions of SFR and M_* in massive disk galaxies at $0.01 < z < 0.02$ and $0.8 < z < 1.8$ and infer the evolution of surface density radial profiles of massive disk galaxies over the last 10 Gyrs. We derive the spatially resolved SFR and M_* in a galaxy using our established spatially resolved spectral energy distribution (SED) fitting method, namely pixel-to-pixel SED fitting. In this method, spatially resolved SEDs of a galaxy are fitted to a set of model SEDs using Bayesian statistics approach to obtain the spatially resolved (at ~ 1 kpc-scale) SFR and M_* of the galaxy. We construct spatially resolved SEDs, which covers rest-frame far-ultraviolet (FUV) to near-infrared (NIR), of a galaxy at $0.01 < z < 0.02$ by combining imaging data-set from GALEX and SDSS. For the sample galaxies at $0.8 < z < 1.8$, we use imaging data-set from CANDELS and 3D-HST, which gives a similar rest-frame FUV to NIR coverage.

We find a relation between SFR surface density ($\Sigma_{\rm SFR}$) and M_* surface density (Σ_*) at sub-galactic scale (~ 1 kpc) namely spatially resolved star formation main sequence (SFMS), which is hold at $z \sim 0$ and $z \sim 1$. In massive star-forming disk galaxies at $0.8 < z < 1.8$ that reside on the global SFMS, this relation is linear over entire Σ_* range, while in massive disk galaxies with lower global specific SFR (sSFR$\equiv$ SFR/M_*) at both $0.8 < z < 1.8$ and $0.01 < z < 0.02$ redshift ranges, the spatially resolved SFMS has a 'flattening' trend at high Σ_* end. The spatially resolved SFMS evolves with cosmic time by decreasing sSFR ($\Sigma_{\rm SFR}/\Sigma_*$) over entire Σ_* range with systematically larger decrease at high Σ_* region compared to that at low Σ_* region leading to an increasing prominence of the 'flattening' at high Σ_* end. The 'flattening' trend at high Σ_* end of the spatially resolved SFMS is consistent with a suppression of sSFR in the central region as shown in the sSFR(r) radial profile. The evolutionary trend shown in the spatially resolved SFMS is consistent with the evolutionary trend of the sSFR(r) radial profile, which shows decreasing sSFR with cosmic time over entire radii with systematically larger decrease in the central region compared to that in the outskirt, agrees with the 'inside-out' quenching scenario. The above evolutionary trend of sSFR(r) radial profile combined with an observed tendency of increasing bulge fraction with decreasing global sSFR suggests a formation and growth of bulge as galaxies undergoing inside-out quenching. In order to quantitatively examine evolution of the spatially resolved SFR and stellar mass of massive disk galaxies, we construct an empirical model for the evolution of the surface density radial profiles (i.e. $\Sigma_{\rm SFR}(r)$, $\Sigma_{*}(r)$, and sSFR(r)). The empirical model could connect between the evolution of the $\Sigma_{\rm SFR}(r)$ radial profile and resolved stellar mass growth depicted by the evolution of the $\Sigma_{*}(r)$. The empirical model suggests that massive disk galaxies undergoing steady stellar mass buildup and quenching of star formation that proceed in 'inside-to-outside' manner.

Contents of this thesis are partially adopted from our following published papers:

1. *Understanding the scatter in the spatially resolved star formation main sequence of local massive spiral galaxies*, Abdurro'uf and M. Akiyama, 2017, MNRAS, 469, 2806. doi: 10.1093/mnras/stx936.

2. *Evolution of spatially resolved star formation main sequence and surface density profiles in massive disc galaxies at* $0 \lesssim z \lesssim 1$*: inside-out stellar mass buildup and quenching*, Abdurro'uf and M. Akiyama, 2018, MNRAS, 479, 5083. doi: 10.1093/mnras/sty1771.

Contents of Chapter 4, which discuss the spatially resolved distributions of SFR and M_{*} in massive disk galaxies at $z \sim 0$, are partially adopted from the first paper. Contents of Chapters 5 and 6, which discuss the spatially resolved distributions of SFR and M_{*} in massive disk galaxies at $z \sim 1$ and evolution of the spatially resolved SFR and M_{*} at $0 \lesssim z \lesssim 1$ are based on the second paper.

Acknowledgements

“*Indeed, in the creation of the sky and the earth and the alternation of the night and the day are signs for those of understanding. Who remember Lord while standing or sitting or [lying] on their sides and give thought to the creation of the sky and the earth, [saying], ’Our Lord, You did not create this aimlessly; exalted are You [above such a thing]...’*” *Quran, 3:190-191*

Alhamdulillah, Praise be to the Lord. I am grateful to my supervisor Masayuki Akiyama for supporting me with huge dedication throughout my master and PhD courses. I have been given opportunities to tackle many interesting research questions with forefront methods. I also want to thank referees of this PhD thesis, Tadayuki Kodama, Masafumi Noguchi, and Takashi Murayama, for their comments and suggestions that improve this thesis.

I really enjoyed research environment at the Astronomical Institute of Tohoku University, where I meet and discuss with a great group of fellow students and postdocs for the last five years. I want to thank assistant professors, postdocs, and my lab-mates: Tsumura Kohji, Hirofumi Noda, Mitsuru Kokubo, Kazuma Mitsuda, Wanqiu He, Xiaoyang Chen, Genki Suzuki, Maho Sato, Daiki Sakurai, Yutaro Tanaka, Hajime Ogane, and Kaoru Ohmoto, for giving insightful questions and discussions every time I present my research progress in weekly group meeting. I also want to thank Takahiro Morishita for insightful discussions and comments on my papers and sharing his experiences in postdoc hunting. I want to thank my Indonesian friends at the Astronomical Institute, Anton T. Jaelani, Stevanus K. Nugroho, and Itsna K. Fitriana, for useful discussions on researches as well as future careers. Throughout my studies at the Astronomical Institute, I enjoyed the great supports of the administrative staff, Nozomi Okamoto and Junko Nagasawa. During my master and PhD course in the Astronomical Institute, I was supported by the Ministry of Education, Culture, Sports, Science and Technology in Japan (MEXT) scholarship, which made this whole PhD thesis works possible.

Finally, I want to give the biggest thanks to my family: my wife Imro’atus S. Hasanah for her supports, motivations, and prayers, my mother Titik Rohimah and mother in law Zuhriyah for their prayers, my one year old son Azka H. Avicenna for making me smile and be motivated every day. I dedicate this thesis to my wife and son. I hope this thesis is not too bad to be a present for my third year wedding anniversary and not too bad to be read 20 years later by Azka.

Sendai, August 2018

Abdurrouf

to my wife Ifa and son Azka

Contents

List of Tables

List of Figures

Chapter 1

Introduction

Galaxy, which consists of stars, gas, and dust, is the biggest visible celestial body in the universe. There are more than 100 billion galaxies spreading all over the universe. This fact make galaxies are considered as 'islands in the universe'. Despite their abundances in the universe, total energy (mass) budget contributed by all the baryonic matters (which make up the visible galaxies) only account for $\sim 5\%$ of the total energy (mass) budget of the universe. Another contributions to the energy (mass) budget come from invisible matters, which are dark matter ($\sim 25\%$) and dark energy ($\sim 70\%$). How do galaxies formed and evolved in the dark universe is one of the biggest question in astronomy. Based on the currently favored cosmological framework, ΛCDM cosmology, galaxies were formed hierarchically as large scale structures in the universe assembled. The assembly of large scale structures is started from tiny primordial density fluctuation (believed to be initiated from quantum fluctuation) which then grow by gravitational attraction. At early cosmic time, all matters (baryon and dark matter) are mixed, then due to radiative energy loss of the dissipative baryons, the baryons are separated from the weakly interacting and non dissipative dark matter. The baryons dissipate their energies and fall toward central gravitational well and become a seed of a galaxy, while the dark matter stay on the outer envelope and become a halo. The seed of galaxy then grow over cosmic time and become a present day galaxy through complex processes that include matter (including gas) accretion by mergers or smooth filamentary accretion and internal processes that include star formation, which transform gas into stars, and feedback process, which slow down the star formation rate. The various complex processes experienced by the galaxies throughout their life make up the diversity of the present day galaxies.

In the first chapter we briefly overview cosmological evolution of global properties of the galaxies and current efforts on analyzing spatially resolved properties in the galaxies at the present day universe and at high redshift. In the final part of this chapter, we describe the goals of this thesis.

1.1 Cosmic star formation history

Observations of star-forming galaxies at different redshifts can provide information on the production rate of stars in the universe as a function of redshift. The time evolution of star formation rate (i.e. star formation history) in the universe can be characterized by cosmic star formation rate density (cSFRD), $\rho_{\rm SFR}(z)$, which is star formation rate per unit comoving volume at redshift z. Deriving the $\rho_{\rm SFR}(z)$ from observations requires estimates of the number density of galaxies as a function of redshift and their star formation rates (SFRs). In practice, one can use the number density of galaxies as a function of luminosity in some waveband, i.e. luminosity function $\psi(L, z)$, which is obtained from spectroscopic surveys of galaxies, to estimate $\rho_{\rm SFR}(z)$ by using following equation

$$\rho_{\rm SFR}(z) = \int d\dot{M}_* \dot{M}_* \int P(\dot{M}_*|L, z)\phi(L, z)dL = \int \langle \dot{M}_* \rangle (L, z)\psi(L, z)dL. \tag{1.1}$$

In the above equation, $P(\dot{M}_*|L, z)d\dot{M}_*$ is the probability for a galaxy with luminosty L (in a given band) at redshift z to have a SFR in the range $(\dot{M}_*, \dot{M}_* + d\dot{M}_*)$, and $\langle \dot{M}_* \rangle (L, z)$ is the mean SFR for galaxies with luminosity L at redshift z. The conversion from luminosity to SFR depends on the rest-frame waveband used to measure the luminosity function. Following the above principle, Madau and Dickinson (2014) used data from redshift surveys of galaxies in the rest-frame UV and IR to compile the $\rho_{\rm SFR}(z)$ and found that the $\rho_{\rm SFR}(z)$ is best-fitted by the following equation

$$\rho_{\rm SFR}(z) = 0.015 \frac{(1+z)^{2.7}}{1 + [(1+z)/2.9]^{5.6}} M_\odot {\rm yr}^{-1} {\rm Mpc}^{-3} \tag{1.2}$$

Fig. 1.1 (left panel) shows the cosmic evolution of star formation rate density in the universe (cSFRD) measured by Madau and Dickinson (2014) (and reference therein). The black line represents best-fit function for the cSFRD (eq. 1.2). It is shown by the figure that the star formation rate density in the universe reached a peak value at $z \sim 2$ and dropped by roughly an order of magnitude after that. The declining trend at $z < 2$ is well fitted with an exponentially declining function with e-folding timescale of 3.9 Gyr. The same trend of cosmic star formation history also observed by the preceding works (e.g. Madau 1995; Lilly et al. 1996; Hopkins 2004; Hopkins and Beacom 2006). Right panel of Fig. 1.1 shows the cosmic evolution of the stellar mass density in the universe. The black line represents the inferred stellar mass density evolution from the best-fit cSFRD (eq. 1.2) (which is derived by integrating the cSFRD). The figure shows that the stellar mass density in the universe is increasing with cosmic time. It is suggested by this figure that about half of the current stellar mass density in the universe is built by the star formation in the galaxies over the last ~ 8.7 Gyrs ($z \lesssim 1.3$).

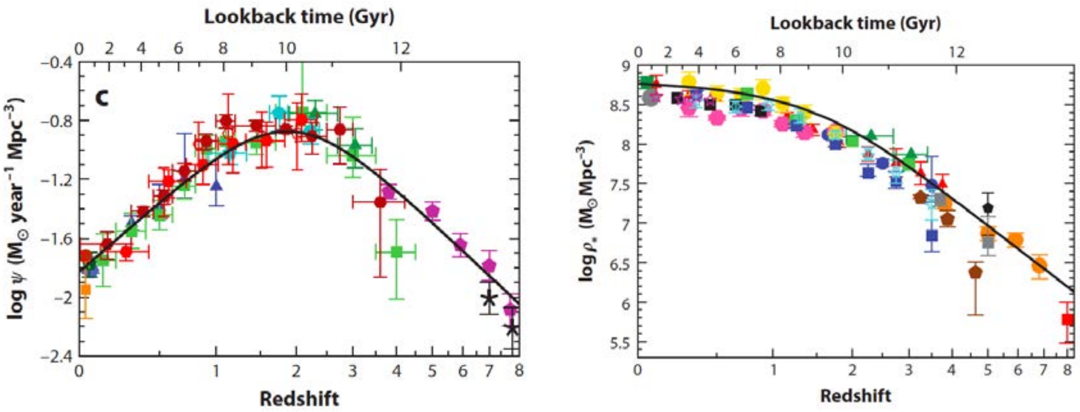

Figure 1.1: Left panel: cosmic evolution of star formation rate density in the universe (cSFRD). Right panel: cosmic evolution of stellar mass density in the universe. This figure is taken from Madau and Dickinson (2014).

1.2 Global properties of galaxies

Thanks to the increasing number of the imaging and spectroscopic surveys of galaxies, we can study galaxy evolution statistically. Over the last decades, the imaging and spectroscopic surveys of galaxies have been focusing on studying the global galaxy properties. Many galaxy scaling relations have been studied and give insights toward the understanding of galaxy evolution. Among the others, those surveys have revealed the following (briefly described in the following subsections) scaling relations that are meaningful for understanding of the galaxy evolution.

1.2.1 Galaxy bimodality: blue and red sequences

Distribution of galaxies on the color versus absolute magnitude (or color versus stellar mass) plane is strongly bimodal (e.g. Strateva et al. 2001; Blanton et al. 2003; Kauffmann et al. 2003a; Baldry et al. 2004). Two sequences are emerged from the distribution of galaxies on that plane, *blue*- and *red sequences* (see left panel of Fig. 1.2). Less populated region between the two sequences is called *green valley*. Low mass galaxies populate the blue sequence, while massive galaxies populate the red sequence. The $(u-r)$ color of local galaxies ($0.02 < z < 0.05$; the redshift range considered in Schawinski et al. (2014)) tell us about age of the stellar population in the galaxies with redder mean older age. Kauffmann et al. (2003a) investigated distribution of galaxies on the D$_\mathrm{n}$(4000) (4000Å) versus M_* plane and found a similar bimodality trend as in the color versus M_* plane, with massive galaxies populate the old sequence and low mass galaxies populate the young sequence, furthermore, they found a typical transition mass (between the old and young sequences) of $\sim 10^{10.5} M_\odot$.

The color bimodality trend mentioned above is correlated with the galaxy morphology. As investigated by Schawinski et al. (2014) (see the two separate color-M_* diagrams for early-type and late-type galaxies in the left panel of Fig. 1.2), majority of the galaxies in the red sequence are early-type or elliptical, while majority of the galaxies in the blue sequence are late-type or disk

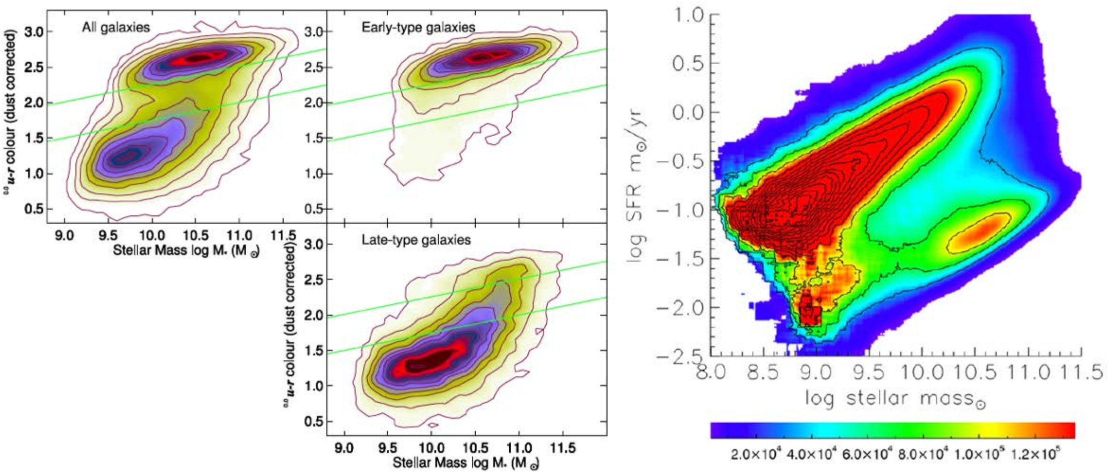

Figure 1.2: Left panel: distribution of local galaxies on the $u - g$ versus M_* plane for all galaxies as well as early-type and late-type galaxies separately. The green lines define the locus occupied by green-valley galaxies. The contours are linear and scaled to the highest value. This figure is taken from Schawinski et al. (2014). Right panel: distribution of galaxies on the SFR versus M_* plane. The color coding represents the number density of galaxies, which has been corrected for the volume incompleteness. The SFR and M_* are taken from the MPA-JHU catalog (Brinchmann et al. 2004). This figure is taken from Renzini and Peng (2015).

galaxies. However, there is a substantial amount of late-type galaxies in the green-valley and red sequence. The authors interpreted the observed trend with two quenching processes, which are fast and slow quenching processes. Red (quiescent) early-type galaxies seem to be a product of fast quenching, which caused by a destruction of gas reservoir by some feedback mechanism (due to e.g. AGN, supernova). The feedback could be triggered by a merger event which could also transform the galaxy morphology from late-type to early-type. Late-type galaxies in the green-valley and red (quiescent) sequence are thought of being experienced slow quenching, which could be caused by a shut off of the cosmic gas accretion, perhaps at the time when its host dark matter halo reaches a critical mass. The shut off of the cosmic gas accretion results in a gradual run out of the remaining gas and declining of the SFR.

Distribution of galaxies on the SFR versus M_* plane also found to be bimodal (see right panel of Fig. 1.2). Two sequences are emerged in the distribution of galaxies on the SFR versus M_* plane, *star-forming sequence* (also called *star formation main sequence*) and *quiescent sequence*. The star formation main sequence is populated by star-forming galaxies, while quiescent sequence is populated by quiescent (also called quenched) galaxies. Sparse region between the star formation main sequence and the quiescent sequence corresponds to the *green-valley*.

Physical mechanisms responsible for the quenching of the star formation in galaxies are still unclear. Several quenching mechanisms have been proposed. Starburst event can rapidly consumes gas in the galaxy and make the galaxy lack the gas. If cold gas inflow into the galaxy shut off due to the stellar feedback associated with the starburst, the star formation in the galaxy could be quenched (e.g. Murray et al. 2005). Moreover, the cold gas supply could also be suppressed by the feedback from an active galactic nuclei (AGN) through quasar or radio feedback mode (e.g. Sanders et al. 1988; Silk and Rees 1998; Springel et al. 2005; Hopkins et al. 2006, 2008; Schawinski et al. 2006; Fabian 2012). The suppression of the cold gas inflow leading to the quenching could also happen once the growth of the dark matter halo reaches a critical mass ($\sim 10^{12} M_{\odot}$) above which newly accreted gas will be shock heated and stay at the virial temperature, i.e. transition from the cold accretion mode to the hot accretion mode (e.g. Birnboim and Dekel 2003; Dekel and Birnboim 2006). On the other hand, growth of the central bulge component could also quenches the star formation in the galaxy through its deep gravitational potential, which could stabilize gas in the disk against local instability and prevent the gas from collapse. This scenario is called a morphological quenching process (e.g. Martig et al. 2009; Genzel et al. 2014).

1.2.2 Global star formation main sequence

As pointed out in the previous section, star-forming galaxies reside in a sequence called star formation main sequence (SFMS) on the SFR versus M_* plane. The nearly linear SFMS suggests that SFR increases with M_* as a power law (SFR $\propto M_*^{\alpha}$ with $\alpha \sim 1$) over at least two orders of magnitude in M_* ($\sim 10^9 - 10^{11} M_{\odot}$). This relation has been studied by many researchers over the last decade (e.g. Brinchmann et al. 2004; Elbaz et al. 2007; Noeske et al. 2007; Salim et al. 2007; Whitaker et al. 2012, 2014; Speagle et al. 2014; Renzini and Peng 2015). The SFMS relation holds up to high redshifts (see Fig. 1.3) and shows evolution in terms of its normalization and slope. The evolution of the normalization shows a factor of ~ 2 dex decrease from $z \sim 6$ to $z \sim 0$ (Speagle et al. 2014). The decreasing normalization with decreasing redshift reflects a decreasing global sSFR with decreasing redshift. While the normalization and slope of the SFMS evolve with redshift, the scatter of the SFMS, which is ~ 0.3 dex, is roughly constant across a wide redshift range (Whitaker et al. 2012; Speagle et al. 2014). Only few galaxies have significantly elevated SFR with respect to the SFMS, and their contributions only account for $\sim 10\%$ of the overall star formation over a redhsift range of $0 < z < 2$ (Rodighiero et al. 2011; Sargent et al. 2012). The tightness of the SFMS implies the importance of internal secular process against stochastic merger process in driving the star formation activity in majority of the galaxies (Noeske et al. 2007). The confinement of galaxies on the SFMS for a long period of time suggests a steady evolution of galaxies governed by quasi-steady gas inflow, gas outflow, and gas consumption by the star formation activity.

1.2.3 Downsizing phenomenon

The bimodal distribution of galaxies on the color-M_* plane suggests that the stellar populations in massive galaxies are systematically older than those in low mass galaxies. The flatter relation of the global SFMS than the linear relation (see a compilation by Speagle et al. (2014)) suggests that specific SFR (sSFR=SFR/M_*) is decreasing with increasing M_* (see e.g. Abramson et al. 2014). The sSFR of a galaxy reflects a ratio between current star formation rate and past integrated star formation

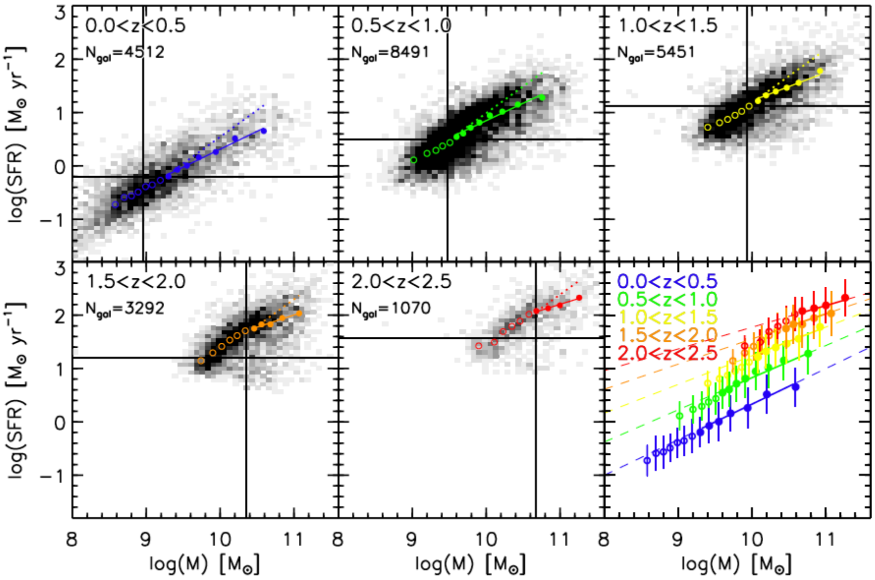

Figure 1.3: Global star formation main sequence relation up to $z \sim 2.5$. The running medians are plotted (with different colors represent different redshift) overlaid on the galaxy distribution. The power-law fit above the M_* and SFR completeness limits are shown with solid line. Comparison among the star formation main sequence relations at the various redshift are plotted in the bottom right panel. This figure is taken from Whitaker et al. (2012).

rate, thereby it reflects the quenching process of the galaxy. Those trends show that massive galaxies are more passive than low mass galaxies. Observations of high redshift galaxies also found a similar trend. Juneau et al. (2005) observed a dependence of cosmic star formation history on the stellar mass (see Fig. 1.4). The figure shows that at entire redshift range ($0.8 < z < 2.0$), average star formation rate density of more massive galaxies is lower than that of less massive galaxies. Moreover, the figure shows that the average SFR density of massive galaxies decline sharper than low mass galaxies in the same redshift range. This trend of the faster quenching of more massive galaxies compared to the less massive galaxies, or in other word, the star formation was proceeded in massive galaxies in the past and transiting toward low mass galaxies in the present day. The transition is called 'downsizing' (firstly suggested by Cowie et al. (1996)).

1.3 Spatially resolved view of the galaxy evolution

Study of the global properties of galaxies over the last decades only considered galaxies as a single point. Information on the global properties of galaxies only give clues regarding scaling relations among the global properties and still lack of insights on the physical mechanism governing the global scaling relations and galaxy evolution processes in general. Recalling that galaxies are complex systems (consisting of stars, gas, dust, and dark matter) that comes with various structures and morphologies, it is important to study structural properties and spatially resolved properties of

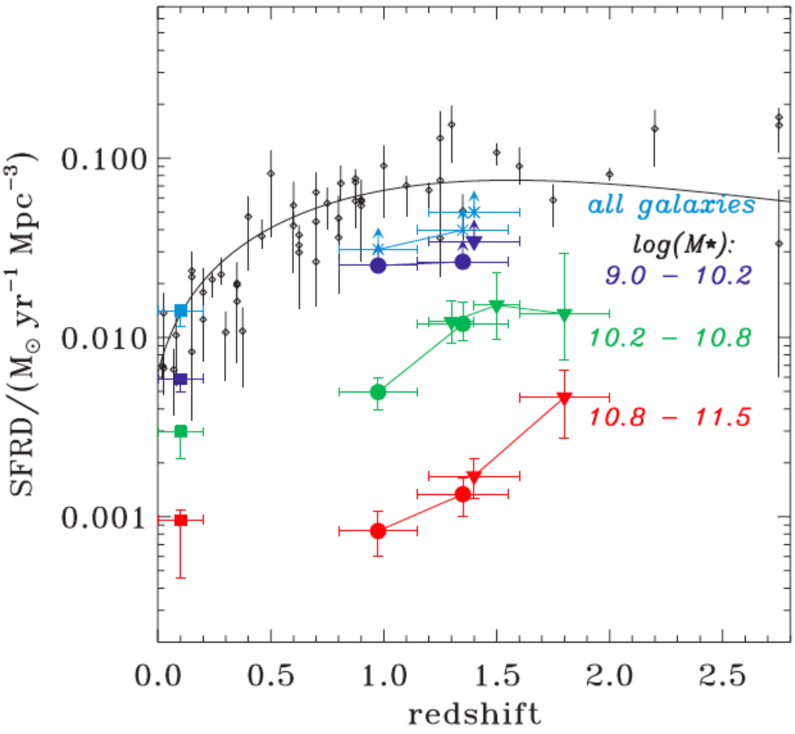

Figure 1.4: Cosmic star formation history as a function of stellar mass. SFR density derived from $L([\mathrm{O_{II}}])$ and from $L(2000\text{Å})$ are shown with circle and triangle, respectively. The symbols are color-coded with the stellar mass ranges. The squares are the SFR densities at the local universe derived by Brinchmann et al. (2004). The small diamonds are SFR densities derived by Hopkins (2004). This figure is taken from Juneau et al. (2005).

galaxies in order to reveal the physical processes governing the galaxy evolution. Nowadays, there is a growing interest on studying spatially resolved properties of galaxies in the local universe as well as at high redshifts by using various instruments and techniques, such as integral field spectroscopy (IFS), grism spectroscopy, and narrow-band imaging. Recent progress in the studies of spatially resolved properties of galaxies have given us clues toward the understanding of the physical processes governing the galaxy evolution. In the following, we highlights some recent progresses made by the studies of spatially resolved properties of galaxies.

1.3.1 Distinct structures between star-forming and quiescent galaxies

As pointed out in Section 1.2.1, there is a morphological difference between galaxies in the blue (star-forming) cloud and red (quiescent) sequence, such that blue cloud is dominated by late-type galaxies, while red sequence is dominated by early-type galaxies. Generally, late-type galaxies have a structure that is dominated by a thin disk with a characteristic spiral pattern and they often have a central spheroidal component (i.e. bulge), while early-type galaxies have round shape and smooth light distribution with isophotes (i.e. lines of constant surface brightness) that have nearly

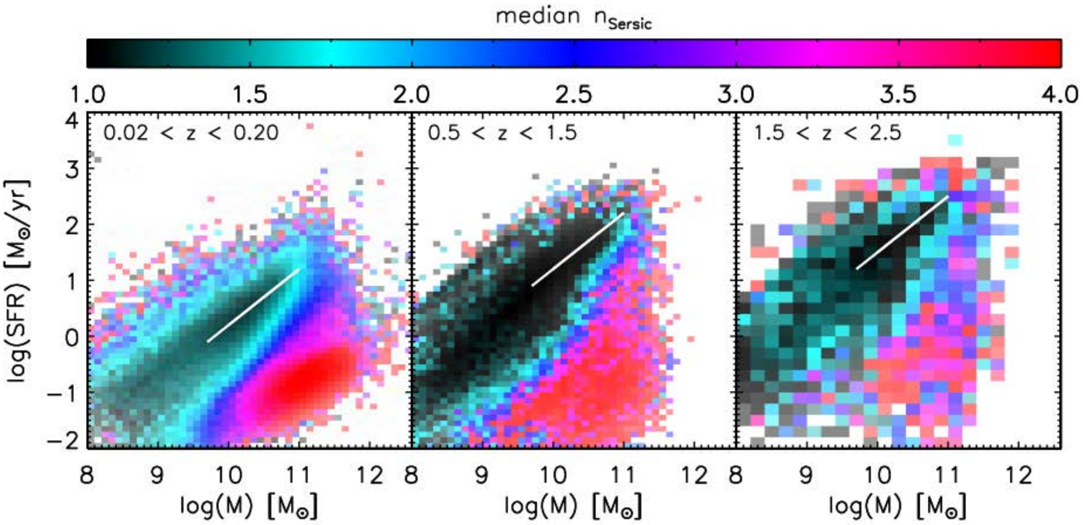

Figure 1.5: Sérsic index of the galaxies across the global SFMS on the SFR versus M_* plane. Sérsic index is represented with the color-coding. Different panel represents different redshift bin. This figure is taken from Wuyts et al. (2011).

elliptical shapes. Optical surface brightness profile of the early-type galaxies is best-fitted with the de Vaucouleurs profile (de Vaucouleurs 1948). More generally, surface brightness profile of late-type and early-type galaxies can be fitted by the Sérsic profile (Sérsic 1963) with late-type galaxies having low Sérsic index ($n \lesssim 2.5$) while early-type galaxies having high Sérsic index ($n \gtrsim 2.5$).

Investigation of the structural properties of galaxies at $0.02 < z < 2.5$ using high spatial resolution images from the *Sloan Digital Sky Survey* (SDSS) and the *Hubbe Space Telescope* (HST) by Wuyts et al. (2011) (see Fig. 1.5) found that star-forming galaxies, which are located on the global SFMS in the SFR vs. M_* plane, have structures that are best-fitted with a low Sérsic index profile ($n \lesssim 2$), while quiescent galaxies, which are located on the quiescent sequence, have structures that are best-fitted with high Sérsic index profile ($n \gtrsim 2$). This trend holds in all redshift bins within the considered redshift range ($0.02 < z < 2.5$) suggesting that the Hubble sequence (firstly proposed by Edwin Hubble, Hubble 1926, 1936) is already in place at $z \sim 2$. It is also implied by this trend that there is a tendency of changing structure from a disk-dominated system to a bulge-dominated system as star-forming galaxies evolve into quenched state. A reverse SFR-n trend is found in the upper envelope of the global SFMS, where galaxies have high n. This reverse trend suggests a rapid buildup of the central mass concentration in the starburst galaxies.

1.3.2 Indications of the inside-out growth

Recent IFS observations have shed lights on the understanding of how galaxies establish their structures. An emerging picture is that galaxies tend to construct their structures (i.e. stellar mass) from their central region first, then the construction propagates toward outskirt (e.g. van Dokkum et al. 2010; Nelson et al. 2012; Morishita et al. 2015; Nelson et al. 2016a; Tacchella et al. 2015; Tadaki et al.

2017). This picture of galaxy growth agrees with the inside-out growth scenario (Kauffmann 1996; Cole et al. 2000; Firmani and Avila-Reese 2000; van den Bosch 2002; Stringer and Benson 2007). One way to investigate how galaxies built their structures is by comparing the spatial extents (sizes) of the spatially resolved distributions of H_α emission and stellar continuum. The H_α emission map tells us about the spatially resolved distribution of the ongoing star formation activities, while the stellar continuum (i.e. flux in the optical band) map tells us about the spatially resolved distribution of the assembled stellar mass by star formation activities in the past. Nelson et al. (2012) compared sizes (i.e. effective radii) of the H_α emission map ($r_e(\mathrm{H}_\alpha)$) and stellar continuum (observed F140W flux or rest-frame R band flux) map ($r_e(\mathrm{R})$; see left panel of Fig. 1.6) of star-forming galaxies at $0.8 < z < 1.3$ and found that the H_α emission map is more extended than the map of rest-frame R band flux (i.e. $r_e(\mathrm{H}_\alpha) > r_e(\mathrm{R})$) for majority of the sample galaxies. This trend ($r_e(\mathrm{H}_\alpha) > r_e(\mathrm{R})$) means that ongoing star formation is distributed in more extended area than the assembled stellar mass, implying that their growth began with smaller area in the central region and has proceeded outward, i.e. inside-out growth. As shown in Fig. 1.6, some galaxies have $r_e(\mathrm{H}_\alpha) < r_e(\mathrm{R})$, implying that they might be experiencing central starburst by which they are constructing their central massive component. The larger size of the H_α map than the stellar continuum map is observed across almost entire M_* range ($\log(M_*/M_\odot) > 9.5$), see the sizes-M_* relation in right panel of Fig. 1.6 from an analyses done by Nelson et al. (2016a). Despite their clear trends of the inside-out growth, the above observational results (especially the $r_e(\mathrm{H}_\alpha)$) have to be taken with a caution, because spatial variation of dust extinction was not taken into account in the analysis of those two works. Centrally concentrated dust extinction profile (as observed by e.g. Nelson et al. 2016b; Tacchella et al. 2018) could shrink the $r_e(\mathrm{H}_\alpha)$.

1.3.3 Indications of the inside-out quenching

Recent IFS observations also have shed lights on an understanding about how galaxies quench their star formation. An emerging picture is that galaxies tend to quench their star formation activity in an 'inside-to-outside' manner, similar as the growth trend discuss in the previous section. Indications of this inside-out quenching are found through various ways. Abramson et al. (2014) analyzed a dependence of the global SFMS slope on the inclusion of bulge component in the calculation of the integrated SFR and M_*. The authors found that the flatter relation, with slope less than unity, of the global SFMS in the local universe is caused by the inclusion of bulge component (which gives little contribution to the total SFR but gives high contribution to the total M_*), implying the existence of quiescent central region in the local galaxies. Using IFS observations, previous researchers found a centrally suppressed sSFR radial profile in massive ($\log(M_*/M_\odot) > 10.0$) local galaxies (e.g. González Delgado et al. 2016; Belfiore et al. 2018) and at high redshifts ($z \sim 1$ by Nelson et al. (2016a) and $z \sim 2$ by Tacchella et al. (2015, 2018)). Fig. 1.7 shows average radial profiles of SFR surface density ($\Sigma_{\mathrm{SFR}}(r)$), M_* surface density ($\Sigma_*(r)$), and sSFR (sSFR(r)) of star-forming galaxies at $z \sim 2$ reported by Tacchella et al. (2015). The authors found that the average

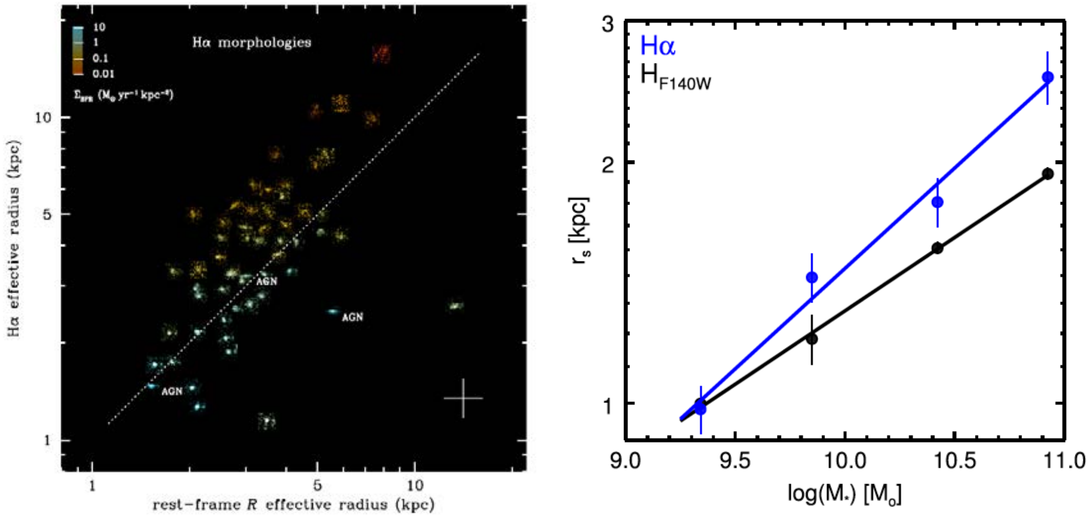

Figure 1.6: Left panel: comparison between the effective radius of the spatially resolved distribution of the H_α emission and the effective radius of the spatially resolved distribution of the rest-frame R band (observed F140W) flux in star forming galaxies at $0.8 < z < 1.3$. Each galaxy in the plot is shown with its morphology in H_α. This figure is taken from Nelson et al. (2012). Right panel: size (i.e. effective radius)-M_* relations for maps of H_α (blue points) and F140W (rest-frame R band) flux (black points) of star-forming galaxies at $0.7 < z < 1.5$. This figure is taken from Nelson et al. (2016a). Spatial variation of the dust extinction is not taken into account in the analysis of those two works.

sSFR radial profile of galaxies in the most massive bin is centrally suppressed. Moreover, Σ_* of the central region of those massive galaxies are similar to those of local early-type galaxies (see the bottom right panel), implying that quiescent central component (i.e. bulge) is already formed in those massive galaxies.

1.4 Open questions and aims of this thesis

The advent of IFS observations has shed lights on the understanding of how galaxies build their structures and quench their star formations (as described in the previous sections). The emerging picture is that galaxies seem to build their structures and quench their star formations in the 'inside-to-outside' manner. However, the two phenomenons (inside-out growth and inside-out quenching) have only been discussed separately in the literature (as mentioned in the previous sections) as if the both phenomenons are independent each other. It is unclear whether the two phenomenons are correlated each other and occur simultaneously or not. Moreover, correlation (i.e. consistency) between the evolution of the spatially resolved SFR and stellar mass buildup in the galaxies is unclear.

In order to study the evolution of the spatially resolved SFR and the stellar mass buildup in the galaxies across the cosmic time, information on the spatially resolved SFR and stellar mass in galaxies in a wide redshift range is needed. Despite the capabilities of the IFS observations in

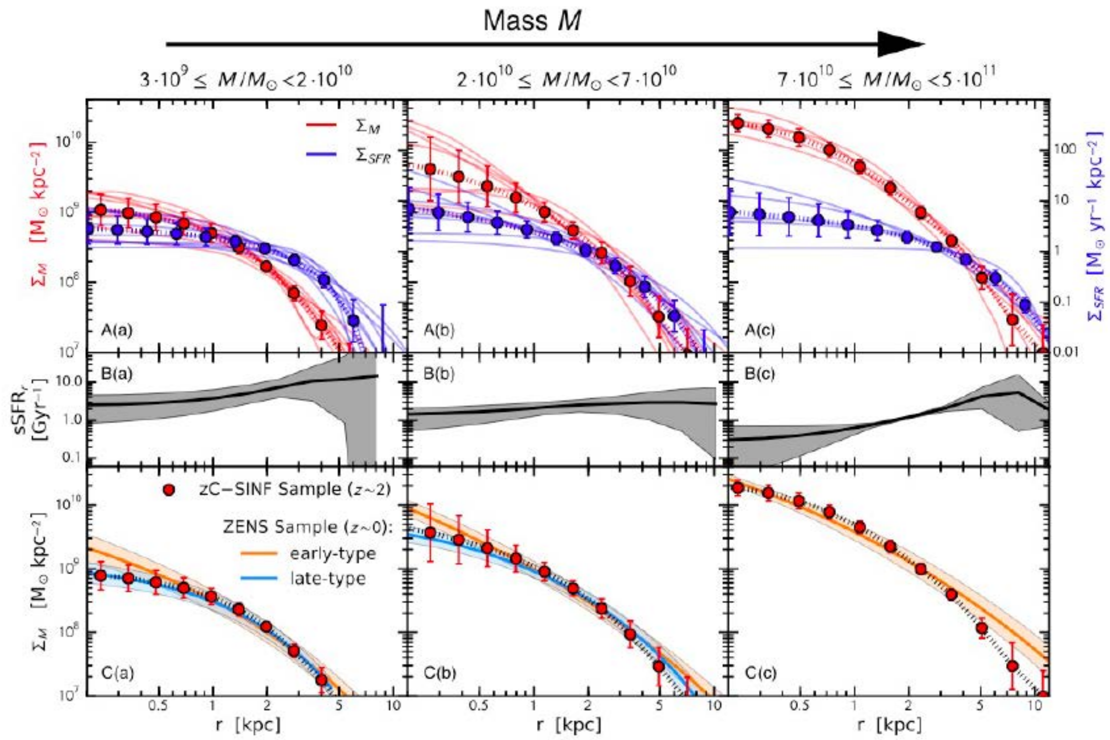

Figure 1.7: Indication of the inside-out quenching from radial profiles of ($\Sigma_{\mathrm{SFR}}(r)$), M_* surface density ($\Sigma_*(r)$), and sSFR (sSFR(r)) of star-forming galaxies at $z \sim 2$. Three columns from left to right show results for three M_* bins containing 9, 8, and 5 galaxies, respectively. Top row shows the $\Sigma_{\mathrm{SFR}}(r)$ (blue) and $\Sigma_*(r)$ (red). Middle row shows the sSFR(r). Bottom row shows comparison between the $\Sigma_*(r)$ of the three mass bins (red) and $\Sigma_*(r)$ of local early-type (orange) and late-type (cyan) galaxies. This figure is taken from Tacchella et al. (2015). Reprinted with permission from AAAS.

resolving physical properties in the galaxies, the IFS observations commonly could only observe sample galaxies at narrow redshift range, and connecting spatially resolved properties of galaxies at wide redshift range derived from various IFS observations is difficult, due to some technical aspects that are addressed in Section 2.3.1. In order to study the spatially resolved SFR and stellar mass of galaxies at wide redshift range consistently, a single method which could be applied to sample galaxies in a wide redshift range is needed. The usage of a single method could reduce biaess that emerges if different methods are used for analyzing sample galaxies at different redshifts.

In this thesis research, we use a different approach in deriving the spatially resolved SFR and stellar mass in galaxies at $z \sim 0$ and $z \sim 1$. We use a method based on spatially resolved spectral energy distribution (SED) fitting, which is called the *pixel-to-pixel SED fitting*. Reason for using this method is that the same method could be applied to sample galaxies at different redshifts, in this case $z \sim 0$ and $z \sim 1$, so the systematic bias (causes by the usage of different method for galaxies at different redshifts) could be reduced. Detailed description about this method is presented in Section 3. By using this method, we analyze spatially resolved SFR and stellar mass in massive

($\log(M_*/M_\odot) \geqslant 10.5$) disk galaxies at $z \sim 1$ and $z \sim 0$ to study stellar mass buildup and quenching process in the massive disk galaxies over the last 10 Gyrs.

As suggested by Schawinski et al. (2014) (which is described in Section 1.2.1), late-type (disk) galaxies in the red-sequence are product of a steady slow quenching of star-forming late-type galaxies, which could require several Gyrs. The authors propose a strangulation process as the possible cause of the slow quenching. In order to investigate what mechanism of the slow quenching that really happens in disk galaxies, and furthermore study the structural evolution of massive disk galaxies, we focus on disk galaxies in this research. If disk galaxies experienced strangulation (stop of gas accretion) and star formation proceed with the remaining gas in the galaxies, we expect to see a steady evolution (i.e. decrease or increase) of the radial profiles of SFR and stellar mass. In addition to that, we also study the scaling relation between surface densities of SFR ($\Sigma_{\rm SFR}$) and M_* (Σ_*) in kpc scale, namely spatially resolved star formation main sequence in massive disk galaxies at $z \sim 1$ and $z \sim 0$, and also its cosmic evolution during $0 \lesssim z \lesssim 1$.

Overall, goals of this thesis are:

1. Study the spatially resolved distributions of SFR and M_* in massive disk galaxies at $0.01 < z < 0.02$. Key aspects include: (a) the scaling relation between $\Sigma_{\rm SFR}$ and Σ_* and effect of global M_* and sSFR on the scatter of this relation; (b) the radial distributions of $\Sigma_{\rm SFR}$, Σ_*, and sSFR, and effect of global M_* and sSFR on those radial distributions; (c) spatially resolved distributions of SFR and M_* in barred- and non-barred galaxies, and effect of bar on the secular evolution of the disk galaxies,

2. Study the spatially resolved distributions of SFR and M_* in massive disk galaxies at $0.8 < z < 1.8$. Key aspects include: (a) the scaling relation between $\Sigma_{\rm SFR}$ and Σ_* and effect of global sSFR on the shape of this relation; (b) the radial distributions of $\Sigma_{\rm SFR}$, Σ_*, and sSFR, and effect of global M_* and sSFR on those radial distributions,

3. Study the evolution of the radial distribution of SFR and radial stellar mass buildup in massive disk galaxies over the last 10 Gyrs by connecting the results from the preceding two analysis. Moreover, deriving an empirical model for the evolution of the surface density radial profiles ($\Sigma_{\rm SFR}(r)$, $\Sigma_*(r)$, and sSFR(r)) and investigate the slow quenching process in massive disk galaxies.

Goals 1, 2, and 3 are addressed in Chapters 4, 5,and 6, respectively. Sample selection for local and high redshift galaxies are described in Chapter 2. Chapter 3 presents details of the methodology. Finally, we present the summary of this thesis and possible future extensions from the current research in Chapter 7. Throughout this thesis, cosmological parameters of $\Omega_m = 0.3$, $\Omega_\Lambda = 0.7$, and $H_0 = 70 {\rm kms}^{-1}{\rm Mpc}^{-1}$ are assumed. M_* is used to represent the integrated stellar mass, while m_* is used to represent a total stellar mass within a sub-galactic region. As will be described in Chapter 2, our sample contains galaxies at $0.01 < z < 0.02$ and galaxies at $0.8 < z < 1.8$. For simplicity, throughout this thesis, we shorten $0.01 < z < 0.02$ as $z \sim 0$ and $0.8 < z < 1.8$ as $z \sim 1$.

Chapter 2

Data sample

2.1 Sample galaxies in the local universe

In order to study the structural evolution of massive disk galaxies over the last 10 Gyrs, we construct samples of massive disk galaxies in the local universe and at $z \sim 1$. The selection criteria for defining the sample galaxies at $z \sim 1$ is described in the next section, while the selection criteria for defining the sample galaxies in the local universe is described in this section. We define our $z \sim 0$ sample using the MPA-JHU (Max-Planck-Institut für Astrophysik - Johns Hopkins University) galaxy catalog [1]. In the catalog, M_* is derived based on fits to the photometry following Kauffmann et al. (2003b) and Salim et al. (2007), and SFR is derived based on emission line indices following Brinchmann et al. (2004). The sample galaxies are defined by applying the following criteria: (1) redshift range of $0.01 < z < 0.02$, (2) M_* higher than $10^{10.5} M_{\odot}$, (3) spiral morphology, and (4) face-on disk with ellipticity less than 0.6 or $b/a > 0.4$ (with b and a are semi-minor and semi-major axes, respectively).

The redshift range is determined to acquire a spatial resolution of $1 - 2$ kpc with the *Galaxy Evolution Explorer* (GALEX) NUV-band point spread function (PSF), which corresponds to 5.3 arcsec and is the largest among the seven imaging bands from the GALEX and *Sloan Digital Sky Survey* (SDSS) (FUV, NUV, u, g, r, i, and z) used in this research. The spatial sampling of the GALEX image ($1.5''$ pixel^{-1}), which also defines the final pixel scale achieved in the analysis of this research as the SDSS image is brought to the same spatial sampling as the GALEX image, corresponds to a physical scale of 0.3 - 0.6 kpc at the $0.01 < z < 0.02$. Because we focus on massive galaxies, we set the M_* limit. As massive galaxies have larger sizes than less massive galaxies, choosing massive galaxies gives another benefit regarding the resolution. Because we focus on disk galaxies, we only select spiral galaxies. We follow the morphological classification (spiral and elliptical) in the SDSS website [2], which adopts the morphological classification by the Galaxyzoo project [3] (Lintott et al. 2008). In addition to that, we also inspect the SDSS *gri* composite image

---

[1] `https://wwwmpa.mpa-garching.mpg.de/SDSS/DR7/`

[2] `http://skyserver.sdss.org/dr10/en/tools/toolshome.aspx`

[3] `https://www.zooniverse.org/projects/zookeeper/galaxy-zoo/`

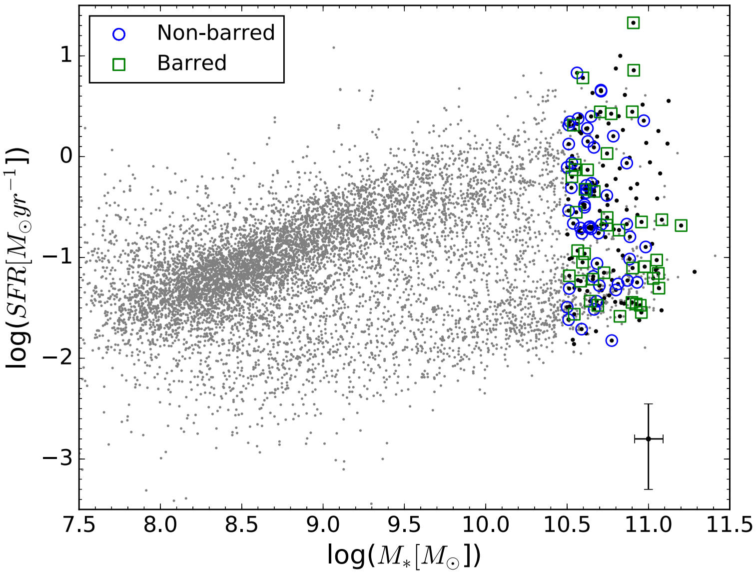

Figure 2.1: Integrated SFR versus M_* of galaxies at $0.01 < z < 0.02$ from MPA-JHU catalog and location of the sample galaxies on the SFR - M_* plane. Black points represent spiral galaxies with $\log(M_*/M_\odot) > 10.5$ that have GALEX imaging. The sample galaxies considered in this research are marked with blue open circles and green open squares for non-barred and barred galaxies, respectively. The cross at bottom right side indicates the average uncertainties of SFR and M_*. This figure is taken from Abdurro'uf and Akiyama (2017).

of each galaxy. We limit our sample to face-on galaxies with ellipticity less than 0.6 or $b/a > 0.4$ to minimize the effect of dust extinction, which tend to be severe in highly-inclined galaxies. By focusing on face-on galaxies, we could also expect to reduce the bias due to the effect of inclination on the spatially resolved analysis. The ellipticities of the selected massive spiral galaxies are derived by averaging the elliptical isophotes of the r-band image, which is obtained using the `ellipse` command in `IRAF`, outside of the effective radius (see Section 4.4.1 for detailed description on this issue). In addition to the above four criteria, we require the sample galaxies to have imaging data in the FUV and NUV bands of GALEX, and we only consider galaxies that have more than four bins (of pixels), where each bin has a signal-to-noise (S/N) of more than 10 in all of the seven bands (see Section 3.1.4 for the description on the pixel binning method). Number of galaxies selected using the above criteria is 152. Fig. 2.1 shows the integrated SFR versus M_* of galaxies at $0.01 < z < 0.02$ from the MPA-JHU catalog. The black points represent spiral galaxies with $\log(M_*/M_\odot) > 10.5$ that have both GALEX and SDSS imaging data. The sample galaxies considered in this research are marked with blue open circles and green open squares, which indicate non-barred and barred galaxies, respectively.

As we consider massive disk galaxies, consequently our sample contains large fraction (∼50% from the entire sample) of barred galaxies. It provides an opportunity to investigate the difference between the spatially resolved properties of barred- and non-barred galaxies and study the role of bar on the secular evolution of galaxies. We classified the barred- and non-barred galaxies based on the morphological types assigned for the sample galaxies by the NASA/IPAC Extragalactic Database (NED) [4] which include barred- and non-barred classification. Number of barred- and non-barred galaxies in the sample are 42 and 51, respectively.

2.2 Sample galaxies at high redshift

In order to trace back the structural evolution of massive disk galaxies over the last 10 Gyrs, sample galaxies at high redshift that have comparable global properties with the sample of local galaxies (with which the analysis results from the sample of local galaxies will be compared) have to be defined. We select sample of high redshift galaxies from the 3D-HST catalog (Skelton et al. 2014; Brammer et al. 2012). We only consider galaxies located in the *Great Observatories Origins Deep Survey - South* (GOODS-S) field. M_* in the catalog is derived through 0.3μm to 8μm SED modeling using the `FAST` code (Kriek et al. 2009). For SFR, we adopt the SFR derived using the combination of rest-frame UV and IR luminosities following Whitaker et al. (2014) instead of the SFR derived by the `FAST` code. Redshift is determined using three methods: (1) 0.3μm to 8μm photometric SED fitting using `EAZY` code (Brammer et al. 2008), (2) two-dimensional grism spectroscopy, and (3) ground-based spectroscopy. Sample of high redshift galaxies are selected using following criteria: (1) redshift range of $0.8 < z < 1.8$, (2) stellar mass higher than $\log(M_*/M_\odot) = 10.5$, (3) observed in the eight bands of the *Cosmic Assembly Near-infrared Deep Extragalactic Legacy Survey* (CANDELS) and 3D-HST (F435W, F606W, F775W, F814W, F850LP, F125W, F140W, and F160W), (4) face-on configuration with an ellipticity less than 0.6 or $b/a > 0.4$, and (5) late-type or disk morphology with Sérsic index (n) less than 2.6.

The redshift range is determined to achieve spatial resolution of ~ 1 kpc with F160W PSF, which is 0.19 arcsec and largest among the eight imaging bands. The PSF corresponds to a physical scale of 1.4 - 1.6 kpc at $0.8 < z < 1.8$, while the pixel scale, which is $0.06''$ pixel^{-1}, corresponds to a physical scale of 0.45 - 0.50 kpc in the redshift range. The upper limit in the redshift range corresponds to a look-back time of 9.90 Gyr, while the redshift range corresponds to a physical time-lag of 3.07 Gyr. Because we focus on massive galaxies, the stellar mass limit is defined, which is the same as that used to define the local galaxies sample. We only select face-on galaxies (which also applied in the selection of local galaxies sample) to minimize the effect of dust extinction, which thought to be severe in highly inclined galaxies, and to minimize bias in analysis of the spatially resolved properties due to the inclination effect. The ellipticity is calculated by averaging the elliptical isophotes of the F125W image outside of the effective radius. The elliptical isophotes are obtained using the `ellipse` command in `IRAF` (see Section 4.4.1 for detailed description on this issue). Because we focus on spiral/disk galaxies, we only select galaxies which show disk morphology. As the spiral arm structure is not prominent in high redshift galaxies (opposite to the local galaxies where spiral arm structure is more prominent and easily recognized), we quantitatively define disk

---

[4] `https://ned.ipac.caltech.edu/`

galaxies using the Sérsic index of the best-fitting Sérsic profile for the stellar mass surface density radial profile ($\Sigma_*(r)$). The calculation of $\Sigma_*(r)$ and the Sérsic index is explained in Section 5.2.3. In addition to the five selection criteria described above, we only select galaxies that have more than four bins of pixels. Each bin has S/N ratio of higher than 10 in all of the eight imaging bands (see Section 3.1.4 for the description on the pixel binning method).

For galaxies (selected by the above criteria) with the photometric redshifts, we do SED fitting to check the reliability of the redshift estimations. The integrated fluxes in the eight bands are calculated to obtain the integrated SED of the galaxy. The model SEDs with which the galaxy's integrated SED is fitted are calculated by assuming the photometric redshift as the true redshift of the galaxy. The SED fitting is done using the maximum likelihood method. Through this checking, we find eight galaxies with strange SED shapes and result in very large χ^2, which indicates unreliable redshift estimates, while the other galaxies have small χ^2, which indicates the reliability of their photometric redshifts. The eight galaxies with strange SED shapes are then excluded from the sample. The above selection processes result in 163 galaxies. Finally, we exclude galaxies with high probability of hosting an active galactic nuclei (AGN) to avoid contamination by the contribution from the non-stellar AGN component to the broad band photometry. We look for the AGN-host galaxies by cross-matching the 163 galaxies with the *Chandra* 7 Ms sources catalog (Luo et al. 2017; Yang et al. 2017). The *Chandra* catalog contains X-ray sources from the $\sim$ 7 Ms exposure in the *Chandra Deep Field-South* (CDF-S), which covers GOODS-S field. We find 11 galaxies that have a luminous X-ray AGN activity ($L_{2-10\mathrm{keV}} > 10^{43}\mathrm{erg\ s}^{-1}$) among the sample. Final sample for this research (after excluding the 11 AGN-host galaxies) contains 152 galaxies. Top panel of Fig. 2.2 shows the integrated SFR versus M_* of the GOODS-S field galaxies at $0.8 < z < 1.8$ taken from the 3D-HST catalog. The blue large points show the 152 sample galaxies, while the purple stars represent the AGN-host galaxies. The black line and gray shaded represent the global SFMS relation by Speagle et al. (2014) that is calculated at the median redshift of the sample galaxies ($z = 1.217$) and the ±0.3 dex scatter around the global SFMS relation, respectively. Bottom panel in Fig. 2.2 shows M_* versus redshifts of the sample galaxies. It is shown that the redshifts of the sample galaxies are spread uniformly within the redshift range.

2.3 Imaging data-set

2.3.1 Reasons why using imaging data-set

Recently, there is a growing interests on studying the spatially resolved distributions of galaxy properties using integral field spectroscopy (IFS) observation. Using IFS observation, one could obtain spatially resolved spectra within a galaxy, i.e. spectrum from each sub-galactic region in the galaxy. Since spectrum is obtained for each sub-galactic region within the galaxy, physical properties that could be derived with a spectrum (including stellar population properties, e.g. stellar age, metallicity, stellar mass, SFR; gas properties, e.g. gas phase metallicity; and kinematics of gas

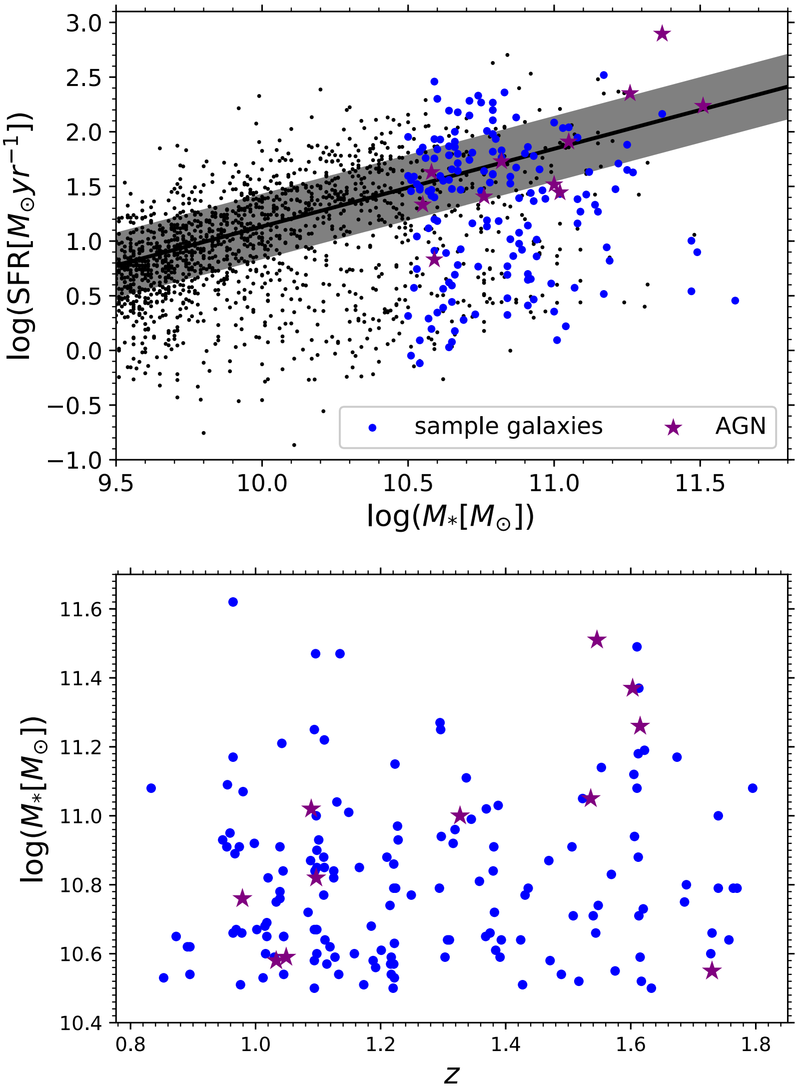

Figure 2.2: Top panel: integrated SFR versus M_* of the GOODS-S field galaxies at $0.8 < z < 1.8$ from the 3D-HST catalog and location of the sample galaxies on the SFR - M_* plane. The large blue points represent the 152 sample galaxies, while purple stars represent AGN-host galaxies which are excluded when selecting the sample galaxies. The black line and gray shaded area represent the global SFMS relation by Speagle et al. (2014) calculated at the median redhsift of the sample galaxies ($z = 1.217$) and the ±0.3 dex scatter around it, respectively. Bottom panel: M_* versus redshift of the sample galaxies. This figure is taken from Abdurro'uf and Akiyama (2018).

and stellar components) could be obtained for each sub-galactic region within the galaxy. It could provide us with the spatially resolved properties of the galaxy. Despite those capabilities of the IFS data-set, the IFS observations are always confined to limited sample of galaxies within a narrow redshift range due to the limited wavelength coverage given by the instrument and the high "cost" of this observation (i.e. expensive due to a long exposure needed for observing each galaxy). Some IFS surveys observed galaxies in the local universe, such as *Calar Alto Legacy Integral Field spectroscopy Area Survey* (CALIFA; Sánchez et al. 2012, redshift range:$0.005 < z < 0.03$), *Sydney-AAO Multi-object Integral field spectrograph galaxy survey* (SAMI; Bryant et al. 2015, redshift range: $z < 0.1$), *Mapping nearby Galaxies at Apache Point Observatory* (MaNGA; Bundy et al. 2015, redshift range: $0.01 < z < 0.15$), and other IFS surveys targeting galaxies at high redshift, such as *Spectroscopic Imaging survey in the Near-infrared with SINFONI* (SINS; Förster Schreiber et al. 2009, redshift range: $1 < z < 4$), 3D-HST (Brammer et al. 2012, redshift range: $1.0 < z < 3.5$), *The Grism Lens-Amplified Survey from Space* (GLASS; Treu et al. 2015), KMOS-3D (Wisnioski et al. 2015, redshift range: $0.7 \leqslant z \leqslant 2.7$), *KMOS Redshift One Spectroscopic Survey* (KROSS; Stott et al. 2016, redshift range: $0.7 < z < 1.5$).

Information on the spatially resolved properties in the galaxies in a wide redhsift range could gives us an opportunity to study the evolution of the internal structures of the galaxies with which insights on the physical mechanisms governing the galaxy evolution could be obtained. Currently provided data-sets from the IFS surveys mentioned above provide us with the pictures of the galaxy structures at various redshifts from which we could qualitatively infer the evolution of the galaxy structures. More quantitative examination of the structural evolution of galaxies need quantitatively connecting the spatially resolved properties of galaxies observed in a wide redhsift range. However, due to difference in specifications of the IFS observations mentioned above, quantitatively connecting the spatially resolved properties of galaxies based on their observations is difficult. Substantial efforts on calibrations need to be done in order to quantitatively connect the results from the various IFS surveys. The difference in specification includes: (1) difference in the spectral resolution, for example grism spectrograph of the 3D-HST has low spectral resolution (R$\sim$ 130) such that the H_α and [NII] emission lines are blended, while high spectral resolution (R$\sim$ 2000) of MaNGA fibre bundle spectrograph could resolve the two emission lines; (2) difference in rest-frame wavelength coverage, for example grism spectrograph of the 3D-HST has narrower rest-frame wavelength coverage compared to the fibre bundle of MaNGA. The rest-frame wavelength coverage of the grism spectrograph 3D-HST is narrow, such that spatially resolved H_α emission line could only be obtained for galaxies at $0.7 < z < 1.5$ and majority of those galaxies with H_α information do not have spatially resolved H_β emission line because the H_β could only be obtained for galaxies at $1.20 < z < 2.35$. Due to this limitation, information regarding spatially resolved dust extinction (which could be estimated using the Balmer decrement, H_α/H_β) could not be obtained for most of the sample galaxies considered by the 3D-HST. Due to this limitation, analysis on the spatially resolved star formation activity done by the 3D-HST assumes uniform dust extinction across the galaxy region (which is derived based on the integrated SED fitting), such as done in Nelson et al. (2012) and Nelson et al. (2016a). It contrasts with the capability of MaNGA survey with its full rest-frame optical wavelength coverage which could obtain spatially resolved distributions of both of the H_α and H_β for all the sample galaxies observed by MaNGA; (3) difference in the spatial resolution among the currently available data-sets from the above mentioned IFS surveys. Physical spatial resolutions of the MaNGA, CALIFA, SAMI, 3D-HST, and KROSS based on their redshift coverage are $\sim 0.5-5.0$ kpc, $\sim 0.26-1.50$ kpc, $\sim 0.17-3.70$ kpc, $\sim 1.0-1.2$ kpc, and $\sim 2.0-3.4$ kpc, respectively.

As described in Section 1.4, motivation of this research is to study the evolution of the spatially resolved star formation activity and its connection with the spatially resolved stellar mass buildup in massive disk galaxies from $z \sim 1$ to $z \sim 0$. In order to do that, information on the spatially resolved SFR and stellar mass of massive disk galaxies at $z \sim 0$ and $z \sim 1$ is required. It is also important to have the spatially resolved SFR and stellar mass of the galaxies at the both redshifts derived using the same methodology so that an unbiased quantitative comparison could be performed to connect the results in the both redshifts. For the reasons described previously, we do not use the spatially resolved spectroscopic data-sets form the IFS surveys targeting galaxies at $z \sim 0$ and $z \sim 1$. In this research, we apply the broad-band SED fitting method, which is commonly used to derive the global SFR and stellar mass of galaxies, to derive the spatially resolved SFR and stellar mass within the galaxies. We use imaging data-sets from the GALEX and SDSS to perform the spatially resolved SED fitting method (which is described in detailed in Section 3) for deriving the spatially resolved SFR and stellar mass of massive disk galaxies at $z \sim 0$, while that for massive disk galaxies at $z \sim 1$, we use imaging data-set from the CANDELS and 3D-HST. Those imaging data-sets have similar rest-frame wavelength coverage, which is FUV-NIR, and spatial resolutions. The rest-frame wavelength coverage and spatial resolution of the 7 bands imaging of GALEX+SDSS are 1500-9134 Å at the median redshift of the $z \sim 0$ sample ($z = 0.0165$) and 1.10-2.15 kpc at the considered redshift range, while those of the 8 bands imaging of CANDELS+3D-HST is 1948-6944 Å at the median redshift of the $z \sim 1$ sample ($z = 1.217$) and 1.4-1.6 kpc at the considered redshift range. Applying the same method, which is the pixel-to-pixel SED fitting (see Section 3), and the similar imaging data-set (similar rest-frame wavelength coverage and spatial resolution) could reduce a systematic biases associated with applying different methods to the sample galaxies at the different redshifts and could allow a consistent quantitative analysis connecting the results for the sample galaxies at both redshifts.

2.3.2 Imaging data-set from GALEX and SDSS

In order to construct spatially resolved SEDs of the galaxies in the $z \sim 0$ sample with rest-frame far-ultraviolet (FUV) to near-infrared (NIR) coverage, we use imaging data-sets from GALEX (Morrissey et al. 2007) and SDSS (Ahn et al. 2014), which cover $1350-10000$ Å. Combination of the two imaging data-sets, which consist of seven bands: FUV, NUV, u, g, r, i, and z, give spatially resolved SED with the rest-frame FUV to NIR coverage for galaxies at the $0.01 < z < 0.02$. Imaging data

Table 2.1: Specification of GALEX imaging data

Band	$\lambda_{\mathrm{central}}$[Å]	Width[Å]	FWHM	Survey type					
				AIS		MIS		DIS	
				exp. time[s]	5σ Depth[mag]	exp. time[s]	5σ Depth[mag]	exp. time[s]	5σ Depth[mag]
FUV	1528	442	$4''.3$	100	19.9	1500	22.6	30000	24.8
NUV	2271	1060	$5''.3$	100	20.8	1500	22.7	30000	24.4

Table 2.2: Specification of SDSS imaging data

Band	$\lambda_{\mathrm{effective}}$[Å]	FWHM	5σ Depth[mag]
u	3590	$1''.3$	22.3
g	4810	$1''.4$	23.3
r	6230	$1''.5$	23.1
i	7640	$1''.5$	22.3
z	9060	$1''.1$	20.8

from GALEX Data Release (DR) 6 [5] are sky-background subtracted. We use GALEX DR6 imaging data from the three survey types: All-sky Imaging Survey (AIS), Medium Imaging Survey (MIS), and Deep Imaging Survey (DIS). Specification of the GALEX imaging data is shown in Table 2.1. GALEX imaging data has spatial sampling of $1''.5$ pixel^{-1}. We use imaging data from SDSS Data Release (DR) 10 [6]. The SDSS imaging data is not sky-background subtracted. Sample sky image of a field is stored in a particular extension (HDU2) in the fits image of the field. By interpolating the sample sky image using the bilinear interpolation, we then can get full sky image of the field. Specification of SDSS imaging data is shown in Table 2.2. SDSS imaging data has spatial sampling of $0''.4$ pixel^{-1}.

2.3.3 Imaging data-set from CANDELS and 3D-HST

For the sample galaxies at $0.8 < z < 1.8$, we use combined imaging data-set from CANDELS (Grogin et al. 2011; Koekemoer et al. 2011) and 3D-HST (Brammer et al. 2012), which covers $4318 - 15396$ Å in the observer frame. We use the combined CANDELS+3D-HST imaging data, consisting of eight bands: F435W, F606W, F775W, F814W, F850LP, F125W, F140W, and F160W, from the 3D-HST public data-set [7]. The 3D-HST survey itself only provides F140W image, while the other seven band imaging are provided by CANDELS survey. The eight band imaging data cover rest-frame wavelength of $2123 - 9315$ Å and $1364 - 5988$ Å at $z = 0.8$ and $z = 1.8$, respectively. The eight band imaging provided by the 3D-HST are sky-background subtracted, brought into the same sampling ($0''.06$ pixel^{-1}), and PSF-matched to the PSF size of the F160W band ($0''.19$), which has the largest PSF size among the eight bands. Specification of the eight band imaging data is shown in Table 2.3.

---

[5] `http://galex.stsci.edu/GR6/`

[6] `http://www.sdss3.org/dr10/`

[7] `https://3dhst.research.yale.edu/Data.php`

Table 2.3: Specification of CANDELS and 3D-HST imaging data

Band	λ_{central}[Å]	Width[Å]	FWHM	5σ Depth[mag]
F435W	4318	993	0.11	27.3
F606W	5919	2225	0.11	27.4
F775W	7693	1491	0.10	26.9
F814W	8057	2358	0.10	27.2
F850LP	9036	2092	0.11	26.5
F125W	12471	2867	0.18	26.1
F140W	13924	3760	0.18	25.6
F160W	15396	2744	0.19	26.4

2.4 Ability of the rest-frame FUV-NIR photometric SED on breaking degeneracies existing in model SEDs

In pixel-to-pixel SED fitting method, spatially resolved SEDs of a galaxy with rest-frame FUV to NIR coverage are fitted with a set of model SEDs. In order to examine the ability of the rest-frame FUV-NIR photometric SED in breaking degeneracies existing in SEDs, especially the degeneracy between age and dust extinction, we calculate tracks of the model stellar populations on color-color diagrams that are made with photometric sampling of the GALEX+SDSS (for the $z \sim 0$) and CANDELS+3D-HST (for the $z \sim 1$). Model stellar populations are generated using the GALAXEV stellar population synthesis model (Bruzual and Charlot 2003) assuming Chabrier (2003) initial mass function (IMF) with a mass range of $0.1 - 100 M_{\odot}$, exponentially declining star formation history (SFH), and reddening effect by dust assuming Calzetti et al. (2000) dust extinction law. Fig. 2.3 shows tracks of model stellar populations on NUV-r versus FUV-NUV color-color diagram. In this figure, model SEDs are calculated at a redshift of $z = 0.019$. Different panel represents model stellar populations with different assumed τ of the exponentially decaying SFH. Clockwise from top left to bottom left panels show model stellar populations with $\tau = 0.8$ Gyr, $\tau = 1.0$ Gyr, $\tau = 8.0$ Gyr, and $\tau = 4.0$ Gyr. In each panel, variation in $E(B-V)$ color excess dust extinction is represented with color, while variation in metallicity is represented with different line style. Blue, green, and red colors represent $E(B-V) = 0$ (no extinction), $E(B-V) = 0.3$, and $E(B-V) = 0.6$, respectively. $Z = 0.004$ and $Z = 0.02$ are represented with solid line and dashed line, respectively.

It is shown by the Fig. 2.3 that the effect of dust extinction and aging could be separated by the NUV-r versus FUV-NUV color-color diagram especially for model stellar population with large τ ($\tau \gtrsim 2$ Gyr). For model stellar populations with large τ, FUV-NUV color is sensitive to the dust extinction effect and less affected by aging effect, while NUV-r color is sensitive to aging affect and less affected by dust extinction effect. In this color-color diagram, dusty star-forming and non dusty quiescent galaxies (or sub-galactic regions) are expected to reside in different locus. Dusty star-forming galaxies (or sub-galactic regions) will reside in top right side, while non dusty quiescent galaxies (or sub-galactic regions) will reside in bottom left side. For model stellar populations with small τ, overlapping among tracks only occur at old age, while the tracks are separated at young

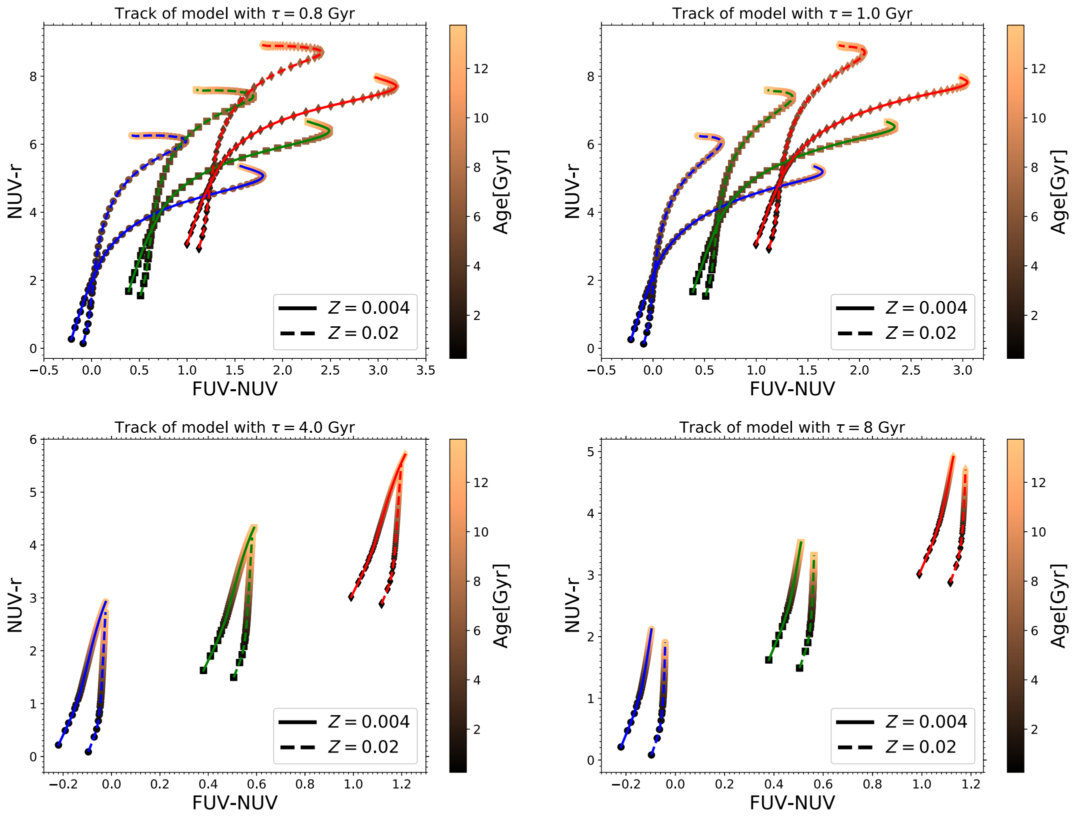

Figure 2.3: Breaking degeneracies in model SEDs with NUV-r versus FUV-NUV color-color diagram. Model SEDs are calculated at a redshift of $z = 0.019$. Different panel represents model stellar population with different assumed τ of decaying SFH. Clockwise from top left represent model SEDs with $\tau = 0.8$ Gyr, $\tau = 1.0$ Gyr, $\tau = 8.0$ Gyr, and $\tau = 4.0$ Gyr. In each panel, tracks of model stellar populations with two values of metallicities [$Z = 0.004$ (solid line) and $Z = 0.02$ (dashed line)] and three values of color excesses dust extinctions [$E(B-V) = 0$ (blue color), $E(B-V) = 0.3$ (green color), and $E(B-V) = 0.6$ (red color)] are shown. Color-coding represents age of the model stellar population.

age. With the NUV-r versus FUV-NUV color-color diagram, effect of Z to the model SED could also be distinguished from the effects of aging and dust extinction.

Fig. 2.4 shows similar analysis as for Fig. 2.3, but now photometric sampling provided by CANDELS+3D-HST imaging data-set is tested. In the figure, model SEDs are calculated at $z = 1.2$ and their tracks on F775W-F125W versus F435W-F606W color-color diagram, which has similar rest-frame coverage as the NUV-r versus FUV-NUV color-color diagram, is shown. Line style and color-coding used in this figure are the same as those used for Fig. 2.3. In the analysis for this figure, maximum value for age is set as the age of the universe at $z = 0.8$ (age$_{\text{max}}$ = 6.6 Gyr, which is the same maximum age that is set in construction of model SEDs to be used for fitting observed spatially resolved SEDs of the sample galaxies at $0.8 < z < 1.8$, as will be discussed in later chapters). Similar trends as shown in the Fig. 2.3 are found in this figure. The effect of dust extinction and aging could be separated by the F775W-F125W versus F435W-F606W color-color

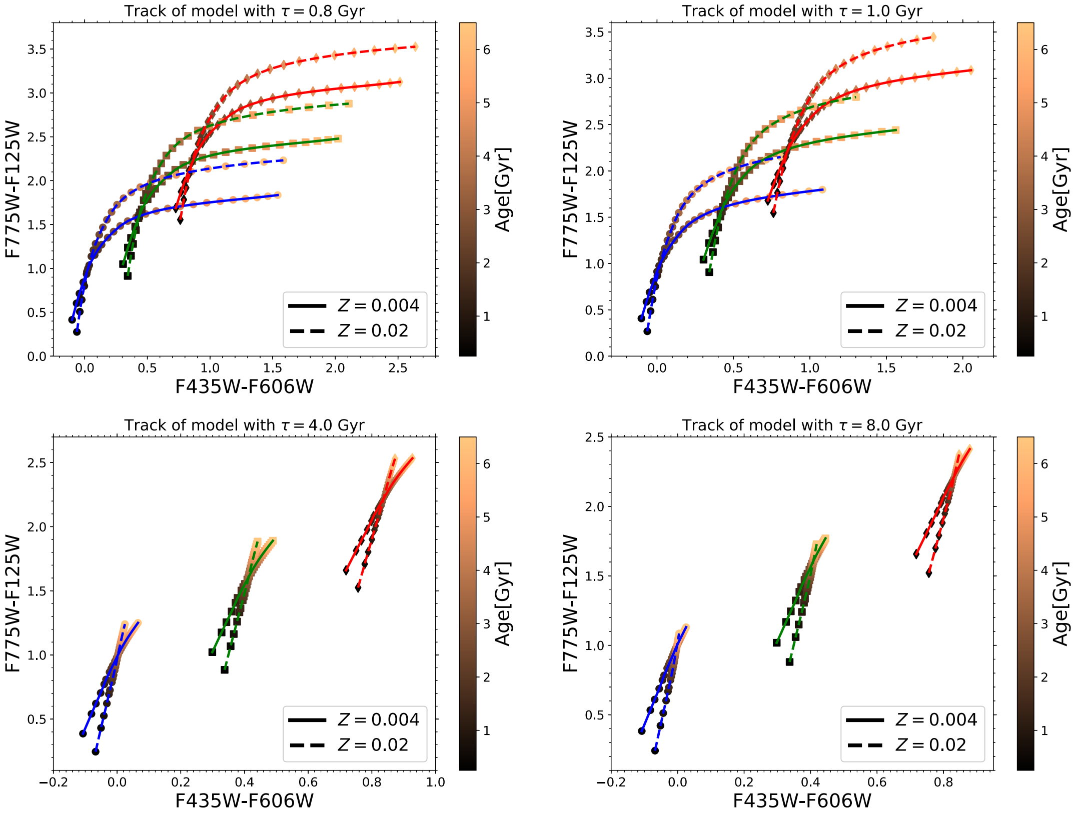

Figure 2.4: Breaking degeneracies in model SEDs with F775W-F125W versus F435W-F606W color-color diagram. Model SEDs are calculated at a redshift of $z = 1.2$. Different panel represents model SEDs with different assumed τ of decaying SFH. Clockwise from top left represent model SEDs with $\tau = 0.8$ Gyr, $\tau = 1.0$ Gyr, $\tau = 8.0$ Gyr, and $\tau = 4.0$ Gyr. In each panel, tracks of model stellar populations with two values of metallicities [$Z = 0.004$ (solid line) and $Z = 0.02$ (dashed line)] and three values of color excesses dust extinctions [$E(B-V) = 0$ (blue color), $E(B-V) = 0.3$ (green color), and $E(B-V) = 0.6$ (red color)] are shown. Color-coding represents age of the model stellar population.

diagram especially for model stellar population with large τ ($\tau \gtrsim 2$ Gyr). For model stellar population with large τ, F435W-F606W color is sensitive to the dust extinction effect and less affected by aging effect, while F775W-F125W color is sensitive to the aging affect and less affected by the dust extinction effect. Similar as for the model SEDs at $z \sim 0$, overlapping among tracks of model stellar populations with small τ only occur at old age, while the tracks are separated at young age. With the F775W-F125W versus F435W-F606W color-color diagram, effect of Z to the model SED could also be distinguished from the effects of aging and dust extinction, although not as good as that achieved with the NUV-r versus FUV-NUV color-color diagram. Thus, by using photometric SED from GALEX+SDSS and CANDELS+3D-HST which cover rest-frame FUV-NIR, degeneracies among model parameters (especially between age and dust extinction) existed in the model SEDs are expected to be resolved.

Chapter 3

Methodology: pixel-to-pixel SED fitting

Throughout this research, we use a single method based primarily on the spatially resolved spectral energy distribution (SED) fitting, namely *pixel-to-pixel SED fitting*, to derive spatially resolved distributions of stellar population properties (especially SFR and M_*) of the galaxies at $0.01 < z < 0.02$ and $0.8 < z < 1.8$. Previous researchers have performed this kind of method to derive spatially resolved stellar population properties of local and high redshift galaxies (e.g. Abraham et al. 1999; Welikala et al. 2008; Zibetti et al. 2009; Wuyts et al. 2012; Sorba and Sawicki 2015; Martínez-García et al. 2018). Those spatially resolved SED fitting implementations come with various techniques. Here, we adopt Bayesian statistics approach, which now commonly used in the integrated SED fitting implementation. Pioneered by Kauffmann et al. (2003b), SED fitting with Bayesian statistics approach now has been used in many integrated SED fitting implementations (e.g. Salim et al. 2007; da Cunha et al. 2008; Noll et al. 2009; Serra et al. 2011; Acquaviva et al. 2011; Han and Han 2014; Rovilos et al. 2014; Chevallard and Charlot 2016).

The pixel-to-pixel SED fitting consists of three main steps: analysis of multiband imaging data, construction of a library of model SEDs, and fitting observed spatially resolved SED with the library of model SEDs using Bayesian statistics. In the following, we describe those three steps in detail.

3.1 Analysis of imaging dataset

In this step, multiband imaging data of a galaxy is spatially-matched and spatially resolved SED in the galaxy is obtained. Then pixel binning is applied to increase signal-to-noise ratio (S/N) of the spatially resolved SED. Imaging dataset from GALEX, SDSS, and 3D-HST are background subtracted so we do not include this step here.

3.1.1 Image registration and PSF matching

First step that has to be done in SED fitting realization is to make the multiband imaging dataset into the same spatial resolution and sampling. Because we want to obtain SED from a particular region in the galaxy by combining the multiband images of the galaxy, so making all images in the same resolution and sampling is very important to avoid overlap of the photometric fluxes from different spatial regions. This step, which is called point spread function (PSF) matching is done by degrading the spatial resolution of image with higher resolution to match the spatial resolution of image with lowest spatial resolution.

Seven bands imaging dataset from GALEX (FUV and NUV) and SDSS (u, g, r, i, and z) have different PSF sizes. The typical PSF FWHM of the SDSS images, GALEX FUV, and GALEX NUV are $1.3''$, $4.2''$, and $5.3''$, respectively (see Tables 2.1 and 2.2). The PSF sizes of the SDSS, GALEX NUV, and GALEX FUV images correspond to physical sizes of 0.3–0.5 kpc, 1–2 kpc, and and 0.8–1.7 kpc respectively, for a galaxy at $0.01 < z < 0.02$. To match the PSFs of the seven imaging dataset, we degrade the PSFs of the FUV, u, g, r, i, and z images to match the PSF of the NUV image, which has largest PSF size among the seven bands.

The PSF matching is done by convolving the image with a PSF matching kernel. We constructed six PSF matching kernels, each for FUV, u, g, r, i, and z band. To construct the PSF matching kernels, first, average PSF of each band (for seven bands) is derived based on average of ~ 50 normalized images of isolated stars. Then based on the average PSF, PSF matching kernel for each band is constructed using `psfmatch` command in `IRAF`. PSF matching process is done in SDSS sampling ($0.4''$ pixel^{-1}), which is higher than GALEX sampling ($1.5''$ pixel^{-1}), as the determination of central position and size of the PSF is expected to be more accurate when it is done in higher sampling compared to if it is done in a lower sampling. For this purpose, the PSF matching kernels are made in SDSS sampling and all images are registered into SDSS sampling using `wregister` command in `IRAF` before the PSF matching. Fig. 3.1 shows PSFs of the NUV, FUV, u, g, r, i, and z bands (top row from left to right), and PSF matching kernels produced by the `psfmatch` command in `IRAF` for the FUV, u, g, r, i, and z (bottom row from left to right). Fig. 3.2 shows PSF profiles of the FUV, NUV, u, g, r, i, and z bands (left panel). In the right panel, resulted PSF profiles after being convolved with the PSF matching kernels are shown. This figure demonstrates reliability of the convolution kernels and performance of the PSF matching process. After PSF matching, all 7 bands images are brought to the GALEX sampling. This process will bin neighboring pixels and increase S/N of pixel's flux in the new sampling. GALEX sampling corresponds to a physical scale of $0.3 - 0.6$ kpc at $0.01 < z < 0.02$.

Eight bands background-subtracted mosaic images (F435W, F606W, F775W, F814W, F850LP, F125W, F140W, and F160W) provided by the 3D-HST [1] are registered to the same sampling of $0.06''$ pixel^{-1} and PSF-matched to the PSF of F160W image, $0.9''$. The PSF size corresponds to $\sim 1.4 - 1.6$ kpc at $0.8 < z < 1.8$. :

---

[1] The background-subtracted PSF-matched imaging dataset is publicly available from the 3D-HST website: `http://3dhst.research.yale.edu/Data.php`

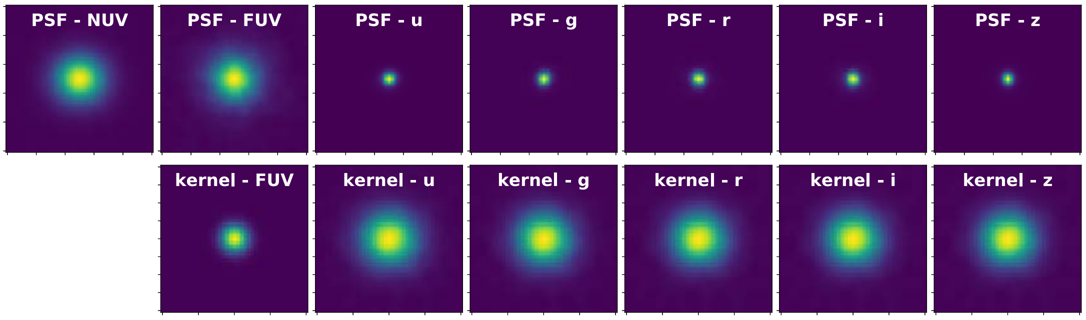

Figure 3.1: First row: from left to right shows point spread functions (PSFs) of NUV, FUV, u, g, r, i, and z bands. Second row: from left to right shows PSF matching kernels for FUV, u, g, r, i, and z bands.

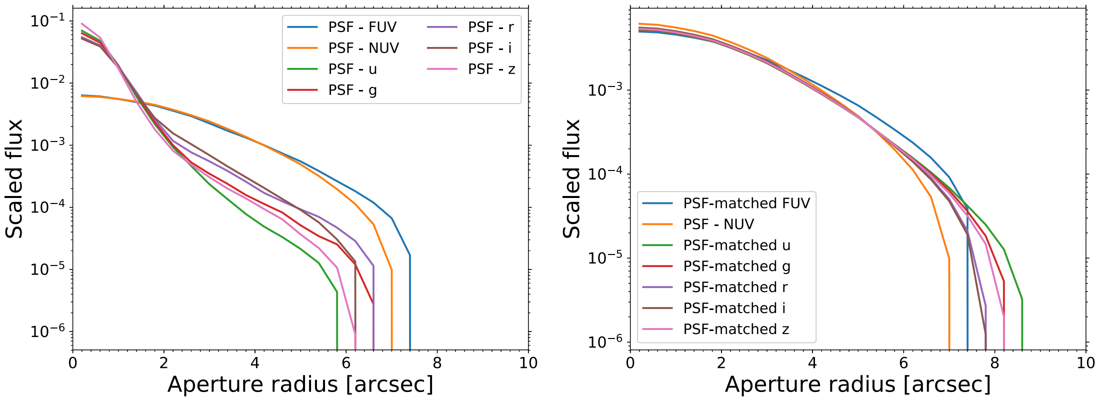

Figure 3.2: Left panel: PSF profiles of the FUV, NUV, u, g, r, i, and z bands, whose PSF images are shown in Fig. 3.1. Right panel: PSF profiles after being convolved with the convolution kernels using the `psfmatch` in `IRAF`.

3.1.2 Defining galaxy's region

After the multiband images are registered to the same sampling and PSF-matched, next step is defining galaxy's region, i.e. region within which we want to apply the pixel-to-pixel 11SED fitting and derive the spatially resolved stellar population properties. We define the galaxy's region based on segmentation map obtained with `SEXTRACTOR` (Bertin and Arnouts 1996). First, we use `SEXTRACTOR` to generate segmentation maps of all detected objects in the image of a field that contain the targeted galaxy with a detection threshold of above 1.5 times higher than the rms scatter outside of the galaxy. In case of the 3D-HST imaging data, `SEXTRACTOR` is applied to the mosaic image and segmentation maps of all detected objects in the mosaic image are obtained. Fig. 3.3 shows example of a segmentation map produced by `SEXTRACTOR` (right panel) for an image of a field that is shown in the left panel. Color coding in the right panel represents pixel value in the detected object which is the same as id of the detected object in a catalog that is produced along with the source detection

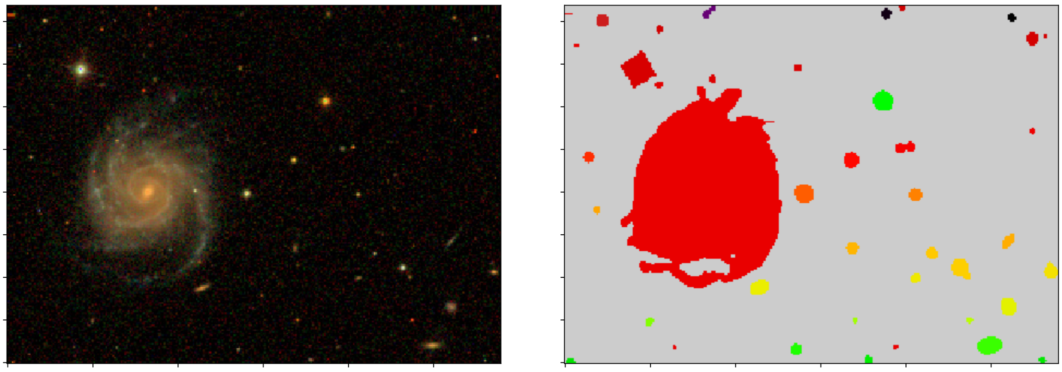

Figure 3.3: Example of segmentation map produced by `SEXTRACTOR`. Left panel: *gri* composite image of a field observed by SDSS. Right panel: segmentation maps produced by `SEXTRACTOR` for the detected objects within the field shown in the left panel. Color-coding represent id of the detected object in the catalog generated by the `SEXTRACTOR`. In this example, the segmentation map is produced based on the image in r band. This image is registered to GALEX sampling ($1.5''$ pixel^{-1}) using `wregister` command in `IRAF`.

process by `SEXTRACTOR`. In this example, the segmentation map is produced based on image in the r band.

Next step is finding the segmentation map of the galaxy. We use position of the galaxy (i.e. central coordinate; based on the galaxy catalog) to locate position of galaxy's central pixel in the `SEXTRACTOR` segmentation map. Then value stored in the central pixel is used as a reference to collect pixels that belong to the galaxy by looking for pixels that have the same pixel value. Sometimes pixels that are not connected with the main area of the galaxy have the same pixel value as the pixels associated with the galaxy's main area. In such case, we exclude those outlier pixels that have no direct connection to the central area pixels. We applied above procedure to each imaging band. At the end of this process, we obtain galaxy's segmentation map in each imaging band.

The segmentation maps in all bands are then merged and the merged-segmentation-map is used as the fitting area of the galaxy. Fig. 3.4 shows an example of segmentation maps in seven bands of a galaxy in the $z \sim 0$ sample (SDSS ObjID 1237652947457998886 or NGC 309) which the field associated with it is shown in Fig. 3.3. Final segmentation map resulted from merging the segmentation maps in seven imaging bands and *gri* composite image showing the optical area covered by the final segmentation map are shown in second row in the figure.

3.1.3 Deriving multiband photometric fluxes and flux uncertainties of pixels in the galaxy

Flux and flux uncertainty associated with a galaxy's pixel is obtained by converting value stored in the pixel, i.e. counts per second which is average number of electrons that hit the CDD's pixel

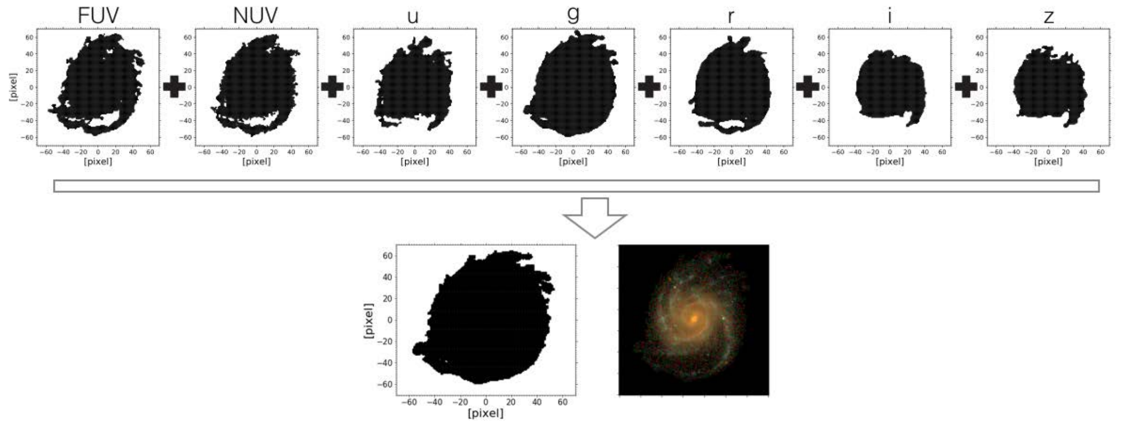

Figure 3.4: Top row: Example of segmentation maps in the seven imaging bands of GALEX+SDSS for a galaxy in the $z \sim 0$ sample (SDSS ObjID 1237652947457998886 or NGC 309). Final segmentation map obtained by merging the seven segmentation maps and *gri* composite image showing the optical area covered by the final segmentation map are shown in the bottom row.

in a second. Next, we will describe procedures to convert from pixel value to the flux and flux uncertainty for imaging dataset from GALEX, SDSS, and HST (CANDELS and 3D-HST).

In GALEX image, pixel value is in unit of counts per second. To convert from pixel values in FUV and NUV images to corresponding fluxes, we use following equations [2]. CPS represents pixel value in counts per second.

$$\text{Flux}_{\text{FUV}}[\text{erg s}^{-1}\text{cm}^{-2}\text{Å}^{-1}] = 1.4 \times 10^{-15} \times \text{CPS} \tag{3.1}$$

$$\text{Flux}_{\text{NUV}}[\text{erg s}^{-1}\text{cm}^{-2}\text{Å}^{-1}] = 2.06 \times 10^{-16} \times \text{CPS} \tag{3.2}$$

To calculate flux uncertainties in FUV and NUV, first, uncertainty of CPS is calculated using

$$\text{CPS}_{\text{err,FUV}} = \frac{\sqrt{\text{CPS} \times \text{exp-time} + (0.050 \times \text{CPS} \times \text{exp-time})^2}}{\text{exp-time}} \tag{3.3}$$

$$\text{CPS}_{\text{err,NUV}} = \frac{\sqrt{\text{CPS} \times \text{exp-time} + (0.027 \times \text{CPS} \times \text{exp-time})^2}}{\text{exp-time}} \tag{3.4}$$

with exp-time represents exposure time. Then based on the uncertainty of CPS, flux uncertainties in FUV and NUV can be calculated using equation 3.1 and 3.2.

---

[2] Following information given in this webpage: `https://asd.gsfc.nasa.gov/archive/galex/FAQ/counts_background.html`

Table 3.1: Gain for CCD cameras of SDSS

camcol	u	g	r	i	z
1	1.62	3.32	4.71	5.165	4.745
2	1.595 (for run<1100) 1.825 (for run>1100)	3.855	4.6	6.565	5.155
3	1.59	3.845	4.72	4.86	4.885
4	1.6	3.995	4.76	4.885	4.775
5	1.47	4.05	4.725	4.64	3.48
6	2.17	4.035	4.895	4.76	4.69

In the SDSS image, pixel value is counts in unit of nanomaggy. To convert the pixel value into flux in unit of erg $\mathrm{s^{-1}cm^{-2}\text{\AA}^{-1}}$, we use following equation [3]

$$\begin{aligned}\mathrm{Flux}_{\lambda,\mathrm{SDSS}}[\mathrm{erg\ s^{-1}cm^{-2}\text{\AA}^{-1}}] = {} & \mathrm{counts[nanomaggie]} \\ & \times 3.631 \times 10^{6} \left[\frac{\mathrm{Jy}}{\mathrm{nanomaggie}}\right] \\ & \times 2.994 \times 10^{-5} \left(\frac{\text{\AA}}{\lambda}\right)^{2} \left[\frac{1}{\mathrm{Jy}}\right]\end{aligned} \tag{3.5}$$

To calculate flux uncertainty in the SDSS image, first, $\mathrm{count_{err}}$ (i.e. uncertainty of counts) is calculated using the following equation

$$\mathrm{count_{err}} = \sqrt{\frac{\left(\frac{\mathrm{count[nanomaggie]}}{\mathrm{NMGY}}\right) + \mathrm{count_{sky}}}{\mathrm{gain}} + \mathrm{dark\ variance}} \tag{3.6}$$

with NMGY is a conversion factor from counts to flux in unit of nanomaggie (i.e. nanomaggie per count) and $\mathrm{count_{sky}}$ is counts associated with sky background image. $\mathrm{count_{sky}}$ at particular point in the image field is obtained by interpolating from sampled sky background counts given in HDU2 of the SDSS fits file using bilinear interpolation method. Gain is a conversion factor from count to the detected number of photo electron and dark variance is an additional source of noise from the read-noise and the noise in the dark current. Values of gain and dark variance are given in Table 3.1 and 3.2 [4], respectively. Those values depend on the camera column (camcol) and filter. After getting $\mathrm{count_{err}}$, flux uncertainty can be calculated using following equation

$$\begin{aligned}\Delta\mathrm{Flux}_{\lambda,\mathrm{SDSS}}[\mathrm{erg\ s^{-1}cm^{-2}\text{\AA}^{-1}}] = {} & \mathrm{counts_{err}} \times \mathrm{NMGY} \\ & \times 3.631 \times 10^{6} \left[\frac{\mathrm{Jy}}{\mathrm{nanomaggie}}\right] \\ & \times 2.994 \times 10^{-5} \left(\frac{\text{\AA}}{\lambda}\right)^{2} \left[\frac{1}{\mathrm{Jy}}\right]\end{aligned} \tag{3.7}$$

---

[3] Based on information taken from: `http://www.sdss.org/dr12/algorithms/magnitudes/`

[4] Based on information taken from: `https://dr10.sdss.org/datamodel/files/BOSS_PHOTOOBJ/frames/RERUN/RUN/CAMCOL/frame.html`

Table 3.2: Dark variances for CCD cameras of SDSS

camcol	u	g	r	i	z
1	9.61	15.6025	1.8225	7.84	0.81
2	12.6025	1.44	1.00	5.76 (for run<1500) 6.25 (for run>1500)	1.0
3	8.7025	1.3225	1.3225	4.6225	1.0
4	12.6025	1.96	1.3225	6.25 (for run<1500) 7.5625 (for run>1500)	9.61 (for run<1500) 12.6025 (for run>1500)
5	9.3025	1.1025	0.81	7.84	1.8225 (for run<1500) 2.1025 (for run>1500)
6	7.0225	1.8225	0.9025	5.0625	1.21

Fig. 3.5 shows example of spatially resolved multiband fluxes (in the seven bands of GALEX and SDSS) of a galaxy in $z \sim 0$ sample (SDSS ObjID 1237652947457998886 or NGC 309, whose the segmentation map is shown in Fig. 3.4). Fig. 3.6 shows the spatially resolved multiband flux uncertainties (in the seven bands) of the galaxy.

Pixel value in the image provided by the 3D-HST is a count in unit of counts per second. To convert the pixel value to flux in unit of erg $\text{s}^{-1}\text{cm}^{-2}\text{Å}^{-1}$, we multiply it with a conversion factor given in the PHOTFLAM header keyword [5]. Flux uncertainty of a pixel is calculated from weight image provided by the 3D-HST. Pixel value in the weight image is an inverse variance of the count and it could be used to calculate uncertainty of the count and the flux uncertainty in unit of erg $\text{s}^{-1}\text{cm}^{-2}\text{Å}^{-1}$ by using the same PHOTFLAM header keyword. Fig. 3.7 shows example of the spatially resolved fluxes in the eight bands for a galaxy in the $z \sim 1$ sample (GS_19186 which located at RA= $53^{\circ}.120750$, DEC= $-27^{\circ}.818984$ and $z = 1.0940$), while the spatially resolved flux uncertainties in the eight bands are shown in Fig. 3.8.

3.1.4 Pixel binning

After getting spatially resolved distributions (in pixel scale) of multiband photometric fluxes of a galaxy, next step is binning neighboring pixels to increase signal to noise (S/N) ratio of the spatially resolved SEDs, thereby increasing constraint to the model SEDs. We develop a new pixel binning technique that taking into account three criteria: (1) closeness, such that only neighboring connected-pixels are binned, (2) similarity of SED shape, such that only pixels that have similar SED shape (i.e. high probability of having similar stellar population properties, e.g. stellar metallicity (Z), stellar age, and dust extinction) are binned, and (3) minimum S/N (i.e. S/N threshold), such that the resulted bin should have S/N in all bands as high as S/N threshold. We do not use publicly available pixel binning code, such as voronoi binning (Cappellari and Copin 2003), because the code does not consider similarity of SED shape among pixels that are binned. Binning the pixels that have different SED shape (i.e. high possibility of having different stellar population properties) could potentially erase information embedded in pixel-scale SED, which is important to be preserved when studying galaxy's spatially resolved properties.

---

[5] Based on information taken from `http://www.stsci.edu/documents/dhb/web/c03_stsdas.fm3.html`

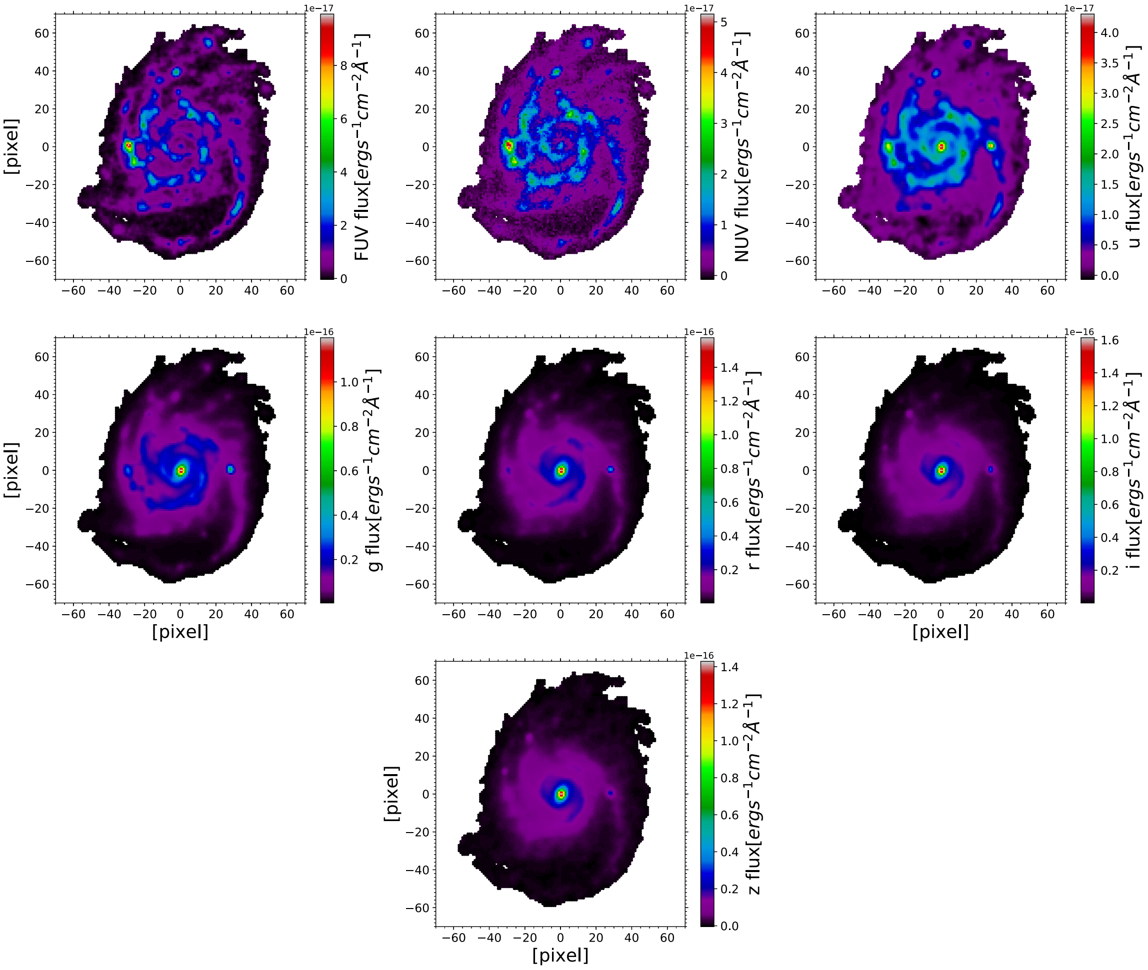

Figure 3.5: Spatially resolved fluxes in the seven bands of GALEX+SDSS for a galaxy in the $z \sim 0$ sample (SDSS ObjID 1237652947457998886 or NGC 0309).

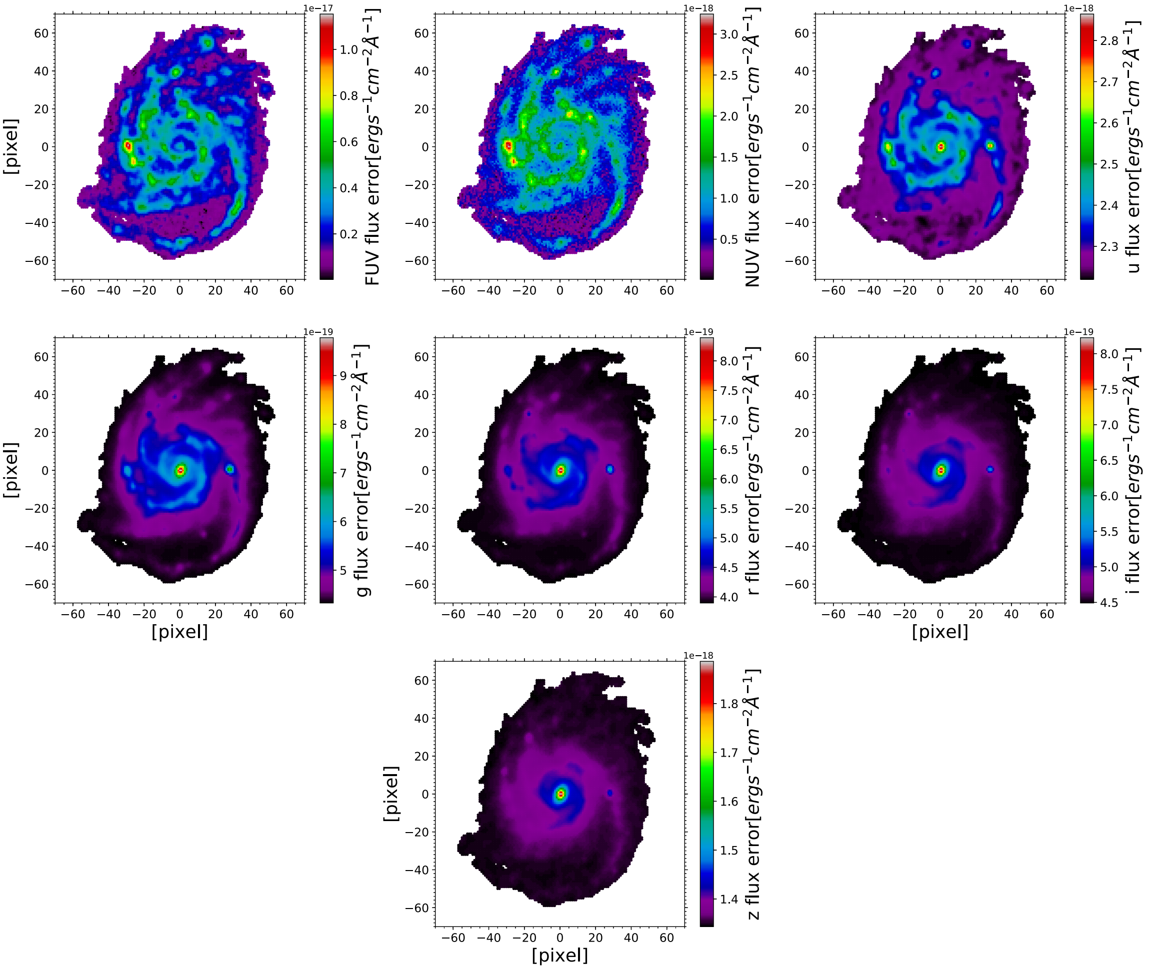

Figure 3.6: Spatially resolved flux uncertainties in the seven bands of GALEX+SDSS for a galaxy in the $z \sim 0$ sample (SDSS ObjID 1237652947457998886 or NGC 0309).

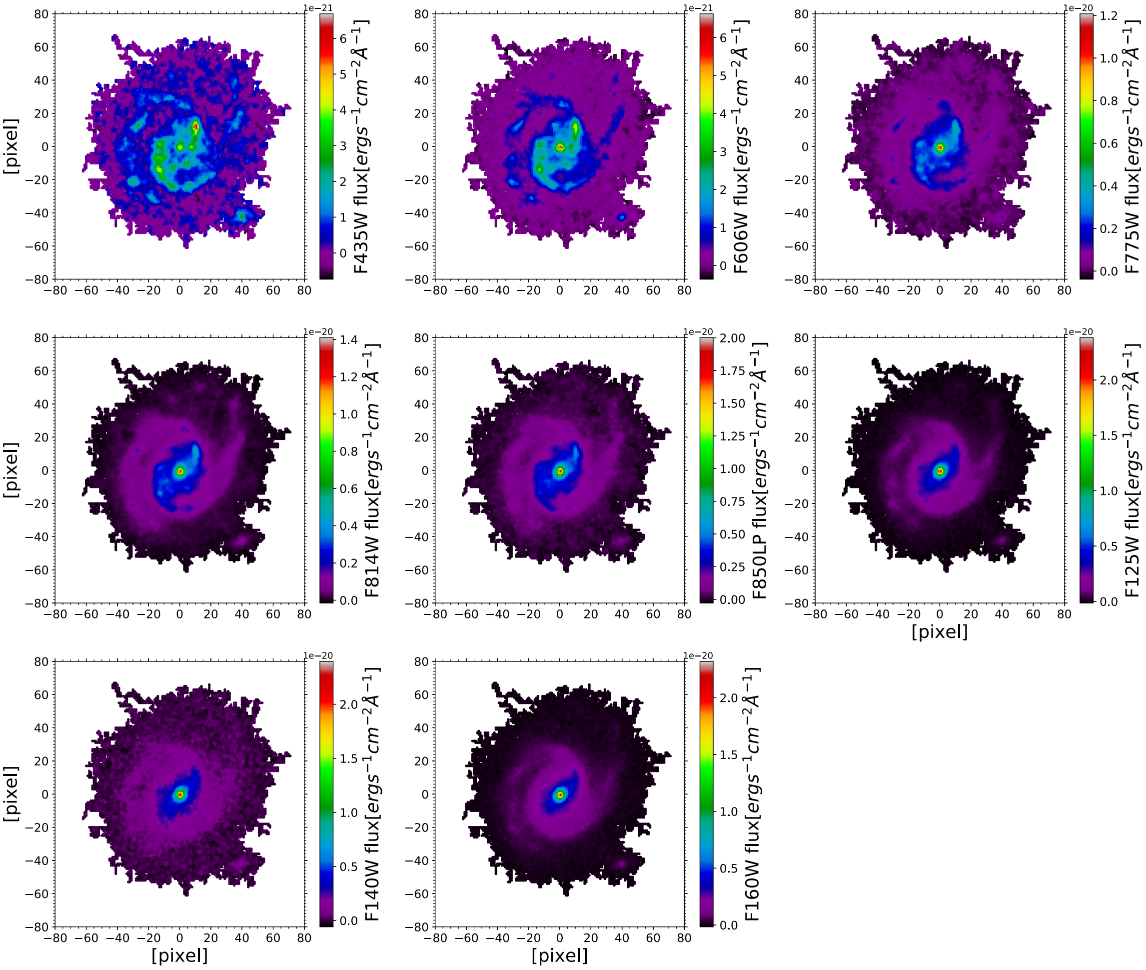

Figure 3.7: Spatially resolved fluxes in the eight bands of CANDELS+3D-HST for a galaxy in the $z \sim 1$ sample, GS_19186 which located at RA$= 53^{\circ}.120750$, DEC$= -27^{\circ}.818984$ and $z = 1.0940$.

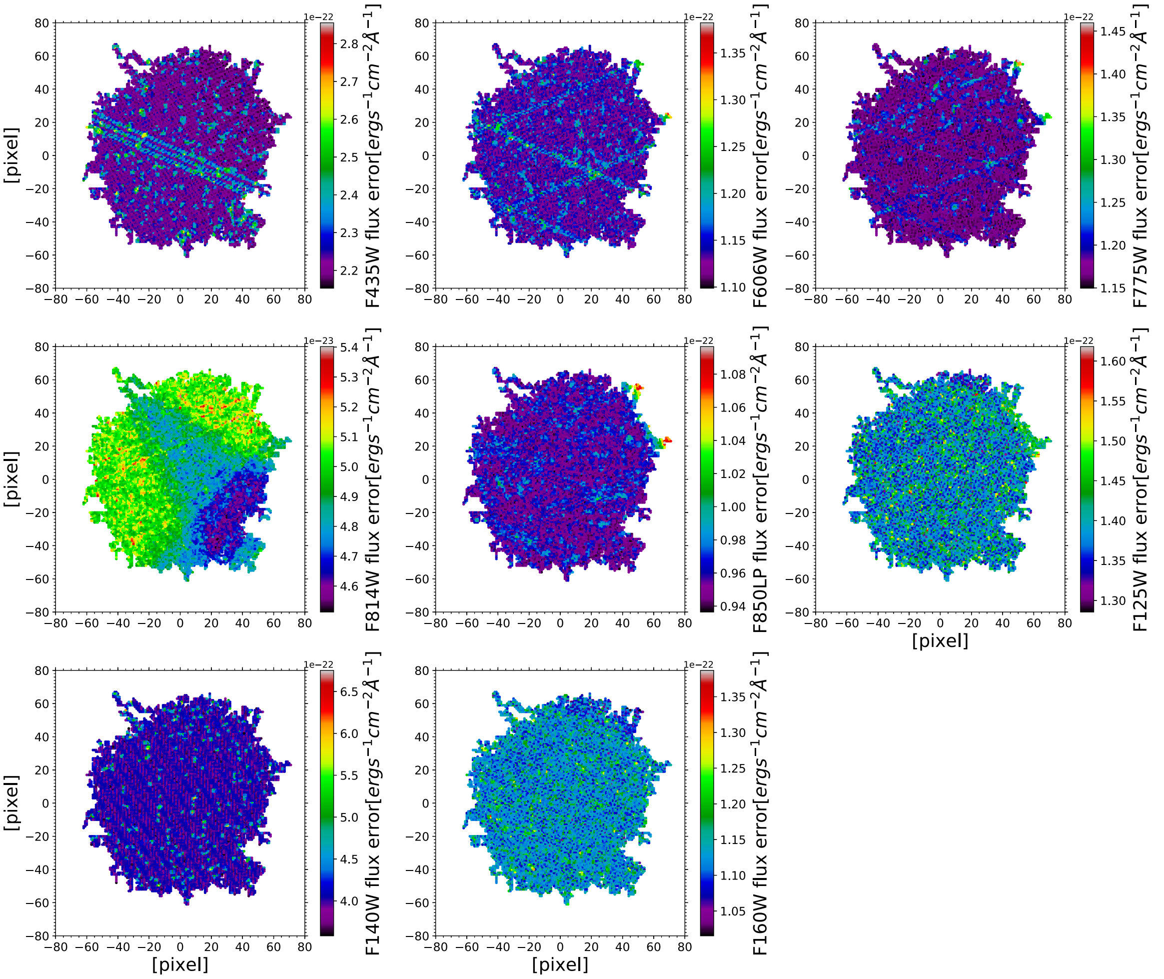

Figure 3.8: Spatially resolved flux uncertainties in the eight bands of CANDELS+3D-HST for a galaxy in the $z \sim 1$ sample, GS_19186 which located at RA$= 53^{\circ}.120750$, DEC$= -27^{\circ}.818984$ and $z = 1.0940$.

In practice, a particular band is chosen as a reference for selecting brightest pixel from which subsequently increasing circular annulus binning is initiated to select (i.e. merge) neighboring pixels with similar SED shape until S/N$\geqslant$S/N threshold (in all bands) is reach. We use r and F125W bands as the reference for selecting the brightest pixel in the pixel binning process for the $z \sim 0$ and $z \sim 1$ samples, respectively. Briefly, the pixel binning is done with the following procedures. First, locate the position of a brightest pixel in the reference band. Location of the brightest pixel is then used as a central position of the bin that will be built and its SED is used as a reference for selecting neighboring pixels with similar SED shape. Pixels lying within a circle with an initial radius of 2 pixels are tested for the similarity of SED shape as that of the central brightest pixel.

The SED similarity test is done through calculating χ^2 as given by

$$\chi^2 = \sum_i \frac{(f_{m,i} - s_{mb} f_{b,i})^2}{\sigma_{m,i}^2 + \sigma_{b,i}^2}, \tag{3.8}$$

with i, b, and m represent indexes for filter/band, the central brightest pixel, and the neighboring pixel that is tested. $f_{m,i}$ and $f_{b,i}$ are i-th band flux of a pixel m and b, respectively, while $\sigma_{m,i}$ and $\sigma_{b,i}$ are i-th band flux uncertainty of the pixel m and b, respectively. s_{mb} represent a correction for scaling difference between the SEDs of the two pixels, which can be calculated using following equation

$$s_{mb} = \frac{\sum_i \frac{f_{m,i} f_{b,i}}{\sigma_{m,i}^2 + \sigma_{b,i}^2}}{\sum_i \frac{f_{b,i}^2}{\sigma_{m,i}^2 + \sigma_{b,i}^2}}. \tag{3.9}$$

If χ^2 is smaller than a χ^2 limit (set as a free parameter), the pixel m is included in the bin.

If the S/N threshold has not been reached in all bands, then radius of the circular annulus is increased by 2 pixels and the same procedure is done to add up more pixels until the resulted S/N in each band reaches the S/N threshold. The selected pixels for the bin that has been built is flag with index of the bin (increasing from 1, which is first bin made for the galaxy, to $\mathrm{n_{bin}}$, which is last bin, i.e. number of bins created). Subsequent bin is made by looking for the position of brightest pixel in the reference band that has not been selected in the previous binning (indicated by its flag) and then do the same procedures as described previously. The binning process proceed until no one bin could be made with available pixels (un-selected in all previous bins). In many cases, the un-selected pixels are located in outskirt. It could happen due to some reasons, such as binning all of those pixels does not meet S/N threshold requirement; those pixels have different SED shape compared to that of pixels selected in the previous bins; and fraction of those pixels do not meet the requirement on similarity of SED shape thereby reducing number of pixels to be binned, which could result in lower S/N than the threshold. In such cases, all those un-selected pixels are binned into one bin.

Fig. 3.9 shows results of pixel binning for a galaxy in the $z \sim 0$ sample (SDSS ObjID 1237652947457998886 or NGC 309) with various values of parameters, i.e. χ^2 limit (maximum value of χ^2 below which two SEDs of pixels are considered as having similar shape) and S/N threshold

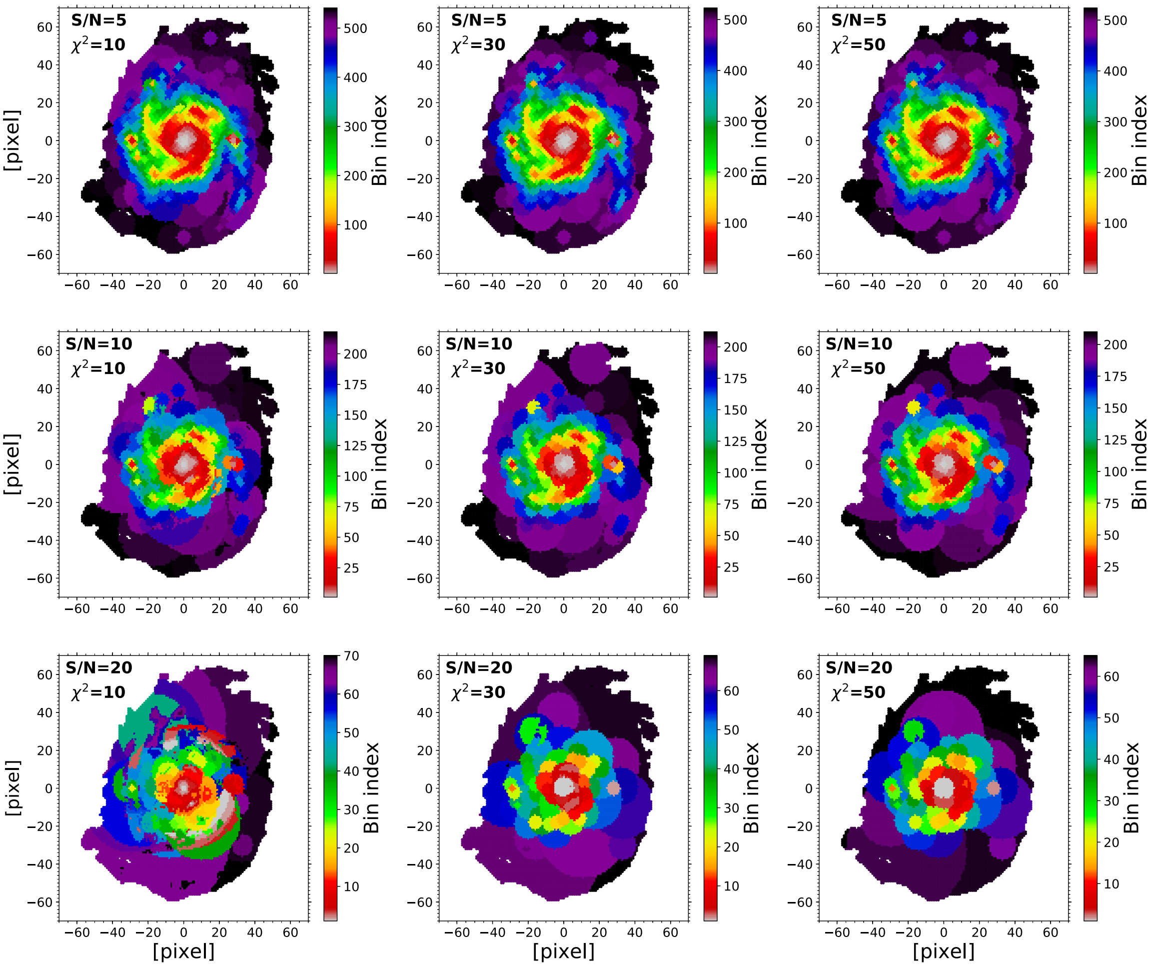

Figure 3.9: Example of pixel binning results with various values of χ^2 limit (maximum value of χ^2 below which two SEDs of pixels are considered as having similar shape) and S/N threshold (minimum S/N in all imaging bands that has to be reached by each bin). The same galaxy (SDSS ObjID 1237652947457998886 or NGC 0309) as used in some figures in previous sections is used for this example. Throughout this research, χ^2 limit of 30 and S/N threshold of 10 are used as the pixel binning parameter.

(minimum S/N in all imaging bands that has to be reached by each bin). Throughout this research, χ^2 limit of 30 and S/N threshold of 10 are used as the pixel binning parameters. Pixel binning result with χ^2 limit of 30 and S/N threshold of 10 is shown in middle panel in the figure. Fig. 3.10 shows example of pixel binning result with χ^2 limit of 30 and S/N threshold of 10 for a galaxy in the $z \sim 1$ sample (GS_19186 which located at RA= 53°.120750, DEC= -27°.818984 and $z = 1.0940$).

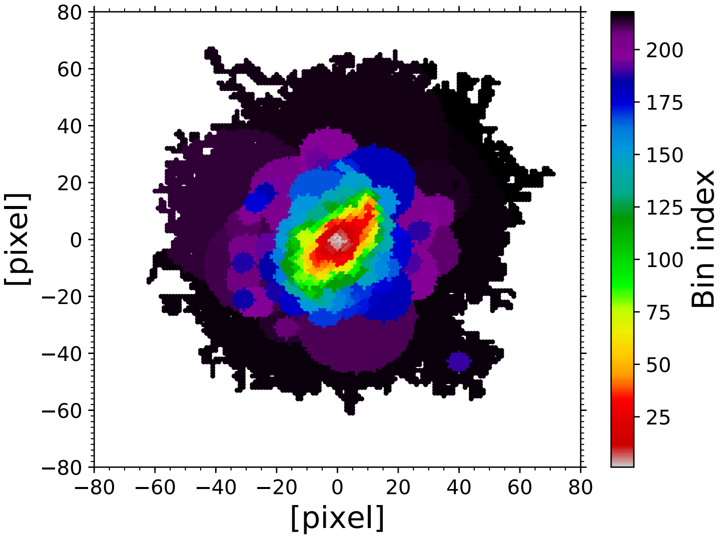

Figure 3.10: Example of a pixel binning result with χ^2 limit of 30 and S/N threshold of 10 for a galaxy in the $z \sim 1$ sample, GS_19186 which located at RA= 53°.120750, DEC= −27°.818984 and $z = 1.0940$.

3.2 Construction of model SEDs

In this step, a library of model SEDs is constructed. The constructed model SEDs are then used for fitting with the observed spatially resolved SEDs (i.e. SED of galaxy's bins). The model SEDs are generated using stellar population synthesis model which have been passed through some processes that more less resembling those of real processes experienced by the emitting spectrum from a stellar population in a galaxy all the way to hitting the camera filter that is used for the observation on earth. In the following, procedures that are done in the construction of the library of model SEDs are described.

3.2.1 Generating rest-frame spectra of the stellar population synthesis model

Rest-frame model spectra with uniform parameter grids are generated using publicly available stellar population synthesis model, `GALAXEV (BC03)` (Bruzual and Charlot 2003). We assume Chabrier (2003) initial mass function (IMF) with mass range between $0.1\mathrm{M}_\odot$ and $100\mathrm{M}_\odot$ and exponentially declining SFR model $\mathrm{SFR}(t) \propto e^{-t/\tau}$ with τ for decaying timescale and t for stellar population age. We use the following grids of parameters to generate the rest-frame model spectra:

1. 100 values of SFR e-folding time, τ, from 0.1 Gyr to 10 Gyr with $\triangle\tau$ of 0.1 Gyr,

2. 55 values of age, t, from 0.25 Gyr to 13.75 Gyr with $\triangle t$ of 0.25 Gyr,

3. 4 values of metallicities, Z : 0.004, 0.008, 0.02, and 0.05.

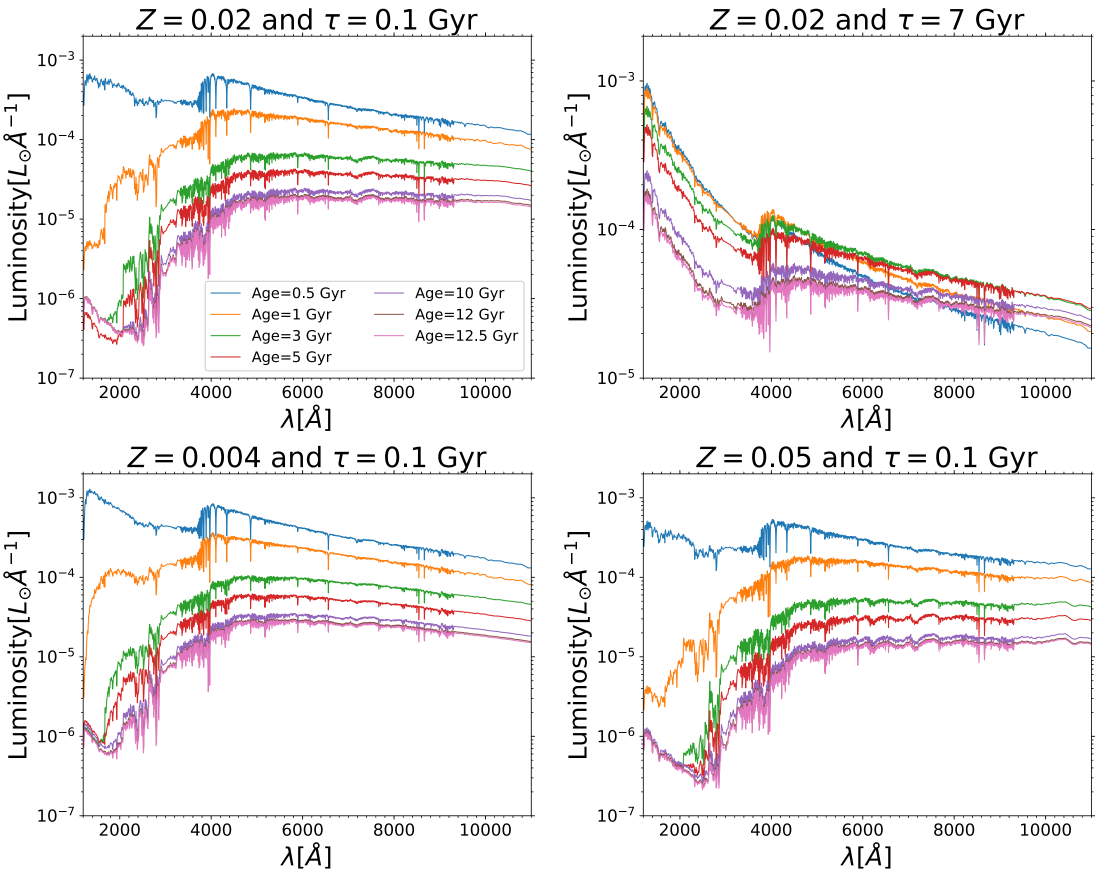

Figure 3.11: Example of rest-frame model spectrum generated using `GALAXEV` with various values of Z, τ, and ages.

Model spectrum generated by *GALAXEV* is in unit of $\mathrm{L}_\odot \mathrm{\AA}^{-1}$ and normalized to the total stellar mass of $1\mathrm{M}_\odot$. Total number of the model spectra generated in this step is $100 \times 55 \times 4 = 22000$. Fig. 3.11 shows example of the rest-frame model spectra with various values of Z, τ, and age. In the first row, effect of τ on the evolution of model spectra is shown. Model stellar population with shorter τ have less number of young stars which is shown by suppression of luminosity in the short wavelength region. In the second row, effect of Z on the evolution of model spectra is shown. It should be noted that each panel in this figure is not a good representation of the evolution of model spectrum from evolving model stellar population because it does not include modeling of metallicity evolution, instead instantaneous metallicity is used.

3.2.2 Attenuation by interstellar dust

To simulate attenuation effect by the interstellar dust to the model spectrum, we assume Calzetti et al. (2000) dust attenuation law for starburst galaxies which has following form

$$\begin{aligned} k(\lambda) &= 2.659\left(-2.156+\frac{1.509}{\lambda}-\frac{0.198}{\lambda^2}+\frac{0.011}{\lambda^3}\right)+R_V \text{ for } 0.12\mu m \leq \lambda \leq 0.63\mu m \\ k(\lambda) &= 2.659\left(-1.857+\frac{1.040}{\lambda}\right)+R_V \text{ for } 0.63\mu m < \lambda \leq 2.20\mu m \end{aligned} \tag{3.10}$$

with $R_V = 4.05$. $k(\lambda)$ is related to attenuation at wavelength λ (A_λ) as $A_\lambda = k(\lambda)E(B-V)$ with $E(B-V)$ is color excess in $B-V$. Change of flux at each wavelength as affected by the dust attenuation can then be calculated with

$$\begin{aligned} f_{\text{obs}}(\lambda) &= f_{\text{int}}(\lambda)10^{-0.4A_\lambda} \\ &= f_{\text{int}}(\lambda)10^{-0.4k(\lambda)E(B-V)} \end{aligned} \tag{3.11}$$

We use Calzetti et al. (2000) dust extinction law because its dust extinction vector could broadly reproduce distribution of the spatially resolved SEDs (of galaxies in the $z \sim 0$ sample) on the FUV-NUV versus FUV-u and FUV-NUV versus NUV-u color-color diagrams (see Appendix A.1).

For each rest-frame model spectrum generated from the previous step, we applied dust attenuation effect with 13 assumed values of $E(B-V)$, 0 (no extinction), 0.05, 0.1, 0.15, 0.2, 0.25, 0.3, 0.35, 0.4, 0.45, 0.5, 0.55, and 0.6 mag. After this step, number of model spectra becomes $22000 \times 13 = 286000$. Fig. 3.12 shows the $k(\lambda)$ as a function of λ of the Calzetti et al. (2000) dust extinction law (in the left panel) and examples of the implementation of Calzetti et al. (2000) dust extinction law to a model rest-frame model spectrum with $Z = 0.02$, $\tau = 7$ Gyr, and age of 10 Gyr. As shown in this figure, effect of dust extinction is more severe in shorter wavelength range than that in the longer wavelength range.

3.2.3 Cosmological redshifting and dimming

Due to expansion of the universe, wavelength of light emitted by a galaxy is stretched as the light travels toward the observer. This effect makes the galaxy's spectrum to be shifted toward longer wavelength (i.e. redshifted) and dimmed. This cosmological redshifting and dimming effect is applied to the model spectra. Flux (F_λ) that we observe on earth from a galaxy at redshift of z that has a luminosity of L_λ can be calculated using the following equation

$$F_\lambda(\lambda) = \frac{L_{\lambda/(1+z)}(\lambda)}{4\pi D_L(1+z)}, \tag{3.12}$$

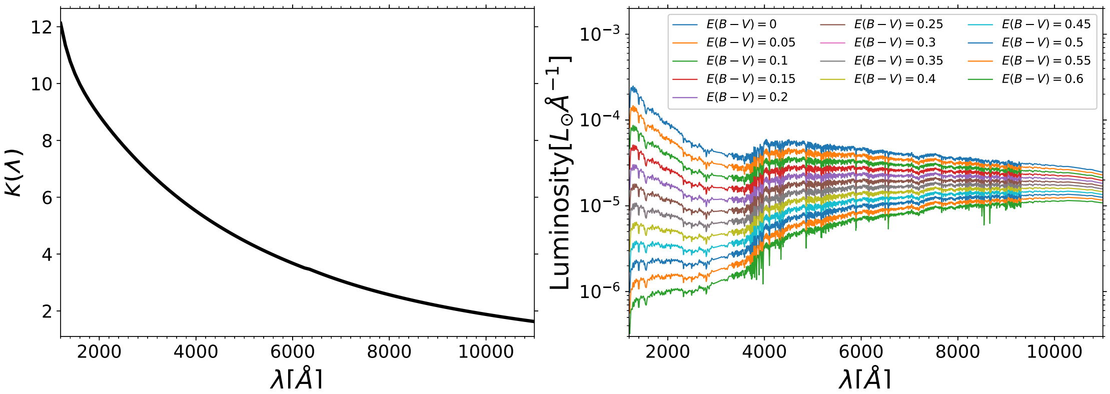

Figure 3.12: Left panel: $k(\lambda)$ of the (Calzetti et al. 2000) dust extinction law. Right panel: example of the implementation of the dust extinction effect to a rest-frame model spectrum. The rest-frame model spectrum used for this example has $Z = 0.02$, $\tau = 7.0$ Gyr, and age of 10 Gyr. Dust extinction effect is more severe in the shorter wavelength region than that in the longer wavelength region.

with D_L is a luminosity distance which depends on the galaxy's redshift through the following equation

$$D_L(z) = \frac{(1+z)c}{H_0} \int_{(1+z)^{-1}}^{1} \frac{da}{\sqrt{a\Omega_m + a^2(1-\Omega_m-\Omega_\Lambda) + a^4\Omega_\Lambda}} \tag{3.13}$$

Flux in the above equation is expressed in the observer frame so that the index $\lambda/(1+z)$ for the luminosity (in the numerator) represents emitting-object frame (i.e. rest-frame). In practice, each wavelength point in the rest-frame spectrum is shifted by multiplying the wavelength with $(1+z)$ and flux associated with that wavelength point (after redshifted) is calculated using the above equation (eq. 3.12). Throughout this research, redshift of the sample galaxies are fixed, adopting redshift information given in the galaxy catalog from which the sample galaxies are defined. Thus, reducing one free parameter in the SED fitting process. As we express the observed spatially resolved fluxes in the sample galaxies in unit of erg $\mathrm{s}^{-1}\mathrm{cm}^{-2}\AA^{-1}$ (see Section 3.1.3), we also expressed flux associated with the model spectrum in the same unit. Throughout this research, we assume the ΛCDM cosmology with the cosmological parameters of $\Omega_m = 0.3$, $\Omega_\Lambda = 0.7$, and $H_0 = 70$km $\mathrm{s}^{-1}\mathrm{Mpc}^{-1}$. Fig. 3.13 shows cosmological redshifting and dimming effect on a model spectrum. Blue spectrum (with y axis shown in the left) shows rest-frame model spectrum, while two red spectra (with y axis shown in the right) show the model spectra as if the model galaxies are placed at $z = 0.1$ and $z = 0.3$. Redshifting and dimming effects are clearly shown in this figure.

3.2.4 Integrating through filter transmission curve

Observed photometric SED of a galaxy is obtained from broadband imaging which catches fraction (within a particular wavelength range) of the galaxy's light by passing the light through a filter which has a unique transmission function (that varies with wavelength). To produce model photometric SEDs that could serve as a template with which the observed SED is fitted, model spectra resulted from the cosmological redshifting and dimming step are then integrated through transmission curves

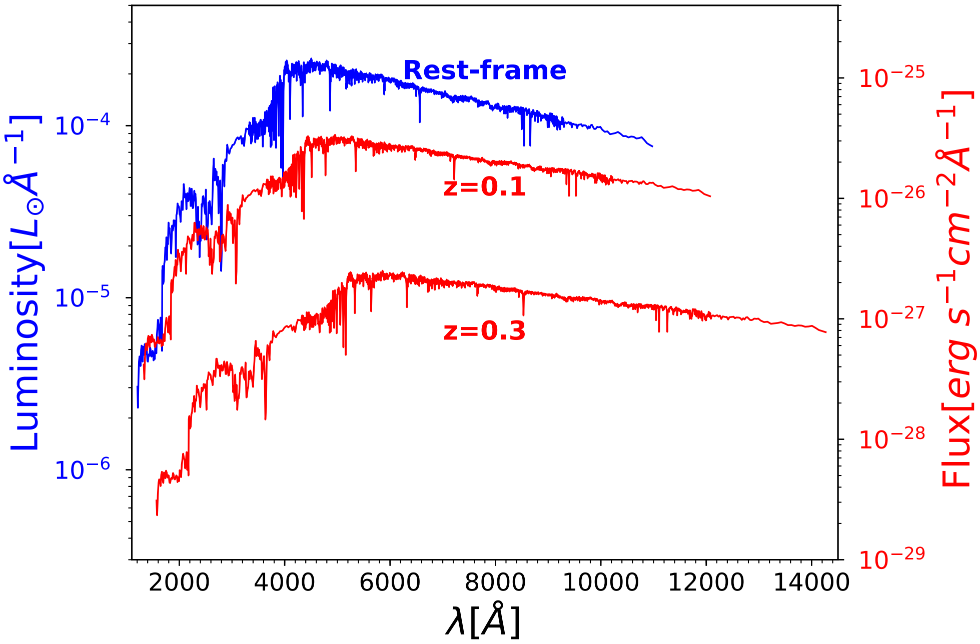

Figure 3.13: Example of applying cosmological redshifting and dimming to a model spectrum. Blue spectrum with y axis shown in the left shows a rest-frame model spectrum, while two red spectra show the model spectra as if model galaxies are placed at $z = 0.1$ and $z = 0.3$.

of filters that are used in the observation. We integrate the model spectra with 7 filter transmission curves of GALEX (FUV and NUV) and SDSS (u, g, r, i, and z) when constructing a library of model SEDs to be used for fitting with the observed spatially resolved SEDs of galaxies in the $z \sim 0$ sample. In the same way, we integrate the model spectra with 8 filter transmission curves of HST (F435W, F606W, F775W, F814W, F850LP, F125W, F140W, and F160W) for constructing the model SEDs to be used for fitting with the observed spatially resolved SEDs of galaxies in the $z \sim 1$ sample. Photometric flux F_i in a particular filter i which has a transmission function of $T_i(\lambda)$ can be calculated using following equation

$$F_i = \frac{\int F_\lambda(\lambda)\lambda T_i(\lambda)d\lambda}{\int \lambda T_i(\lambda)d\lambda}. \tag{3.14}$$

The λ factor in both the numerator and denominator accounts for the fact that the number of photons per unit of flux varies with wavelength. Fig. 3.14 shows example of the integrating model spectrum through filter transmission curves of GALEX+SDSS (top panel) and CANDELS+3D-HST (bottom panel). Model spectrum redshifted from a model galaxy placed at $z = 0.015$ is used in the top panel, while model spectrum redshifted from a model galaxy placed at $z = 1.2$ is used in the bottom panel. Red points show the photometric fluxes resulted from the integration.

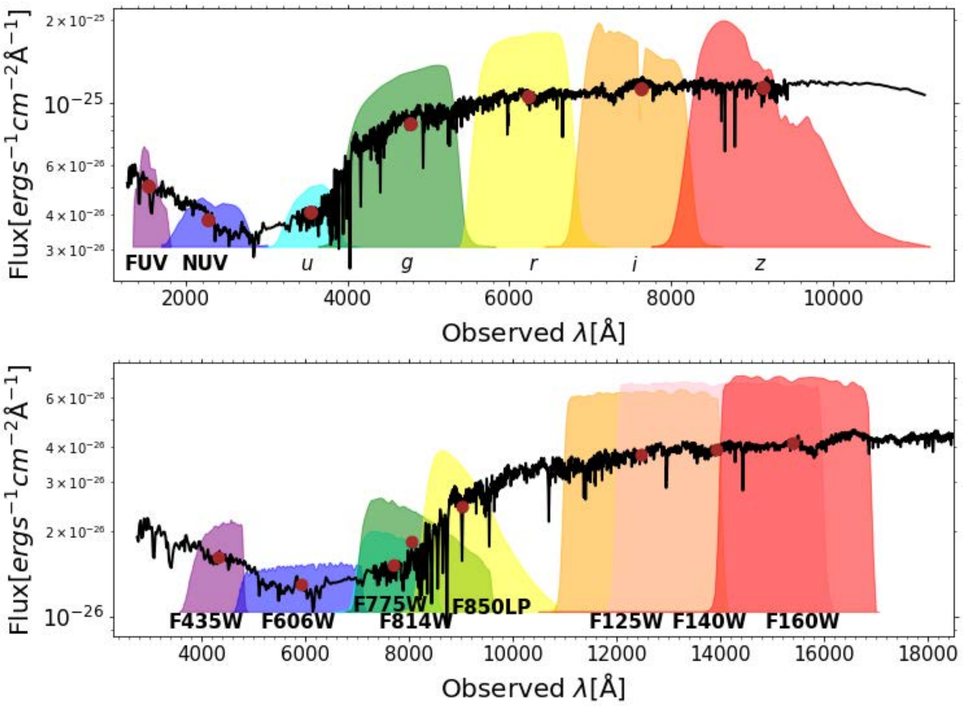

Figure 3.14: Example of integrating model spectrum through filter transmission curves. Top panel: a model spectrum emitted by a model galaxy that is placed at $z = 0.015$ is integrated through 7 filter transmission curves of GALEX+SDSS. Bottom panel: a model spectrum emitted by a model galaxy that is placed at $z = 1.2$ is integrated through 8 filter transmission curves of CANDELS+3D-HST. Red points in the two panels show the photometric fluxes resulted from the integration.

3.2.5 Model SED interpolation

Last step in constructing a library of model SEDs is to interpolate parent model SEDs generated by the previous steps. The interpolation is done in 4 dimensional parameters space (Z, τ, $E(B-V)$, and age). By the interpolation, model SEDs with random parameters (in the Z, τ, $E(B-V)$, and age) are derived. The interpolation also could fill the gap given by the parameter grids in the parent model SEDs, especially for Z where only four Z could be generated from the `GALAXEV`. The randomized parameters and their uniformity within a large range is important for the Bayesian SED fitting that we adopt (which will be described in the next section). The interpolation method consists of two steps, (1) interpolation in three dimensional parameters space of τ, $E(B-V)$, and age (t) for each "fix" value of Z using tricubic interpolation technique and (2) interpolation in one dimensional parameter space of Z using cubic spline interpolation technique.

The tricubic interpolation in three dimensional space of τ, $E(B-V)$, and age (t) for "fix" value of Z is done by solving the following equation in a cube of the three parameters

$$f(E(B-V), t, \tau) = \sum_{i=0}^{3}\sum_{j=0}^{3}\sum_{k=0}^{3} a_{ijk} E(B-V)^i t^j \tau^k. \tag{3.15}$$

Then the cubic spline interpolation in one dimensional space of Z is done by solving the following equation

$$f(Z) = \sum_{i=0}^{3} a_i Z^i. \tag{3.16}$$

Fig 3.15 shows example of results obtained from the tricubic and cubic spline interpolation steps. Two cubes of model photometric fluxes in the first row show the parent model SEDs that are generated following steps described in the previous sections, while two cubes in the second row show full-cube of model SEDs resulted from the tricubic interpolation method. It is shown by the plots that the tricubic interpolation method could interpolate the model SEDs considerably good. Two plots in the third row show example of cubic spline interpolation in one dimensional space of Z. In combination, those two interpolation steps will interpolate model SEDs in four dimensional space. Using the 286000 parent model SEDs, model interpolation process produces 300000 model SEDs with all have completely random values of the model parameters.

3.3 SED fitting with Bayesian statistics approach

Once spatially resolved distribution (in bin space) of the observed SEDs in a galaxy and a set of model SEDs (the 300000 model SEDs) that is redshifted according to the redshift of the galaxy are obtained, next step is fitting each bin SED with the set of model SEDs. Here, we apply SED fitting that adopts Bayesian statistics for parameter inference. It is a method of statistical inference in which Baye's theorem is used to update the probability of a hypothesis (i.e. prior) as more information (i.e. data) becomes available. Bayes' theorem has the following form

$$P(\theta|X) = \frac{P(X|\theta)P(\theta)}{\int P(X|\theta)P(\theta)d\theta} \tag{3.17}$$

with θ and X represent model parameter and data, respectively. $P(\theta|X)$, $P(X|\theta)$, and $P(\theta)$ represent posterior probability of the model parameter given the data, probability of the data given the model (i.e. likelihood function), and prior, respectively. We do not set special form of prior for all the model parameters, except range of value for each parameter (as described in section 3.2.1). Thus, uniform prior is applied for all the model parameters.

The likelihood function ($P(X|\theta)$) is calculated based on the χ^2 statistics. The χ^2 value of the m-th model for the SED of a d-th bin can be calculated with

$$\chi_m^2 = \sum_i (\frac{f_{d,i} - s f_{m,i}}{\sigma_{d,i}})^2, \tag{3.18}$$

with i represents index for filter. $f_{d,i}$, $f_{m,i}$, and σ_i represent observed flux in the i-th band of the d-th bin, model flux in the i-th band of the m-th model, and uncertainty of the observed flux in the i-th band of the d-th bin, respectively. s represents the scaling (i.e. normalization) of the model SED. s is set as a free parameter. It is randomly drawn between $0.1 \times s_{\rm least}$ to $10 \times s_{\rm least}$, where

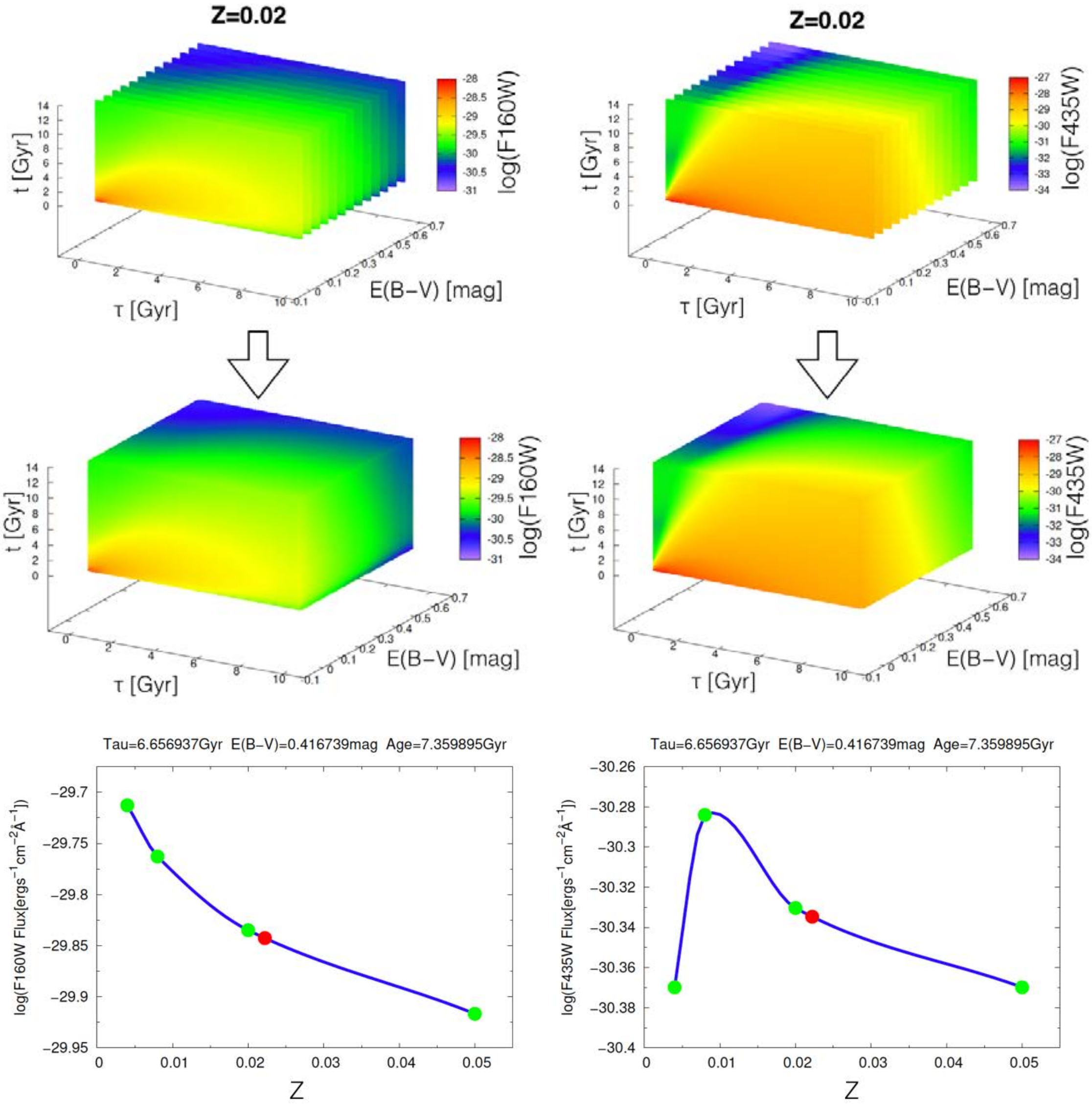

Figure 3.15: Example of the interpolation of model SEDs in four dimensional parameters space (Z, τ, $E(B-V)$, and t). In this example, the model SEDs are assumed to be emitted by a galaxy at $z = 1.5$. Two cubes in the first row show the parent model SEDs, while two cubes in the second row show fulled-cube of model SEDs resulted from the tricubic interpolation method. Two plots in the third row show example of results of the cubic spline interpolation in one dimensional space of Z. Four green points and red point represent parent models and interpolated model (with random Z), respectively.

$s_{\rm least}$ is the model normalization if χ^2 minimization (i.e. maximum likelihood) applied, that is

$$s_{\rm least} = \frac{\sum\limits_i \frac{f_{d,i} f_{m,i}}{\sigma_i^2}}{\sum\limits_i \frac{f_{m,i}^2}{\sigma_i^2}}. \tag{3.19}$$

For each model SED, 100 random s are generated and χ^2 of model SED with each s (total number of models becomes 30000000) is calculated. The likelihood function is assumed to have a form of the Student's t distribution as follows

$$P(X|\theta_m) = \frac{\Gamma\left(\frac{\nu+1}{2}\right)}{\sqrt{\nu\pi}\,\Gamma\left(\frac{\nu}{2}\right)} \left(1 + \frac{(\chi_m^2)^2}{\nu}\right)^{-\frac{\nu+1}{2}} \tag{3.20}$$

We assume the degree of freedom of the Student's t-distribution, ν, as 3, because that distribution gives the consistent sSFR estimate as tested with mock SEDs and also gives the best SFR estimate as compared to 24μm observations (see Appendix A.2). Adopting the Student's t-distribution for the likelihood function could give higher probability to a model with large χ^2 compared to the Gaussian distribution ($P(\theta|X) \propto \exp(-\chi^2/2)$), which is commonly used in the Bayesian SED fittings (e.g., Kauffmann et al. 2003b; Salim et al. 2007; da Cunha et al. 2008; Han and Han 2014).

With the uniform prior, the likelihood function associated with a model parameter could be thought as a weight for the model parameter and the posterior probability of the model parameter then has the following form

$$P(\theta_m|X) = \frac{P(X|\theta_m)}{\sum\limits_{m=1}^{N} P(X|\theta_m)} \tag{3.21}$$

with m is index for model such that θ_m represent value of a model parameter θ associated the m-th model and N is the number of models. In order to derive the best estimate for a model parameter of θ, a posterior mean of θ is calculated with the following equation

$$\bar{\theta} = \sum_{m=1}^{N} \theta P(\theta_m|X) \tag{3.22}$$

$$= \frac{\sum\limits_{m=1}^{N} \theta P(X|\theta_m)}{\sum\limits_{m=1}^{N} P(X|\theta_m)} \tag{3.23}$$

For each model SED, there are seven parameters associated with it, Z, τ of SFR decaying timescale, $E(B-V)$, stellar population age (t), model normalization (s), SFR, and stellar mass (m_*). The m_* and SFR are not first principal model parameters, instead they are multiplication between other model parameters. Because each model SED generated with the GALAXEV (Bruzual and Charlot 2003) is normalized with a stellar mass of 1 M$_\odot$, the estimated s corresponds to the

m_*. Instantaneous SFR is derived with

$$SFR = \frac{m_*}{1 - \exp(-t/\tau)} \times \frac{\exp(-t/\tau)}{\tau} \tag{3.24}$$

where the first multiplication term in the right-hand side serve as a scaling between integrated mass and instantaneous SFR. Throughout this research, we only focus on the spatially resolved distributions of SFR and stellar mass. Therefore, currently we only extract SFR and m_* from the fitting process. In this case, SFR and m_* of each bin are derived by calculating their posterior means using eq. 3.22 (with θ being replaced by SFR or m_*).

Once the posterior means of SFR and m_* of each bin are calculated, those values are divided into the pixels that belong to the bin. To divide the SFR and m_* of a bin into pixels that are associated with the bin, we assume that the SFR and m_* of a pixel are proportional to its fluxes in waveband with the shortest and longest wavelength (FUV and z fluxes for the $z \sim 0$ sample and F435W and F160W fluxes for the $z \sim 1$ sample), respectively, such that SFR and m_* of pixel could be calculated using following equation

$$\mathrm{SFR}_{\mathrm{pixel}} = \frac{\mathrm{Flux}_{\mathrm{FUV\ (or\ F435W,pixel)}}}{\mathrm{Flux}_{\mathrm{FUV\ (or\ F435W,bin)}}} \times \mathrm{SFR}_{\mathrm{bin}} \tag{3.25}$$

$$m_{*,\mathrm{pixel}} = \frac{\mathrm{Flux}_{z\ \mathrm{(or\ F160W,pixel)}}}{\mathrm{Flux}_{z\ \mathrm{(or\ F160W,bin)}}} \times m_{*,\mathrm{bin}} \tag{3.26}$$

We also calculate uncertainties of SFR and m_* of each bin by calculating the standard deviation of the probability distribution function (PDF) associated with the posterior probability distributions of SFR and m_*. The uncertainties of SFR and m_* of pixels that belong to the bin are then calculated using the propagation error of the above equations.

3.4 Examples of the pixel-to-pixel SED fitting result

3.4.1 Matrix of the posterior probability distribution functions

Fig. 3.16 and 3.17 show examples of posterior probability distribution functions of the model parameters outputted by the pixel-to-pixel SED fitting method. This kind of diagram is obtained for each galaxy's bin (collection of pixels). By using model weighting (likelihood) with Student's t form (see Section 3.3 for detailed description on the SED fitting method), reasonably higher weight is given to each model SED compared to the weight if Gaussian likelihood is assumed. By giving reasonably higher weight to all the model SEDs, the degeneracies existing in the model SEDs are statistically considered in estimating the SFR and stellar mass. As shown in the Fig. 3.16, degeneracy between dust extinction and age is depicted in 2D posterior probability distribution function (between age and $E(B-V)$) as well as in 1D posterior probability distribution function (that of $E(B-V)$). Small box in the upper right side of each figure shows observed SED of the bin.

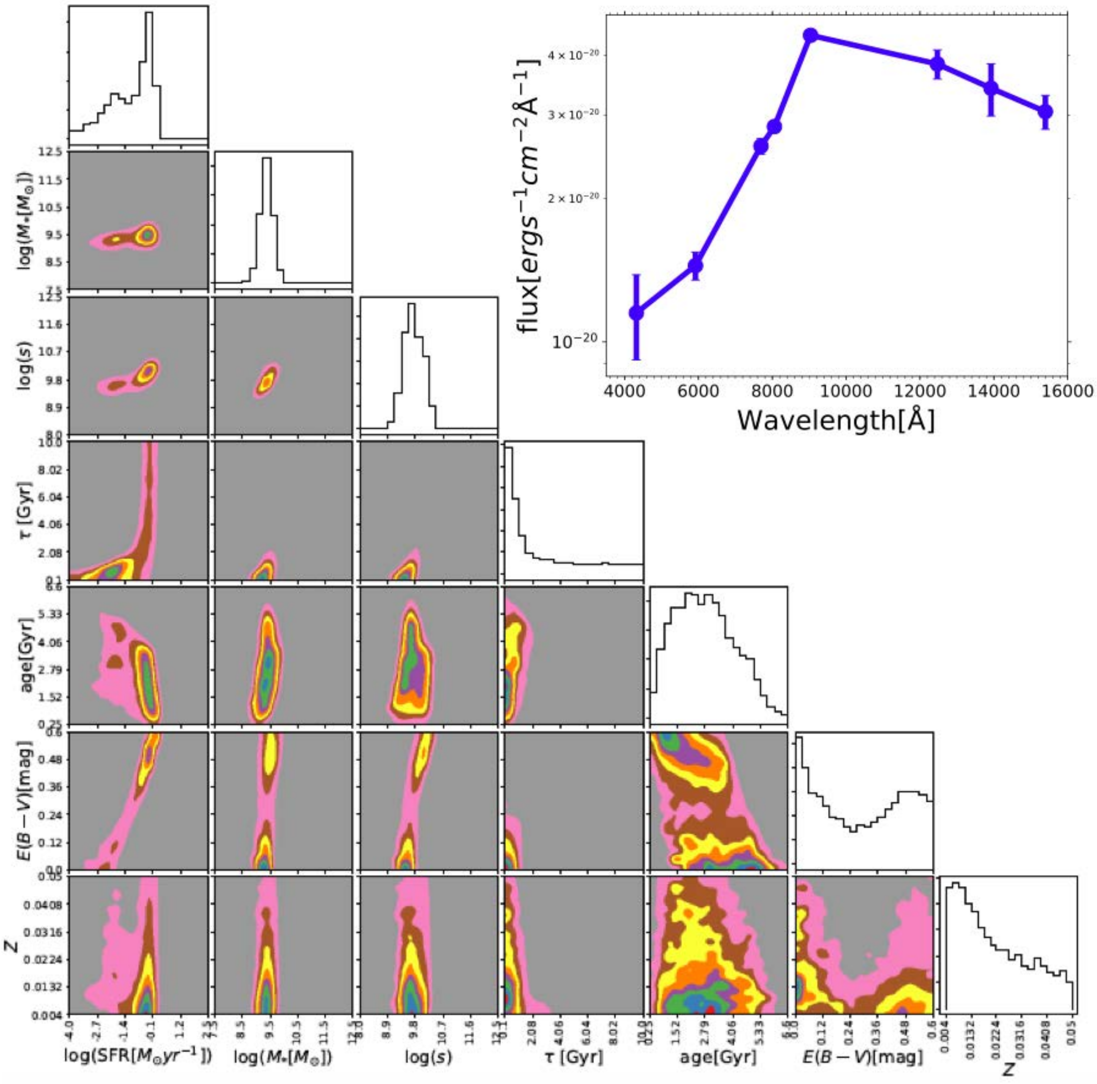

Figure 3.16: Example of a posterior probability distributions of the model parameters in the Bayesian SED fitting adopted in the pixel-to-pixel SED fitting. This posterior probability distribution represents a fitting result for 10th bin of the galaxy GS_3236 in the $z \sim 1$ sample. As a product of the pixel-to-pixel SED fitting, each bin (collection of pixels) in a galaxy has this kind of diagram. Small box in the top right side shows observed SED of the bin.

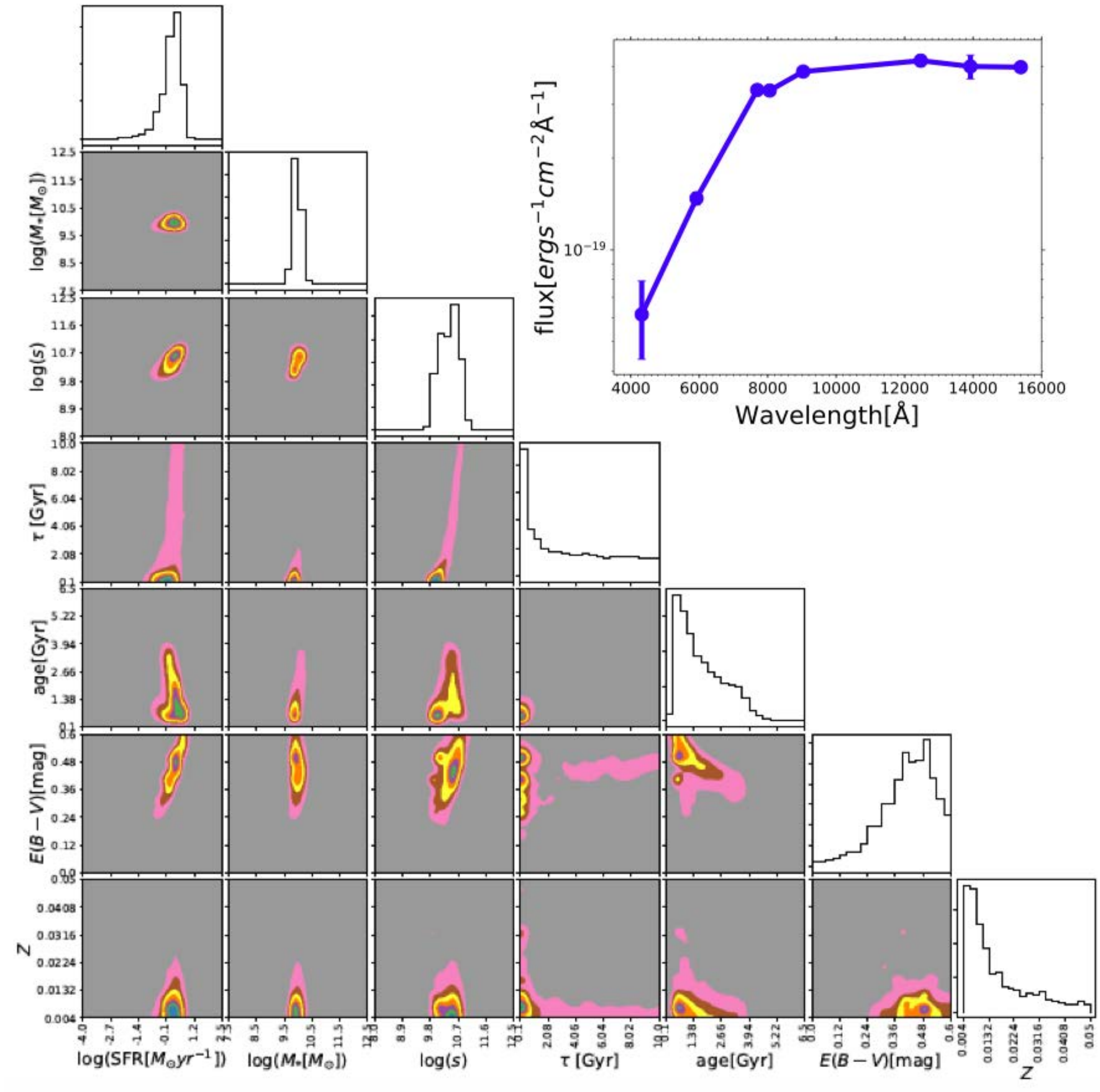

Figure 3.17: Same as in Fig. 3.16 but for 4th bin of the galaxy GS_6494 in the $z \sim 1$ sample.

In many cases, 1D posterior probability distribution functions of SFR and m_* are relatively tight (with small standard deviation), while those of other stellar population properties (Z, τ, $E(B-V)$, and age) are wide (with large standard deviation) and even have two peaks due to the degeneracy among the model parameters, such as shown in the Fig. 3.16. Due to the degeneracy, it is not appropriate to pick a single best-fitting model SED and use its properties as the best estimate for the parameters. Any estimate of parameter resulted from this fitting process must be followed with appropriate averaging with weighting by probability. In this research, we only extract SFR and M_* from the fitting process. Given relatively tight 1D posterior probability distribution functions of the SFR and M_*, it is appropriate to calculate posterior means, while for other stellar population properties, calculating posterior means could be misleading, given their broad 1D posterior probability distribution functions. Due to those reasons, we do not discuss the spatially resolved distributions of other properties. It will be the focus of future work to further develop the methodology and find an appropriate technique to extract the other stellar population properties.

3.4.2 Example of the pixel-to-pixel SED fitting results: Σ_* and $\Sigma_{\rm SFR}$ maps

Fig. 3.18 shows the pixel-to-pixel SED fitting result, consisting Σ_* (top left), Σ_* uncertainty (bottom left), $\Sigma_{\rm SFR}$ (top right), and $\Sigma_{\rm SFR}$ uncertainty (bottom right), for a galaxy (SDSS ObjID 1237652947457998886 or NGC 309) in the $z \sim 0$ sample whose pixel binning result is shown in Fig. 3.9, and the maps of the multiband fluxes and flux uncertainties are shown in Fig. 3.5 and Fig. 3.6, respectively. Fig. 3.19 shows the pixel-to-pixel SED fitting result, consisting Σ_* (top left), Σ_* uncertainty (bottom left), $\Sigma_{\rm SFR}$ (top right), and $\Sigma_{\rm SFR}$ uncertainty (bottom right), for a galaxy (GS_19186) in the $z \sim 1$ sample whose the pixel binning result is shown in Fig. 3.10, and maps of the multiband fluxes and flux uncertainties are shown in Fig. 3.7 and Fig. 3.8, respectively. Fig. 3.20 and Fig. 3.21 show pixel-to-pixel SED fitting results for four galaxies in the $z \sim 0$ and $z \sim 1$ samples, respectively. In each figure, different column represents result for different galaxy. In each column, from top to bottom show: pixel binning result, Σ_*, Σ_* uncertainty, $\Sigma_{\rm SFR}$, and $\Sigma_{\rm SFR}$ uncertainty.

We have checked the reliability of the pixel-to-pixel SED fitting method through some tests that include pixel-by-pixel comparison of the estimated SFR from this method with that converted from the 24μm image using a nearby resolved galaxy, the M51 galaxy, comparison of the integrated SFR and M_* derived using this method with those taken from the MPA-JHU and 3D-HST catalogs, and fitting test with mock SEDs to verify the Bayesian SED fitting approach adopted by this method. In addition to that, we also checked the reliability of the Calzetti et al. (2000) dust extinction law by comparing a dust extinction vector calculated based on the dust extinction law with a distribution of the spatially resolved SEDs of the $z \sim 0$ sample galaxies on a color-color diagram. We discuss this issues in Appendix A.

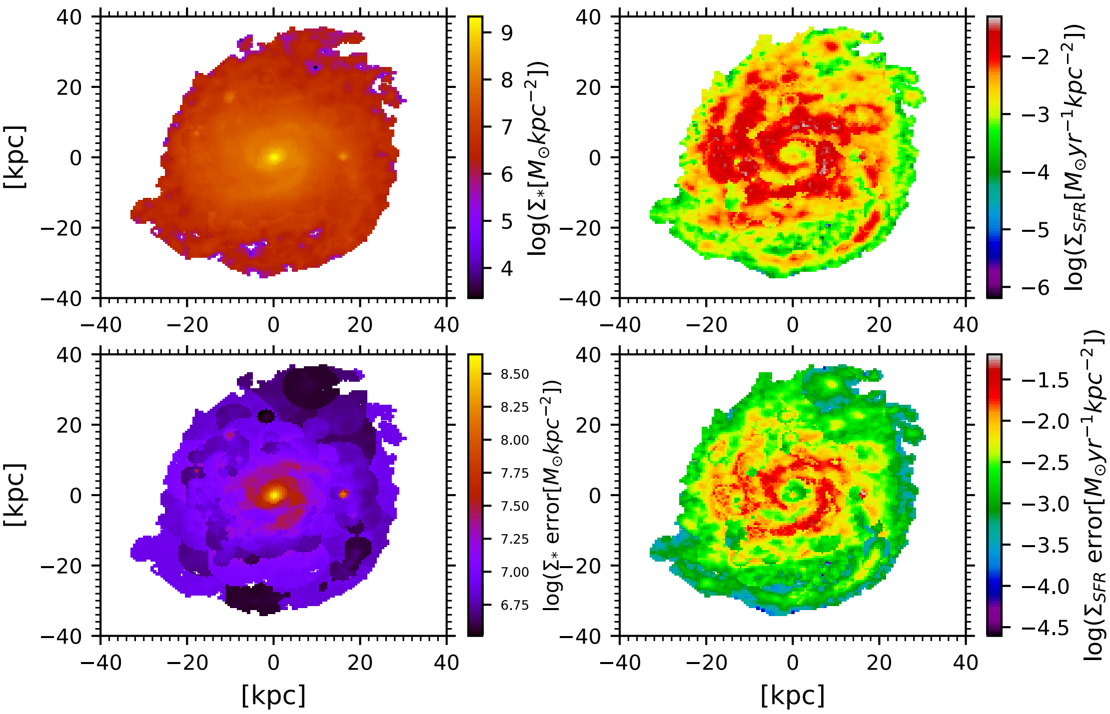

Figure 3.18: Example of the pixel-to-pixel SED fitting results for a galaxy (SDSS ObjID 1237652947457998886 or NGC 0309) in the $z \sim 0$ sample whose the pixel binning result is shown in Fig. 3.9, and the maps of the multiband fluxes and flux uncertainties are shown in Fig. 3.5 and Fig. 3.6, respectively. Top left, top right, bottom left, and bottom right panels show the spatially resolved distributions of Σ_{*}, $\Sigma_{\rm SFR}$, Σ_{*} uncertainty, and $\Sigma_{\rm SFR}$ uncertainty, respectively.

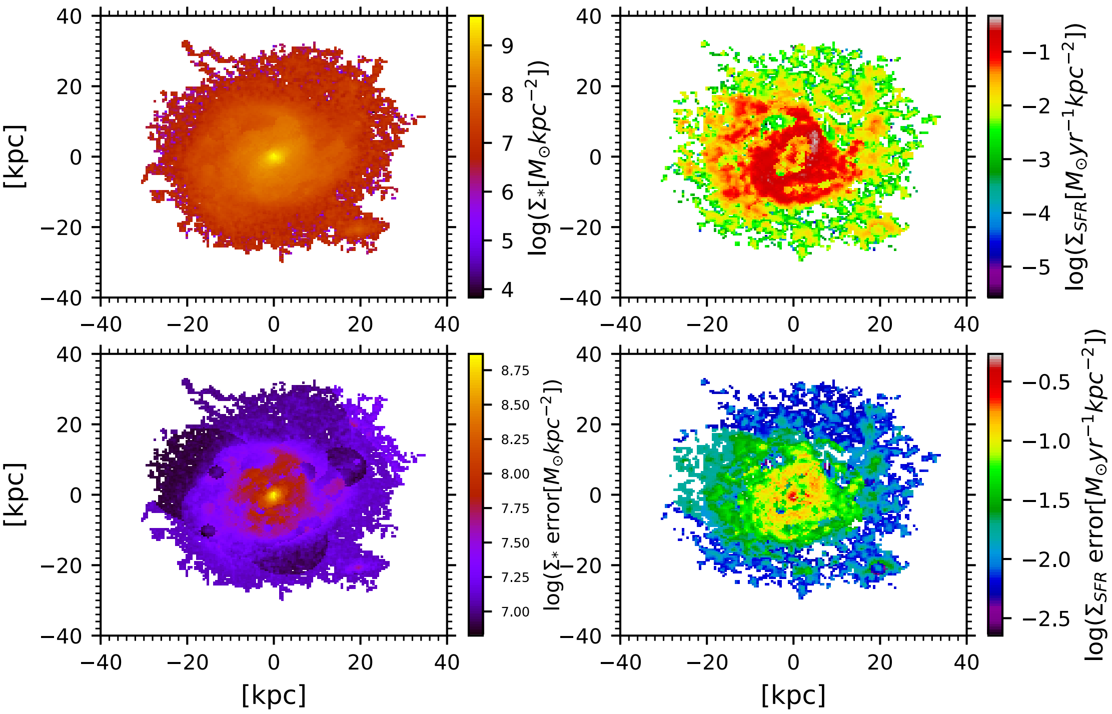

Figure 3.19: Example of the pixel-to-pixel SED fitting results for a galaxy (GS 19186) in the $z \sim 1$ sample whose the pixel binning result is shown in Fig. 3.10, and the maps of the multiband fluxes and flux uncertainties are shown in Fig. 3.7 and Fig. 3.8, respectively. Top left, top right, bottom left, and bottom right panels show the spatially resolved distributions of Σ_*, $\Sigma_{\rm SFR}$, Σ_* uncertainty, and $\Sigma_{\rm SFR}$ uncertainty, respectively. This figure is taken from Abdurro'uf and Akiyama (2018).

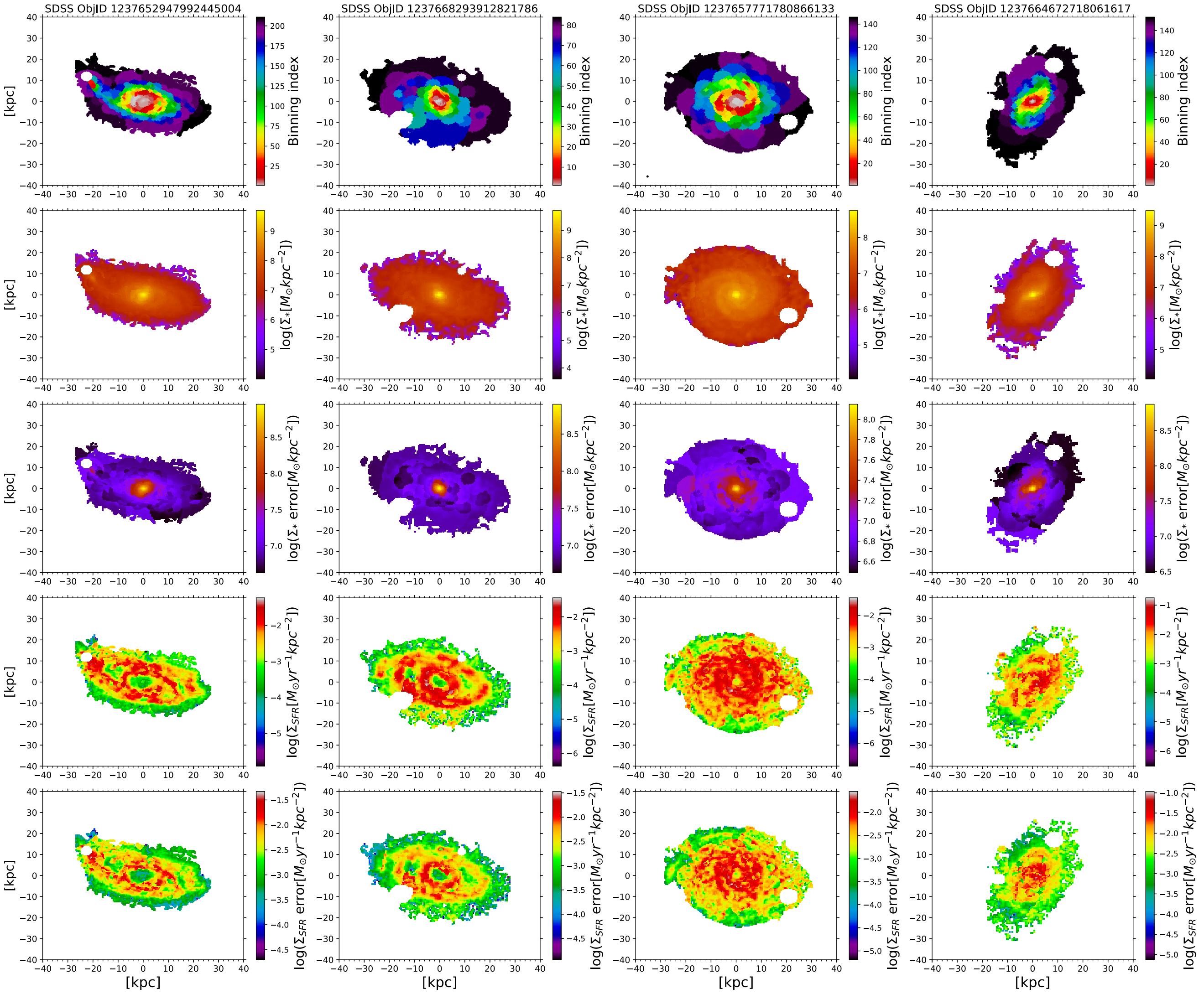

Figure 3.20: Another example of the pixel-to-pixel SED fitting results for galaxies in the $z \sim 0$ sample. Different column represent fitting result for different galaxy. In each column, from top to bottom show: pixel binning result, Σ_* map, Σ_* uncertainty map, Σ_{SFR} map, and Σ_{SFR} uncertainty.

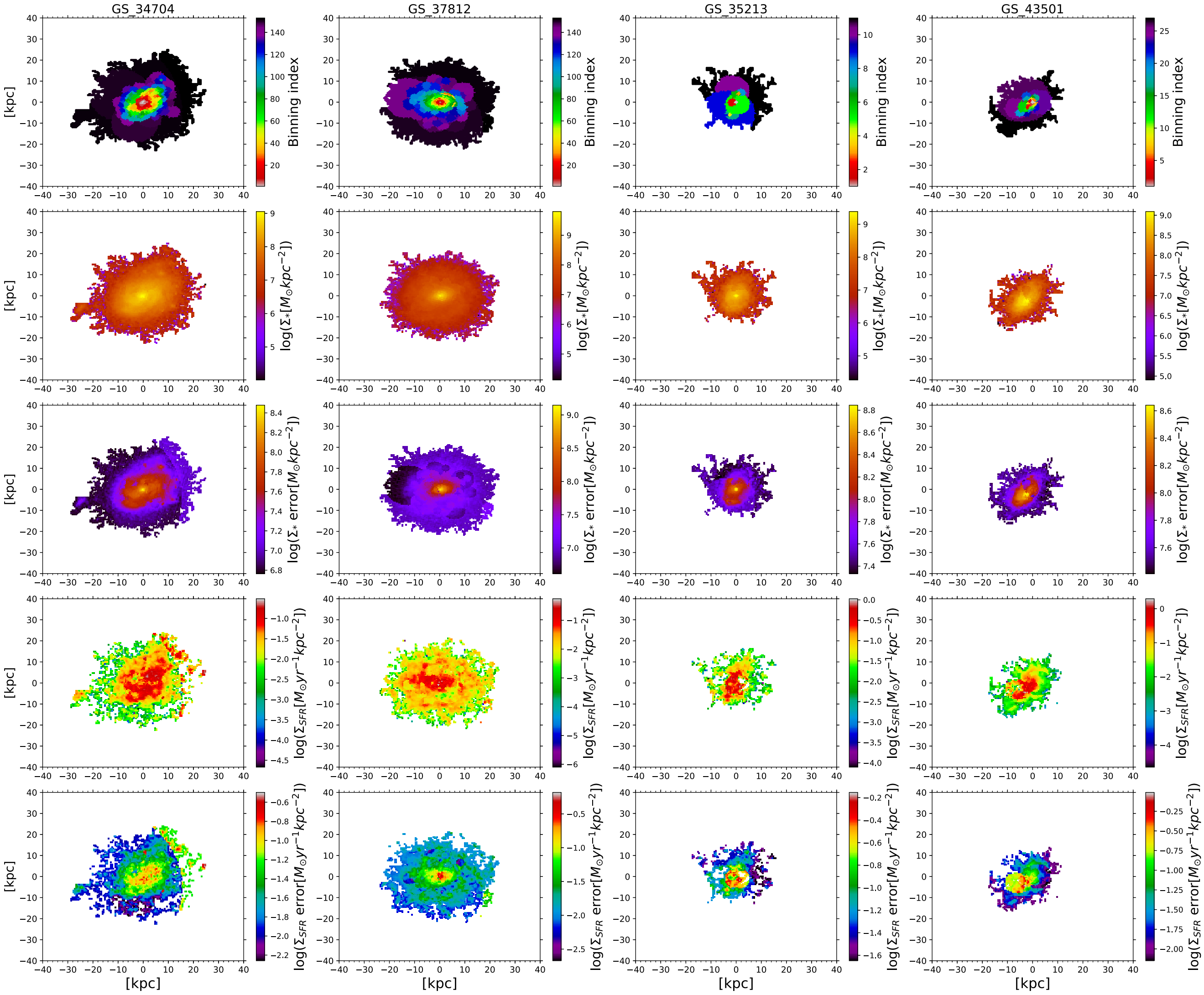

Figure 3.21: Another example of the pixel-to-pixel SED fitting results for galaxies in the $z \sim 1$ sample. Different column represent fitting result for different galaxy. In each column, from top to bottom show: pixel binning result, Σ_* map, Σ_* uncertainty map, $\Sigma_{\rm SFR}$ map, and $\Sigma_{\rm SFR}$ uncertainty.

Chapter 4

Spatially resolved distributions of SFR and M_* in massive disk galaxies at $z \sim 0$

4.1 Spatially resolved star formation main sequence (SFMS) in massive disk galaxies at $z \sim 0$

In order to investigate the possible relation between surface densities of SFR ($\Sigma_{\rm SFR}$) and stellar mass (Σ_*) at ~ 1 kpc scale, we plot all pixels of the 93 galaxies in the $z \sim 0$ sample (which contains 375215 pixels) on the $\Sigma_{\rm SFR}$ versus Σ_* plane. The resulted plot is shown in the Fig. 4.1. In the left panel of the figure, $\Sigma_{\rm SFR}$ - Σ_* relation is shown. The contours show regions in the plots with similar number of pixels which is accounted based on a 0.1×0.1 dex^2 bin. The contour is color-coded by the number of pixels associated with it. The tight relation between $\Sigma_{\rm SFR}$ and Σ_* is evidenced by the contours with high number. This relation, which is called spatially resolved star formation main sequence (SFMS), is also observed by other researchers (e.g. Wuyts et al. 2013; Magdis et al. 2016; Cano-Díaz et al. 2016; Maragkoudakis et al. 2017; Lin et al. 2017; Hsieh et al. 2017; Medling et al. 2018; Liu et al. 2018).

Red dashed line in the left panel represents result of a linear function fitting with the form of

$$\log \Sigma_{\rm SFR} = \alpha \log \Sigma_* + \beta \tag{4.1}$$

to all the scattered data. It has slope (α) of 0.33, zero-point (β) of -5.23, and scatter (σ) of 0.70 dex (see Table 4.1). The fitting is done using the least square method. Black circles with errorbars represent mode of $\Sigma_{\rm SFR}$ distribution associated with each Σ_* bin with 0.3 dex width. The errorbar represents standard deviation around the mode value and it is calculated separately

Table 4.1: Coefficients of the best-fitting linear function to the various spatially resolved SFMS definition

Coefficient	Best-fitting linear function			
	linear part of the mode profile	100% of the data	80% of the data	50% of the data
Slope (α)	1.00	0.33	0.53	0.67
Zero-point (β)	-9.58	-5.23	-6.52	-7.31
Scatter (σ)[dex]		0.7	0.48	0.31

above and below the mode value. It should be noted that the errorbar does not represent uncertainty associated with the mode value, instead it is only intended to show the distribution of pixels above and below the mode value. The mode profile clearly shows linear increasing trend at low Σ_* region ($\log(\Sigma_*[M_{\odot}\text{kpc}^{-2}]) < 7.55$), while a flattening tendency is observed at high Σ_* end ($\log(\Sigma_*[M_{\odot}\text{kpc}^{-2}]) \geq 7.55$). This 'flattening' trend suggests that a significant number of sub-galactic regions with high Σ_* have suppressed specific star formation rate (sSFR$\equiv \Sigma_{\rm SFR}/\Sigma_*$). This 'flattening' trend is responsible for the shallow slope of the red dashed line which makes it largely deviates from the linear trend at the low Σ_* region suggested by the contours with high number. The linear part in the mode profile (consists of four mode values, excluding two mode values with lowest Σ_* because they are affected by the detection limit) could be best-fitted with a linear function with a slope (α) of 1.00 and zero-point (β) of -9.58 (see Table 4.1), as shown by black line.

Right panel in the Fig. 4.1 shows the spatially resolved SFMS shown with contours which represent percentage of number of enclosing pixels with respect to the total number of pixels. The increasing percentage is calculated from the bin that contains largest number of pixels toward the bin with lowest number of pixels. It is shown from this figure that most of the pixels (80%) reside within a narrow locus. Brown solid line shows result of linear function fitting (with least square fitting method) to the pixels within the 80% contour. The line has a slope (α) of 0.53, zero-point (β) of -6.52, and scatter (σ) of 0.48 dex (see Table 4.1). This line is steeper than the red dashed line in the left panel and the scatter around this line is much smaller than the scatter if 100% of the data is used. Brown dashed line represents best-fitting linear function to the 50% of the data. It has steeper slope ($\alpha = 0.67$) and smaller scatter ($\sigma = 0.31$ dex) compared to the best-fitting linear function if 80% and 100% of the data are used. The increasing slope from the red dashed line in the left panel to the brown solid and dashed lines in the right panel further demonstrates effect of the 'flattening' on decreasing the slope of the best-fitting function. Characteristic slopes, zero-points, and scatters of the best-fitting linear functions that are shown in the Fig. 4.1 are compiled in Table 4.1.

Fig. 4.2 shows sSFR versus Σ_* of all 375215 pixels of the sample galaxies. Similar as in the left panel of Fig. 4.1, contours connect regions with similar number of pixels that is accounted based on a bin with 0.1×0.1 dex^2 area. The black circles with errorbars represent mode values of the sSFR distributions associated with Σ_* bins with 0.3 dex width. Similar as in the Fig. 4.1, the errorbar is obtained by calculating standard deviation around the mode value and it is calculated separately above and below the mode value. It is shown by the figure that in the sub-galactic scale, sSFR is decreasing

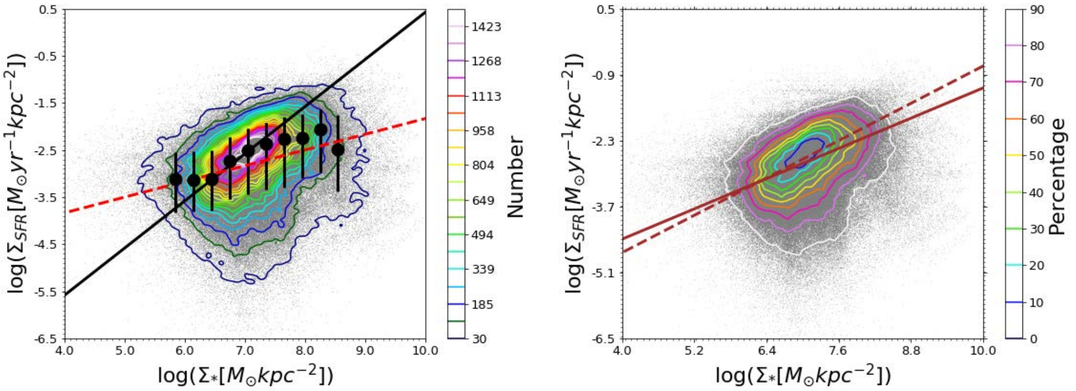

Figure 4.1: Spatially resolved star formation main sequence (SFMS) constructed from all pixels in the sample galaxies. Left panel: spatially resolved SFMS shown with color contour representing number of pixel within each 0.1×0.1 dex^2 bin. Gray points show the scattered data. Black circles show mode of $\Sigma_{\rm SFR}$ distribution associated with each Σ_* bin with 0.3 dex width. Red dashed line represents result of linear function fitting to all the scattered data, while black solid line represents result of linear function fitting to the linear increasing part of the mode profile (with four mode value excluding two model values with lowest Σ_* which affected by the detection limit). Right panel: spatially resolved SFMS shown with contour representing increasing percentage of number of enclosed pixels. Brown solid and dashed lines represent linear function fitting to the data enclosed within 80% and 50% contours, respectively.

with increasing Σ_*. The decreasing sSFR is sharper at high Σ_* end ($\log(\Sigma_*[M_\odot {\rm kpc}^{-2}]) \geq 7.55$), while roughly constant sSFR across Σ_* is shown at low Σ_* ($\log(\Sigma_*[M_\odot {\rm kpc}^{-2}]) < 7.55$, excluding two point in the lowest Σ_* because they are affected by the detection limit), agrees with what is implied by the spatially resolved SFMS (Fig. 4.1).

As we will see later in the discussions on the radial profiles of $\Sigma_*(r)$, $\Sigma_{\rm SFR}(r)$, and sSFR(r) (such as in Sections 4.4 and 5.2), sub-galactic regions associated with high Σ_* are located in the central regions of the galaxies. The 'flattening' trend at high Σ_* end in the spatially resolved SFMS is possibly responsible for the shallower slope (less than 1) of the global SFMS relation observed in the local universe. This result agrees with Abramson et al. (2014) who found that slope of the global SFMS relation in the local universe is nearly unity if the quiescent bulge component is excluded when calculating the integrated SFR and M_* of galaxies, while the slope becomes shallower (< 1) if the bulge region is included.

The mode profile could serve as an objective definition for the spatially resolved SFMS relation. As suggested by Renzini and Peng (2015), the global SFMS could be objectively defined with the ridge line of the number density contours on the SFR-M_* plane. The ridge line could be obtained quantitatively with the mode of the SFR distribution for each M_* bin, as we adopted here for the spatially resolved SFMS relation. Later on, we will use the mode profile to define the spatially resolved SFMS.

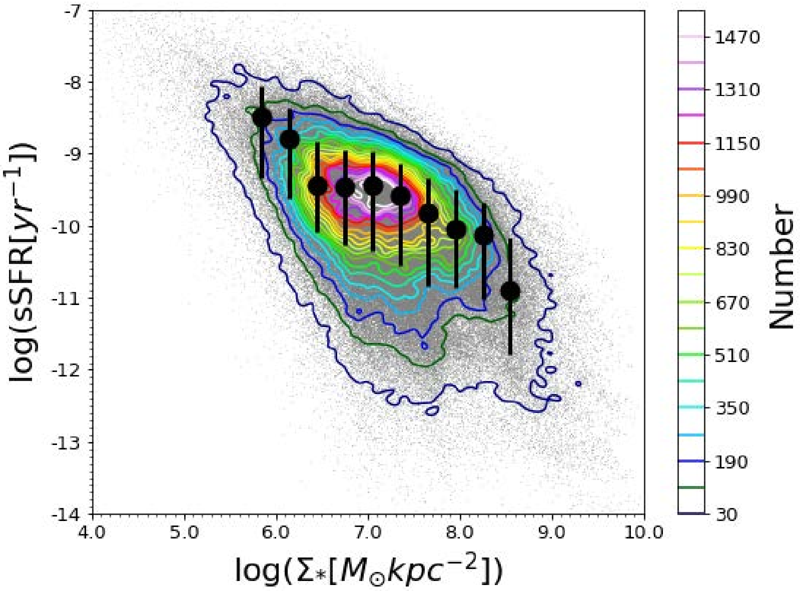

Figure 4.2: Spatially resolved sSFR versus Σ_* of all 375215 pixels of the galaxies in the $z \sim 0$ sample. Contours represent number of pixels within each 0.1×0.1 dex^2 bin and black circles with errorbars represent mode values of the $\Sigma_{\rm SFR}$ distributions associated with Σ_* bins with 0.3 dex width. The errorbar represent standard deviation around the mode value and it is calculated separately above and below the mode value. This figure is taken from Abdurro'uf and Akiyama (2017).

4.2 Spatially resolved SFMS as a function of distance from the global SFMS

In order to get insights on the quenching process in massive disk galaxies (and all galaxies in general), it is important to compare the spatially resolved distributions of SFR and stellar mass in the galaxies across the global SFMS (i.e. SFR versus M_* plane). Spatially resolved SFMS relation provides a unique information about the spatially resolved SFR and stellar mass in the galaxies with a particular global properties. Therefore it could be used to investigate the connection between global properties and spatially resolved properties associated with the star formation activity. Here, we use the spatially resolved SFMS to investigate the connection between global properties of galaxy associated with distance from the global SFMS (which corresponds to the global sSFR) and the spatially resolved properties associated with SFR and stellar mass.

First, sample galaxies at $z \sim 0$ are divided into three groups based on their distances from the global SFMS relation. Fig. 4.3 shows integrated SFR versus M_* of the 93 galaxies in the $z \sim 0$ sample. We adopt global SFMS relation by Speagle et al. (2014) that is calculated at median redshift of the $z \sim 0$ sample ($z = 0.0165$), which is shown by black solid line, to divide the sample galaxies. Galaxies which reside above $+0.3$ dex, within ± 0.3 dex, and below -0.3 dex from the global SFMS are grouped as z0-ΔMS1, z0-ΔMS2, and z0-ΔMS3, respectively. Number of galaxies in the z0-ΔMS1, z0-ΔMS2, and z0-ΔMS3 are 50, 34, and 9, respectively. It should be noted that

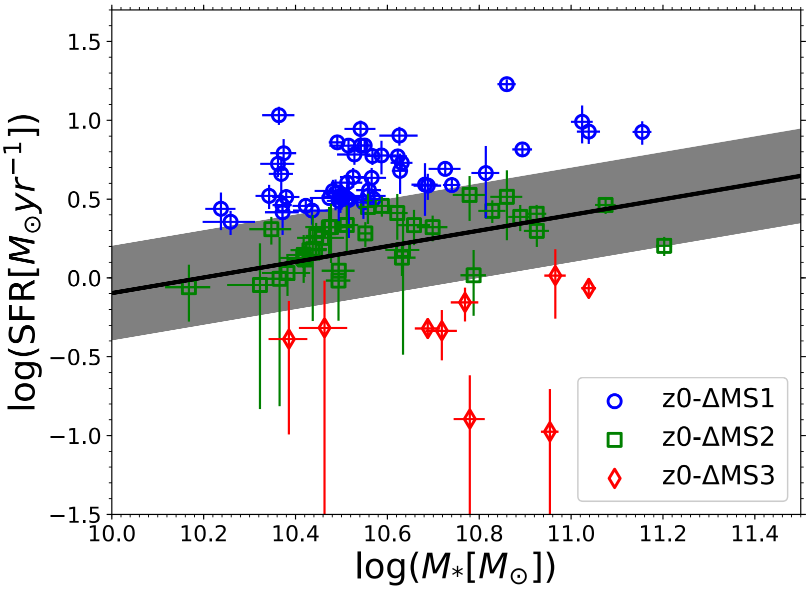

Figure 4.3: Integrated SFR versus M_* of the sample galaxies at $z \sim 0$. Sub-samples that are defined based on distance from the global SFMS are indicated with different symbols. Blue circles, green squares, and red diamonds represent z0-ΔMS1, z0-ΔMS2, and z0-ΔMS3 sub-samples. The global SFMS relation by Speagle et al. (2014) that is calculated at median redshift of the $z \sim 0$ sample galaxies ($z = 0.0165$) is adopted and it is shown by black line. Gray shaded area represents ±0.3 dex around the global SFMS relation.

this classification is based on the global sSFR. Variation on slope and normalization of the global SFMS reported in the literature (see Speagle et al. (2014) for the compilation) could give different result in the galaxy classification based on the distance from the global SFMS relation.

Fig. 4.4 shows spatially resolved SFMS in the z0-ΔMS1 (top left panel; which consists of 218593 pixels), z0-ΔMS2 (top right panel; which consists of 120161 pixels), and z0-ΔMS3 (bottom left panel; which consists of 36461 pixels) galaxies. Spatially resolved SFMS in the z0-ΔMS1 galaxies is tight, which is evidenced by the contours with high number. Blue circles, cyan squares, and red triangles represent mode values of the $\Sigma_{\rm SFR}$ distribution for each Σ_* bin with 0.3 dex width. Errorbar associated with the mode value represents standard deviation around the mode value and it is calculated separately above and below the mode value. The spatially resolved SFMS in the z0-ΔMS1 is linear at low Σ_* ($\log(\Sigma_*[M_\odot \text{kpc}^{-2}]) \leq 7.55$) and flattened at high Σ_* end. Best-fitting linear function to the linear increasing part of the mode profile (consisting four mode values) has a slope (α) of 0.99 and zero-point (β) of −9.59, which is shown by black solid line. Black dashed lines in the three panels is the same as the black solid line in the Fig. 4.1. Spatially resolved SFMS in the z0-ΔMS2 galaxies has stronger 'flattening' tendency at high Σ_* end. As shown in the bottom left panel, spatially resolved SFMS seems to be broken in the z0-ΔMS3 galaxies.

Bottom right panel shows comparison of the mode profiles associated with the spatially resolved SFMS in the three groups. It is shown that $\Sigma_{\rm SFR}$ difference is larger at high Σ_* region compared

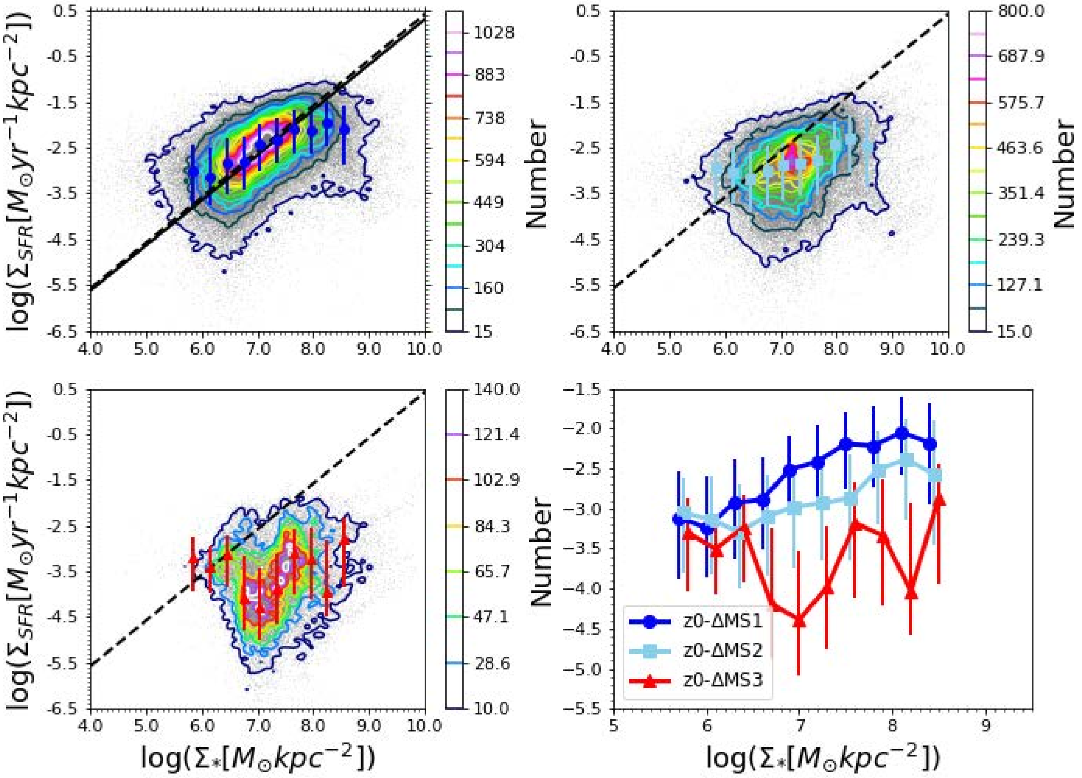

Figure 4.4: Spatially resolved star formation main sequence (SFMS) in z0-ΔMS1 (top left), z0-ΔMS2 (top right), and z0-ΔMS3 (bottom left) galaxies. Bottom right panel shows comparison of those three spatially resolved SFMS. Black solid line in the top left panel represents linear function fitting to the linear increasing part of the mode profile, which consists of four mode values, while black dashed line in three panels are the same as the black solid line in left panel of Fig. 4.1. For clarity, blue circles are shifted by 0.05 to the left from their actual positions and red triangles are shifted by 0.05 to the right from their actual positions. This figure is taken from Abdurro'uf and Akiyama (2017).

to that at low Σ_* region. Normalization in the global SFMS (which also means sSFR) is spatially preserved, in the sense that sSFR of the z0-ΔMS1 galaxies are higher than the sSFR of z0-ΔMS2 galaxies over the entire Σ_* range and sSFR of the z0-ΔMS2 galaxies are higher than sSFR of the z0-ΔMS3 galaxies over the entire Σ_* range. It should be noted that errorbar associated with each mode value does not represent uncertainty of the mode value.

As commonly known for galaxies in general, radial profile of the Σ_* is increasing with decreasing radius (which also implied by the radial profile of the optical surface brightness). Therefore, increasing Σ_* in the spatially resolved SFMS plot (such as shown in Fig. 4.1 and Fig. 4.4) roughly corresponds to a decreasing radius toward the central region of the galaxies. In this sense, bottom right panel in Fig. 4.4 suggests that there is a tendency of decreasing sSFR in the central region as galaxies progressing to quench. In Section 4.4, we will investigate the $\Sigma_*(r)$, $\sigma_{\rm SFR}(r)$, and sSFR(r) radial profiles to get insight on the quenching process in massive disk galaxies.

4.3 Understanding the scatter of the spatially resolved SFMS

Spatially resolved SFMS exists with a relatively larger scatter (~ 0.48 dex if sub-galactic regions from all sample galaxies are considered; see Section 4.1) than that of the global SFMS (~ 0.3 dex regardless of redshift). Scatter in the spatially resolved SFMS corresponds to the variation of $\Sigma_{\rm SFR}$ for 'fix' Σ_{*} which also means variation of sSFR for 'fix' Σ_{*}. Investigating the origin of the scatter in the spatially resolved SFMS could give insights on the causes of the variation of the sub-galactic sSFR. Thus, quenching of star formation activity in sub-galactic scale could be studied. In this section, we will discuss the local variation of sSFR which gives contribution to the scatter in the spatially resolved SFMS and try to study what causes the local variation of sSFR. Given that we only focus on the SFR and M_{*} (globally and locally) in this research, we only discuss the origin of the scatter in the spatially resolved SFMS in term of those properties. Other stellar population properties (e.g. metallicity, age) and gas properties (density and metallicity) might give effect on the local variation of sSFR. However, it is outside of the scope of this thesis to discuss about that and they will be the focus of future researches.

As suggested by Fig. 4.4, global sSFR gives effect on the normalization of the spatially resolved SFMS, such that the spatially resolved SFMS of galaxies with higher global sSFR has higher normalization than that of the spatially resolved SFMS of galaxies with lower global SFMS. Thus, global sSFR gives contribution to the scatter in the spatially resolved SFMS. Next, we will investigate the contributions from global stellar mass.

4.3.1 Effect of global stellar mass to the scatter of the spatially resolved SFMS

In order to investigate effects of the global M_{*} on the scatter of the spatially resolved SFMS, we divide the $z \sim 0$ sample into two groups based on the integrated M_{*}. Median value of the M_{*} of the sample galaxies ($3.5 \times 10^{10} M_{\odot}$) is used as the threshold. Number of galaxies in each group (i.e. high-mass and low-mass groups) is 46. Then we investigate spatially resolved SFMS of the two groups. Left panel in Fig. 4.5 shows comparison between the mode values (i.e. mode profiles) of the spatially resolved SFMS of galaxies in the low-mass (shown with gray color) and high-mass groups (shown with black color). The mode value is calculated with the same method as used for the spatially resolved SFMS of all sample galaxies (see Section 4.1). There is a systematic dependence of the normalization of the spatially resolved SFMS on the global M_{*}, such that the spatially resolved SFMS of more massive galaxies tend to have lower normalization than that of the spatially resolved SFMS of less massive galaxies. It should be noted that the errorbar plotted along with the mode value is not the uncertainty associated with the mode value, instead it is intended to show the distribution of pixels around the mode value (i.e. peak of the number density) as it

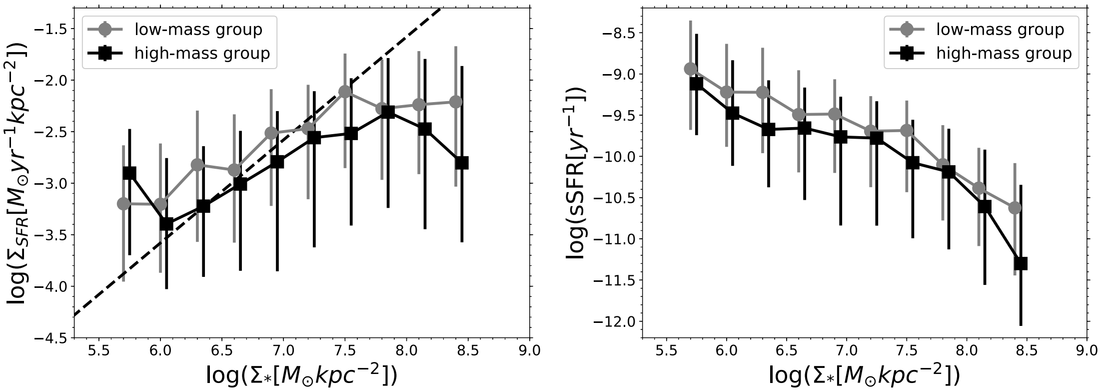

Figure 4.5: Effect of global M_* on the normalization (i.e. scatter) in the spatially resolved SFMS. Left panel: mode values (i.e. mode profiles) associated with the spatially resolved SFMS of galaxies in the low-mass group (shown in gray) and high-mass group (shown in black). Black dashed line is the same as black solid line in the left panel of Fig. 4.1. Right panel: mode profiles associated with the sSFR versus Σ_* in sub-galactic scale of the galaxies in the low-mass group (shown in gray) and high-mass group (shown in black). For clarity, gray circles are shifted by 0.05 dex to the left from their actual positions. Figure in the right panel is adopted from Abdurro'uf and Akiyama (2017).

is calculated with the standard deviation. Uncertainty associated with the mode value (calculated with e.g. bootstrap resampling) could result in lower uncertainty.

Right panel in the Fig. 4.5 shows the mode values of the sSFR distributions associated with the Σ_* bins with 0.3 dex width. It is shown by this figure that there is a systematic dependence of the sub-galactic sSFR on the global M_*, such that more massive galaxies tend to have lower sub-galactic sSFR than that of less massive galaxies. The lower sub-galactic sSFR in more massive galaxies is observed over the entire Σ_* range. It is already known that more massive galaxies tend to quench earlier than less massive galaxies, i.e. "downsizing" scenario (e.g. Cowie et al. 1996; Juneau et al. 2005). Right panel in the Fig. 4.5 shows an indication that the "downsizing" is happen not only in the global scale but also in the local kpc-scale.

4.3.2 Local variation of the sSFR and its contribution to the scatter of the spatially resolved SFMS

In order to get insights on the origin of the scatter of the spatially resolved SFMS relation and what drives the relation, we investigate the $\Sigma_{\rm SFR}$ - Σ_* relation in individual galaxy. For each galaxy, we plot the distribution of the pixels (that belong to the galaxy) on the $\Sigma_{\rm SFR}$ versus Σ_* plane. We found that the spatially resolved SFMS relation is hold in individual galaxy. Figures 4.6, 4.7, and 4.8 show examples of the spatially resolved SFMS relations (leftmost column in each figure) in the individual galaxies that belong to the z0-ΔMS1, z0-ΔMS2, and z0-ΔMS3 groups, respectively. In each figure, black line in each panel in the leftmost column represents best-fitting linear function to the $\Sigma_{\rm SFR}$-Σ_* relation for pixels located outside of a half-mass radius. Slope (α), zero-point (β), and scatter (σ) of the best-fitting linear function is shown along with the figure. The half-mass radius is defined as a radius (along the semi-major axis) which covers half of the total M_*. The method to calculate semi-major axis (i.e. ellipticity and position angle) of a galaxy is described in Section 4.4.1. Pixels located within the half-mass radius are shown with the red points. Blue and green points represent pixels located outside of the half-mass radius that reside above and below the best-fitting linear function (the black solid line), respectively. Spatial locations of the red, blue, and green points are shown in a panel in the middle column in each figure. The linear function fitting is done for the sub-galactic regions located outside of the half-mass radius because those regions seem to form a linear relation in the $\Sigma_{\rm SFR}$-Σ_* plane, while the sub-galactic regions located within the half-mass radius seem to make a $\Sigma_{\rm SFR}$ suppression trend at high Σ_* end. This $\Sigma_{\rm SFR}$ suppression trend at high Σ_* is responsible for the 'flattening' trend at high Σ_* end in the spatially resolved SFMS formed with all pixels of the sample galaxies (Fig. 4.1) as well as with pixels that belong to the z0-ΔMS1 and z0-ΔMS2 galaxies. Only in few cases, such as in galaxies with SDSS ObjIDs of 1237649962454941712 (Fig. 4.6), 1237655463774191765 (Fig. 4.7), and 1237663716555489322 (Fig. 4.8), the sub-galactic regions within the half-mass radius seem to follow the same linear trend as followed by the sub-galactic regions outside of the half-mass radius.

To get perspective on the location of each $\Sigma_{\rm SFR}$-Σ_* relation with respect to the spatially resolved SFMS relation formed with all pixels of the galaxies in the $z \sim 0$ sample (see Fig. 4.1), we plot black dashed line which is the same as black solid line in the Fig. 4.1 (which represents best-fitting linear function to the linear part of the mode profile associated with the spatially resolved SFMS with all pixels of the sample galaxies). It is shown by the figures that the spatially resolved SFMS in individual galaxy that belong to lower sSFR group has systematically lower normalization and tendency to lower slope. Some galaxies in the z0-ΔMS3 group even have negative slope, such as SDSS ObjID 1237663783144128544 (Fig. 4.8). The negative slope is consistent with the spatially resolved distribution of sSFR in the galaxy (shown in rightmost panel), which appears to has large central void followed by a ring-like structure. We will see in Section 4.5 that this feature (ring-like structure in the spatially resolved distribution of sSFR) is common for barred galaxies.

In the rightmost column, the spatially resolved distribution of sSFR is shown to get perspective on the local variation of the sSFR and how it is connected with the scatter of the spatially resolved SFMS in individual galaxy. Regions indicated with blue points roughly correspond to the spiral arms and some knots where relatively intense star formation activities take place. It is shown from this figure that the scatter in the spatially resolved SFMS (in individual galaxy) is corresponds to the spatial (i.e. local) variation of the sSFR which usually associated with some distinguished features, such as spiral arm and knots of star formation. It is also shown that the 'flattening' at high Σ_* end in the spatially resolved SFMS is correspond to the central quiescent region (which has low sSFR).

Slope (α) of 1 in the $\Sigma_{\rm SFR}$-Σ_* relation means constant sSFR across the entire region (whole Σ_* range), while a slope below 1 represents decreasing sSFR with increasing Σ_*. The sSFR which represent the stellar mass growth rate roughly corresponds to an efficiency of a star formation. Therefore, the slope of the spatially resolved SFMS in individual galaxy could give important information regarding the star formation efficiency within the galaxy. Any dependence of the slope on the global

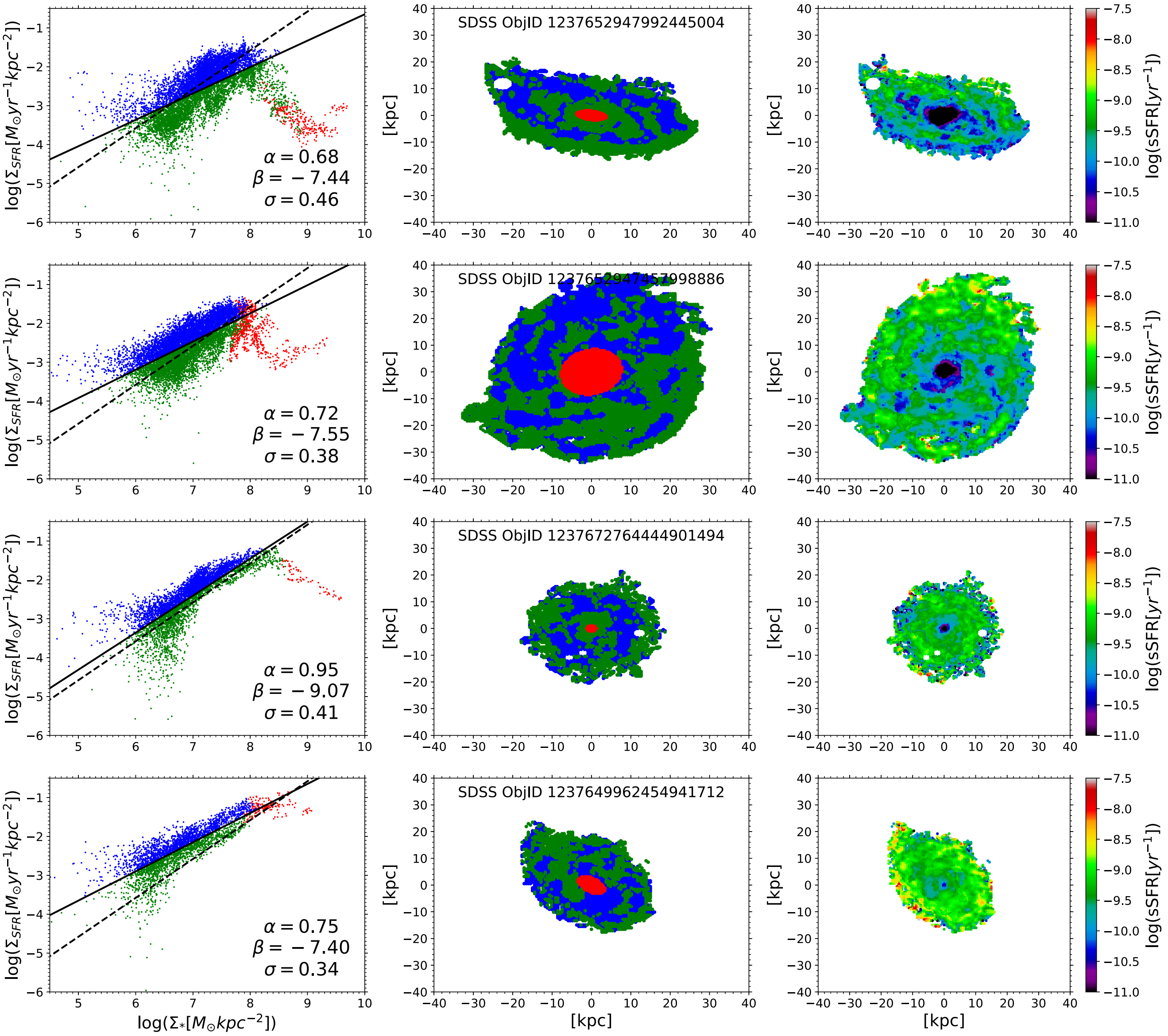

Figure 4.6: Left column: example of spatially resolved SFMS hold in individual galaxies that belong to the z0-ΔMS1 group. Black solid line represents best-fitting linear function to the $\Sigma_{\rm SFR}$-Σ_{*} relation formed with sub-galactic regions (i.e. pixels) located outside the half-mass radius. Slope (α), zero-point (β), and scatter (σ) of the best-fitting linear function are shown along with the figure. Black dashed line is the same as black solid line in the Fig. 4.1. Red points represent sub-galactic regions located within the half-mass radius, while blue and green points represent sub-galactic regions located outside the half-mass radius and reside above and below the best-fitting linear function, respectively. Middle column: spatial locations of the red, blue and green points within the galaxy. Right column: spatially resolved distribution of sSFR.

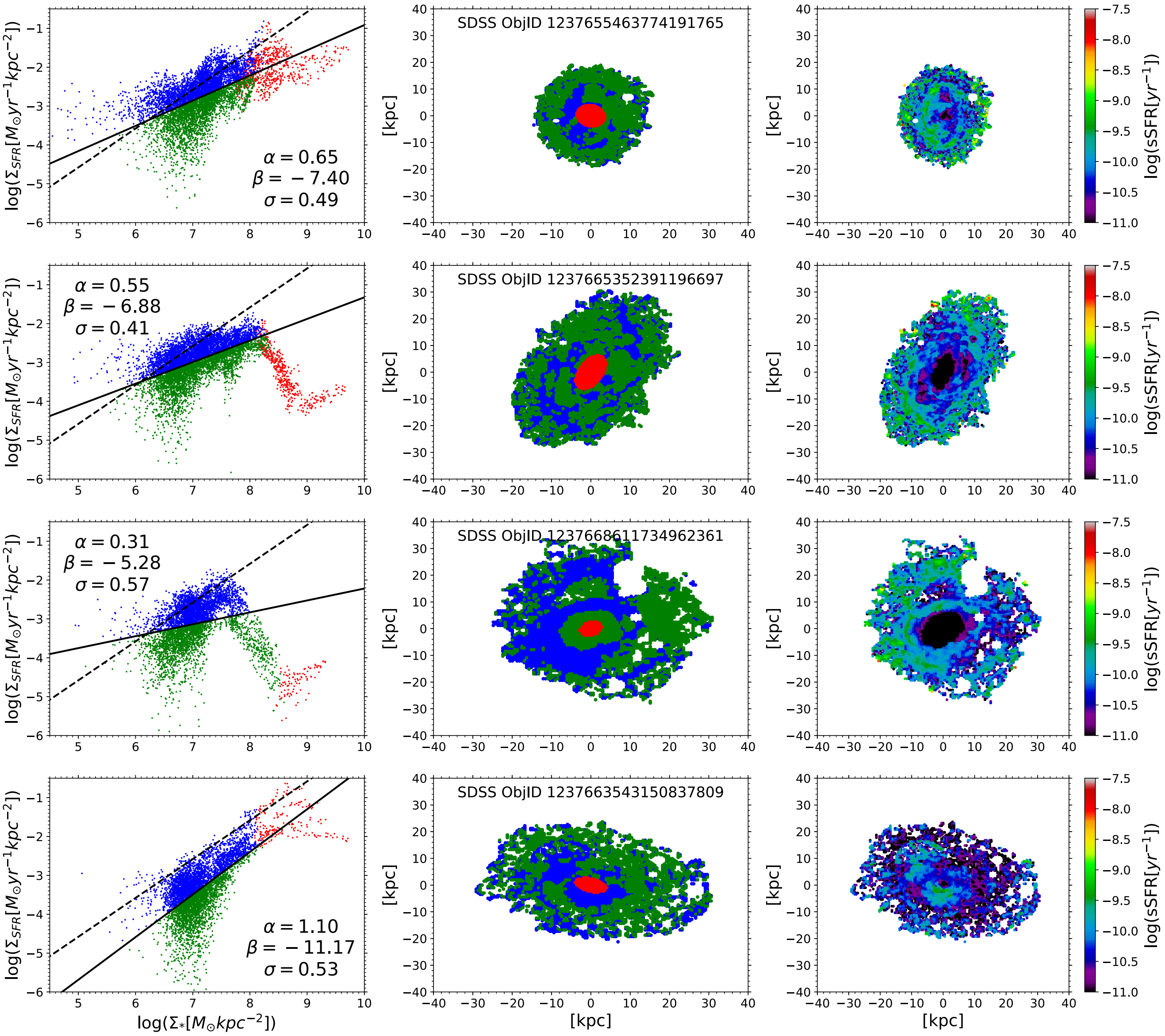

Figure 4.7: Same as Fig. 4.6 but now for some galaxies in the z0-ΔMS2 group.

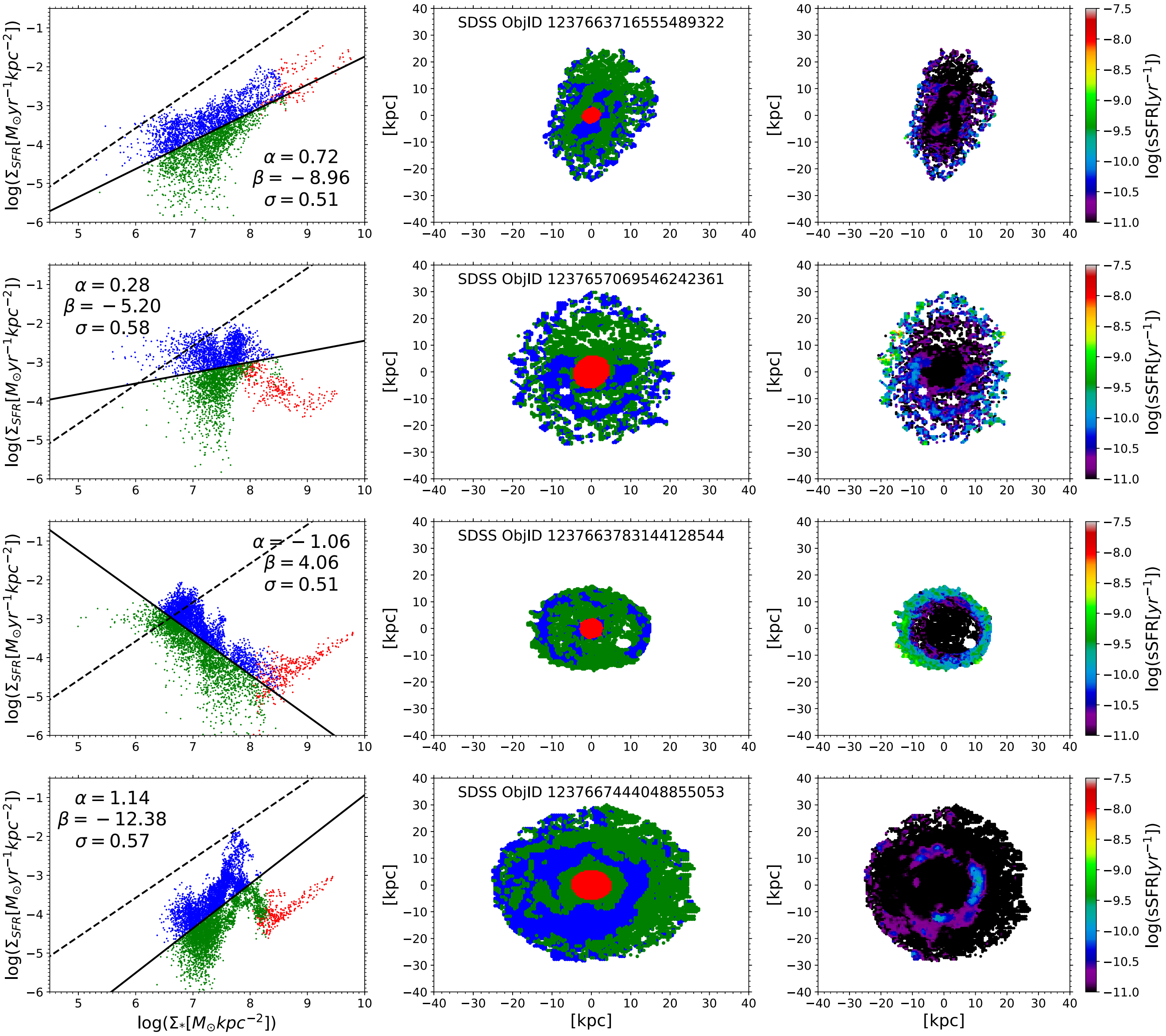

Figure 4.8: Same as Fig. 4.6 but now for some galaxies in the z0-ΔMS3 group.

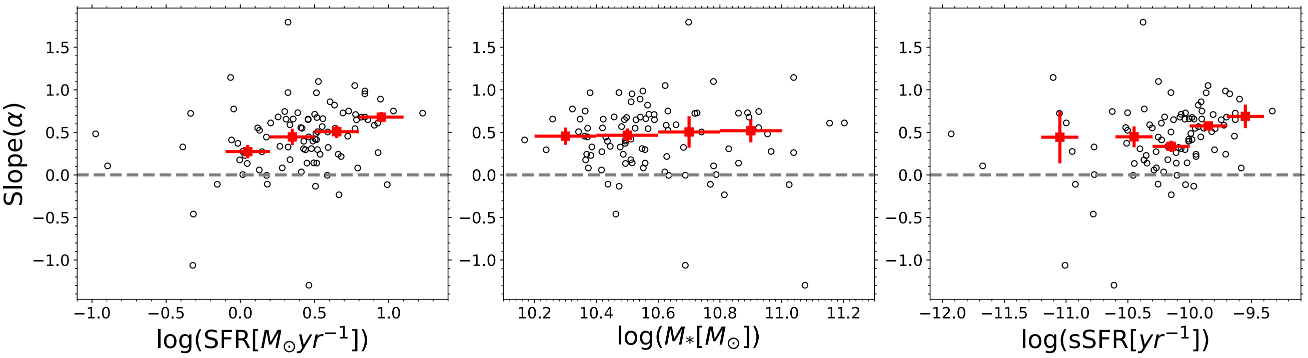

Figure 4.9: Slopes of the spatially resolved SFMS in individual galaxies as functions of SFR (left panel), M_{*} (middle panel), and sSFR (right panel). The vertical errorbar represents the uncertainty of the median of the slope which is calculated through bootstrap resampling method, while the horizontal errorbar represents the width of the global property considered in calculating the median of the slope.

properties of galaxy (such as SFR, M_{*}, and sSFR) might give insight on the connection between global phenomenon (related to the global properties, such as global gas accretion) and the local star formation activity in the galaxy. We investigate dependence of the slope of the spatially resolved SFMS in individual galaxy on the global properties of SFR, M_{*}, and sSFR. Fig. 4.9 shows the slope as functions of the SFR (left panel), M_{*} (middle panel), and sSFR (right panel). The red squares with errorbars represent median of the slope associated with each global property with width of 0.3 dex, 0.2 dex, and 0.3 dex for the SFR, M_{*}, and sSFR, respectively. The vertical errorbar represents the uncertainty of the median of the slope which is calculated through bootstrap resampling method, while the horizontal errorbar represents the width of the global property considered in calculating the median of the slope. This figure shows that there seems a dependence of the spatially resolved SFMS slope in an individual galaxy on the SFR of the galaxy, in such a way that the galaxy with higher SFR tend to have spatially resolved SFMS with steeper slope. It means that in galaxies with higher SFR (might be due to higher gas content/gas accretion), star formation efficiency tend to be uniform within their regions.

4.4 Radial profiles of $\Sigma_{*}(r)$, $\Sigma_{\rm SFR}(r)$, and sSFR(r)

4.4.1 Deriving the $\Sigma_{*}(r)$, $\Sigma_{\rm SFR}(r)$, and sSFR(r) radial profiles for individual galaxy

Throughout this thesis, average surface density radial profiles ($\Sigma_{*}(r)$, $\Sigma_{\rm SFR}(r)$, and sSFR(r)) of galaxies with a particular global properties is derived by averaging over individual radial profiles of the galaxies. It is different from the methods used by other researchers (e.g. Nelson et al. 2016a) where the spatially resolved maps (of Σ_{*} and $\Sigma_{\rm SFR}$) are stacked then the radial profiles from the stacked-maps are calculated. In order to derive $\Sigma_{*}(r)$, $\Sigma_{\rm SFR}(r)$, and sSFR(r) radial profiles of a galaxy, first, elliptical isophotes fitting is done to obtain the best-fitting elliptical isophotes (with certain values of ellipticity and position angle) associated with the spatially resolved distribution of r-band fluxes in the galaxy. Spatially resolved r-band flux is chosen as a reference to obtain the characteristic elliptical isophotes because r band is roughly located in the central part of the SED. The elliptical isophotes fitting is done by applying `ellipse` command in `IRAF` to the r-band image of the galaxy. Result of this fitting is a fits table which contains a set of elliptical isophotes with various semi-major axis (increasing from central region toward outskirt), ellipticities, and position angles. The position angle represents orientation of the semi-major axis and it is expressed as an angle in degree measured counterclockwise from the positive y axis. In many cases, central coordinates of those isophotes are slightly different (within ~ 1 pixel). However, those central coordinates are close to the coordinate of the brightest pixel in r-band.

Next step is averaging the best-fitting elliptical isophotes obtained from the previous step. We assume the central coordinate of the galaxy as the coordinate of brightest pixel in r-band. The ellipticities and position angles of the best-fitting elliptical isophotes are averaged. To avoid bias toward isophotes located in the central region (in many cases, elliptical isophotes located in the central region have different ellipticities and position angles compared to those in the underlying disk due to bar structure and bulge), only elliptical isophotes located outside of the half-mass radius (i.e. semi-major axis within which half of total M_* is enclosed) are averaged. The half-mass radius is defined using elliptical isophotes obtained by averaging all the elliptical isophotes regardless of their radial positions (i.e. including those reside in the central region).

After getting the average ellipticity and position angle, next step is deriving the $\Sigma_*(r)$ and $\Sigma_{\rm SFR}(r)$ of each galaxy in the $z \sim 0$ sample. The $\Sigma_*(r)$ and $\Sigma_{\rm SFR}(r)$ are derived by calculating average Σ_* and $\Sigma_{\rm SFR}$ within elliptical annuli (which are constructed based on the average ellipticity and position angle) with semi-major axis that is sampled by 2 kpc steps within 6 kpc radius and 4 kpc steps outside of it. The radial profile of sSFR(r) is derived by dividing the $\Sigma_{\rm SFR}(r)$ with the $\Sigma_*(r)$.

Fig. 4.10 shows example of the elliptical isophotes fitting results and derived radial profiles of $\Sigma_*(r)$ and $\Sigma_{\rm SFR}(r)$ for three galaxies in the $z \sim 0$ sample. Row from top to bottom shows: (1) results of the elliptical isophotes fitting using `ellipse` command in `IRAF` overlaid on the map of r band flux. The generated isophotes are shown with green ellipses; (2) Elliptical isophotes after averaging the best-fitting isophotes outside of the half-mass radius (generated by the `ellipse` command in the previous step) overlain on the map of r band flux; (3) The elliptical isophotes overlaid on the Σ_* map; (4) The elliptical isophotes overlaid on the $\Sigma_{\rm SFR}$ map; Elliptical annuli defined by the set of elliptical isophotes shown in figures in the second, third, and fourth rows are used in the radial profile calculation; (5) Derived radial profiles of $\Sigma_*(r)$; and (6) derived radial profiles of $\Sigma_{\rm SFR}(r)$.

In later analysis, we investigate the surface density radial profiles as function of global properties (M_* and distance from the global SFMS, i.e. sSFR) by averaging the radial profiles of galaxies with similar global properties. It is useful to have the radial profiles with the same radial extent when averaging the radial profiles otherwise the averaged radial profile might be bias (especially in the

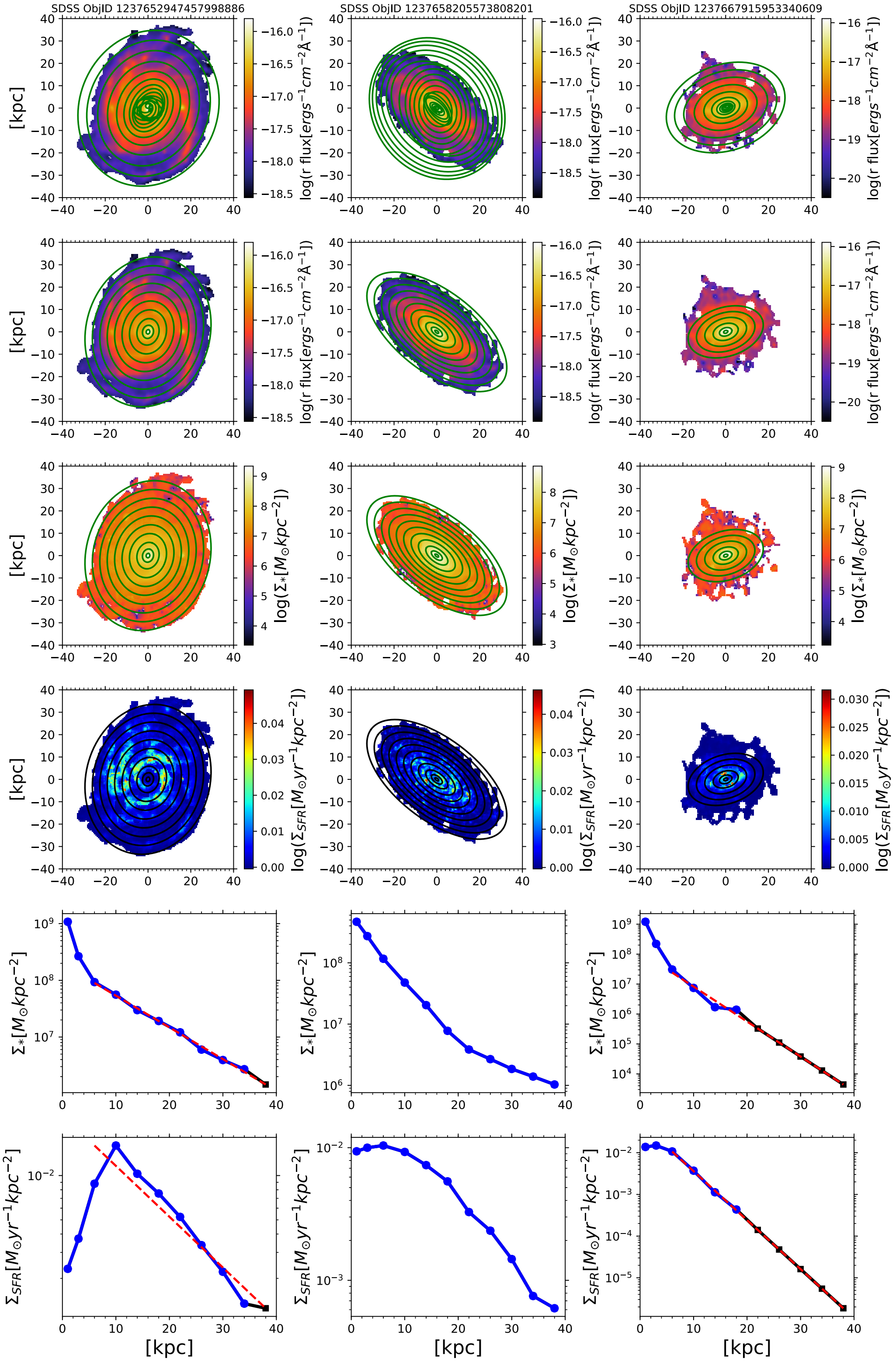

SDSS ObjID 1237652947457998886

SDSS ObjID 1237658205573808201

SDSS ObjID 1237667915953340609

Figure 4.10: Example of the results of elliptical isophote fitting and derivation of the radial profiles of $\Sigma_*(r)$ and $\Sigma_{\rm SFR}(r)$ for individual galaxy.

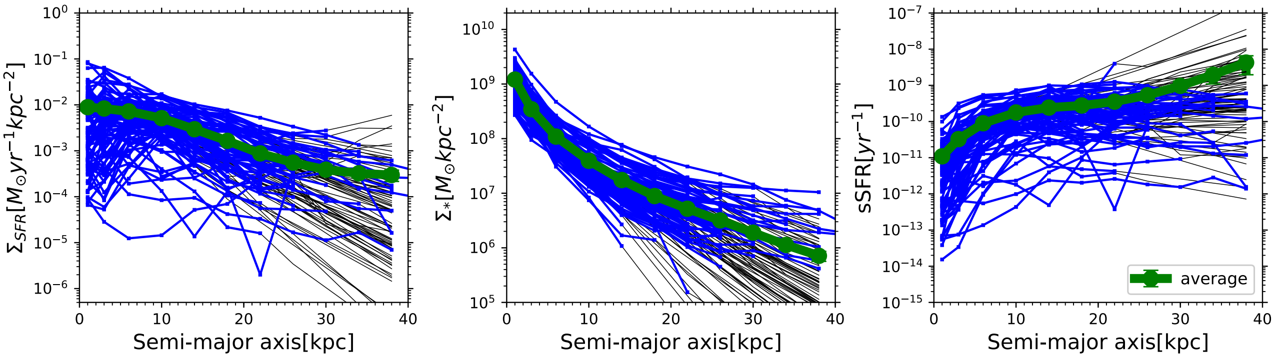

Figure 4.11: Radial profiles of $\Sigma_{*}(r)$, $\Sigma_{\rm SFR}(r)$, and sSFR(r) of sample galaxies at $z \sim 0$. Blue squares with lines represent radial profiles of all 93 galaxies in the $z \sim 0$ sample, while black line represents extrapolated part which obtained by exponential function fitting from the original radial profile. Green circles with lines represent average radial profiles. Figure in the right panel is adopted from Abdurro'uf and Akiyama (2017).

outskirt) by the radial profiles of massive bright galaxies. An exponential function fitting is done to extrapolate the radial profile if the radial profile does not reach radius of 38 kpc. Red dashed line on each radial profile represents best-fitting exponential function with the form of

$$\psi(r) = \psi_0 e^{r/h} \tag{4.2}$$

to the radial profile. ψ in the above equation stand for Σ_{*} and $\Sigma_{\rm SFR}$. ψ_0 and h represent zero-point and radial scale-length, respectively. The fitting is only done to the outskirt part of the radial profile, $r \geq 6$ kpc, to avoid effect of the central components, e.g. bar and bulge. The galaxy shown in the middle column has the radial profiles that reach radius of 38 kpc so the exponential function fitting is not applied to this galaxy. Black points in each radial profile represent the extrapolated part for the radial profile.

4.4.2 Average surface density radial profiles over all sample galaxies

Fig. 4.11 shows radial profiles of $\Sigma_{\rm SFR}(r)$ (left panel), $\Sigma_{*}(r)$ (middle panel), and sSFR(r) (right panel) of all the 93 sample galaxies (shown with blue squares with line). Black lines represent extrapolated part of the radial profiles which are obtained by fitting each radial profile with an exponential function, as described in Section 4.4.1. Green radial profile in each panel represents the average radial profile. Errorbars in the average radial profiles represent their uncertainties and they are calculated with standard error of mean.

On average, $\Sigma_{\rm SFR}(r)$ is centrally peaked, i.e. decreasing with increasing radius. However, it is shown in the left panel of Fig. 4.11 that significant fraction of the galaxies have $\Sigma_{\rm SFR}(r)$ that are centrally suppressed. As we will see later in Section 4.5.2, the centrally suppressed $\Sigma_{\rm SFR}(r)$ radial profiles are associated with barred galaxies. $\Sigma_{*}(r)$ radial profiles are centrally peaked with

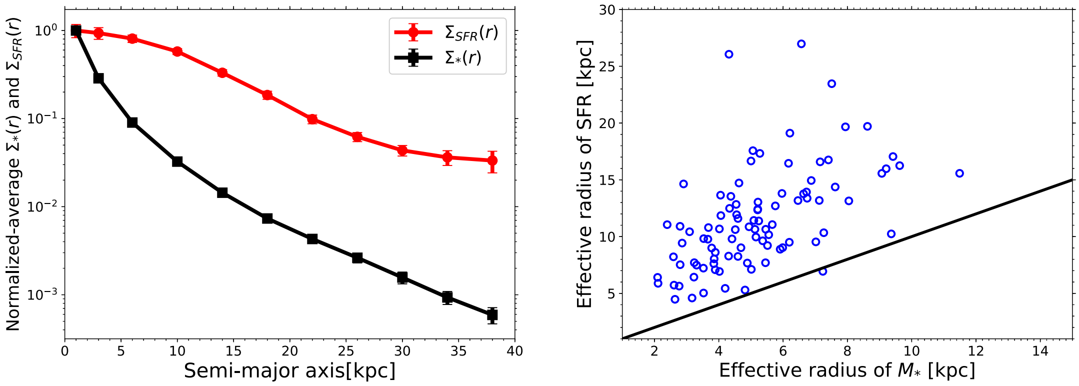

Figure 4.12: Left panel: comparison between normalized of the average radial profiles of $\Sigma_{*}(r)$ and $\Sigma_{\rm SFR}(r)$. Right panel: Comparison between effective radius of SFR and M_{*} of the 93 galaxies in the $z \sim 0$ sample. Figure in the right panel is taken from Abdurro'uf and Akiyama (2017).

'cuspy' shape toward the galactic center, which suggests the existence of central massive component. sSFR(r) radial profiles of all the sample galaxies are centrally suppressed (within $r < 6$ kpc) and roughly flat in the outskirt with slightly increasing with radius in the outermost region. Centrally suppressed sSFR(r) radial profile (i.e. increasing sSFR with radius) of local galaxies also observed by other researchers e.g. González Delgado et al. (2016); Belfiore et al. (2018) using integral field spectroscopy observations. Positive gradient of the sSFR(r) means a ratio of current to past average SFR is lower in the central region compared to that in the outskirt. This trend suggests that quenching of star formation activity is progressed in "inside-to-outside" manner. This "inside-out" quenching trend is one of the focus of this thesis. Quantitative analysis of the inside-out quenching trend is discussed in Chapter 6.

The positive gradient of the sSFR(r) also suggests that spatially resolved distribution of the ongoing star formation activities in the galaxies is more extended than the spatially resolved distribution of the stellar masses. Left panel of Fig. 4.12 shows a comparison between the averages $\Sigma_{\rm SFR}(r)$ and $\Sigma_{*}(r)$ radial profiles which have been normalized by their central ($r = 1$ kpc) values. It is clearly shown in this figure that the normalized-average $\Sigma_{\rm SFR}(r)$ is much more extended compared to the normalized-average $\Sigma_{*}(r)$. Right panel of the Fig. 4.12 shows a comparison between effective radius of SFR and M_{*}, which are radius (i.e. semi-major axis) that encloses half of the total SFR and M_{*}, respectively. It is shown in this figure that the effective radius of SFR is systematically larger than the effective radius of M_{*} for almost all of the sample galaxies. This trend suggests that ongoing star formation activities are distributed in more extended area compared to the assembled stellar masses. It could also be thought that the galaxies are currently building their disk and growing. This observed trend agrees with the inside-out growth scenario (e.g. Kauffmann 1996; Cole et al. 2000; Firmani and Avila-Reese 2000; van den Bosch 2002; Stringer and Benson 2007).

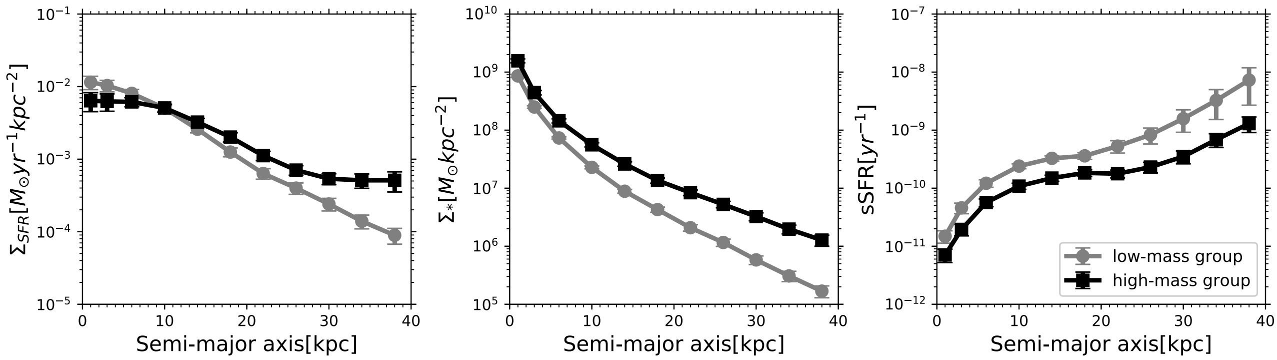

Figure 4.13: Radial profiles of $\Sigma_{\rm SFR}(r)$ (left panel), $\Sigma_{*}(r)$ (middle panel), and sSFR(r) (right panel) of low mass (gray) and high mass (black) groups in the $z \sim 0$ sample.

4.4.3 Surface density radial profiles as a function of the global stellar mass

In order to investigate the effect of global M_{*} on the spatially resolved distributions of $\Sigma_{\rm SFR}$, Σ_{*}, and sSFR, we divide the $z \sim 0$ sample into two groups based on the integrated M_{*} and then compare the average $\Sigma_{\rm SFR}(r)$, $\Sigma_{*}(r)$, and sSFR(r) radial profiles of the two groups. Median value of the integrated M_{*} of the galaxies in the $z \sim 0$ sample ($3.5 \times 10^{10} M_{\odot}$) is used as the threshold. Number of galaxies in each group (i.e. high-mass and low-mass groups) is 46. We then calculate average radial profiles of $\Sigma_{*}(r)$, $\Sigma_{\rm SFR}(r)$, and sSFR(r) of the low-mass and high-mass groups. Fig. 4.13 shows comparison of the $\Sigma_{\rm SFR}(r)$ (left panel), $\Sigma_{*}(r)$ (middle panel), and sSFR(r) (right panel) between the low-mass (shown in gray color) and high-mass groups (shown in black color).

More massive galaxies tend to have higher SFR in the outskirt and lower SFR in the central region than less massive galaxies. More massive galaxies tend to have higher Σ_{*} in the entire region compared to less massive galaxies with larger difference shown in the outskirt. It suggests that central region of both galaxy groups might have reached a saturation (i.e. critical Σ_{*}) point while the building of the disk (by star formation) is ongoing, especially in the low-mass group. Interesting feature is shown in the sSFR(r) where average sSFR(r) of more massive galaxies is lower in all radii compared to the sSFR(r) of less massive galaxies. Recalling that sSFR represents the ratio of the current to the past averaged SFR, this sSFR(r) trend suggests that more massive galaxies tend to quench their star formations over the entire region earlier compared to less massive galaxies. This picture agrees with the global 'downsizing' scenario and furthermore suggests that the 'downsizing' signal might be preserved in the kpc-scale within a galaxy. The preservation of 'downsizing' in kpc-scale also observed by Pérez et al. (2013) and Ibarra-Medel et al. (2016) using integral field spectroscopy observations. Using the integral field spectroscopy data they investigated the radially-resolved history of the stellar mass growth in galaxies with various M_{*} ($\log(M_{*}/M_{\odot}) \sim 9.0 - 11.0$). They found that more massive galaxies tend to built their stellar mass faster over entire radius compared to less massive galaxies.

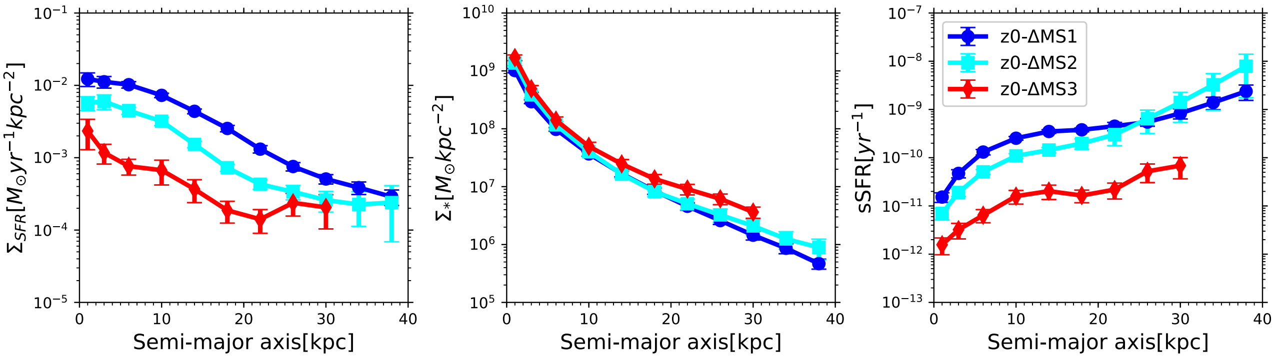

Figure 4.14: Radial profiles of $\Sigma_{\rm SFR}(r)$, $\Sigma_{*}(r)$, and sSFR(r) as a function of distance from the global SFMS.

4.4.4 Surface density radial profiles as a function of distance from the global SFMS

In order to investigate the dependence of the spatially resolved distributions of $\Sigma_{\rm SFR}$, Σ_{*}, and sSFR on the global sSFR (i.e. distance from the global SFMS), we calculate the average $\Sigma_{\rm SFR}(r)$, $\Sigma_{*}(r)$, and sSFR(r) radial profiles of the galaxies located above the global SFMS (z0-ΔMS1), on the global SFMS (z0-ΔMS2), and below the global SFMS (z0-ΔMS3). See Section 4.2 for detail of the z0-ΔMS1, z0-ΔMS2, and z0-ΔMS3 classification. Fig. 4.14 shows the average $\Sigma_{\rm SFR}(r)$ (left panel), $\Sigma_{*}(r)$ (middle panel), and sSFR(r) (right panel) of the z0-ΔMS1 (shown in blue), z0-ΔMS2 (shown in cyan), and z0-ΔMS3 (shown in red).

On average, normalization with respect to the global SFMS is preserved in kpc-scale as shown by the average radial profiles of $\Sigma_{\rm SFR}(r)$ and sSFR(r). The z0-ΔMS1 galaxies have higher $\Sigma_{\rm SFR}$ and sSFR in entire radii compared the z0-ΔMS2 galaxies and the z0-ΔMS2 galaxies have higher $\Sigma_{\rm SFR}$ and sSFR in entire radii compared to those of the z0-ΔMS3 galaxies. The Σ_{*} of the three groups are roughly similar to each other in all radii. Belfiore et al. (2018) using data from integral field spectroscopy observation also found that local massive ($\log(M_{*}/M_{\odot}) \geq 10.5$) green-valley galaxies have systematically lower sSFR in the entire region compared to the local massive (with the same stellar mass range) star-forming galaxies.

4.5 Spatially resolved SFR and M_{*} in barred- and non-barred galaxies

4.5.1 Global properties of barred- and non-barred galaxies

More than $\sim 30\%$ of massive ($\log(M_{*}/M_{\odot}) \gtrsim 9.5$) spiral galaxies in the local universe have central non-axisymmetric feature with a bar-like shape (Laurikainen et al. 2004; Gavazzi et al. 2015; Consolandi et al. 2016). Those galaxies are called barred galaxies. Bar is thought to play a significant

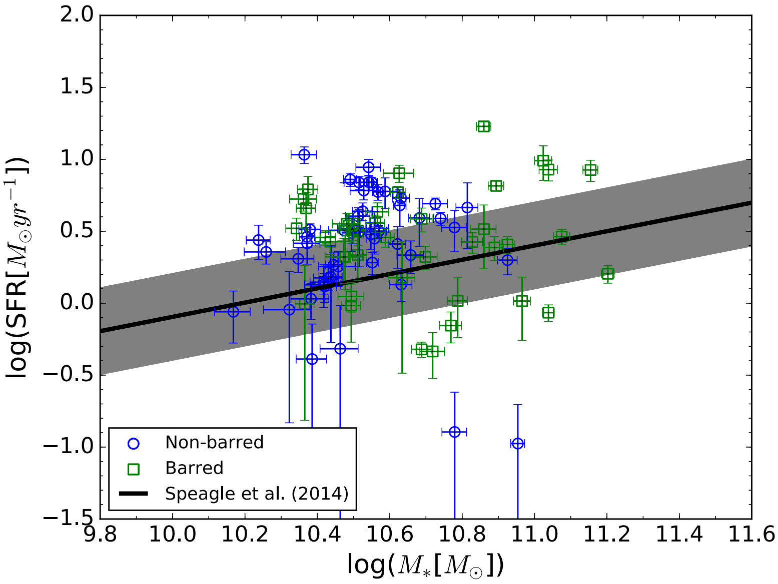

Figure 4.15: Integrated SFR versus M_* of barred- and non-barred galaxies in $z \sim 0$ sample. Barred galaxies are shown with green squares, while non-barred galaxies are shown with blue circles. Black line represents global SFMS relation by Speagle et al. (2014) which calculated at the median redshift of the sample galaxies ($z = 0.0165$), while gray shaded area represents the ± 0.3 dex scatter around the global SFMS. This figure is taken from Abdurro'uf and Akiyama (2017).

role in the secular evolution of the disk galaxy. Bar could drive a strong gas inflow toward the galactic center (Athanassoula 1992) and trigger central starbursts (Hunt and Malkan 1999; Laurikainen et al. 2004; Jogee et al. 2005). In longer time-scale, gas transport toward the central region and consumption of gas by the central starburst could affect star formation activity in the central region within the bar extent. In order to investigate the effect of bar on the internal star formation activity in the galaxy, we study the difference on the spatially resolved SFR and M_* between barred and non-barred galaxies in the $z \sim 0$ sample. The $z \sim 0$ sample contains 42 barred- and 51 non-barred galaxies (see Section 2.1 for the method used for classifying barred and non-barred galaxies). Fig. 4.15 shows integrated SFR versus M_* of the barred- and non-barred galaxies in the $z \sim 0$ sample. Barred- and non-barred galaxies are shown with green squares and blue circles, respectively. Black solid line and gray shaded area represent the global SFMS relation by Speagle et al. (2014) that is calculated at the median redshift of the $z \sim 0$ sample ($z = 0.0165$) and the ± 0.3 dex scatter around the global SFMS relation, respectively. It is shown by the figure that the distributions of the barred- and non-barred galaxies with respect to the global SFMS are similar, they spread similarly around the global SFMS. A clear systematic difference is found in the integrated M_*, where barred galaxies tend to have higher integrated M_* than those of non-barred galaxies.

Fig. 4.16 shows histograms for the distributions of the integrated SFR (left panel), M_* (middle panel), and sSFR (right panel) of barred (shown with green dashed line) and non-barred galaxies (shown with blue solid line). In order to quantitatively check the differences in the distributions of

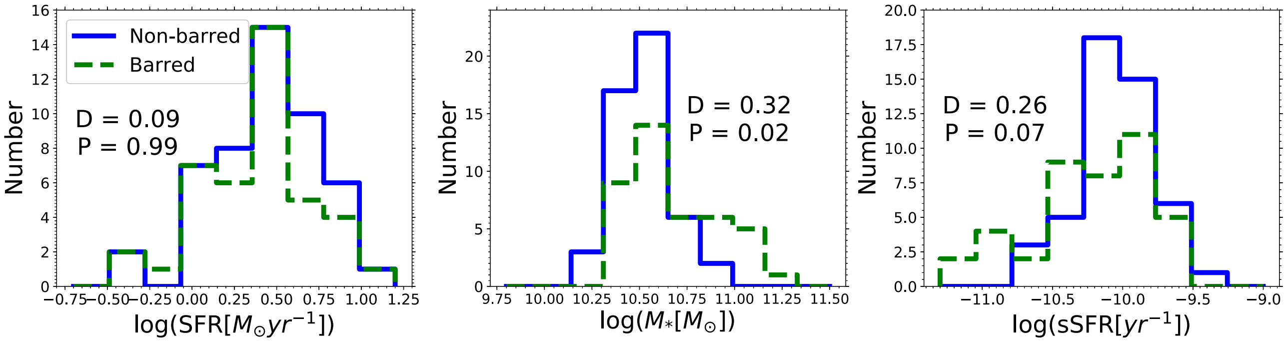

Figure 4.16: Histograms of the distributions of the integrated SFR (left panel), M_* (middle panel), and sSFR (right panel) of barred- (shown with green dashed line) and non-barred galaxies (blue solid line) in the $z \sim 0$ sample. D and P values of the Kolmogorov–Smirnov (KS) test are shown along with the histograms.

those integrated properties between those of barred- and non-barred galaxies, we do the Kolmogorov-Smirnov (KS) test. The figure shows that barred- and non-barred galaxies have similar integrated SFR with P value nearly one. The M_* distributions of barred- and non-barred galaxies are different within a significant level of 0.05 emphasizing that barred galaxies indeed have systematically higher M_* compared to non-barred galaxies. The sSFR distributions of barred- and non-barred galaxies are mildly different (with P=0.07) with barred galaxies have a tendency of having slightly lower sSFR. Previous researchers (e.g. Cheung et al. 2013; Gavazzi et al. 2015) observed that barred galaxies have systematically lower sSFR compared to non-barred galaxies but here we see less significant sSFR suppression in the barred galaxies. Next, we will study the spatially resolved distributions of SFR, M_*, and sSFR in the barred- and non-barred galaxies to investigate their differences in kpc-scale and get insights on the bar-driven secular evolution of the galaxies.

4.5.2 Spatially resolved SFR and M_* in barred- and non-barred galaxies

First, we compare the $\Sigma_{\rm SFR}(r)$, $\Sigma_*(r)$, and sSFR(r) radial profiles of barred- and non-barred galaxies to get a first glance on the structural difference between them. Fig. 4.17 shows $\Sigma_{\rm SFR}(r)$ (left panel), $\Sigma_*(r)$ (middle panel), and sSFR(r) (right panel) radial profiles of barred- (shown with light-green color) and non-barred (shown with light-blue color). Gray lines are extrapolated part of their radial profiles which are derived through fitting the radial profiles with an exponential function as described in Section 4.4.1. Average radial profiles of barred- and non-barred galaxies are shown by large circles with thick lines in green and blue colors, respectively. It is shown by the figure that $\Sigma_{\rm SFR}(r)$ radial profiles of most of the barred galaxies have suppression of $\Sigma_{\rm SFR}$ in their central regions which make their average $\Sigma_{\rm SFR}(r)$ shows lower $\Sigma_{\rm SFR}$ in the central region compared to the average $\Sigma_{\rm SFR}(r)$ radial profile of non-barred galaxies. Higher $\Sigma_{\rm SFR}$ in the outskirt of barred galaxies should be taken with caution due to the effect of the detection limit. Middle panel shows that there is no systematic difference between the $\Sigma_*(r)$ radial profiles of the barred- and non-barred galaxies. On

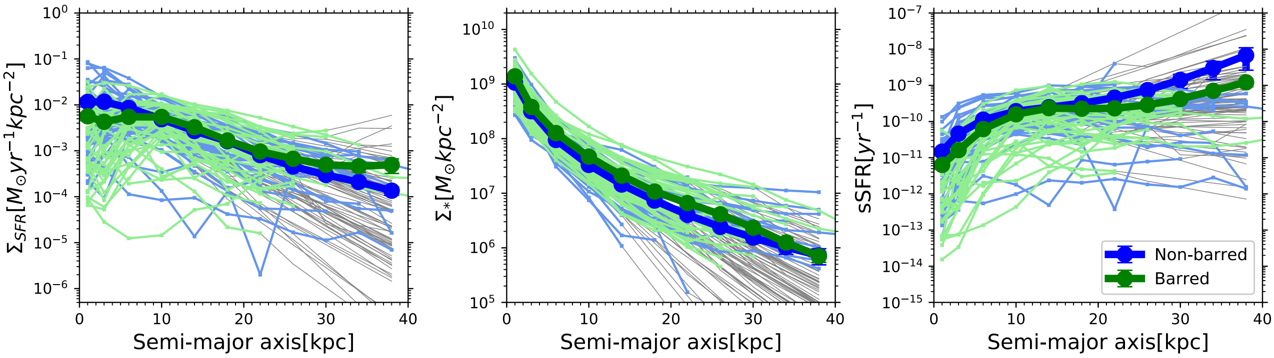

Figure 4.17: Radial profiles of $\Sigma_{SFR}(r)$ (left panel), $\Sigma_*(r)$ (middle panel), and sSFR(r) (right panel) of barred (shown with light-green color) and non-barred galaxies (shown with light-blue color) in the $z \sim 0$ sample. Average radial profiles of barred- and non-barred galaxies are shown by large circles with thick line in green and blue colors, respectively.

average, sSFR(r) radial profiles of barred galaxies show only slightly lower sSFR in the central region compared to those of the sSFR(r) radial profiles of non-barred galaxies.

In order to get insights on the $\Sigma_{\rm SFR}$ suppression in the central region, we check the spatially resolved distribution of $\Sigma_{\rm SFR}$ of the barred galaxies. We found that region within the bar extent commonly corresponds to a void in the $\Sigma_{\rm SFR}$ and sSFR maps, which means that the region has low star formation activity. We also check the spatially resolved distribution of FUV flux in the barred galaxies. The FUV map of the barred galaxies typically have central void within the bar extent (i.e. systematically lower flux compared to the outskirt region). Fig. 4.18 shows example of three barred galaxies in the $z \sim 0$ sample. Each column represents different galaxy. In each column, from top to bottom panel show *gri* composite image; spatially resolved distribution of FUV flux; spatially resolved distribution of the $\Sigma_{\rm SFR}$; spatially resolved distribution of the sSFR; $\Sigma_{\rm SFR}(r)$ radial profile; and sSFR(r) radial profile. It is shown from this figure that the $\Sigma_{\rm SFR}$ and sSFR maps of the three galaxies have a void in the central region that corresponds to the bar size. It agrees with the FUV flux maps which also show void in the central region associated with the bar size. The $\Sigma_{\rm SFR}(r)$ radial profiles show declining trend within a radius associated with the bar size, while increasing trend toward shorter radius is shown in the region outside of the bar extent. The sSFR(r) radial profiles show declining trend in the central region and roughly flat trend in the outskirt.

Based on the scenario of a bar being an efficient gas transporter toward the galactic center, accumulation of stellar mass in the central region is expected to be high due to a central starburst that happen following the rapid gas transport. Central (within the bar extent) SFR is expected to be low after a long time if gas accretion into the galaxy is suppressed (due to e.g. decreasing cosmic gas accretion rate) while gas consumption rate in the galactic center is high. While the suppression of $\Sigma_{\rm SFR}$ in the central region of barred galaxies is evidenced by the $\Sigma_{\rm SFR}(r)$ radial profiles (in both of the average radial profile over all the sample galaxies and in individual galaxies), systematically different Σ_* in the central region between barred- and non-barred galaxies is not evidenced from the

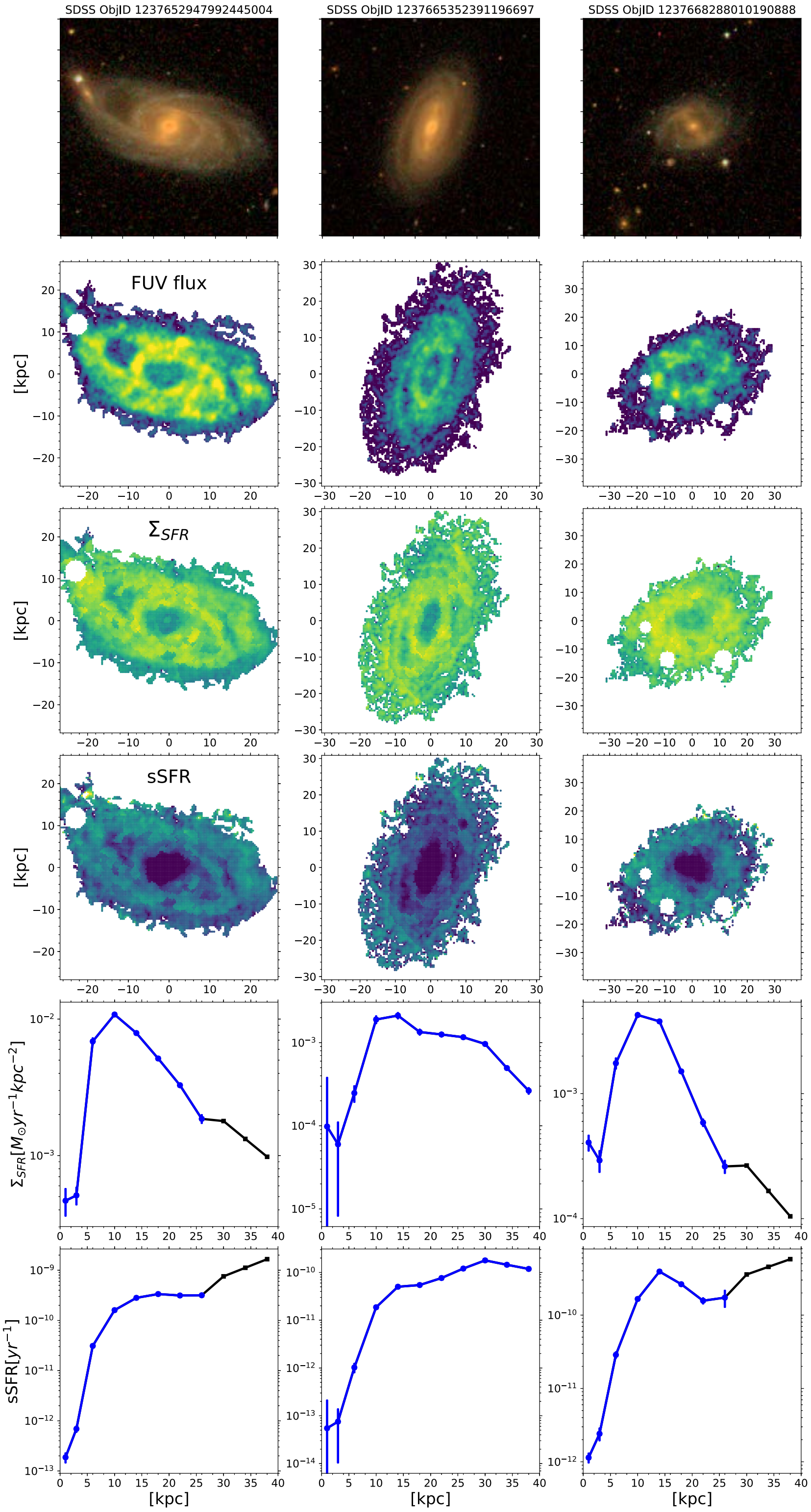

Figure 4.18: Example of the spatially resolved distributions of FUV flux, Σ_{SFR}, and sSFR of three barred galaxies in the $z \sim 0$ sample. Each column represent different galaxy. In each column, from top to bottom panel: *gri* composite image; spatially resolved distribution of FUV flux; spatially resolved distribution of $\Sigma_{\rm SFR}$; spatially resolved distribution of sSFR; radial profile of $\Sigma_{\rm SFR}(r)$; and radial profile of $\rm sSFR(r)$.

average $\Sigma_*(r)$ radial profiles. It should be noted that due to the relatively wide elliptical annulus (2 kpc width for the annuli within 6 kpc radius and 4 kpc width for the annuli outside 6 kpc radius) that is assumed for deriving the radial profiles, the variation of Σ_* in small scale within around the galactic center is not resolved, i.e. smoothed out with the Σ_* contribution from the circumnuclear region.

Next, we will quantitatively examine the differences of SFR, M_*, and sSFR in various radial regions between the barred- and non-barred galaxies. Now we use radial distance that is normalized with the half-mass radius in order to probe further into the structural feature of the galaxies.

First, we examine whether there is a difference in term of a radial gradient of the sSFR between the barred- and non-barred galaxies. Specifically, we want to examine whether the central suppression of the sSFR in the barred galaxies is stronger compared to that in the non-barred galaxies. We do it by calculating the ratio between total sSFR within the half-mass radius to the total sSFR outside of the half-mass radius ($\mathrm{sSFR}_{\mathrm{inside}}/\mathrm{sSFR}_{\mathrm{outside}}$) for each galaxy, then compare that quantity in the barred- and non-barred galaxies. Fig. 4.19 shows the $\mathrm{sSFR}_{\mathrm{inside}}/\mathrm{sSFR}_{\mathrm{outside}}$ versus integrated SFR of the barred- and non-barred galaxies. Barred- and non-barred galaxies are shown with green squares and blue circles, respectively. Histograms in the right panel shows the distributions of the $\mathrm{sSFR}_{\mathrm{inside}}/\mathrm{sSFR}_{\mathrm{outside}}$ of barred- (green dashed line) and non-barred galaxies (blue solid line). While the integrated SFR and sSFR of barred- and non-barred galaxies do not show a systematic difference (see Fig. 4.16), the $\mathrm{sSFR}_{\mathrm{inside}}/\mathrm{sSFR}_{\mathrm{outside}}$ of barred galaxies tend to be lower than that of non-barred galaxies. The median values of $\mathrm{sSFR}_{\mathrm{inside}}/\mathrm{sSFR}_{\mathrm{outside}}$ for barred- and non-barred galaxies are -1.08 and -0.78 dex, respectively. We do the KS test to check if the $\mathrm{sSFR}_{\mathrm{inside}}/\mathrm{sSFR}_{\mathrm{outside}}$ distributions of barred- and non-barred galaxies are indeed different. The KS test result (the D and P values which are are shown along with the histogram) suggests that the both distributions are indeed different within a significant level of 0.05, supporting the argument that the $\mathrm{sSFR}_{\mathrm{inside}}/\mathrm{sSFR}_{\mathrm{outside}}$ of barred galaxies are systematically lower than those of non-barred galaxies.

To check further into the structural difference between the barred- and non-barred galaxies, we divide the galaxy's region into three: *core* defined as a region inside $10^{-0.5}r_{e,M_*}$, *middle* defined as a region with $10^{-0.5}r_{e,M_*} < r \leqslant r_{e,M_*}$, and *outside* defined as a region with $r > r_{e,M_*}$. The r_{e,M_*} represents a half-mass radius, i.e. radius along the semi-major axis that encloses half of the integrated M_*. The same division of a galaxy into the sub regions was also used by Wuyts et al. (2013). Then total SFR, stellar mass (m_*), and sSFR in the three regions are calculated. Fig. 4.20 shows histograms for the distributions of the total SFR (left column), m_* (middle column), and sSFR (right column) in the *core* (first row), *middle* (second row), and *outside* (third row) regions. Histograms for the barred- and non-barred galaxies are shown with green dashed line and blue solid line, respectively. We do the KS test to check the possible difference in the histograms of the two groups. The figure shows that there is no difference in SFR in the three regions between the barred- and non-barred galaxies. The D and P values of the KS test suggest that the distributions of SFR in the three regions are similar. Total m_* in the *core* of barred galaxies are systematically higher than

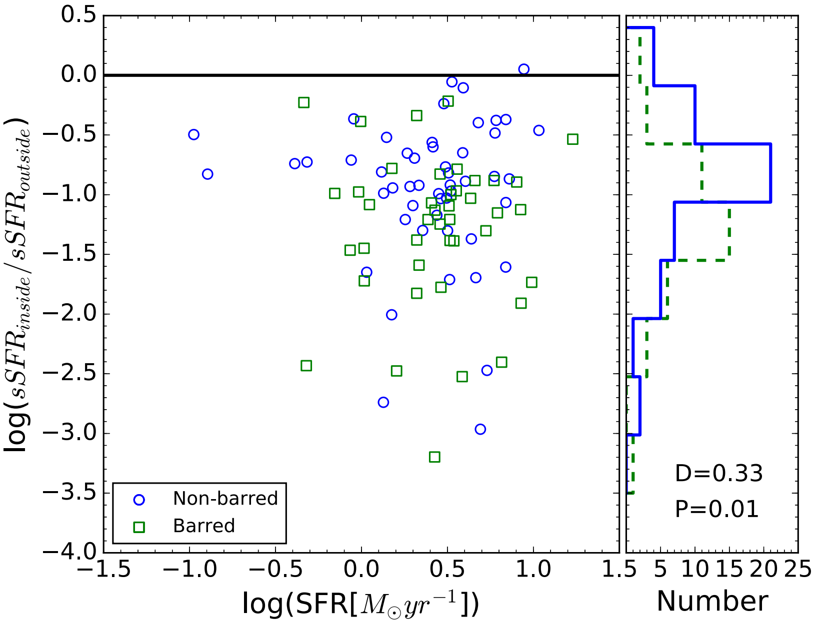

Figure 4.19: Left panel: Integrated SFR versus ratio of the sSFR inside and outside of the half-mass radius ($\mathrm{sSFR_{inside}/sSFR_{outside}}$) in barred- and non-barred galaxies. Barred- and non-barred galaxies are represented by green squares and blue circles, respectively. Right panel: histograms for the $\mathrm{sSFR_{inside}/sSFR_{outside}}$ distributions of the barred- (green dashed line) and non-barred galaxies (blue solid line). The D and P values of the Kolmogorov–Smirnov (KS) test are shown along with the histogram.

those of non-barred galaxies. The D and P values from the KS test suggests that the distributions of m_* in the *core* of barred- and non-barred galaxies are systematically different. In the *middle* and *outside* region, the m_* of barred- and non-barred galaxies are slightly different with barred galaxies tend to have higher m_* than non-barred galaxies. In the *core* and *middle* regions, the sSFR of barred- and non-barred galaxies are slightly different with barred galaxies show tendency of having lower sSFR than non-barred galaxies. The sSFR in the *outside* (i.e. outskirt) of barred- and non-barred galaxies are similar.

It has been suggested by other researchers whose analyzed global properties (SFR and sSFR) of local barred- and non-barred galaxies that a bar structure could promote the quenching of star formation in galaxies (e.g. Cheung et al. 2013; Gavazzi et al. 2015). However, we found here that bar structure tend to give effect only in the central region of galaxies. The effect given by the bar structure is a suppression of sSFR and higher stellar mass in the most central part (i.e. *core*) of the galaxies. Total SFR and sSFR in the outskirt of barred- and non-barred galaxies are similar leading to the similar integrated SFR and sSFR. Thus, we conclude that with only secular process driven by bar, it is not enough to quench an entire galaxy.

Our observed structural trend of barred- and non-barred galaxies is in a good agreement with a result of cosmological zoom-in hydrodynamical simulation of barred galaxy evolution run by Spinoso

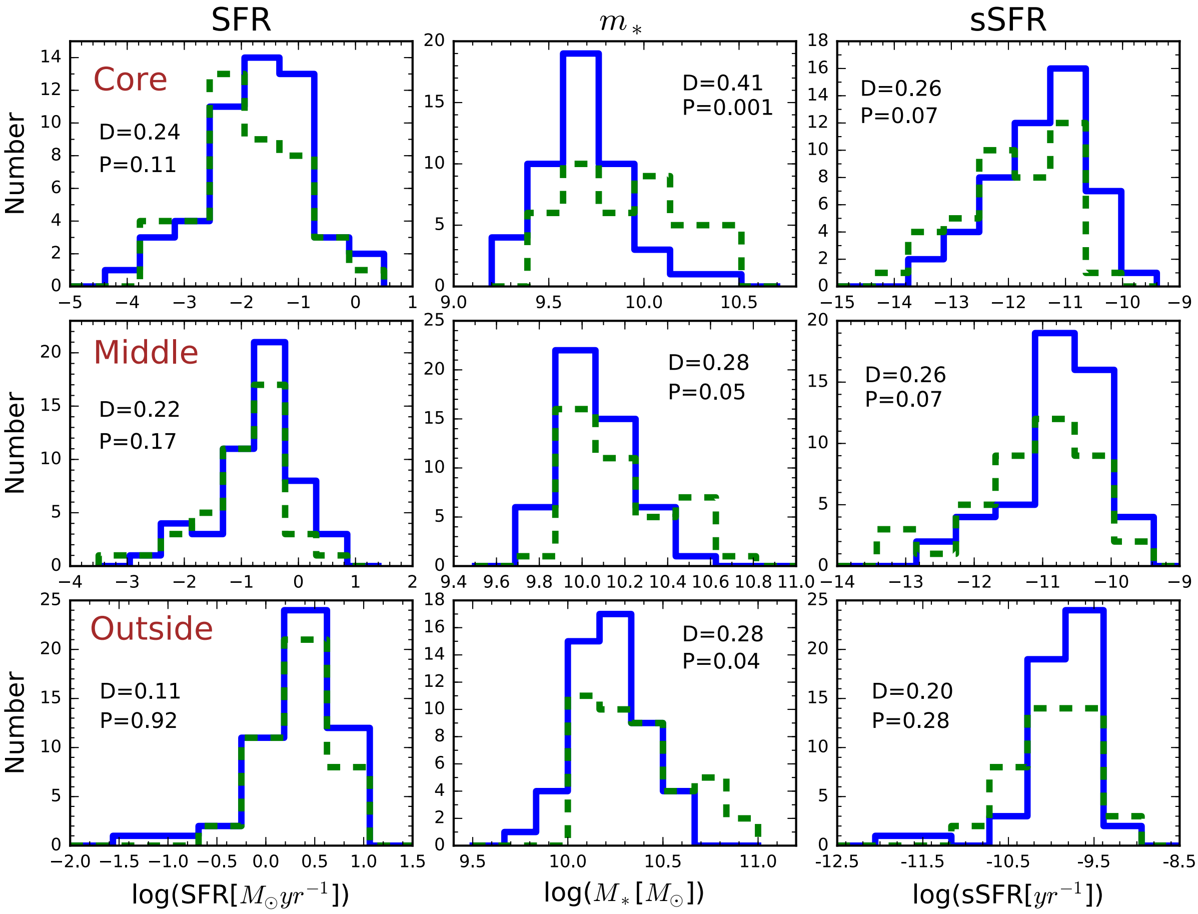

Figure 4.20: Histograms for the distributions of total SFR (left column), M_* (middle column), and sSFR (right column) in "core" (first row), "middle" (second row), and "outside" (i.e. outskirt; third row) of barred- (shown with green dashed line) and non-barred galaxies (shown with blue solid line). D and P values from the KS test are shown along with the histograms. "Core", "middle", and "outside" are defined as region inside $10^{-0.5}r_{e,M_*}$, $10^{-0.5}r_{e,M_*} < r \leqslant r_{e,M_*}$, and $r > r_{e,M_*}$, respectively.

et al. (2017). The simulation by Spinoso et al. (2017) suggests that during the bar formation and its early growth, the bar exerts a strong torque on the gas and drives rapid gas inflows toward the galactic center which triggers nuclear starburst. The nuclear starburst rapidly consumes gas in the central region such that the gas in the central region (within the bar extent) could run out once the bar reaches its maximum length and strength. Thus, star formation rate within the bar extent is low due to the low gas density in the region. The authors also argue that observations of barred galaxies will likely observe the barred galaxies when they are in the stage of centrally-quenched which is when the bar structure is prominent because detecting barred galaxies in the stage of early bar formation (that expected to happen at high redshift), where the bar structure is not prominent, is difficult with current instrument sensitivity, while it is easy to recognize the barred galaxies when the bar structure is matured. While evolution of star formation activity in the central region of a barred galaxy is discussed in this simulation work, the evolution of star formation activity in the outskirt of the barred galaxy is not discussed.

Chapter 5

Spatially resolved distributions of the SFR and M_* in massive disk galaxies at $z \sim 1$

5.1 Spatially resolved SFMS in massive disk galaxies at $z \sim 1$

5.1.1 Spatially resolved SFMS with all the sample galaxies

In order to investigate the relation between $\Sigma_{\rm SFR}$ and Σ_* (i.e. spatially resolved SFMS) at ~ 1 kpc-scale in the massive disk galaxies at $z \sim 1$, we plot the $\Sigma_{\rm SFR}$ versus Σ_* of all 597651 pixels of the 152 galaxies in the $0.8 < z < 1.8$ sample. For simplicity, we call the $0.8 < z < 1.8$ sample as $z \sim 1$ sample throughout this chapter. Fig. 5.1 shows the $\Sigma_{\rm SFR}$ versus Σ_* of all the pixels. Contours show regions in the plot with similar number of pixels, which is counted based on the bin with 0.1×0.1 dex^2 area. The contour is color-coded by the number of pixels. Relatively tight spatially resolved SFMS relation is evidenced by the contours with high number. This figure shows that the spatially resolved SFMS is hold in the massive disk galaxies at $z \sim 1$. Black circles with errorbars represent modes of the $\Sigma_{\rm SFR}$ distributions associated with each Σ_* bin with 0.3 dex width. The errorbars are obtained by calculating the standard deviation around the mode value and it is calculated separately above and below the mode value.

The mode profile with which the spatially resolved SFMS is defined shows a linear trend at low Σ_* but flattened at high Σ_* end. Slight deviation from the linear trend of two mode values at low Σ_* end is caused by the detection limit which sets the limiting values for the Σ_* and $\Sigma_{\rm SFR}$. The limiting values for the Σ_* and $\Sigma_{\rm SFR}$ are shown by the vertical and horizontal black lines in the bottom and left axes, respectively. Those limiting values are the median values of the Σ_* and $\Sigma_{\rm SFR}$ of pixels located in the outermost 8 kpc elliptical annulus of all the sample galaxies. Those pixels commonly have low S/N, ~ 0.5pixel^{-1}. The linear part of the mode profile (consisting of five mode

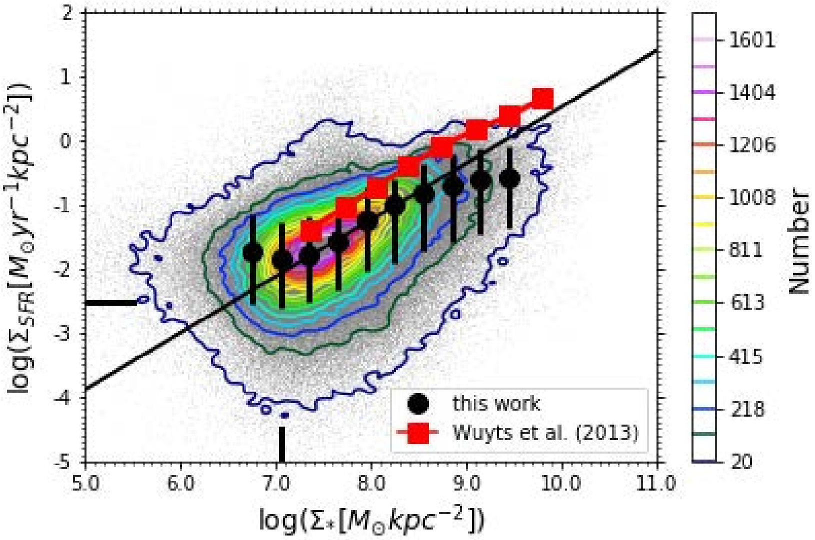

Figure 5.1: Spatially resolved SFMS relation with all 597651 pixels of the 152 galaxies in the $z \sim 1$ sample. Contours show regions in the plot with similar number of pixels, which is counted based on the bin with $0.1 \times 0.1\mathrm{dex}^2$ area. The contour is color-coded by the number of pixel. Black circles with errorbars represent modes of the $\Sigma_{\rm SFR}$ distributions in each Σ_* bin with 0.3 dex width. The errorbars are obtained by calculating standard deviation around the mode value and it is calculated separately above and below the mode value. Black horizontal (vertical) lines in the left (bottom) axes represent limiting values for the $\Sigma_{\rm SFR}(\Sigma_*)$ which are median values of the $\Sigma_{\rm SFR}(\Sigma_*)$ of pixels located in outskirt (outermost 8 kpc elliptical annulus). Red squares with solid line represent spatially resolved SFMS reported by Wuyts et al. (2013). This figure is taken from Abdurro'uf and Akiyama (2018).

values with $\log(\Sigma_*[M_*\mathrm{kpc}^{-2}]) \lesssim 8.5$, excluding the two mode values with lowest Σ_* because they are below the limiting value of Σ_*) is best-fitted by a linear function (eq. 4.1) with a slope (α) of 0.88 and zero-point (β) of -8.31, which is shown by the black line. The nearly unity slope of the spatially resolved SFMS at low Σ_* region (which corresponds to the disk region) also observed for the spatially resolved SFMS in the galaxies at $z \sim 0$ (see Sections 4.1 and 4.2).

The red squares with line in the Fig. 5.1 shows the spatially resolved SFMS relation in massive ($\log(M_*/M_\odot) > 10$) star-forming galaxies at $0.7 < z < 1.5$ reported by Wuyts et al. (2013). The relation was defined with the median of $\Sigma_{\rm SFR}$ distribution associated with each Σ_* bin. As shown by the figure, the 'flattening' tendency at high Σ_* end reported by the authors is not as pronounced as the 'flattening' tendency obtained in this work. The systematically lower normalization of the spatially resolved SFMS obtained by this work compared to that reported by Wuyts et al. (2013) is in part caused by the different sample selection. Wuyts et al. (2013) only considered massive star-forming galaxies, while here we consider not only massive star-forming galaxies but also green-valley and quiescent galaxies which have lower $\Sigma_{\rm SFR}$ for a fixed Σ_* at high Σ_* region as will be discussed in next section.

5.1.2 Spatially resolved SFMS as a function of distance from the global SFMS

As observed for the sample galaxies at $z \sim 0$ (see Section 4.3.2), the spatially resolved SFMS shown in Fig. 5.1 is also expected to be a combination of the spatially resolved SFMS relations of the individual galaxies. Therefore it is important to investigate the spatially resolved SFMS relation for group of galaxies with similar properties or being in the similar phase in their evolution. One meaningful way is to group the sample galaxies based on their distances from the global SFMS in the SFR-M_* plane since it tells us about the evolutionary phases of the galaxies. Here, we divide the $z \sim 1$ sample galaxies into three groups based on their distances from the global SFMS. As we used the global SFMS relation by Speagle et al. (2014) for dividing the $z \sim 0$ sample galaxies, here we also use the same relation for dividing the $z \sim 1$ sample galaxies.

Fig. 5.2 shows the integrated SFR versus M_* of the 152 galaxies in the $z \sim 1$ sample. The integrated SFR and M_* of a galaxy are derived by summing up the SFR and m_* of the pixels that belong to the galaxy. The global SFMS relation at the median redshift of the $z \sim 1$ sample ($z = 1.217$) and the 0.3 dex scatter around the relation is shown by the black solid line and gray shaded area, respectively. The black dashed line represents -0.8 dex from the global SFMS relation. Distribution of the sample galaxies on the SFR-M_* plane in this figure is different compared to that shown in Fig. 2.2, which the SFR and M_* are taken from the 3D-HST catalog. This difference is mainly caused by a discrepancy in integrated M_* where our estimated M_* is systematically higher than that reported in the 3D-HST catalog. This issue is discussed in Appendix A.4. Galaxies that are located within the scatter (± 0.3 dex) of the global SFMS (shown with blue circles), between -0.3 dex and -0.8 dex from the global SFMS (shown with green squares), and below -0.8 dex from the global SFMS (shown with red diamonds) are grouped as z1-ΔMS1, z1-ΔMS2, and z1-ΔMS3, respectively. Number of galaxies in the z1-ΔMS1, z1-ΔMS2, and z1-ΔMS3 groups are 47, 72, and 33, respectively. Median values of the $\log(\mathrm{sSFR}[yr^{-1}])$ of the z1-ΔMS1, z1-ΔMS2, and z1-ΔMS3 groups are -9.28, -9.70, and -10.07, respectively. The above sSFR grouping is chosen such that most of the z1-ΔMS1 and z1-ΔMS3 are star-forming and quiescent galaxies, respectively. The upper limit in the sSFR for defining the z1-ΔMS3 is chosen such that most of the galaxies located below it are quiescent galaxies, by verifying it with the UVJ diagram. In Appendix B, we show positions of the sample galaxies on the UVJ diagram and the verification that most of the galaxies in the z1-ΔMS1 and z1-ΔMS3 groups are star-forming and quiescent galaxies, respectively.

Pixels belong to the galaxies in the z1-ΔMS1 (consists of 160210 pixels), z1-ΔMS2 (consists of 286721 pixels), and z1-ΔMS3 (consists of 150720 pixels) groups are plotted on the Σ_{SFR}-Σ_* plane to investigate the spatially resolved SFMS relation of those three groups. Fig. 5.3 shows that the spatially resolved SFMS hold by the sub-galactic regions (i.e. pixels) in the galaxies that belong to the z1-ΔMS1 (top left panel), z1-ΔMS2 (top right panel), and z1-ΔMS3 (bottom left panel). Contours in each plot show regions in the plot with similar number of pixels that is counted based on a bin with 0.1×0.1 dex^2 area. The figure shows that relatively tight spatially resolved SFMS

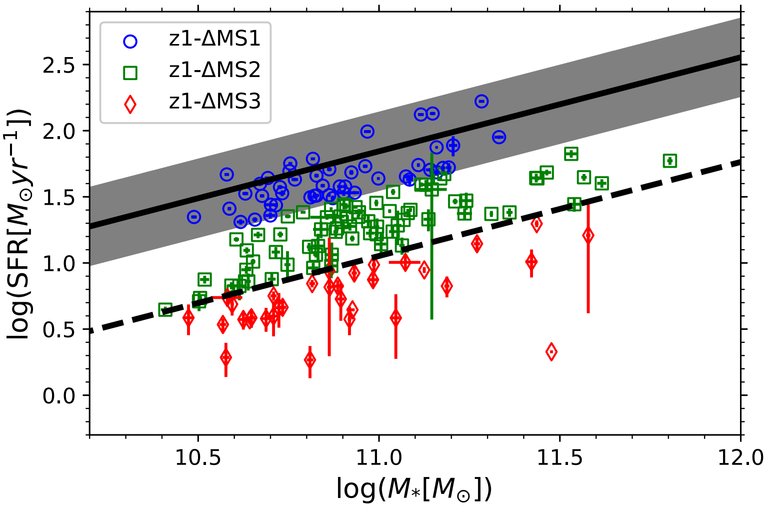

Figure 5.2: Integrated SFR versus M_* of the 152 galaxies in the $z \sim 1$ sample and the sample division based on the distance from the global SFMS relation. The black line and gray shaded area represent the global SFMS by Speagle et al. (2014) calculated at the median redshift of the $z \sim 1$ sample ($z = 1.217$) and the 0.3 dex scatter around the global SFMS relation, respectively. The black dashed line represents -0.8 dex from the global SFMS. Blue circles, green squares, and red diamonds are galaxies that belong to the z1-ΔMS1, z1-ΔMS2, and z1-ΔMS3 sub-samples, respectively. This figure is taken from Abdurro'uf and Akiyama (2018).

relations are hold in the three groups. The circles with errorbars overlaid on the contours are mode values of the $\Sigma_{\rm SFR}$ distributions associated with each Σ_* bin with 0.3 dex width. An interesting feature shown by this figure is that the mode profile for the spatially resolved SFMS of the z1-ΔMS1 is linear over the entire Σ_* range, which is different compared to the spatially resolved SFMS relations of the other groups in the $z \sim 1$ sample (z1-ΔMS2 and z1-ΔMS3) and also those of the $z \sim 0$ sample (z0-ΔMS1, z0-ΔMS2, and z0-ΔMS3). The black line in the top left panel represents the best-fitting linear function to the mode profile of the spatially resolved SFMS of the z1-ΔMS1 (with eight mode values, excluding the one with the lowest Σ_*, which is affected by the Σ_* limit), which has slope of 1.01 and zero-point of -9.24. To get a perspective on the location of the spatially resolved SFMS of each group on the spatially resolved SFMS plot with all pixels of the $z \sim 1$ sample galaxies (Fig. 5.1), we also plot the black dashed line which is the same as the black solid line in the Fig. 5.1. The linear spatially resolved SFMS relation across the entire Σ_* range with the slope of unity implies the similar star formation efficiency across the entire regions in the star-forming galaxies at $z \sim 1$ (z1-ΔMS1).

As the regions with high Σ_* end are mostly residing in the central regions of the galaxies, we also see an onset of quenching happen in the central regions of the z1-ΔMS2 galaxies as their spatially resolved SFMS relation shows a slight flattening tendency at high Σ_* end. The 'flattening' at high Σ_* is more pronounced in the spatially resolved SFMS of the z1-ΔMS3 galaxies. Comparison among the spatially resolved SFMS relations of the three groups (which are represented with their mode

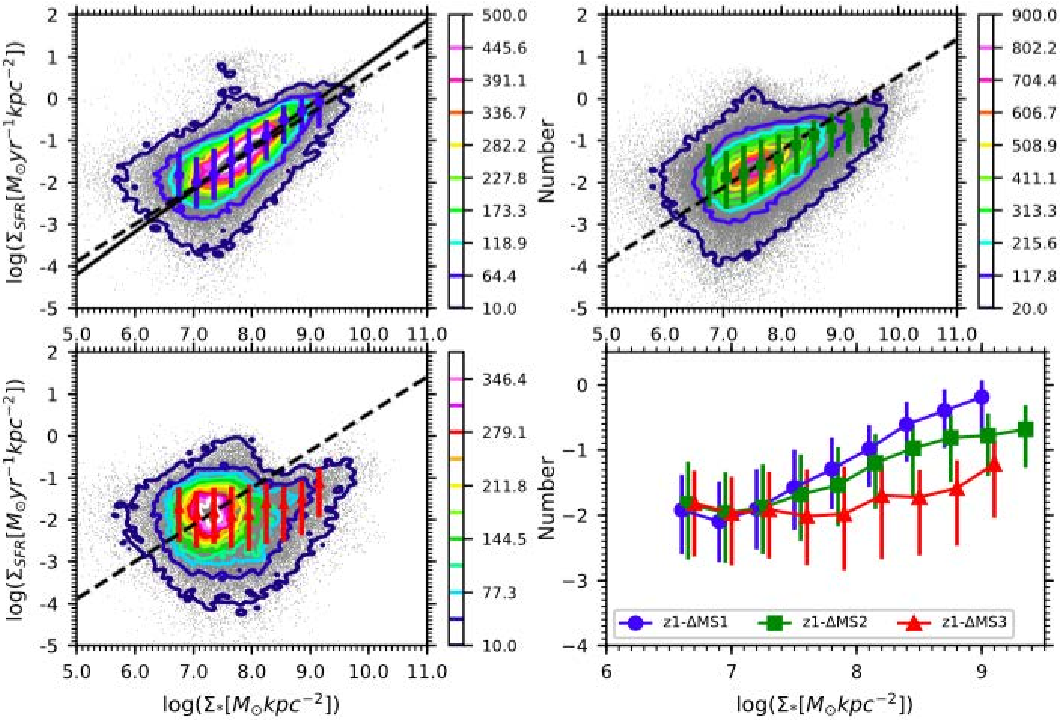

Figure 5.3: Spatially resolved SFMS at $z \sim 1$ as a function distance from the global SFMS. Top left panel: spatially resolved SFMS relation of the z1-ΔMS1 galaxies. Top right panel: spatially resolved SFMS of the z1-ΔMS2. Bottom left panel: spatially resolved SFMS of the z1-ΔMS3. In each of the three panels, contours connect regions in the plot which have similar number of pixels, while circles with errorbars are mode values of the $\Sigma_{\rm SFR}$ distributions associated with Σ_* bins with 0.3 dex width. The errorbars represent standard deviation around the mode values which are calculated separately above and below the mode values. Bottom right panel: comparison between the spatially resolved SFMS of the three groups. For clarity, blue circles are shifted by 0.05 dex to the left and red triangles are shifted by 0.05 dex to the right. This figure is taken from Abdurro'uf and Akiyama (2018).

profiles) is shown in the bottom right panel. It is clearly shown that the difference between the spatially resolved SFMS relations is larger at high Σ_* than that at low Σ_* region. It reflects a larger sSFR difference in the sub-galactic regions with high Σ_* compared to that in the sub-galactic regions with low Σ_*. Next, we will investigate this possible evolutionary trend of the star formation activity in the sub-galactic regions by examining the $\Sigma_{\rm SFR}(r)$, $\Sigma_*(r)$, and sSFR(r) radial profiles of the galaxies in the z1-ΔMS1, z1-ΔMS2, and z1-ΔMS3 groups.

5.2 Radial profiles of $\Sigma_*(r)$, $\Sigma_{\rm SFR}(r)$, and sSFR(r) of massive disk galaxies at $z \sim 1$

In order to get insights on the structures of massive disk galaxies at $z \sim 1$, we investigate the $\Sigma_{\rm SFR}(r)$, $\Sigma_*(r)$, and sSFR(r) radial profiles of the galaxies in the $z \sim 1$ sample. First, $\Sigma_{\rm SFR}(r)$

and $\Sigma_*(r)$ radial profiles of each galaxy are derived. In order to derive the radial profiles for the individual galaxy, we apply the same method as we used for deriving the radial profiles for the galaxies in the $z \sim 0$ sample, which is explained in Section 4.4.1. Briefly, the procedures are as follows. First, elliptical isophotes fitting is done to the F125W image using the `ellipse` command in `IRAF`. Then average ellipticity and position angle are calculated based on the elliptical isophotes outside of the half-mass radius. The half-mass radius is calculated based on the elliptical isophote that is averaged over the elliptical isophotes in the entire galaxy region. After getting the average ellipticity and position angle, the $\Sigma_{\rm SFR}(r)$ and $\Sigma_*(r)$ radial profiles are derived by averaging the $\Sigma_{\rm SFR}$ and Σ_* of pixels within each elliptical annulus. The radial profile is sampled with 2 kpc step along the semi-major axis. Once $\Sigma_{\rm SFR}(r)$ and $\Sigma_*(r)$ are obtained, the sSFR(r) is derived by dividing the $\Sigma_{\rm SFR}(r)$ by the $\Sigma_*(r)$.

5.2.1 Average surface density radial profiles over all the sample galaxies

In order to get a glance of the overall structures of the galaxies in the $z \sim 1$ sample, we plot the $\Sigma_{\rm SFR}(r)$, $\Sigma_*(r)$, and sSFR(r) of all the sample galaxies. Fig. 5.4 shows the $\Sigma_{\rm SFR}(r)$, $\Sigma_*(r)$, and sSFR(r) of all the 152 galaxies in the $z \sim 1$ sample (shown in blue). The radial profiles are cut up to a radius of 17 kpc considering low S/N of the majority of pixels outside of it. The black lines are extrapolation part of the radial profiles which do not reach the radius of 17 kpc. The extrapolation is based on fitting the outskirt part of the radial profile ($r > 3$ kpc) with an exponential function (eq. 4.4.1). Average radial profiles are shown with the large circles with line in green color. The figure shows that on average, $\Sigma_{\rm SFR}(r)$ and $\Sigma_*(r)$ of the sample galaxies are centrally peaked, i.e. increasing with decreasing radius. Interestingly, the average sSFR(r) is roughly flat over the entire radial range. The flat average sSFR(r) suggests the similarity of star formation efficiency across the region within majority of the sample galaxies. The 'flattening' tendency at high Σ_* end of the spatially resolved SFMS relation with all sub-galactic regions in the sample galaxies (Fig. 5.1) suggests a suppression of sSFR in the sub-galactic regions with high Σ_*, which mostly located in the central regions of the galaxies, while the linear trend at low Σ_* suggests a constant sSFR across the sub-galactic regions with low Σ_*, which mostly located in the disks. The suppression of sSFR in the central region is not shown by the average sSFR(r). However, sSFR(r) of some galaxies in the sample indeed show low sSFR (log(sSFR$[yr^{-1}]$)) in their central regions. Next, we will examine the average $\Sigma_{\rm SFR}(r)$, $\Sigma_*(r)$, and sSFR(r) of galaxies based on their distances from the global SFMS (i.e. z1-ΔMS1, z1-ΔMS2, and z1-ΔMS3 groups) and global M_* to investigate the possible dependence of the radial profiles on the galaxy global properties.

5.2.2 Surface density radial profiles as a function of the global stellar mass

In order to investigate the effect of global M_* on the radial variation of the $\Sigma_{\rm SFR}$, Σ_*, and sSFR, we examine the average $\Sigma_{\rm SFR}(r)$, $\Sigma_*(r)$, and sSFR(r) radial profiles of high-mass (with integrated

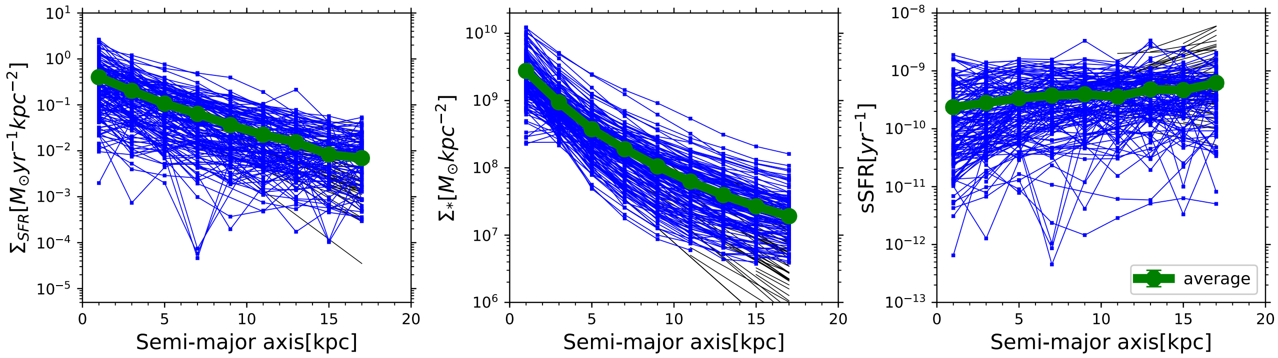

Figure 5.4: $\Sigma_{\rm SFR}(r)$ (left panel), $\Sigma_{*}(r)$ (middle panel), and sSFR(r) (right panel) radial profiles of the 152 galaxies in the $z \sim 1$ sample. The radial profile of each galaxy is shown in blue color. The black lines represent extrapolation of the radial profiles which do not reach radius of 17 kpc. The extrapolation is based on an exponential function fitting to the outskirt part ($r > 3$ kpc) of the radial profile. The radial profiles shown in green represent the average radial profiles over all the radial profiles of the sample galaxies. This figure is taken from Abdurro'uf and Akiyama (2018).

M_{*} higher than the median M_{*} of $7.8 \times 10^{10} M_{\odot}$) and low-mass (with integrated M_{*} lower than the median M_{*}) groups. Both high-mass and low-mass groups consists of 76 galaxies. On average, the galaxies in high-mass group have higher $\Sigma_{\rm SFR}$ and Σ_{*} over entire radii compared to the galaxies in low-mass groups. On average, high-mass group have lower sSFR over entire radii than low-mass group. This trend is also found in the local massive disk galaxies as discussed in Section 4.4.3 (see Fig. 4.13). This observational trend suggests that the 'downsizing' signal is spatially preserved in the galaxies in such a way that more massive galaxies tend to quench their star formation activities earlier over their entire regions than less massive galaxies. Indication of this spatially resolved 'downsizing' is also observed in local galaxies across wide global M_{*} range ($9.0 \lesssim \log(M_{*}/M_{\odot}) \lesssim 11.5$) by integral field spectroscopy observations (e.g. Pérez et al. 2013; Ibarra-Medel et al. 2016) with integral field spectroscopy observations. The authors tried to reconstruct the radially-resolved star formation history which then used to infer the radially-resolved stellar mass assembly history. They found that the stellar mass buildup in the entire region of more massive galaxies tend to be faster than that in less mass galaxies.

The differences of sSFR in the entire radii between the high-mass group and low-mass group are roughly similar such that the global M_{*} only determines the normalization of the sSFR radial profile. The lower sSFR(r) normalization of the more massive galaxies compared to the less massive galaxies also observed at $0.7 < z < 1.5$ by Nelson et al. (2016a) using grism spectroscopy observation with the 3D-HST survey. However, the authors found an additional effect promoted by the global M_{*}, which is an increasing positive slope of the sSFR(r) from the galaxies with $\log(M_{*}/M_{\odot}) \sim 9.25$ (which shows roughly zero slope, i.e. flat radial profile) to the galaxies with $\log(M_{*}/M_{\odot}) \sim 10.75$ (which shows large positive slope, i.e. steeply increasing with radius). In this work, we only see similar slight declining trend toward the central region in sSFR radial profiles of both of the low-mass and high-mass groups. We tried to find an indication of the steeper decline toward the central region in the sSFR(r) by further dividing the sample galaxies into four groups using the quartile values of the M_* distribution as the threshold. The lower right panel shows the average sSFR radial profiles of the galaxies in the four groups; first quarter as the galaxies with $M_* \leqslant M_{*,\mathrm{Q1}}$; second quarter as the galaxies with $M_{*,\mathrm{Q1}} < M_* \leqslant M_{*,\mathrm{Q2}}$; third quarter as the galaxies with $M_{*,\mathrm{Q2}} < M_* \leqslant M_{*,\mathrm{Q3}}$; and fourth quarter as the galaxies with $M_* > M_{*,\mathrm{Q3}}$. The $M_{*,\mathrm{Q1}}$, $M_{*,\mathrm{Q2}}$, and $M_{*,\mathrm{Q3}}$ represent first, second, and third quartiles in the M_* distribution, which correspond to $5.26{\times}10^{10}M_{\odot}$, $7.84{\times}10^{10}M_{\odot}$, and $1.22\times10^{11}M_{\odot}$, respectively. Each group contain 38 galaxies. The figure shows that the average sSFR(r) of the fourth quarter group has a slight steeper suppression toward the central region.

Since Nelson et al. (2016a) did not take into account the radial variation of the dust extinction, the steep central suppression in the average sSFR radial profile of massive ($\log(M_*/M_{\odot}) > 10$) galaxies they observed is suffered from the dust extinction effect, which is expected to be high in the central region of massive galaxies (see e.g. Tacchella et al. 2018). In the companion paper, Nelson et al. (2016b), they estimated the average radial profile of the dust extinction of the galaxies at $1.35 < z < 1.5$ from the Balmer decrement (within which they could get the spatially resolved distributions of both H_{α} and H_{β}) and found that the dust extinction radial profile is steeply increasing toward the central region for massive galaxies ($9.8 < \log(M_*/M_{\odot}) < 11.0$). It implies that the true sSFR(r) for massive galaxies must be less suppressed in the central region compared to the sSFR(r) they derived with the assumption of a uniform dust extinction across the galaxy region.

5.2.3 Surface density radial profiles as a function of distance from the global SFMS

The linear spatially resolved SFMS relation with a slope of nearly unity for the z1-ΔMS1 suggests the flat sSFR radial profile over the entire radii or similar star formation efficiency across the entire regions in the galaxies, while the flattening tendency at high Σ_* in the spatially resolved SFMS relations for the z1-ΔMS2 and z1-ΔMS3 suggests a decline of the sSFR in sub-galactic regions with high Σ_*, which are mostly located in the central regions of the galaxies. Here, we examine the $\Sigma_{\mathrm{SFR}}(r)$, $\Sigma_*(r)$, and sSFR(r) of galaxies in the z1-ΔMS1, z1-ΔMS2, and z1-ΔMS3 groups to check those expected trends and furthermore investigate the effect of global sSFR on the local star formation activity and stellar mass.

Fig. 5.6 shows average $\Sigma_{\mathrm{SFR}}(r)$ (left panel), $\Sigma_*(r)$ (middle panel), and sSFR(r) (right panel) radial profiles of galaxies in the z1-ΔMS1 (shown in blue color), z1-ΔMS2 (shown in green color), and z1-ΔMS3 (shown in red color) groups. The figure shows that the $\Sigma_{\mathrm{SFR}}(r)$ radial profiles of galaxies in the three groups are increasing toward the central region. On average, the z1-ΔMS1 galaxies have higher Σ_{SFR} than the z1-ΔMS2 galaxies over their entire regions and the z1-ΔMS2 galaxies have higher Σ_{SFR} than the z1-ΔMS3 galaxies over their entire regions. The average $\Sigma_*(r)$ radial profiles of the z1-ΔMS2 and z1-ΔMS3 galaxies show steeper increase toward the central region (within $r \leqslant 5$ kpc) compared to that of the average $\Sigma_*(r)$ of the z1-ΔMS1 galaxies.

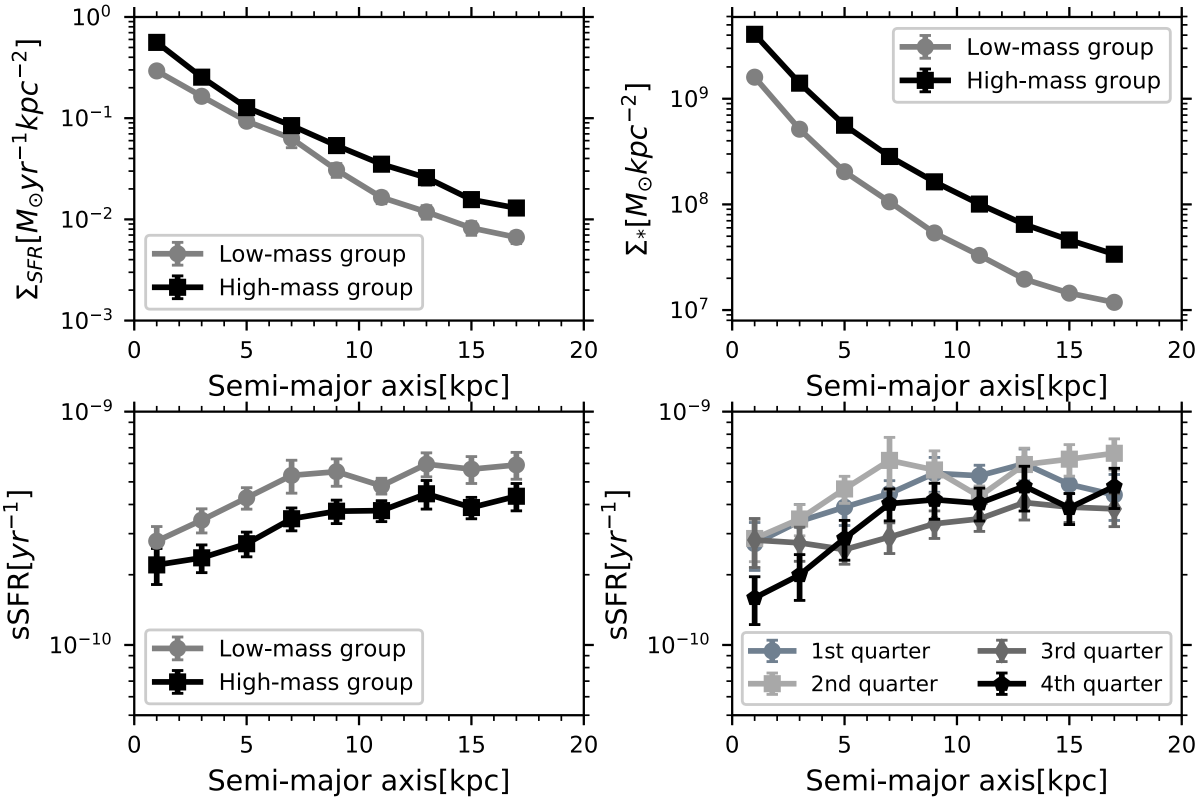

Figure 5.5: Effect of the global M_* on the $\Sigma_{\rm SFR}(r)$, $\Sigma_*(r)$, and sSFR(r) radial profiles of the sample galaxies at $0.8 < z < 1.8$. In top left panel, top right panel, and bottom left panel, the average $\Sigma_{\rm SFR}(r)$, $\Sigma_*(r)$, and sSFR(r) of galaxies in low-mass (shown in gray) and high-mass groups (shown in black) are compared. The bottom right panel shows comparison among average sSFR radial profiles of four galaxy groups which is defined with the quartile in the M_* distribution of the sample galaxies.

Interesting feature is shown in the comparison of the sSFR(r) among the three groups. The average sSFR(r) of the z1-ΔMS1 galaxies is flat over the entire radii, while the average sSFR(r) of the z1-ΔMS2 and z1-ΔMS3 galaxies show declining trend toward the galactic center. The declining trend toward the galactic center is steeper in the sSFR(r) of the z1-ΔMS3 galaxies than that of the z1-ΔMS2 galaxies. Systematic difference of sSFR among those three groups is not only observed in the central region but also in the outskirt. However the sSFR difference in the outskirt is much smaller compared to that in the central region. The sSFR differences between the z1-ΔMS1 and z1-ΔMS2 at radii of 1 kpc and 17 kpc are 0.61 dex and 0.1 dex, respectively, while the sSFR differences between the z1-ΔMS1 and z1-ΔMS3 ar radii of 1 kpc and 17 kpc are 1.21 dex and 0.35 dex, respectively. In order to check if the declining trend toward the galactic center in the sSFR(r) of the z1-ΔMS2 and z1-ΔMS3 is real and not biased toward the lower sSFR due to central quiescent regions in an only few quiescent galaxies, we examine the sSFR distributions in the central ($r \leqslant 4$ kpc), middle ($4 < r \leqslant 10$ kpc), and outskirt ($r > 10$ kpc) regions of the galaxies in the three groups. Histograms of the sSFR distributions in the central, middle, and outskirt regions of the

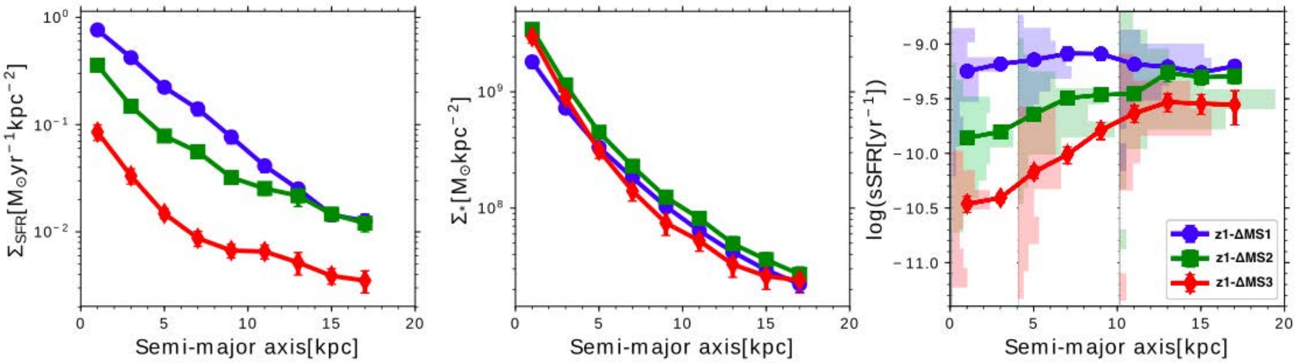

Figure 5.6: Radial profiles of $\Sigma_{\rm SFR}(r)$ (left panel), $\Sigma_*(r)$ (middle panel), and sSFR(r) (right panel) of sample galaxies at $0.8 < z < 1.8$ as a function of their distances from the global SFMS. In each panel, radial profiles for the z1-ΔMS1, z1-ΔMS2, and z1-ΔMS3 galaxies are shown with blue, green, and red colors, respectively. Histograms in the right panel show distributions of the sSFR in the central ($r \leqslant 4$ kpc), middle ($4 < r \leqslant 10$ kpc), and outskirt ($r > 10$ kpc) of the z1-ΔMS1, z1-ΔMS2, and z1-ΔMS3 that are shown with the same colors as those used for the corresponding group. This figure is taken from Abdurro'uf and Akiyama (2018).

three groups are shown in the right panel of the Fig. 5.6 with the same colors as for the sSFR(r) of the corresponding group. The histograms show the systematically lower sSFR in the central and middle regions of the z1-ΔMS2 and z1-ΔMS3 compared to that of the z1-ΔMS1. The slightly lower sSFR in the outskirt of the z1-ΔMS2 and z1-ΔMS3 compared to that of the z1-ΔMS1 also shown by the histograms. The histograms for the sSFR in the central, middle, and outskirt of the z1-ΔMS1 tend to peak at nearly the same sSFR, log(sSFR$[yr^{-1}]$) ~ -9.2, agrees with the flat average sSFR(r) of this group. Thus, the trend shown by the average sSFR(r) of the z1-ΔMS1, z1-ΔMS2, and z1-ΔMS3 galaxies indeed represent the difference of local sSFR among the three groups.

The trend shown by the average sSFR(r) of the z1-ΔMS1, z1-ΔMS2, and z1-ΔMS3 suggest that the quenching process in the massive disk galaxies is started from the central region then propagate toward the outskirt, agrees with the inside-out quenching scenario. Observational evidences for the inside-out quenching also observed by other researchers, e.g. Tacchella et al. (2015, 2018) which investigated sSFR(r) of massive galaxies at $z \sim 2$; González Delgado et al. (2016) and (Belfiore et al. 2018) which investigated sSFR(r) of galaxies in the local universe. In order to check if the central regions of the z1-ΔMS2 and z1-ΔMS3 are indeed quiescent system, as suggested by their sSFR(r) radial profiles that show strong suppression in the central region, and not mistaken for dusty star-forming system, we examined the U, V, and J magnitudes of the galaxy pixels located in the central, middle, and outskirt to check their locations on the UVJ diagram. We found that pixels located in the central regions of the z1-ΔMS2 and z1-ΔMS3 have systematically older and more passive SEDs compared to the pixels located in the outskirt of those galaxies. We discuss this issue in appendix B.

The centrally more concentrated average $\Sigma_*(r)$ of the z1-ΔMS2 and z1-ΔMS3 galaxies compared to that of the z1-ΔMS1 galaxies suggests a possible morphological difference, which is related to

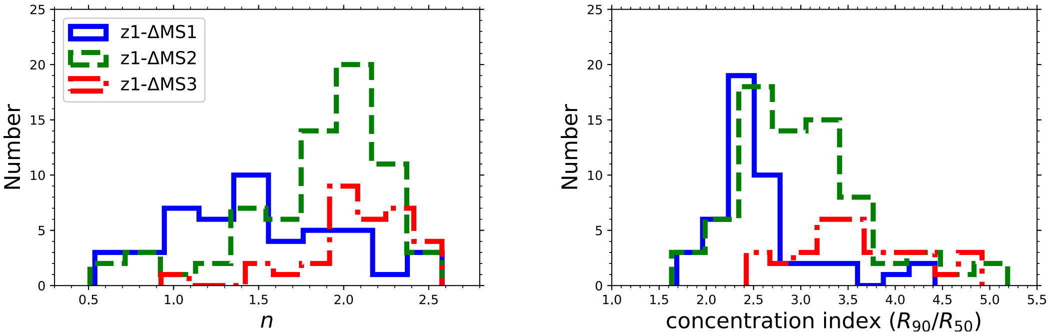

Figure 5.7: Histograms for the distributions of the Sérsic index (n; left panel) and R_{90}/R_{50} concentration index (right panel) of the z1-ΔMS1 (shown with blue solid line), z1-ΔMS2 (shown with green dashed line), and z1-ΔMS3 (shown with red dashed dotted line) galaxies. This figure is taken from Abdurro'uf and Akiyama (2018).

the bulge to total mass fraction (B/T), among them. In order to investigate the morphological difference among the z1-ΔMS1, z1-ΔMS2, and z1-ΔMS3 galaxies, we examine the Sérsic index (n) and concentration index (R_{90}/R_{50}) of the galaxies in those three groups. n is calculated by fitting the $\Sigma_*(r)$ with Sérsic profile, $\Sigma_*(r) = \Sigma_*(r_0)\exp\left(-\left(\frac{r}{h}\right)^{1/n}\right)$. First, the exponential function ($n = 1$) fitting is done to get the initial guess for the radial scale length (h) and the zero point ($\Sigma_*(r_0)$). Then the random set of n, h and $\Sigma_*(r_0)$ are generated according to the following parameter ranges: $n[0.5, 5]$, $\Sigma_*(r_0)[0.1\Sigma_*(r_0, n = 1), 10\Sigma_*(r_0, n = 1)]$ and $h[1, 10h_{n=1}]$. The best-fitting Sérsic profile is determine based on the lowest χ^2 value. The R_{50} and R_{90} in the concentration index are calculated with the semi-major axis that enclose 50% and 90% of the total M_*, respectively. Fig. 5.7 shows distributions of the Sérsic index (left panel) and R_{90}/R_{50} concentration index (right panel) of the z1-ΔMS1 (blue solid line), z1-ΔMS2 (green dashed line), and z1-ΔMS3 (red dashed dotted line) galaxies. It is shown by the figure that the Sérsic index and concentration index of the z1-ΔMS3 galaxies are systematically higher than those of the z1-ΔMS1 galaxies, while the Sérsic index and concentration index of the z1-ΔMS2 are in the intermediate between those of the z1-ΔMS1 and z1-ΔMS3. This trend suggests an increasing bulge to total mass ratio (B/T) from the star-forming galaxies to the quiescent galaxies. This trend might indicate the formation of the bulge component and increasing prominence of the bulge following the quenching of the star formation in the galaxies.

5.3 Investigating galaxies with high possibility being experiencing gas compaction event (i.e. blue nugget phase) which will lead to the onset of inside-out quenching

The trend shown by the average sSFR(r) radial profiles of the z1-ΔMS1, z1-ΔMS2, and z1-ΔMS3 galaxies (as discussed in Section 5.2.3) implies the inside-out quenching process in massive disk galaxies at $z \sim 1$. Moreover, the trend suggests an onset of the inside-out quenching in galaxies at the intermediate between the z1-ΔMS1 and z1-ΔMS2. The trend shown by the Sérsic index and concentration index (i.e. B/T) of the z1-ΔMS1, z1-ΔMS2, and z1-ΔMS3 galaxies (as also discussed in the Section 5.2.3) suggests the connection between the inside-out quenching process and bulge formation and growth, such that bulge might be under construction in the z1-ΔMS1 galaxies, while it is already formed in the z1-ΔMS2 galaxies, and getting matured in the z1-ΔMS3 galaxies.

The physical mechanism responsible for the inside-out quenching and the bulge formation is still unclear. Cosmological zoom-in hydrodynamical simulations run by Ceverino et al. (2014), Zolotov et al. (2015), Tacchella et al. (2016b) and Tacchella et al. (2016a) suggest that the onset of the inside-out quenching could be started by an event of gas compaction toward the galactic center. The gas compaction event could be caused by a gas-rich merger or smoother gas stream, such as counter rotating stream which frequently occur at high redshift for galaxies with $\log(M_*) \sim 10$. The compaction of gas toward the galactic center could trigger nuclear starburst which rapidly consumes gas in the central region and make a large accumulation of stellar mass in the galactic center, which then become bulge component. Gas in the central region could run out if subsequent gas inflow into the central region stopped due to e.g. AGN feedback or radiation feedback from the nuclear starburst. The depletion of gas, suppression of SFR, and large stellar mass accumulation in the central region could lead to the centrally-suppressed sSFR(r) (as that of the z1-ΔMS2, and z1-ΔMS3 galaxies shown in Fig. 5.6).

The evolutionary scenario described above suggests an occurrence of three phases around the onset of the inside-out quenching: gas compaction event which usually called blue nugget phase in which nuclear starburst is ongoing; post compaction event or post blue nugget phase in which bulge component formed and gas in the central region depleted; and centrally-quenched phase in which bulge getting matured. Those evolutionary phases could be traced by using the sSFR(r). Galaxy in the blue nugget phase is expected to have centrally-peaked sSFR(r) because of the ongoing nuclear starburst, while galaxy in the centrally-quenched phase is expected to have centrally-suppressed sSFR(r) because of the depletion of gas density and SFR in central region of the galaxy, and also large accumulation of stellar mass in the central region. Given the diversity of the sSFR(r) among the galaxies in our $z \sim 1$ sample, it is possible that our sample contains galaxies in the three phases: blue nugget, post blue nugget, and centrally-suppressed phase.

By using information on sSFR(r), we look for galaxies (in the $z \sim 1$ sample) with high possibility being in the blue nugget phase (hereafter called blue nugget candidates) indicated by centrally-peaked sSFR(r), post blue nugget phase (hereafter called post blue nugget candidates) indicated by roughly flat sSFR(r) or showing an indication of departure from being centrally-peaked in the past, and centrally-quenched phase (hereafter called centrally-quenched candidates) indicated by centrally-suppressed sSFR(r). Here we only highlight some candidates of those three phases. It is outside the scope of this thesis to study in detailed on this issue by classifying all the sample galaxies into the three phases and study the characteristics of the three phases (e.g. typical global M_*, sSFR, and age at which the three phases occur). Since we only limited our sample on massive disk galaxies

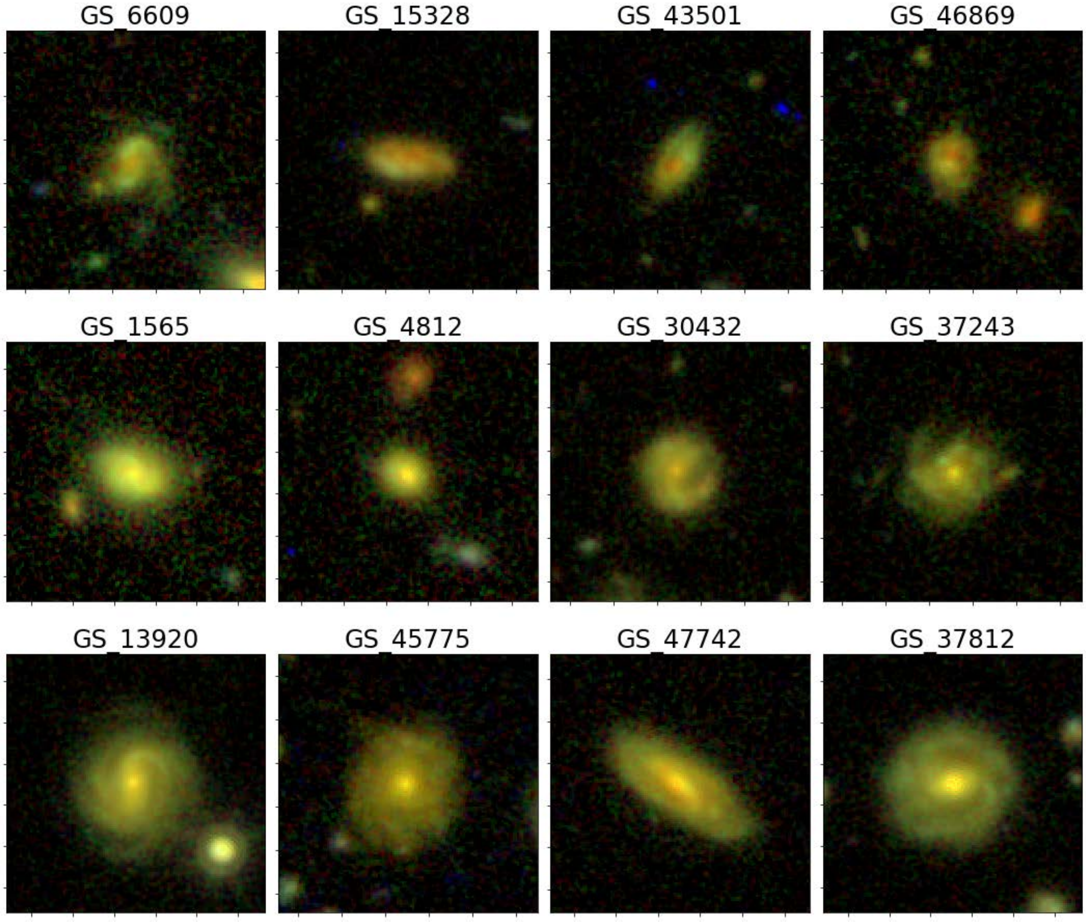

Figure 5.8: Optical composite images (which are made from combination of F814W-F125W-F160W images) of galaxies with high probability being in the blue nugget phase (first row), post blue nugget phase (second row), and centrally-quenched nugget phase (third row).

in this research, discussion on the characteristics of those three phases might affected by some bias. That topic will be a focus of future research using larger sample.

Fig. 5.8 shows optical images (which are composite of F814W-F125W-F160W images or roughly equal to the rest-frame *gri* images that is transformed into RGB format with F160W for red, F125W for green, and F814W for blue) of four blue nugget candidates (first row), post blue nugget candidates (second row), and centrally-quenched candidates (third row) selected from the $z \sim 1$ sample. Index above each image represents id of the galaxy in the 3D-HST catalog for GOODS-S galaxies. Spatial structures of those galaxies are shown in Fig. 5.9 (for blue nugget candidates), Fig. 5.10 (for post blue nugget candidates), and 5.11 (for centrally-quenched candidates). In each figure, different column represents different galaxy, and in each column from top to bottom shows F435W flux map, F160W flux map, $\Sigma_{\rm SFR}$ map, Σ_{*} map, $\Sigma_{\rm SFR}(r)$, $\Sigma_{*}(r)$, and sSFR(r), respectively.

Some structural properties that emerges from this analysis are as follow. The blue nugget candidates have centrally-peaked $\Sigma_{\rm SFR}(r)$ and sSFR(r) radial profiles, and relatively low Σ_{*} in the central region ($< 10^{9}M_{\odot}$kpc^{-2} within a radius of ~ 1 kpc). Those galaxies mostly reside in the upper envelope of the global SFMS. The post blue nugget candidates have centrally-peaked $\Sigma_{\rm SFR}(r)$, but the sSFR(r) shows departure from being centrally-peaked. Their central regions have relatively high Σ_{*} ($> 10^{9}M_{\odot}$kpc^{-2} within a radius of ~ 1 kpc). Those galaxies mostly reside around the mean global SFMS relation and lower envelope of the scatter. The more massive central region in the post blue nugget phase than that in the blue nugget phase might indicate accumulation of the stellar mass produced during the nuclear starburst, when the galaxy was in the blue nugget phase. Majority of the centrally-quenched candidates have centrally-suppressed $\Sigma_{\rm SFR}(r)$, steep declining sSFR(r) radial profile toward the central region, and relatively massive central region ($> 10^{9}M_{\odot}$kpc^{-2} within a radius of ~ 1 kpc). All of those galaxies reside below the global SFMS. Integrated M_{*} of the blue nugget candidates are $9.3\times10^{10}M_{\odot}$ (GS_6609), $4.8\times10^{10}M_{\odot}$ (GS_15328), $4.7\times10^{10}M_{\odot}$ (GS_43501), and $5.6\times10^{10}M_{\odot}$ (GS_46869) with an average of $6.1\times10^{10}M_{\odot}$. Integrated M_{*} of the post blue nugget candidates are $9.2 \times 10^{10}M_{*}$ (GS_1565), $4.5 \times 10^{10}M_{\odot}$ (GS_4812), $5.7 \times 10^{10}M_{\odot}$ (GS_30432), and $1.3\times10^{11}M_{\odot}$ (GS_37243) with an average of $8.1\times10^{10}M_{\odot}$. Integrated M_{*} of the centrally-quenched candidates are $7.4 \times 10^{10}M_{\odot}$ (GS_13920), $1.5 \times 10^{11}M_{\odot}$ (GS_45775), $1.2 \times 10^{11}M_{\odot}$ (GS_47742), and $8.6 \times 10^{10}M_{\odot}$ (GS_37812) with an average of $1.1 \times 10^{11}M_{\odot}$. Redshift of each galaxy is shown along with the F435W map of the galaxy in the Fig. 5.9, Fig. 5.10, and 5.11. There seems to be an increasing M_{*} trend from the blue nugget phase to the red nugget phase supporting the idea that those three phases might represent phases in galaxy evolution.

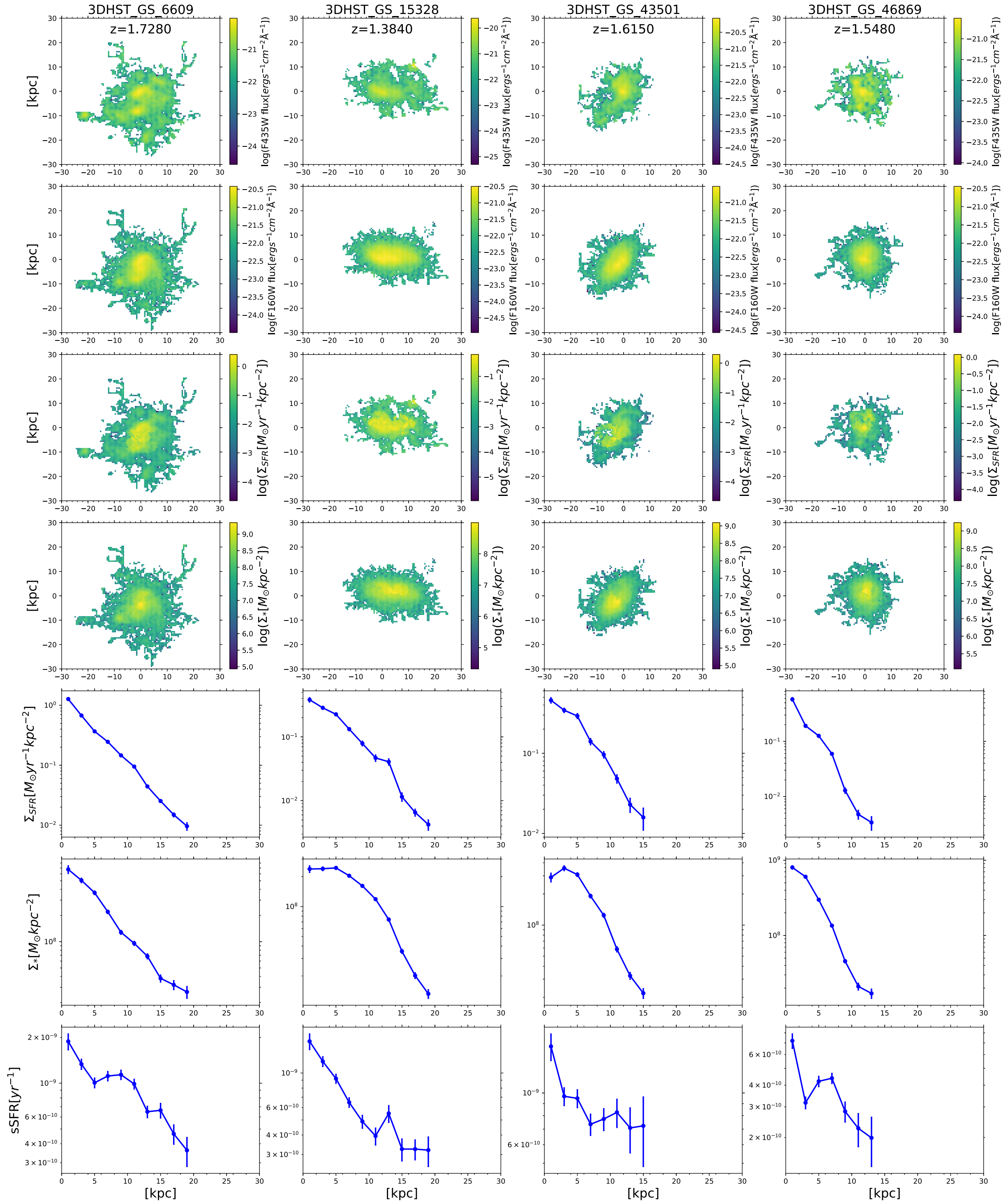

Figure 5.9: Four galaxies in the $z \sim 1$ sample with high probability being in the blue nugget phase, i.e. experiencing gas compaction event. Different column show different galaxy. In each column, from top to bottom show spatially resolved distributions of the F435W flux, F160W flux, $\Sigma_{\rm SFR}$, Σ_*, $\Sigma_{\rm SFR}(r)$, $\Sigma_*(r)$, and sSFR(r).

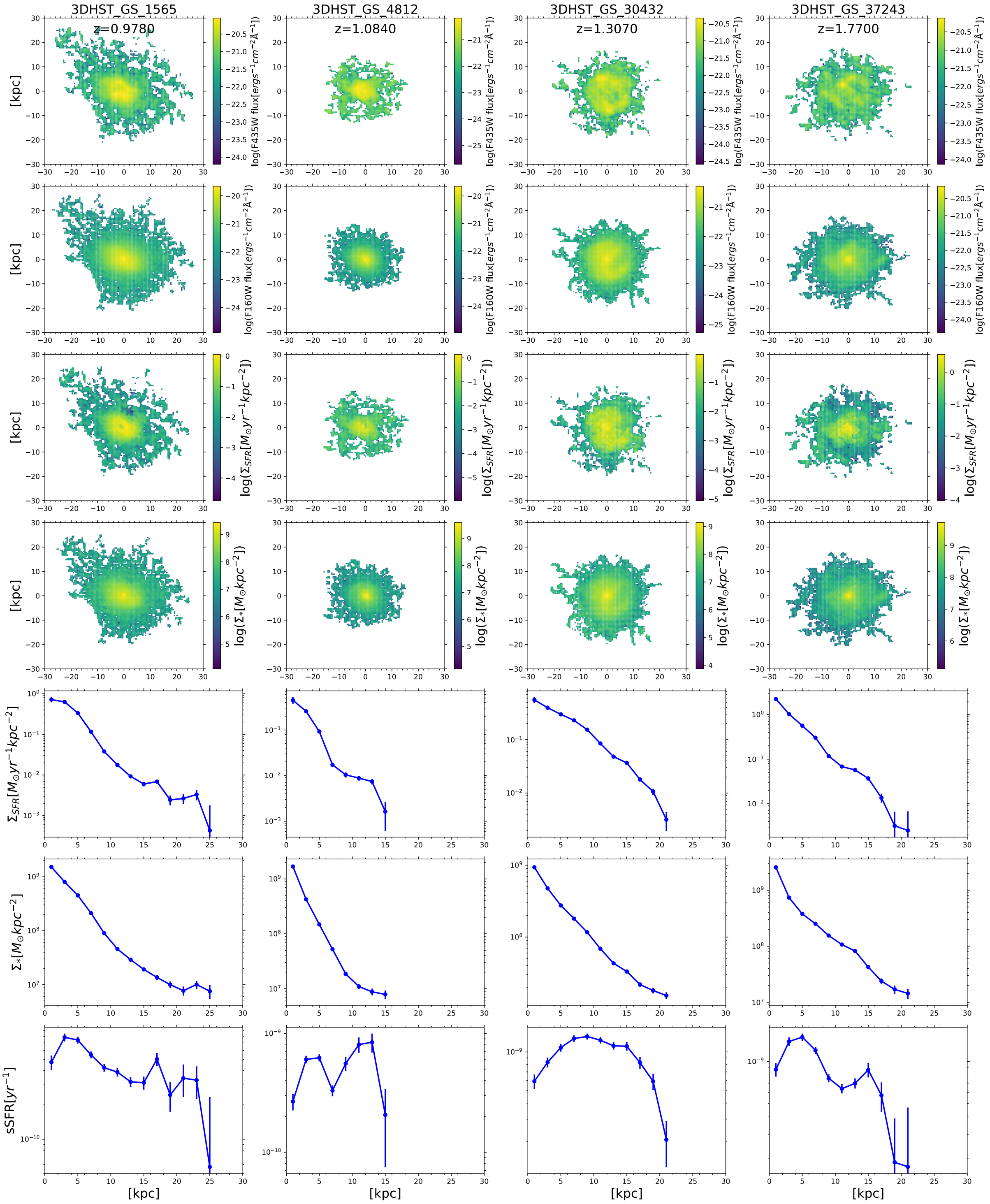

Figure 5.10: Same as in Fig. 5.9 but now for galaxies with high probability being in the post blue nugget phase.

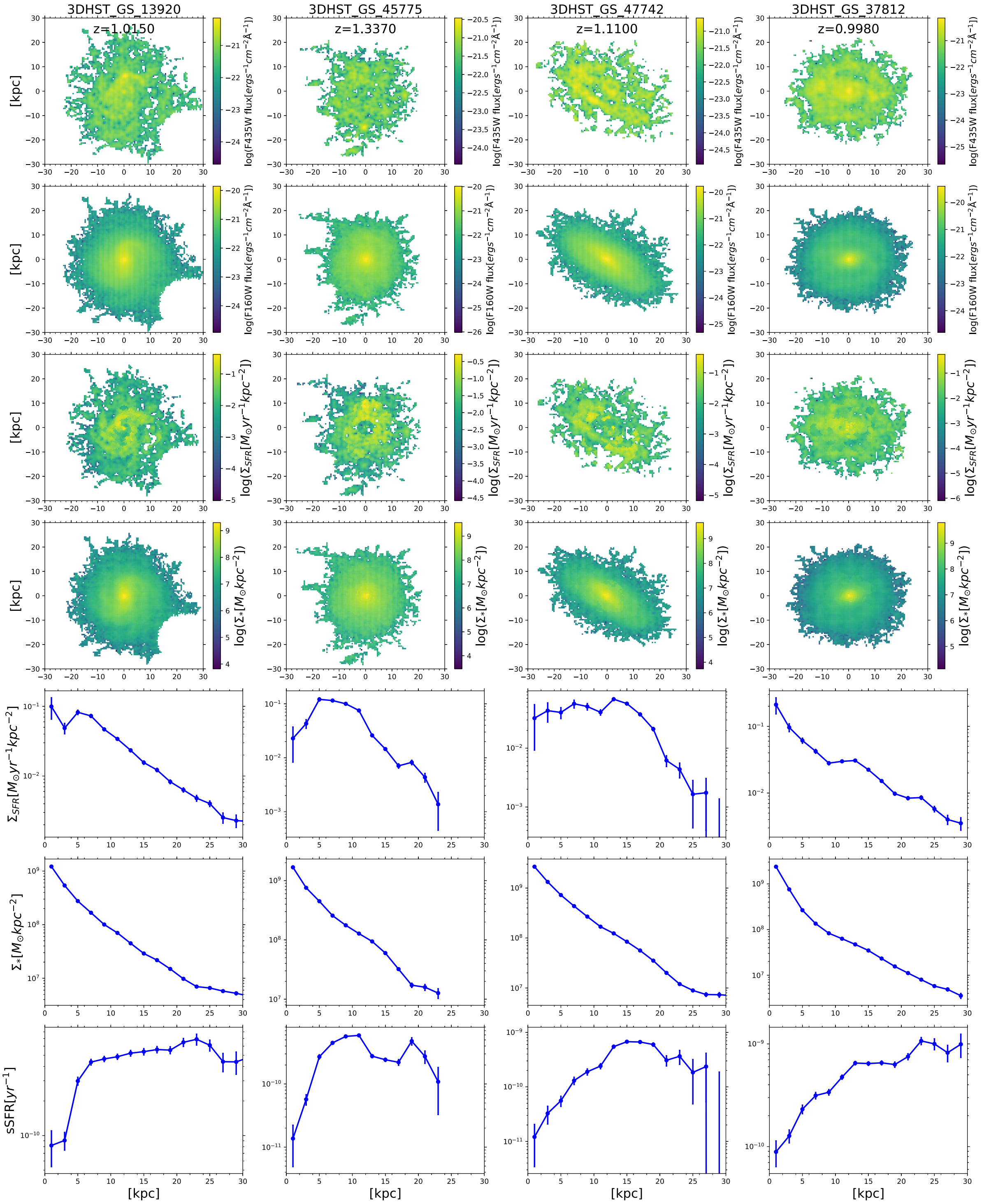

Figure 5.11: Same as in Fig. 5.9 but now for galaxies with high probability being in the centrally-quenched phase.

Chapter 6

Connecting local and high-z samples: Empirical model for the evolution of the surface density radial profiles of massive disk galaxies over the last 10 Gyrs

6.1 Observed evolutionary trend of the spatially resolved SFMS at $0 \lesssim z \lesssim 1$

In order to get insights on the evolutionary trend of the spatially resolved SFMS relation from $z \sim 1$ to $z \sim 0$, we compare among the spatially resolved SFMS relations of the six galaxy groups that are defined based on the distances of the sample galaxies from the global SFMS relation, i.e. z0-ΔMS1, z0-ΔMS2, z0-ΔMS3, z1-ΔMS1, z1-ΔMS2, and z1-ΔMS3. The z0-ΔMS1, z0-ΔMS2, and z0-ΔMS3 are sub-samples in the $z \sim 0$ sample which are defined based on the distances (on the SFR-M_* plane) of the sample galaxies from the global SFMS relation by Speagle et al. (2014) that is calculated at the median redshift of the sample, $z = 0.0165$ (see Section 4.2). Briefly, the z0-ΔMS1, z0-ΔMS2, and z0-ΔMS3 groups are defined as galaxies in the $z \sim 0$ sample that reside above $+0.3$ dex, within ± 0.3 dex, and below -0.3 dex from the global SFMS relation, respectively. The z1-ΔMS1, z1-ΔMS2, and z1-ΔMS3 are sub-samples in the $z \sim 1$ sample that are defined based on the distances (on the SFR-M_* plane) of the sample galaxies from the global SFMS relation by Speagle et al. (2014) that is calculated at the median redshift of the sample, $z = 1.217$ (see Section 5.1.2). Briefly, the z1-ΔMS1, z1-ΔMS2, and z1-ΔMS3 groups are defined as galaxies in the $z \sim 1$ sample that reside within ±0.3 dex, between −0.3 dex and −0.8 dex, and below −0.8 dex from the global SFMS relation, respectively.

Fig. 6.1 shows the comparison among the spatially resolved SFMS relations (which are defined as the mode values, i.e. mode profile) of the z0-ΔMS1 (dark blue open circles with dashed line), z0-ΔMS2 (dark green open squares with dashed line), z0-ΔMS3 (dark red open triangles with dashed line), z1-ΔMS1 (blue solid triangles with solid line), z1-ΔMS2 (green solid pentagons with solid line), and z1-ΔMS3 (red solid diamonds with solid line). The evolutionary trend shows an increasing prominence of the flattening at high Σ_* end from $z \sim 1$ to $z \sim 0$. It suggests a larger decrease of the sSFR (from $z \sim 1$ to $z \sim 0$) in the sub-galactic regions with high Σ_* than in the sub-galactic regions with low Σ_*. Quantitative comparison between the spatially resolved SFMS of galaxies in the highest sSFR groups in the both redshifts, which are z1-ΔMS1 and z0-ΔMS1, shows the sSFR difference of 0.4 dex at $\log(\Sigma_*[M_\odot \mathrm{kpc}^{-2}]) = 7.0$ and the sSFR difference of 1.5 dex at $\log(\Sigma_*[M_\odot \mathrm{kpc}^{-2}]) = 8.5$. Recalling that the $\Sigma_*(r)$ radial profile always has increasing trend with decreasing radial distance from the galactic center, the sub-galactic regions with high Σ_* should mostly be residing in the central region, while those with low Σ_* should mostly be residing in the disk. Thus, the evolutionary trend of the spatially resolved SFMS suggests that as the galaxies evolving from $z \sim 1$ to $z \sim 0$ the star formation activity in their disks are less suppressed compared to the star formation activity in their central regions.

The shift toward higher Σ_* of the spatially resolved SFMS of the galaxies in the $z \sim 1$ sample compared to the spatially resolved SFMS of the galaxies in the $z \sim 0$ sample is caused by the fact that the $z \sim 1$ sample contains galaxies that are systematically more massive than the galaxies in the $z \sim 0$. As will be discussed later, large number of massive ($\log(M_*/M_\odot) \leqslant 11.0$) disk galaxies in the $z \sim 1$ sample are thought to evolve into massive (with the same M_* range) elliptical galaxies at $z \sim 0$. Because we only consider spiral galaxies for the $z \sim 0$ sample, such massive galaxies at $z \sim 0$ are missed.

6.2 Connecting the $z \sim 0$ and $z \sim 1$ samples: looking for the progenitors and descendants galaxies

In order to infer the structural evolution of the massive disk galaxies at $0 \lesssim z \lesssim 1$ and construct an empirical model for it, connecting the sample galaxies at $z \sim 1$ and $z \sim 0$ with high possibility being in the same evolutionary path (i.e. progenitors and descendants pair) is needed. The selection criteria used in this research (massive disk galaxies) does not guarantee that the galaxies in the $z \sim 0$ are descendant of the galaxies in the $z \sim 1$ sample. However, it is possible that some galaxies in the $z \sim 1$ and $z \sim 0$ samples are likely to be in the same evolutionary path, i.e. progenitors and descendants. The $z \sim 1$ and $z \sim 0$ samples cover similar comoving volumes ($4.5 \times 10^5 \mathrm{Mpc}^3$ and $4.3 \times 10^5 \mathrm{Mpc}^3$ for $z \sim 1$ and $z \sim 0$ samples, respectively). However, the median M_* of the $z \sim 1$ sample ($7.8 \times 10^{10} M_\odot$) is systematically higher than that of the $z \sim 0$ sample ($3.5 \times 10^{10} M_\odot$).

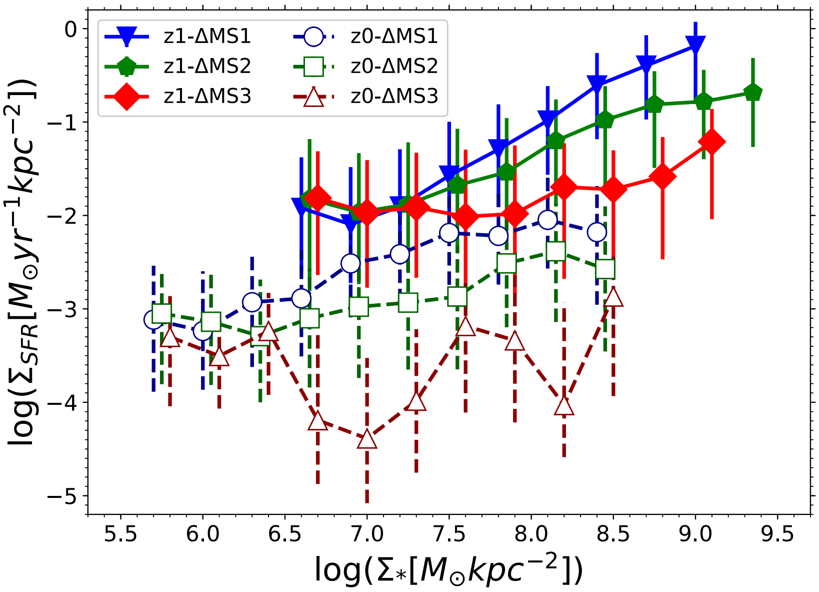

Figure 6.1: Evolutionary trend of the spatially resolved SFMS relation from $z \sim 1$ to $z \sim 0$ implied by the comparison among the six spatially resolved SFMS relations (which are defined from the mode values, i.e. mode profile) derived from the $z \sim 1$ sample (z1-ΔMS1 (blue solid tiangles with solid line), z1-ΔMS2 (green solid pentagons with solid line), and z1-ΔMS3 (red solid diamonds with solid line)) and $z \sim 0$ sample (z0-ΔMS1 (dark blue open circles with dashed line), z0-ΔMS2 (dark green open squares with dashed line), and z0-ΔMS3 (dark red open triangles with dashed line)). For clarity, blue solid triangles and dark blue open circles are shifted by 0.05 dex to the left, while red solid diamonds and dark red open triangles are shifted by 0.05 dex to the right from their actual positions.

It is due to the fact that there are many galaxies (50) more massive than $\log(M_{*}/M_{\odot}) = 11.0$ in the $z \sim 1$ sample, while only few (6) such massive galaxies in the $z \sim 0$ sample. Those massive disk galaxies at $z \sim 1$ are thought to evolve into massive elliptical galaxies at $z \sim 0$. We do not have many galaxies with $\log(M_{*}/M_{\odot}) > 11.0$ in the $z \sim 0$ sample as the disk/spiral galaxies are commonly have lower M_{*} than the elliptical galaxies in the local universe. We checked the comoving number densities (N) and stellar mass densities (ρ) of disk galaxies with $\log(M_{*}/M_{\odot}) \geqslant 11.0$ in the $z \sim 1$ sample and elliptical galaxies with the same mass range at $0.01 < z < 0.02$ (which is taken from the MPA-JHU catalog) and found that their N and ρ are comparable. The comoving number density and stellar mass density of the $z \sim 1$ massive disc galaxies are $\log(N[\mathrm{Mpc}^{-3}]) = -3.9$ and $\log(\rho[M_{\odot}\mathrm{Mpc}^{-3}]) = 7.3$, while those of the local elliptical galaxies are $\log(N[\mathrm{Mpc}^{-3}]) = -4.4$ and $\log(\rho[M_{\odot}\mathrm{Mpc}^{-3}]) = 6.7$, respectively.

We try to look for the progenitors and descendants pairs from the $z \sim 1$ and $z \sim 0$ samples using a model evolutionary track drawn on the sSFR-M_{*} plane. The model evolutionary track is derived by assuming a star formation history (SFH). The model evolutionary track is drawn using the following procedure: (1) first, initial sSFR and M_{*} at $z = 2$ are assumed for the model evolutionary track. The initial sSFR and M_{*} are assumed to lie within ±0.3 dex from the global SFMS relation at $z = 2$,

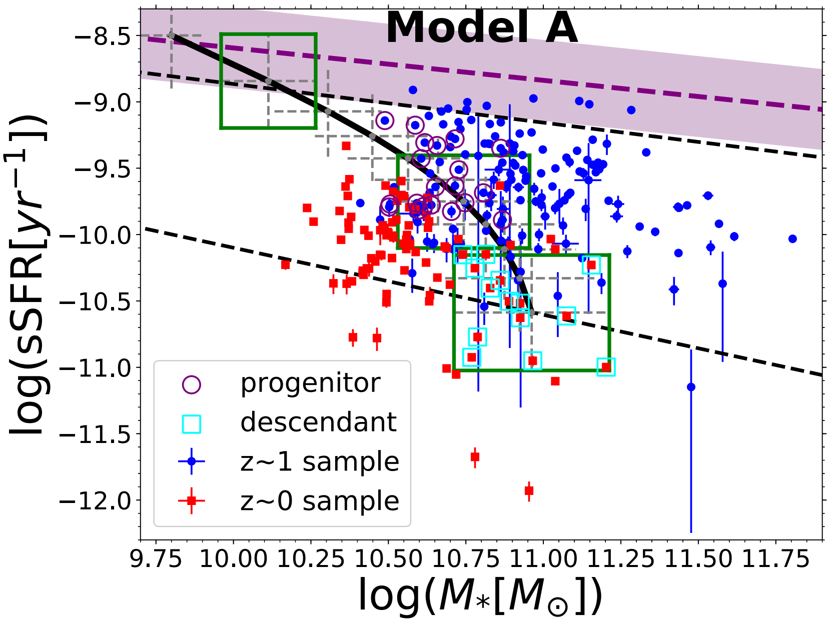

Figure 6.2: Connecting the $z \sim 1$ and $z \sim 0$ samples using a model evolutionary track assuming an exponentially declining SFH with $9.7 \leqslant \log(M_*(t_0)/M_\odot) \leqslant 9.9$, $-8.6 \leqslant \log(\mathrm{sSFR}(t_0)/\mathrm{yr}^{-1}) \leqslant -8.4$, and $4.0\mathrm{Gyr} \leqslant \tau \leqslant 6.0\mathrm{Gyr}$ (which is called model A) on the global sSFR versus M_* plane. The black line represents the model evolutionary track if the middle value of each model parameter range is used. The gray dashed-line show the range of sSFR(t) and $M_*(t)$ if the model parameter ranges are considered. Three green boxes show the ranges of sSFR(t) and $M_*(t)$ given by the horizontal and vertical 'errorbars' of the model evolutionary track calculated at $z = 1.8$, 0.8, and 0. The selected progenitors and descendants are shown by the purple open circles and cyan open squares, respectively. This figure is taken from Abdurro'uf and Akiyama (2018).

which is based on Speagle et al. (2014). (2) The SFH is assumed to be in the exponentially declining form, $\mathrm{SFR}(t) = \mathrm{SFR}(t_0)e^{-\Delta t/\tau}$ with $t = t_0 + \Delta t$ and t_0 as the age of the universe at $z = 2$. The sSFR and M_* at time t can then be calculated using

$$M_*(t) = M_*(t_0) + \tau \mathrm{SFR}(t_0)\left(1 - e^{-\Delta t/\tau}\right), \tag{6.1}$$

$$\mathrm{sSFR}(t) = \frac{e^{-\Delta t/\tau}}{\mathrm{sSFR}^{-1}(t_0) + \tau\left(1 - e^{-\Delta t/\tau}\right)}. \tag{6.2}$$

(3) A set of model parameters, which are $M_*(t_0)$, sSFR(t_0) and τ, are chosen such that it could connect as many as possible galaxies in the $z \sim 1$ and $z \sim 0$ samples, so that the model evolutionary track could be thought as a possible evolutionary path connecting the two samples.

We consider three different evolutionary paths: two assume the exponentially declining SFH with short and long τ and the other one only assume a same M_* range. A certain range for each model parameter is assumed so that the model evolutionary track has broad ranges of the sSFR(t) and $M_*(t)$, instead of a single value for each model parameter which produces a model evolutionary track with a single line. The two models with exponentially declining SFH are: (a) model with parameter

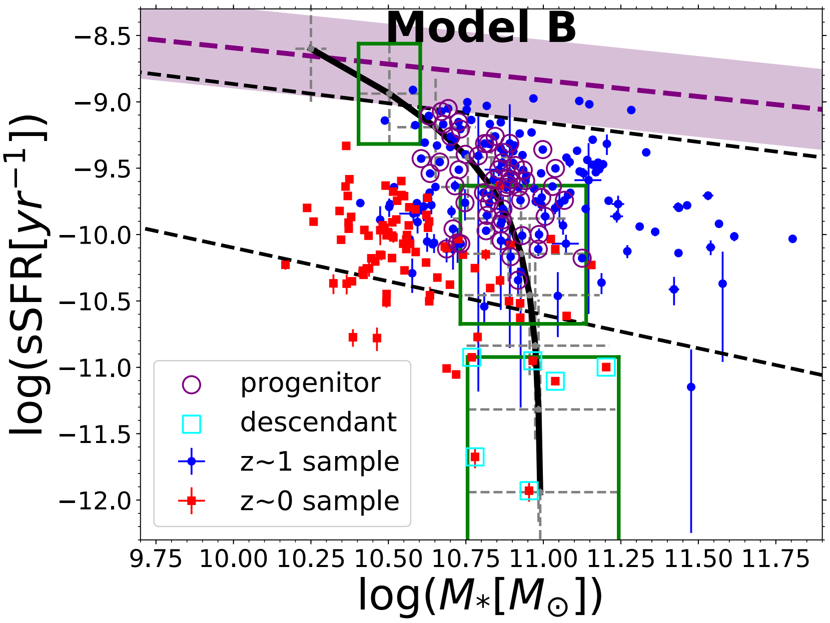

Figure 6.3: Connecting the $z \sim 1$ and $z \sim 0$ samples using a model evolutionary track assuming an exponentially declining SFH with $10.2 \leqslant \log(M_*(t_0)/M_\odot) \leqslant 10.3$, $-8.7 \leqslant \log(\mathrm{sSFR}(t_0)/\mathrm{yr}^{-1}) \leqslant -8.5$, and $1.3\mathrm{Gyr} \leqslant \tau \leqslant 2.5\mathrm{Gyr}$ (which is called model B) on the global sSFR versus M_* plane. Usage of symbols is the same as in Fig. 6.2. This figure is taken from Abdurro'uf and Akiyama (2018).

ranges of $\log(M_*(t_0)) = [9.7 : 9.9]$, $\log(\mathrm{sSFR}(t_0)) = [-8.6 : -8.4]$ and $\tau = [4.0 : 6.0]$, hereafter called model A; and (b) model with $\log(M_*(t_0)) = [10.2 : 10.3]$, $\log(\mathrm{sSFR}(t_0)) = [-8.7 : -8.5]$ and $\tau = [1.3 : 2.5]$, hereafter called model B. The M_*, sSFR and τ are in unit of $M_\odot$, yr^{-1} and Gyr, respectively. The third model, which is called model C, only connects galaxies in the M_* range of $10.85 \leqslant \log(M_*/M_\odot) \leqslant 11.2$ and without assuming any assumption on the SFH.

Fig. 6.2, 6.3, and 6.4 show the model evolutionary tracks and selected progenitors and descendants using model A, model B, and model C, respectively. In Fig. 6.2 and 6.3, black line represents model evolutionary track if middle values of the model parameters are assumed. Vertical and horizontal 'errorbars' shown with gray dashed lines represent the ranges of sSFR and M_* (at redshift step of 0.2) if the model parameter ranges are considered. The vertical 'errorbars' are extended by 0.3 dex above and below from the actual length to roughly mimic the scatter around the global SFMS, which is expected to be able to account for the fluctuations of a real galaxy evolutionary path from the simple exponentially decaying form, while the horizontal 'errorbars' are kept in the original length. The extension for the vertical 'errorbar' also intended to take into account the higher estimated uncertainty of SFR compared to the estimated uncertainty of M_* of the sample galaxies. Purple open circles and cyan open squares represent progenitors and descendants galaxies, respectively. The progenitors (descendants) galaxies are defined as galaxies in the $z \sim 1$ ($z \sim 0$) samples that are fall within the sSFR(t) and $M_*(t)$ ranges (which form a 'box') given by the vertical and horizontal 'errorbars', evaluated at the redshifts of the galaxies, i.e. t is age of the universe at $z = 2$. Three

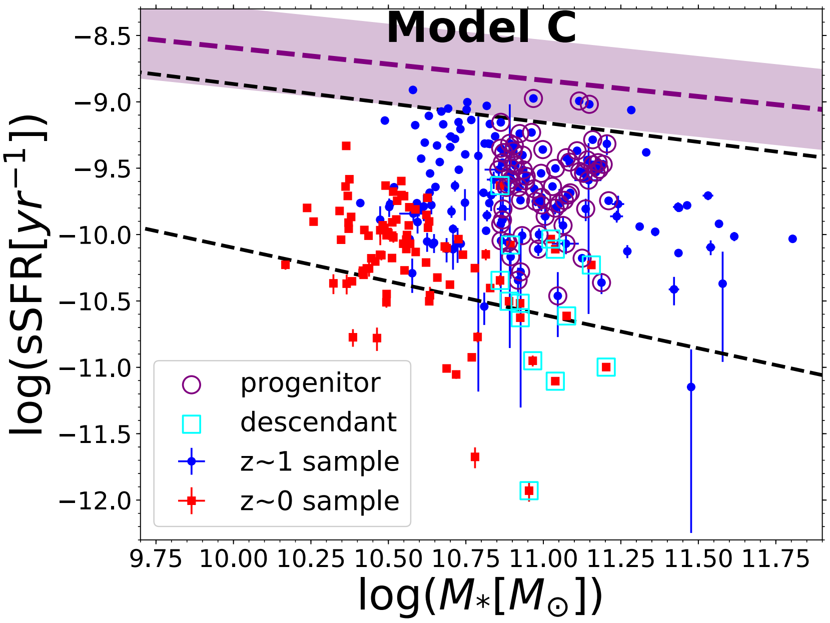

Figure 6.4: Connecting the $z \sim 1$ and $z \sim 0$ samples without assuming an evolutionary tracks, instead only M_* range is assumed, i.e. model C. The selected progenitors and descendants are shown by the purple open circles and cyan open squares, respectively. This figure is taken from Abdurro'uf and Akiyama (2018).

green boxes show examples of the sSFR(t) and $M_*(t)$ ranges calculated at $z = 1.8$, 0.8, and 0. The purple dashed line and purple shaded region represent the global SFMS relation at $z = 2$ and ±0.3 dex scatter around it, respectively. The black dashed-lines represent the global SFMS relations at $z = 1.2$ and $z = 0.015$. In Fig. 6.4, progenitor and descendant galaxies, which are defined by assuming a M_* range, are shown by the purple open circles and cyan open squares, respectively. Number of progenitors (descendants) selected using the model A, B and C are 20 (14), 57 (6) and 71 (14), respectively. As expected from the larger value of τ, the sSFR of model A decline more slowly compared to that of model B.

6.3 Empirical model for the evolution of the $\Sigma_*(r)$, $\Sigma_{\rm SFR}(r)$, and sSFR(r) radial profiles at $0 \lesssim z \lesssim 1$

In order to quantitatively examine the structural evolution of the massive disk galaxies from $z \sim 1$ to $z \sim 0$, we try to construct an empirical model for the evolution of the $\Sigma_*(r)$, $\Sigma_{\rm SFR}(r)$, and sSFR(r) radial profiles. First, average $\Sigma_*(r)$, $\Sigma_{\rm SFR}(r)$, and sSFR(r) radial profiles of the progenitors and descendants galaxies selected using each of the three model evolutionary paths (model A, B, and C, see Section 6.2) are derived. Fig. 6.5 shows the average $\Sigma_{\rm SFR}(r)$ (left column), $\Sigma_*(r)$ (middle column), and sSFR(r) (right column) of the progenitors (shown by blue circles with solid line) and descendants (shown by red open squares with dashed line) selected using the model evolutionary paths of the model A (first row), B (second row), and C (third row). The average $\Sigma_{\rm SFR}(r)$ and sSFR(r) of the progenitors and descendants galaxies selected with all of the three models suggest a declining star formation rate over the entire region of the galaxies from $z \sim 1$ to $z \sim 0$ with larger decline of star formation rate in the central region compared to that in the outskirt. This evolutionary trend shows a progression of quenching process in the galaxy that propagates from the central region to the outskirt, agrees with the inside-out quenching scenario. The average $\Sigma_*(r)$ of the progenitors and descendants galaxies selected with the evolutionary path of the model A and B show larger increase of the Σ_* toward the outskirt from $z \sim 1$ to $z \sim 0$, which shows buildup of stellar mass in the disks and indicates an inside-out growth trend. The Σ_* increase is larger (over entire radii) for the progenitors and descendants pair with model A compared to that with model B as expected by the larger τ of the SFH assumed for the model A than that assumed for the model B. The average $\Sigma_*(r)$ of the progenitors and descendants selected with model C, which does not assume any SFH formalism and only assume M_* range, does not show stellar mass buildup over the entire radii from $z \sim 1$ to $z \sim 0$.

Next, radial profile of the SFH is estimated in order to quantitatively infer the evolution of the $\Sigma_{\rm SFR}(r)$, $\Sigma_*(r)$, and sSFR(r). Here, we assume exponentially declining SFH at each radius as follows

$$\Sigma_{\rm SFR}(r,t) = \Sigma_{\rm SFR}(r,t_0)e^{-\Delta t/\tau(r)} \tag{6.3}$$

where $t = t_0 + \Delta t$ with t_0 is the age of the universe at the median redshift of the progenitors. The median redshift of the selected progenitors (descendants) using the evolutionary paths of the model A, B and C are 1.064 ± 0.026 (0.016 ± 0.001), 1.133 ± 0.043 (0.017 ± 0.002) and 1.216 ± 0.044 (0.017 ± 0.002), respectively. The uncertainty of the median redshift, which is calculated using bootstrap resampling method, is used in later analysis for calculating the uncertainty of model properties, such as radial profile of SFH, $\Sigma_*(r)$ and sSFR(r).

Based on the average $\Sigma_{\rm SFR}(r)$ of the progenitors and descendants and using the SFH form of Eq. 6.3 with Δt as the time difference between the median redshifts of the progenitors and descendants (which are 7.74 ± 0.10, 7.97 ± 0.17 and 8.25 ± 0.12 Gyr for the model A, B and C, respectively), we calculate the τ at each radius, i.e. $\tau(r)$. The $\tau(r)$ of all of the three models are shown in the left column of Fig. 6.6. The $\tau(r)$ of all of the three models are increasing with radius. The black diamonds with errorbars represent the $\tau(r)$ calculated at all the radial points in the average $\Sigma_{\rm SFR}(r)$ in Fig. 6.5. The errorbar at each radius represents the 1σ uncertainty calculated using Monte-Carlo method, which calculates $\tau(r)$ randomly by varying the average $\Sigma_{\rm SFR}(r)$ of the progenitors and descendants and Δt within their uncertainties assuming Gaussian distribution for both parameters. The uncertainty of Δt is calculated using Monte-Carlo method, which calculates Δt randomly by varying the median redshifts of the progenitors and descendants within their uncertainties assuming Gaussian distribution for both of the median redshifts. We then fit the $\tau(r)$ of each model with an exponential function. The red line shows the best-fitting exponential function to the $\tau(r)$, while the

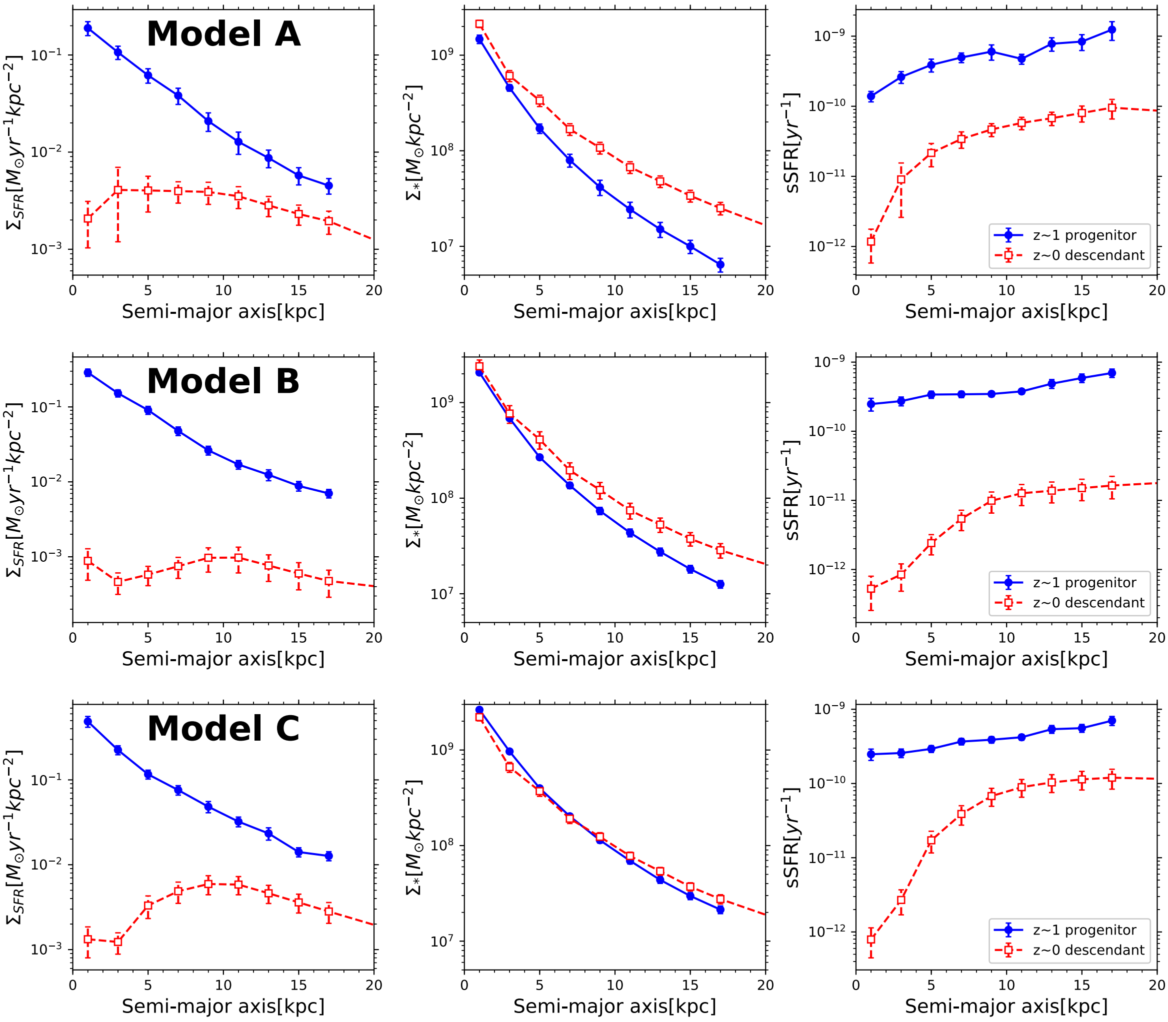

Figure 6.5: Average $\Sigma_{\mathrm{SFR}}(r)$ (left column), $\Sigma_*(r)$ (middle column) and sSFR(r) (right column) radial profiles of the progenitors (shown by the blue circles with solid line) and descendants (shown by the red open squares with dashed line) selected using the evolutionary paths of the model A (first row), B (second row) and C (third row). This figure is taken from Abdurro'uf and Akiyama (2018).

red shaded area around the best-fitting line represents 1σ uncertainty of the best-fitting function. The exponential function fitting is done with Bayesian statistics method.

The middle column in Fig. 6.6 shows the average $\Sigma_*(r)$ of the progenitors (shown by blue circles with solid line) and descendants (shown by red open squares with dashed line), and predicted $\Sigma_*(r)$ at the median redshift of the descendants (shown by black diamonds with solid line) for the model A (first row), B (second row), and C (third row). The right column shows the average sSFR(r) of the progenitors (shown by blue circles with solid line) and descendants (shown by red open squares with dashed line), and predicted sSFR(r) at the median redshift of the descendants (shown by black diamonds with solid line) for the model A (first row), B (second row), and C (third row). The predicted $\Sigma_*(r)$ and sSFR(r) by the model A and B are consistent with the average radial profiles of the descendants, while those of model C show large discrepancy from the average radial profiles of the descendants. Thus, the simple exponentially declining radial SFH model could explain the stellar mass buildup by the star formation in the massive disk galaxies.

Next, we mathematically describe the empirical model for the evolution of the $\Sigma_{\rm SFR}(r)$, $\Sigma_*(r)$ and sSFR(r) radial profiles of massive disk galaxies from $z \sim 1$ to $z \sim 0$. We derive it based on the model A. In order to construct the mathematical prescription, we first fit the average $\Sigma_{\rm SFR}(r)$ and $\Sigma_*(r)$ of the progenitors with an exponential function and Sérsic profile, respectively. The best-fitting profiles are then used for the initial condition (i.e. initial radial profiles, $\Sigma_{\rm SFR}(r, t_0)$ and $\Sigma_*(r, t_0)$) from which the radial profiles at subsequent time is calculated. The best-fitting profiles are as follow

$$\Sigma_{\rm SFR}(r, t_0) = (0.21 \pm 0.03) e^{-r/(4.18 \pm 0.24)}, \tag{6.4}$$

$$\Sigma_*(r, t_0) = (8.43 \times 10^9 \pm 4.43 \times 10^8) e^{-\left(\frac{r}{0.35 \pm 0.02}\right)^{\left(\frac{1}{1.96 \pm 0.03}\right)}}. \tag{6.5}$$

The time scale of the decaying SFH at each radius is determined by an exponential function fitting to the $\tau(r)$ (black diamonds with errorbars in the left panel of first row in the Fig. 6.6) as

$$\tau(r) = (1.66 \pm 0.22) e^{r/(9.32 \pm 2.21)}, \tag{6.6}$$

The best-fitting exponential function is shown in the left panel of the first row in Fig. 6.6 with a red line. The mathematical prescription for the radial profile evolutions are as follows

$$\Sigma_{\rm SFR}(r, t) = \Sigma_{\rm SFR}(r, t_0) e^{-(t - t_0)/\tau(r)}, \tag{6.7}$$

$$\Sigma_*(r, t) = \Sigma_*(r, t_0) + \tau(r) \Sigma_{\rm SFR}(r, t_0) \left(1 - e^{-(t - t_0)/\tau(r)}\right), \tag{6.8}$$

where t_0 and t are the age of the universe at the median redshift of the progenitors and the cosmic time within $0 \lesssim z \lesssim 1$, respectively. Example of the implementation of the above empirical model for the $\Sigma_*(r, t)$ and sSFR(r, t) at $z = 0.8$, 0.6, 0.4 and 0.2 are shown with gray lines in the middle and right panels in the first row of Fig. 6.6.

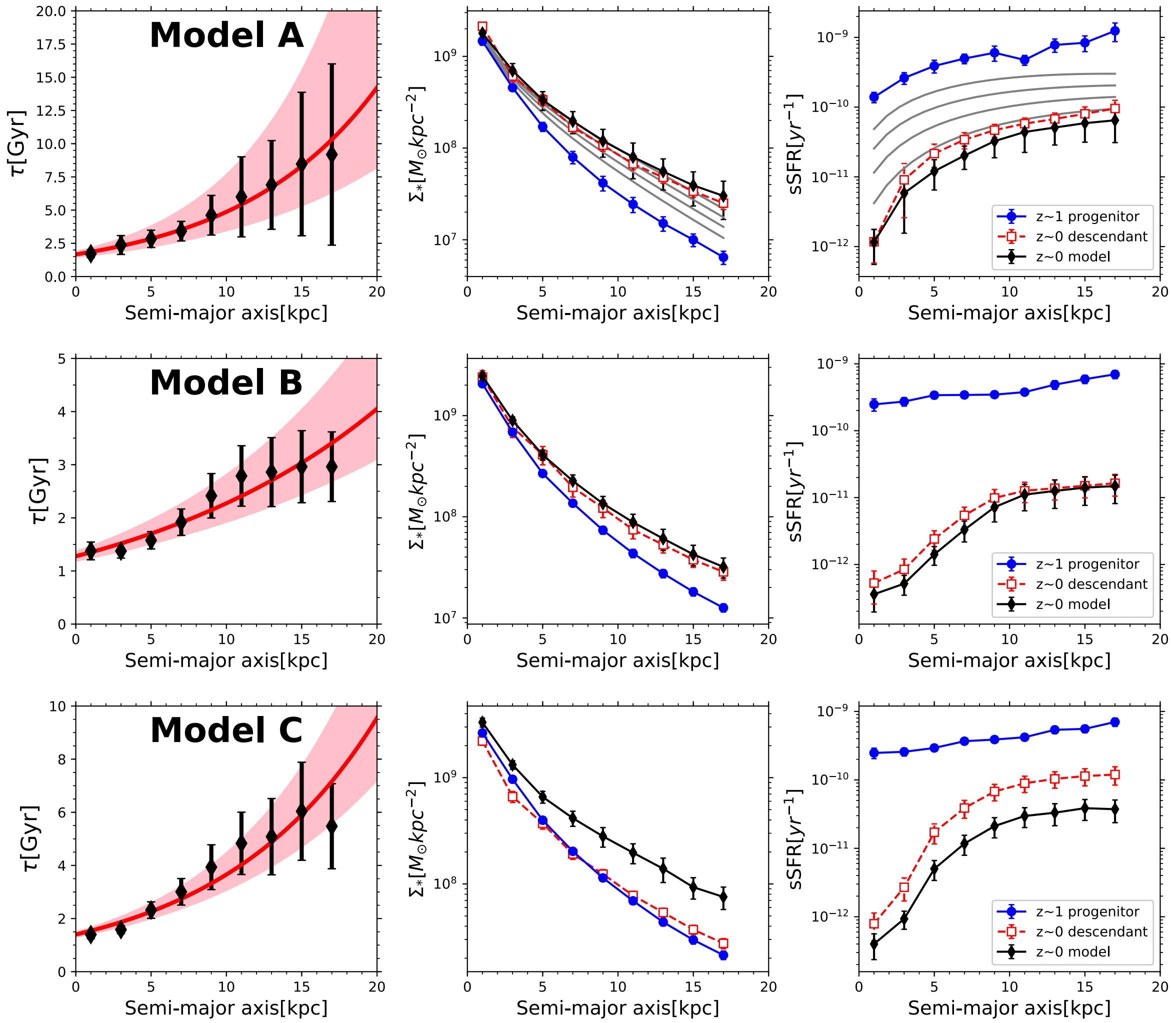

Figure 6.6: Empirical model for the evolution of the $\Sigma_{\rm SFR}(r)$, $\Sigma_*(r)$, and sSFR(r) at $0 \lesssim z \lesssim 1$. In each row from top to bottom, left, middle, and right panels show the radial profile of $\tau(r)$, observed and predicted radial profiles of $\Sigma_*(r)$ at $z \sim 0$, and observed and predicted radial profiles of sSFR(r) at $z \sim 0$. Each row corresponds to different model; first, second, and middle rows show the resulted calculations for model A, B, and C, respectively. The black diamonds with errorbars in the left panel in each row show the $\tau(r)$ for each model, while the red line and red-shaded region around it show the best-fitting exponential function of the $\tau(r)$ and its 1σ uncertainty, respectively. In the middle (right) column, the average $\Sigma_*(r)$ (sSFR(r)) of the progenitors and descendants is shown by the blue circles with solid line and red open squares with dashed line, respectively, while the predicted $\Sigma_*(r)$ (sSFR(r)) at the median redshift of the descendants is shown by black diamonds with solid line. This figure is taken from Abdurro'uf and Akiyama (2018).

The evolution of the $\Sigma_*(r)$ implied by the empirical model shows a buildup of stellar mass gradually in 'inside-to-outside' manner, such that the region located at smaller radius accumulate their stellar mass earlier compared to the region located at larger radius. This trend agrees with the inside-out growth scenario. Evidences for the inside-out stellar mass buildup in the galaxies also observed by previous researchers e.g. van Dokkum et al. (2010); Nelson et al. (2016a); Morishita et al. (2015); Tadaki et al. (2017). The evolution of the sSFR(r) implied by the empirical model shows a gradual quenching process that propagate from the central region toward the outskirt. This trend agrees with the inside-out quenching scenario. Evidences of the inside-out quenching also observed by previous researchers e.g. Tacchella et al. (2015, 2017); González Delgado et al. (2016); Belfiore et al. (2018). However, the discussion on the inside-out growth and inside-out quenching have only been discussed separately as if they are independent phenomenons. Here, we show that the two phenomenons are correlated, such that the inside-to-outside trend of the stellar mass buildup is implication of the earlier quenching of the star formation in region located at smaller radius.

The empirical model implies a steady slow quenching in the disk regions (as will be quantitatively discussed in Section 6.4) and steady stellar mass buildup in the disk with all best represented with exponentially declining SFH over entire radii. This result agrees with the slow quenching scenario of disk galaxies and furthermore gives insights on the spatially resolved process of the slow quenching. As strangulated galaxy (which no longer receive gas accretion and could be regarded as 'closed-box' system) consumed its remaining gas in a rate that best represented by exponentially declining function of time, it is possible that the sample galaxies considered in this research (especially those defined as the progenitors sample) might have been experiencing strangulation during a fraction of their life from $z \sim 1$. However, further investigation (using e.g. observation of spatially resolved gas surface density and gas phase metallicity) is needed to prove it.

Inside-out stellar mass buildup in galaxies has been predicted by many simulations of galaxy formation and evolution (e.g. Kauffmann 1996; Cole et al. 2000; Firmani and Avila-Reese 2000; van den Bosch 2002; Stringer and Benson 2007). Inside-out growth is thought to be a consequence of the dark matter halo properties of the galaxies. Galaxies receive gas accretion from the cosmic web at a rate that determined by the mass of their dark matter halo (e.g. White and Rees 1978; Dekel et al. 2013). The gas cools and fall onto the disk of the galaxy with radial distribution set by the angular momentum distribution of the halo. At any time, the surface density of the accreted gas on the disk is increasing with decreasing radius (Nuza et al. 2018), leading to the inside-out growth. Another key aspect that lead to the inside-out growth is that the global gas accretion into the galaxy have to be significantly stronger at early time but more steady at later time (Chiappini et al. 1997).

Unlike the understanding of the inside-out growth scenario that has been established, the physical mechanism responsible for the inside-out quenching is unclear. Some efforts have been done to address that question. Cosmological zoom-in hydrodynamical simulation by Zolotov et al. (2015) and Tacchella et al. (2016a) suggests that compaction of gas toward the galactic center due to gas-rich merger or smoother gas streams, such as counter-rotating stream, which frequently occur at high redshift for galaxies with $\log(M_*) \sim 10$, could triggers central/nuclear starburst. The nuclear starburst then make large accumulation of stellar mass in the galactic center which then become the central bulge component. The nuclear starburst consume gas rapidly so that the gas in the central region could run out if subsequent gas inflow into the central region is stopped due to e.g. AGN feedback, radiation feedback from the nuclear starburst. Once it happens, onset of the inside-out quenching started which is indicated by central suppression in the radial profiles of gas surface density and sSFR. The subsequent quenching over entire region of the galaxy could be reached by several ways, e.g. due to the suppression of accretion into the galaxy once the host dark matter halo reaches a critical mass ($\sim 10^{12}M_{\odot}$) of the transition from the cold mode accretion to the hot mode accretion (e.g. Birnboim and Dekel 2003; Dekel and Birnboim 2006), and morphological quenching, which is a quenching in the disk region that caused by the stabilization of gas (against collapse) in the disk by the gravitational potential of the bulge (e.g. Martig et al. 2009; Genzel et al. 2014).

6.4 Radial profile of the quenching timescale

In order to quantitatively examine the inside-out quenching process of the sample galaxies, we estimate the quenching timescale at each radius, i.e. radial profile of quenching timescale ($t_{\text{quench}}(r)$), using the empirical model for the evolution of the $\Sigma_{\text{SFR}}(r)$ and $\Sigma_{*}(r)$ derived in the previous section. The quenching timescale at a radius is assumed to be the time needed for the sSFR of the radius ($\Sigma_{\text{SFR}}(r,t)/\Sigma_{*}(r,t)$) to reach a critical value of $10^{-10}yr^{-1}$. The critical sSFR, which corresponds to the mass doubling time of 10 Gyr (larger than the Hubble time at $z \gtrsim 0.5$), is commonly used to separate between star-forming and quiescent galaxies (e.g. Peng et al. 2010) and star-forming and quiescent sub-galactic region (e.g. González Delgado et al. 2016). Fig. 6.7 (the black line) shows $t_{\text{quench}}(r)$ from $z = 1.1$. The 1σ uncertainty associated with the $t_{\text{quench}}(r)$ is shown with the gray shaded area around the line. The 1σ uncertainty is calculated using the Monte-Carlo method which is done by randomly varying all the parameters involved in the calculation ($\Sigma_{\text{SFR}}(r,t0)$, $\Sigma_{*}(r,t0)$ and $\tau(r)$) within their uncertainties by assuming Gaussian distribution, then calculate the standard deviation of t_{quench} at each radius.

The $t_{\text{quench}}(r)$ profile clearly shows the inside-out quenching trend. The $t_{\text{quench}}(r)$ shows that the central regions ($r \sim 1$ kpc) will be quenched by ~ 200 Myr from $z = 1.1$, while the outskirt ($r \sim 15$ kpc) will be quenched by ~ 5.2 Gyr from $z = 1.1$. We compare the $t_{\text{quench}}(r)$ from this work with the radial quenching timescale of massive ($10.8 \leqslant \log(M_{*}/M_{\odot}) < 11.7$) star-forming galaxies at $z \sim 2$ reported by Tacchella et al. (2015) (shown by the blue profile) which has been subtracted by the cosmic time interval between $z = 1.1$ and $z = 2.2$. The model A from which the empirical model is derived has an initial mass at $z = 2$ of $9.7 \leqslant \log(M_{*}/M_{\odot}) \leqslant 9.9$, while the progenitor galaxies selected using this model have $10.5 < \log(M_{*}/M_{\odot}) < 10.9$ at $z \sim 1.1$. Thus, the $t_{\text{quench}}(r)$ from this work could be thought as the radial profile of quenching timescale of galaxies with smaller M_{*} compared to those of the sample galaxies considered in Tacchella et al. (2015). The $t_{\text{quench}}(r)$ profile of Tacchella et al. (2015) is derived based on the average $\Sigma_{*}(r)$ and $\Sigma_{\text{SFR}}(r)$ of massive galaxies at $z \sim 2$ and the average $\Sigma_{*}(r)$ of early-type galaxies with the similar mass at $z \sim 0$. By assuming

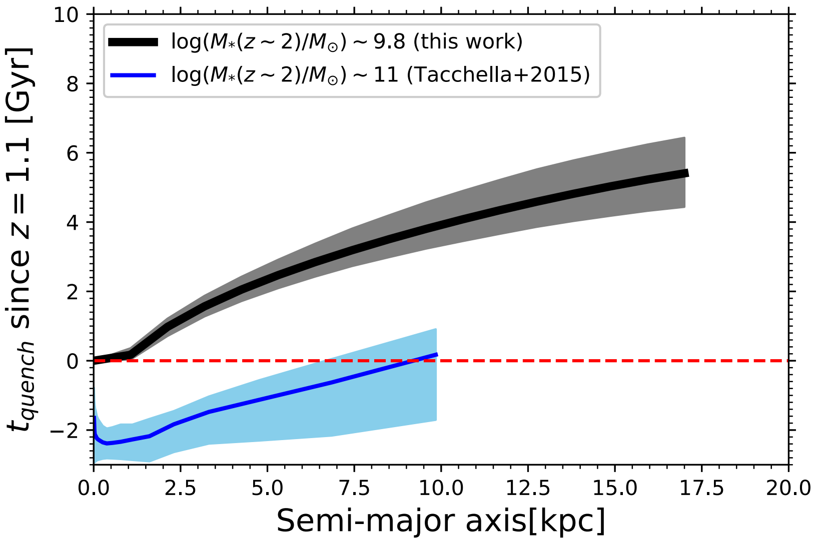

Figure 6.7: Radial profile of the quenching timescale ($t_{\rm quench}(r)$) from the age of the universe at $z = 1.1$ estimated using the empirical model. Negative time corresponds to the cosmic time at $z > 1.1$. The black line represents $t_{\rm quench}(r)$ obtained from this work for $10.5 < \log(M_*/M_\odot) < 10.9$ galaxies at $z = 1.1$, which corresponds to the low-mass galaxies ($9.7 \lesssim \log(M_*/M_\odot) \lesssim 9.9$) at $z = 2$ (according to model A, see Section 6.2). The blue line represents $t_{\rm quench}(r)$ profile reported by Tacchella et al. (2015) for massive galaxies, with stellar mass range of $10.8 \leqslant \log(M_*/M_\odot) < 11.7$ at $z \sim 2$. This figure is taken from Abdurro'uf and Akiyama (2018).

that the $z \sim 2$ galaxies keep forming stars with their observed $\Sigma_{\rm SFR}(r)$, they estimated the time needed for each radius to stop their star formation in order not to overshoot the $\Sigma_*(r)$ of the $z \sim 0$ galaxies. By the calculation, they shown that the integrated SFR at any given time follows that of the typical main-sequence galaxies.

The blue profile shows the inside-out quenching trend of the $z \sim 2$ massive star-forming galaxies, which tend to be quenched in their central region since $z \sim 2$, and are fully quenched in their entire regions by $z \sim 1$. The figure shows that the $t_{\rm quench}(r)$ of low mass (this work) is higher (i.e. later) than that of the massive galaxies (Tacchella et al. 2015), while their slopes are similar. These trends suggest that more massive galaxies tend to quench their entire regions earlier than less massive galaxies. This result agrees with the 'downsizing' scenario (e.g. Cowie et al. 1996; Juneau et al. 2005) and furthermore suggests that the 'downsizing' phenomenon appear even in the spatial scale within a galaxy. By using the integral field spectroscopy data for deriving the spatially resolved stellar mass assembly history in local galaxies, Pérez et al. (2013) and Ibarra-Medel et al. (2016) also found the indication that the 'downsizing' phenomenon is spatially preserved within galaxies. They found that the stellar mass assembly of massive galaxies is faster than that of low mass galaxies in both inner and outer regions.

6.5 Reproduction of the observed evolutionary trend of spatially resolved SFMS by the evolutionary empirical model

In order to check the consistency between the empirical model derived previously and the spatially resolved SFMS at $z \sim 0$ and $z \sim 1$, and furthermore get insights on the evolution of the spatially resolved SFMS, we construct spatially resolved SFMS relations from the empirical model of $\Sigma_{\rm SFR}(r,t)$ and $\Sigma_{*}(r,t)$. Fig. 6.8 (black circles) shows the spatially resolved SFMS relations at redshift interval of 0.11 between $0 \leqslant z \leqslant 1.1$ constructed from the empirical model. The spatially resolved SFMS relations constructed from the empirical model are best-fitted with second order polynomial function. The best-fitting second order polynomial functions are shown by the red lines. The spatially resolved SFMS relations at $z = 1.1$ and $z = 0$ constructed from the empirical model are consistent with the observed spatially resolved SFMS relation at $z \sim 1$ (that of the z1-ΔMS2; shown by the blue triangles) and at $z \sim 0$ (that of the z0-ΔMS2; shown by the green squares), respectively. The spatially resolved SFMS relations at $z = 1.1$ and $z = 0$ constructed with the empirical model are compared with the observed spatially resolved SFMS relations of the z1-ΔMS2 and z0-ΔMS2 because majority of progenitors and descendant galaxies with which the empirical model is derived are belong to those two groups.

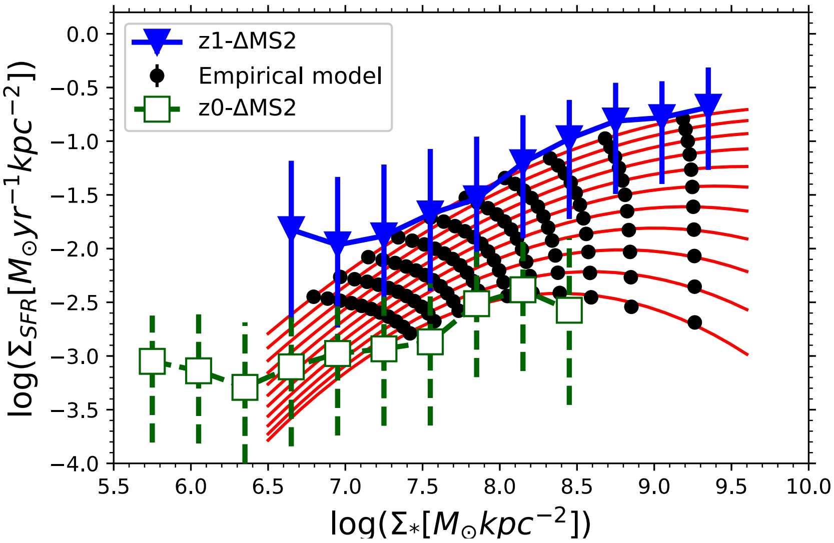

Figure 6.8: Evolution of the spatially resolved SFMS relation at $0 \lesssim z \lesssim 1$ inferred by the empirical model of the $\Sigma_{\rm SFR}(r,t)$ and $\Sigma_{*}(r,t)$ radial profiles. The black circles show the spatially resolved SFMS relations at 0.11 redshift steps between $z = 0$ and $z = 1.1$ constructed from the empirical model. The best-fitting second order polynomial functions to the constructed spatially resolved SFMS relations are shown by the red lines. The blue triangles with solid line and green squares with dashed line represent observed spatially resolved SFMS of z1-ΔMS2 and z0-ΔMS2, respectively. This figure is taken from Abdurro'uf and Akiyama (2018).

Chapter 7

Summary and future prospects

7.1 Summary

In this thesis, we have studied the spatially resolved (at the ~ 1 kpc-scale) distributions of SFR and M_* in massive ($\log(M_*/M_\odot) > 10.5$) face-on disk galaxies at $0.01 < z < 0.02$ and $0.8 < z < 1.8$. We derived the spatially resolved SFR and M_* in a galaxy by using the spatially resolved SED fitting technique, namely pixel-to-pixel SED fitting, which fit the spatially resolved SED of the galaxy with a set of model SEDs using Bayesian statistics approach. The spatially resolved SEDs (with rest-frame FUV to NIR) of a galaxy at $0.01 < z < 0.02$ are constructed using imaging data-sets from GALEX and SDSS, while those for a galaxy at $0.8 < z < 1.8$ are constructed using imaging data-set from CANDELS and 3D-HST. For simplicity, we call the $0.01 < z < 0.02$ as $z \sim 0$ and $0.8 < z < 1.8$ as $z \sim 1$.

Our results can be summarized as follows:

1. Global star formation main sequence (SFMS) is preserved at the kpc-scale within galaxies. It is evidenced from the existences of the $\Sigma_{\rm SFR}$-Σ_* relation, which is called spatially resolved star formation main sequence, in the galaxies at $z \sim 0$ and $z \sim 1$. This relation implies a universality of the star formation process at various scales.
2. The running mode values of the spatially resolved SFMS show linear trend with slope nearly unity at low Σ_* and flattened at high Σ_* end, except in the star-forming galaxies (which lie within ±0.3 dex from the global SFMS) at $z \sim 1$, where the spatially resolved SFMS show linear trend with slope of nearly unity over entire Σ_* range.
3. Evolutionary trend of the spatially resolved SFMS show decreasing sSFR over entire Σ_* range with decreasing redshift. Larger sSFR decrease shown at high Σ_* region than at low Σ_* region. The larger sSFR decrease at high Σ_* region results in increasing prominence of the 'flattening' at high Σ_* end.

4. Contributions toward the scatter in the spatially resolved SFMS are at least come from these three factors: (a) global sSFR. Normalization of the spatially resolved SFMS is determined by the global sSFR, in the sense that galaxies with lower global sSFR have spatially resolved SFMS with systematically lower normalization compared to those of galaxies with higher global sSFR; (b) local variation of sSFR. Sub-galactic regions with higher sSFR than the mean spatially resolved SFMS relation (in individual galaxy) are located in the spiral arms or knots of star formation; (c) global M_*. Galaxies with higher global M_* have spatially resolved SFMS with systematically lower normalization compared to those of galaxies with lower global M_*.

5. On average, SFR surface density radial profiles ($\Sigma_{\rm SFR}(r)$) of massive disk galaxies at $z \sim 0$ are centrally peaked. However, a significant fraction of the galaxies have centrally suppressed $\Sigma_{\rm SFR}(r)$, despite increasing trend toward smaller radius still shown in their outskirts. Majority of those galaxies with centrally suppressed $\Sigma_{\rm SFR}(r)$ are barred galaxies. On average, sSFR radial profiles of massive disk galaxies at $z \sim 0$ are centrally suppressed with roughly flat in the outskirt, agrees with the inside-out quenching scenario.

6. Normalized average $\Sigma_{\rm SFR}(r)$ is more extended compared to the normalized average $\Sigma_*(r)$ and effective radius of the spatial distribution of $\Sigma_{\rm SFR}$ is larger than effective radius of the spatial distribution of Σ_* for almost all the sample galaxies at $z \sim 0$. This trend implies the inside-out growth trend.

7. Average sSFR radial profile (sSFR(r)) of more massive galaxies is lower over entire radii than average sSFR(r) of less massive galaxies. This trend is found in both redshifts, $z \sim 0$ and $z \sim 1$. This trend suggests that the 'downsizing' signal is spatially preserved within galaxies, i.e. spatially resolved downsizing.

8. On average, sSFR(r) of galaxies with lower global sSFR are lower over entire radii compared to the sSFR(r) of galaxies with higher global sSFR. This trend is hold at both redshifts, $z \sim 0$ and $z \sim 1$. While sSFR(r) of all galaxies in the $z \sim 0$ sample are centrally suppressed, the sSFR(r) of galaxies in the $z \sim 1$ sample are varies. The average sSFR(r) of star-forming galaxies (which reside within the scatter of the global SFMS) at $z \sim 1$ is flat over entire radii, while the average sSFR(r) of green-valley galaxies (which reside within -0.8 to -0.3 dex from the global SFMS) is centrally suppressed, and sharper central suppression is observed for the average sSFR(r) of quiescent galaxies (which reside below -0.8 dex from the global SFMS). This trend indicates an onset of the inside-out quenching as galaxies move from being star-forming to green-valley phase.

9. By connecting the $z \sim 1$ and $z \sim 0$ samples through selecting pairs of possible progenitor and descendant from the two samples, we derived empirical model for the evolution of the surface density radial profiles, i.e. $\Sigma_{\rm SFR}(r)$, $\Sigma_*(r)$, and sSFR(r). The empirical model is derived based on the average $\Sigma_{\rm SFR}(r)$ of the progenitors and descendants by assuming exponentially declining star formation history (SFH) at each radius. The empirical model could reproduce

the observed $\Sigma_*(r)$ and sSFR(r) at $z \sim 0$, and also consistent with the spatially resolved SFMS at $z \sim 1$ and $z \sim 0$.

10. The evolution of the $\Sigma_{\rm SFR}(r)$ and sSFR(r) suggested by the empirical model show sharper decrease in the central region compared to that in the outskirt, implying inside-out quenching process. The evolution of the $\Sigma_*(r)$ show gradual stellar mass buildup that propagates toward the outskirt, i.e. inside-out stellar mass buildup. The sSFR decrease in the outskirt indicates slow steady quenching in the disk region. Moreover, the goodness of the radial exponentially declining SFH to fit the evolution of the surface density radial profiles implies a steady processes of gas consumption through star formation. This result consistent with a picture of slow quenching in disk galaxies and indicates that strangulation might work on the galaxy during the slow quenching process.

11. Using the empirical model for the evolution of the sSFR(r), we quantitatively examine the inside-out quenching process by estimating a time needed for the sub-galactic regions in each radius in the galaxy to quench, i.e. radial quenching time-scale ($t_{\rm quench}(r)$). The $t_{\rm quench}(r)$ is estimated by assuming a critical sSFR$= 10^{-10}$yr^{-1} below which sub-galactic region is regarded as quenched. The $t_{\rm quench}(r)$ is increasing with radius.

7.2 Future prospects

Here we highlight some possible future extensions from this research.

1. **Tracing radially resolved gas accretion history into massive disk galaxies over the last 10 Gyrs**

   The empirical model for the evolution of the surface density radial profiles ($\Sigma_{\rm SFR}(r)$, $\Sigma_*(r)$, and sSFR(r)) derived in Section 6.3 suggests a steady stellar mass buildup by star formation activity in the disk and gradual inside-out quenching process. The steady stellar mass buildup in the disk requires a steady gas accretion from outside of the halo into the galaxy, while the exponentially declining star formation history, which seems to work well in reproducing the history of star formation activity in the entire region of the galaxies, implies a decreasing rate of gas inflow into the galaxies. The empirical model provides a unique tool for probing the history of gas accretion into the galaxies. By combining the empirical model with the metal enrichment (including gas phase and stellar metallicities) model, the history of gas accretion into the galaxies and metal enrichment in the interstellar medium could be traced. This modeling could give insights on the understanding of the physical interplay among the gas inflow, galaxy growth by star formation, and metal enrichment in the interstellar medium of the galaxy.

   Gas regulator modeling, such as done by Peng and Maiolino (2014) could be used. The gas regulator modeling incorporates gas accretion rate into the dark matter halo based on the best-fitting function to the dark matter halo merger history which is obtained from the cosmological simulation (e.g. Faucher-Giguère et al. 2011; Dekel and Mandelker 2014). In order to trace the radially resolved gas accretion history into massive disk galaxies, the gas regulator modeling which commonly applied at global galaxy scale should be brought into the radially-resolved fashion. The evolution of the $\Sigma_{\rm SFR}(r)$ and $\Sigma_{*}(r)$ inferred by the empirical model serve as the observational constraint for the radially-resolved gas regulator modeling. Other observational constraints associated with boundary conditions (initial and final states) also needed to assist the semi-analytical modeling. Initial gas surface density radial profile at $z \sim 1$ could be obtained from the spatially resolved distribution of CO emission observed with *Atacama Large Millimeter/submillimeter Array* (ALMA). Initial gas phase metallicity radial profile at $z \sim 1$ could be adopted from the observed gas phase metallicity gradient at $z \sim 1$ reported in the literature (e.g. Wang et al. 2017; Jones et al. 2010). Observed radial profiles of gas phase metallicity at $z \sim 0$ from MaNGA data-set and gas density radial profiles at $z \sim 0$ obtained from the *The HERA CO Line Extragalactic Survey* (*HERACLES;* Leroy et al. 2009) and *The HI Nearby Galaxy Survey* (*THINGS;* Walter et al. 2008) data-sets could be used as additional constraints.

Goals of this radially-resolved gas regulator modeling is to reproduce all of the observational constraints (the radial profiles of gas phase metallicity at $z \sim 0$ and $z \sim 1$ and the empirical model for the evolution of the $\Sigma_{\rm SFR}(r)$ and $\Sigma_{*}(r)$) by adjusting the time evolution of the radially-resolved gas accretion rate into the galaxy. The obtained results will give insights on the radially-resolved gas accretion history into the galaxy and the interplay among the gas inflow, star formation activity and metal enrichment in the galaxies for the last 10 Gyrs. Moreover, we could investigate the role of the strangulation on the galaxy quenching.

2. **Investigation of the blue nugget phase in the high redshift galaxies to get insights on the onset of the inside-out quenching and bulge formation**

   The trend shown by the average sSFR(r) of the z1-ΔMS1, z1-ΔMS2, and z1-ΔMS3 (as discussed in Section 5.2.3) suggests the onset of the inside-out quenching process in massive disk galaxies at $z \sim 1$. In order to understand the physical mechanism that triggers the start of the inside-out quenching and test whether the gas compaction scenario (as suggested by (Zolotov et al. 2015; Tacchella et al. 2016a)) is really happen and responsible for it, information regarding the spatially resolved distributions of the molecular gas and FIR dust continuum (tracer for dusty star formation activity) are needed. High spatial resolution imaging of CO emission and FIR dust continuum could be obtained with ALMA. Information on the dynamics of gas also important for this study. It could be obtained using integral field spectroscopy (IFS) observation. Target galaxies could be selected from the galaxies with high possibility being experiencing a gas compaction event (i.e. blue nugget phase), post blue nugget phase, and centrally-quenched phase as some of them shown in Fig. 5.9, Fig. 5.10, and Fig. 5.11. It is also important to enlarge the current sample by considering low-mass galaxies

($\log(M_*/M_\odot) \leqslant 10.5$) in order to further investigate characteristics of the gas compaction event. If this blue nugget phase is happen in general population of galaxies, it must play an important role in the evolution of galaxies. If so, it is important to investigate the characteristic global properties in which galaxies experience blue nugget phase, e.g. characteristic M_*, sSFR, and age. In order to do that, similar analysis using the pixel-to-pixel SED fitting method could be used to derive the spatially resolved distributions of the SFR and M_* of large number of galaxies with $\log(M_*/M_\odot) > 9.5$ at $0.8 < z < 2.0$ which are located in the five fields, GOODS-S, GOODS-N, UDS, COSMOS, and AEGIS. Then based on the sSFR(r), galaxies with high probability being in the blue nugget, post blue nugget, and centrally-quenched phases could be selected for further followup study.

3. **Investigation of the physical mechanism of the 'mass quenching' and 'environmental quenching'**

   In order to understand how the quenching process promoted by local galaxy environment and global stellar mass, information on the spatially resolved SFR, M_*, and sSFR of large number of galaxies over wide area (such that various local galaxy number density, from low- to high density, are covered) at the local universe and high redshift is needed. Similar analysis using the pixel-to-pixel SED fitting as we do in the research for this thesis could be done to obtain the spatially resolved SFR, M_*, and sSFR of large number of galaxies over wide area and redshift range. For the local galaxies, the five bands imaging data-set from SDSS could be used. With wide area covered by the SDSS survey, purpose of this research could be achieved. In order to study the effect of local galaxy environment and stellar mass on the quenching process, wide stellar mass range (such as $9.5 < \log(M_*/M_\odot) < 11.5$) should be considered in selecting the sample galaxies, then galaxies in each bin of stellar mass and local galaxy number density are analyzed for their $\Sigma_{\rm SFR}(r)$, $\Sigma_*(r)$, and sSFR(r) radial profiles. In order to trace back the progress made by the 'environmental quenching' and 'mass quenching' and bring the analysis into cosmological context, similar analysis should be done for galaxies at high redshift, such as $0.8 < z < 1.8$. This analysis could be done using the upcoming data-sets from large imaging and spectroscopic surveys, such as The Large Synoptic Survey Telescope (LSST), Euclid, and Wide Field Infrared Survey Telescope (WFIRST). Having maps of the spatially resolved stellar population properties of large number of galaxies across wide redshift range ($z < 1.8$), we could statistically study the physical mechanisms of the 'mass quenching' and 'environmental quenching'. The problems that will be addressed in this research are part of the classical problems in the study of galaxy evolution, which is related to the effects of 'Nature' versus 'Nurture' in galaxy evolution. Thus, by using this research, insights on this classical problems could be obtained.

4. **Study of the stellar mass buildup and quenching in galaxies from cosmic noon to the present day**

The optical to NIR light of galaxies at $z \gtrsim 2$ is redshifted beyond the HST limit ($\lambda \sim 1.6\mu m$). With the launch of the *James Webb Space Telescope* (JWST), similar analysis using the pixel-to-pixel SED fitting as has been done in the research for this thesis could be done for galaxies around the cosmic noon epoch ($2 \lesssim z \lesssim 3$). Multiband imaging data from the NIRCam/JWST could be combined with the multiband imaging data from the HST to increase the wavelength sampling in the spatially resolved SED of the galaxies thereby increasing constraint on the SED fitting process. The combination of the imaging data from the HST and NIRCam/JWST covers rest-frame FUV to NIR for galaxies at $1.8 < z < 3.8$, which is similar as the rest-frame wavelength coverage provided by the GALEX+SDSS for galaxies at $0.01 < z < 0.02$ and CANDELS+3D-HST for galaxies at $0.8 < z < 1.8$ that is analyzed in this thesis. PSF size of the combined HST+NIRCam imaging ($0.19''$) corresponds to the physical scale of $\sim 0.6 - 0.8$ kpc at the $1.8 < z < 3.8$, which is similar as the physical spatial resolution achieved in the analysis of this thesis. The similar rest-frame wavelength coverage and spatial resolution that could be achieved by this prospected research and those achieved in the analysis in this thesis make this prospected research as important extension of this thesis. With this research, we could study the stellar mass buildup and quenching in the galaxies around the epoch when the cosmic star formation history shows turns around from increasing SFR to decreasing SFR. It is expected that at this epoch we will see first quiescent galaxy and first bulge formation.

Appendix A

Reliability of the pixel-to-pixel SED fitting method

A.1 Dust extinction vector of Calzetti et al. (2000) dust extinction law

In order to check reliability of the Calzetti et al. (2000) dust extinction law, we compare the dust extinction vector of the Calzetti et al. (2000) with distribution of the spatially resolved SEDs of the galaxies in the $z \sim 0$ sample on the FUV-NUV versus FUV-u and FUV-NUV versus NUV-u color-color planes. Fig. A.1 shows distribution of the spatially resolved SEDs (in bin space; consisting 4768 bins; shown with gray points) of galaxies in the $z \sim 0$ sample on the color-color planes and the dust extinction vectors of the Calzetti et al. (2000) dust extinction law on the planes (shown with red curves). As a comparison, we also calculate dust extinction vectors of the Milky Way dust extinction law (Seaton 1979; Cardelli et al. 1989) which are shown with green curves. The dust extinction vectors are calculated based on a model SED with $Z = 0.02$, $\tau = 8.6$ Gyr, and age$= 13.75$ Gyr. The model parameters are selected as they are the typical parameters of the best-fitting models with zero dust extinction. It is shown by the figure that the dust extinction vectors by the Calzetti et al. (2000) law could follow the distribution of the observed spatially resolved SEDs better than the Milky Way dust extinction law. The systematically lower reddening effect in the FUV-NUV color of the Milky Way dust law is caused by the bump feature at around 2175Å (near the central wavelength of the NUV band) in the Milky Way dust law. Because the Calzetti et al. (2000) dust law could broadly reproduce the distribution of the observed spatially resolved SEDs on the color-color diagrams, we use this dust extinction law in this research.

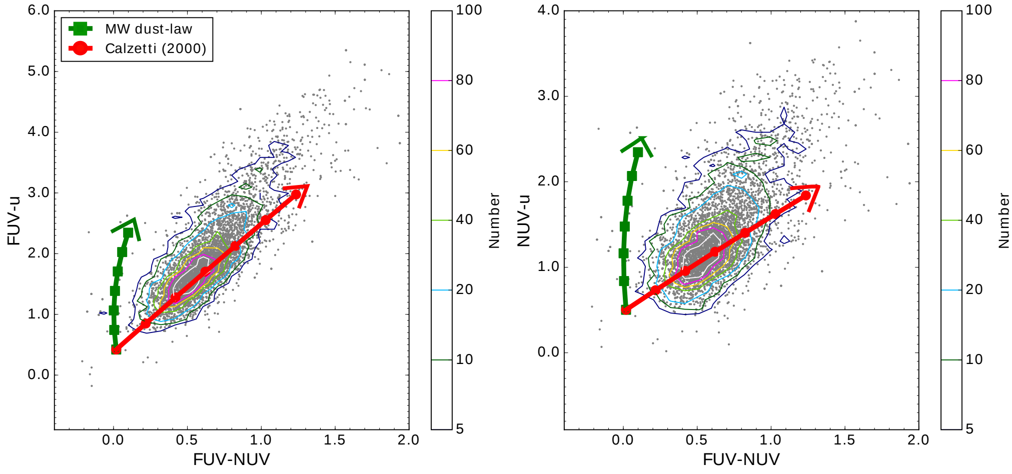

Figure A.1: Comparison between the dust extinction vector of the Calzetti et al. (2000) (shown with red curves) and Milky Way dust extinction law (shown with green curves) on the FUV-NUV vs. FUV-u and FUV-NUV vs. NUV-u color-color planes. The gray points are spatially resolved SEDs of the galaxies in the $z \sim 0$ sample. The contours are color coded by the number of points. This figure is taken from Abdurro'uf and Akiyama (2017).

A.2 Fitting test with mock SEDs: verification of the Bayesian SED fitting with the likelihood adopting the Student's t distribution

Our new method of the Bayesian SED fitting with the likelihood following the Student's t distribution form with $\nu = 3$ is verified using SED fitting tests with mock SEDs in addition to the verification with other methods (as will be discussed in later sections). We construct mock SEDs with the following procedures. First, SEDs with random parameters (Z, τ, $E(B-V)$, and age) are selected from a library of model SEDs generated following the procedures discussed in Section 3. The SEDs are sampled with the 7 bands of GALEX and SDSS. A normalization that is randomly selected within a range of 10^7 to 10^{13} is applied to each SED. A random S/N ratio is applied to each SED then uncertainty of the multiband fluxes in the SED is calculated based on the S/N ratio. To simulate the observational effect, we apply random noise, which is obtained by randomly varying the flux around the flux uncertainty following the Gaussian distribution.

We do the SED fitting tests by applying Bayesian SED fitting with 11 different likelihood forms to the mock SEDs. The 11 assumed likelihood forms are: flat (no-weighting), Student's t distribution with $\nu = 0.001, 1, 3, 5, 6, 8, 10, 15, 20$, and Gaussian ($P(\theta|X) \propto \exp(-\chi^2/2)$). Each fitting is done with two different set of model SEDs, one with τ ranging from 0.1 to 10 Gyr and the other with a range of 0.1 to 2 Gyr, to test the stability of the method against the choice of model parameter ranges.

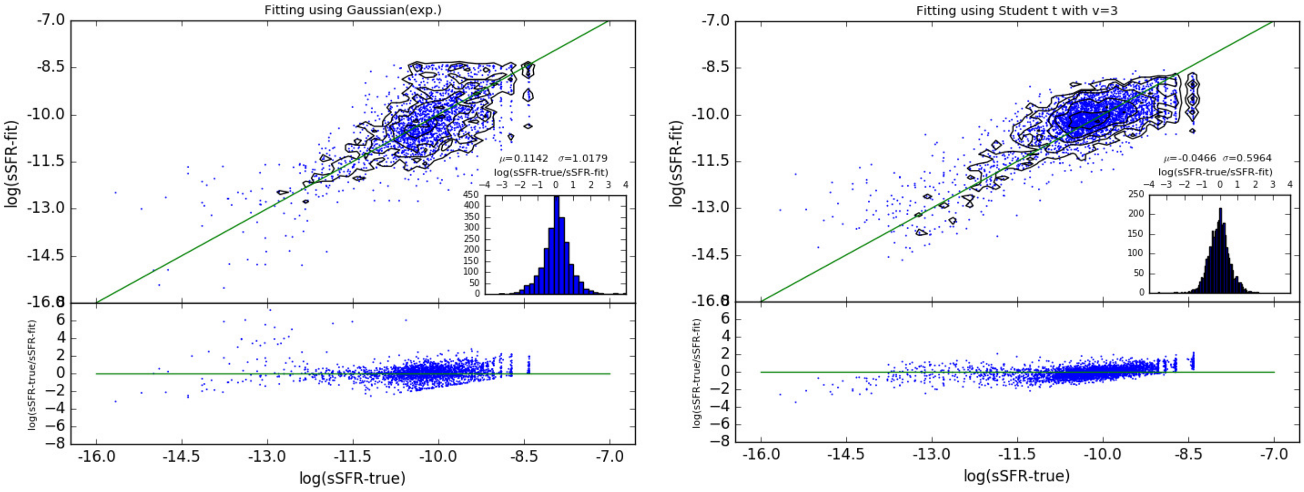

Figure A.2: Example of the fitting test results with mock SEDs that uses Bayesian SED fitting method with likelihood in the forms of Gaussian, i.e. $P(\theta|X) \propto \exp(-\chi^2/2)$ (left panel) and Student's t distribution with $\nu = 3$ (right panel). This figure is taken from Abdurro'uf and Akiyama (2017).

Fig. A.2 shows example of two fitting results (showing $\mathrm{sSFR}_{\mathrm{true}}$ versus $\mathrm{sSFR}_{\mathrm{fit}}$), mock SEDs with τ from 0.1 to 10 Gyr using Bayesian method with likelihood following Gaussian form (left panel) and Student's t distribution with $\nu = 3$ (right panel). Histogram in the inset shows distributions of $\log(\mathrm{SFR}-\mathrm{true}/\mathrm{SFR}-\mathrm{fit})$. The distributions indicate that Bayesian method with likelihood in the form of the Student's t distribution with $\nu = 3$ (which results the $\log(\mathrm{SFR}-\mathrm{true}/\mathrm{SFR}-\mathrm{fit})$ distribution with mean of -0.0466 and scatter of 0.5964) is better than that with Gaussian form likelihood (which results the $\log(\mathrm{SFR}-\mathrm{true}/\mathrm{SFR}-\mathrm{fit})$ distribution with mean of 0.1142 and scatter of 1.0179). A compilation of the results of the fitting test in term of the means and scatters in the resulted $\log(\mathrm{SFR}-\mathrm{true}/\mathrm{SFR}-\mathrm{fit})$ distributions is shown in Fig. A.3. The means and scatters in the resulted $\log(\mathrm{SFR}-\mathrm{true}/\mathrm{SFR}-\mathrm{fit})$ distributions are shown in the left panel and right panel, respectively. In each panel, x-axis show various Bayesian fitting method with ν indicate the ν value of Student's t distribution. The red triangles and yellow pentagons represent fitting results using model SEDs with $\tau = 0.1 - 2.0$ Gyr and $\tau = 0.1 - 10.0$ Gyr, respectively. The Bayesian method with the likelihood following the form of the Student's t distribution with $\nu = 3$ gives the best result compared to the other likelihood forms in the fitting tests.

A.3 Pixel-by-pixel comparison with SFR from 24μm image: case example of the M51 galaxy

In order to check the reliability of the pixel-to-pixel SED fitting method in estimating the spatially resolved SFR, we perform the pixel-to-pixel SED fitting to the M51 galaxy which has 24μm imaging

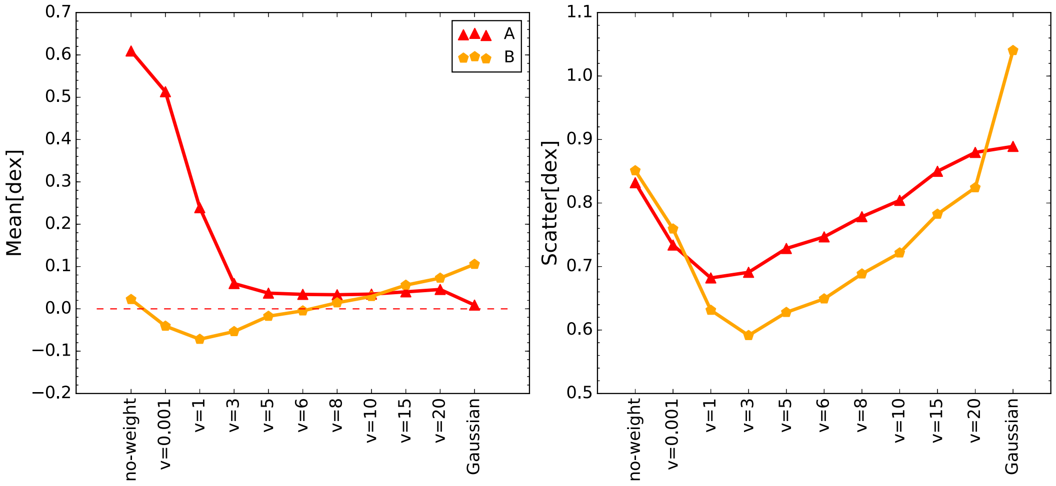

Figure A.3: Compilation of the results of the SED fitting tests showing the means (left panel) and scatters (right panel) of the resulted $\log(\mathrm{SFR}_{\mathrm{true}}/\mathrm{SFR}_{\mathrm{fit}})$ distributions. x-axis in each panel shows various Bayesian SED fiting procedures. Left most point in the x-axis shows the result with flat likelihood, while the right most point shows the result using Gaussian form likelihood. The rest points in the x-axis show results using Student's t form likelihood with various values of ν indicated in the x-axis. This figure is taken from Abdurro'uf and Akiyama (2017).

from the Spitzer Infrared Nearby Galaxies Survey (SINGS) (Kennicutt et al. 2003). The fitting is done only in the central region of the galaxy. Fig. A.4 shows the pixel-to-pixel SED fitting results for this galaxy. Pixel binning result, Σ_* map, and Σ_{SFR} map are shown in the top left panel, bottom left panel, and bottom right panel, respectively. We also put spatially resolved distribution of the 24μm flux in the figure (top right panel) for an immediate comparison with the spatially resolved distribution of the Σ_{SFR}. Spiral arms regions with high 24μm flux are roughly traced in the Σ_{SFR} map, while the discrepancy in the most central region is possibly caused by an AGN activity (some researchers have observed AGN activity in the nuclear region of M51 e.g. Makishima et al. (1990); Querejeta et al. (2016); Brightman et al. (2018)) which could contaminates the SEDs of the central region.

We further check the reliability of the spatially resolved SFR estimation from the pixel-to-pixel SED fitting by comparing it with the spatially resolved SFR derived from the 24μm image. The conversion from 24μm flux to the SFR is based on Rieke et al. (2009) prescription. The comparison between the spatially resolved SFR (in bin space) from the pixel-to-pixel SED fitting method and that converted from the 24μm flux is shown in the middle panel of Fig. A.5. In order to get senses on how good is our Bayesian SED fitting method, we also do the comparison using SFR estimation from other SED fitting methods, which are maximum likelihood method (χ^2 minimization; shown in left panel) and Bayesian method with likelihood in the form of Gaussian distribution ($P\theta|X) \propto \exp(-\chi^2/2)$; shown in right panel). It is shown by the figure that the Bayesian method with the likelihood in the form of the Student's t distribution with $\nu = 3$ (which is adopted in the pixel-to-pixel SED fitting) gives the best SFR estimation as evidenced by its smaller scatter from the proportionality

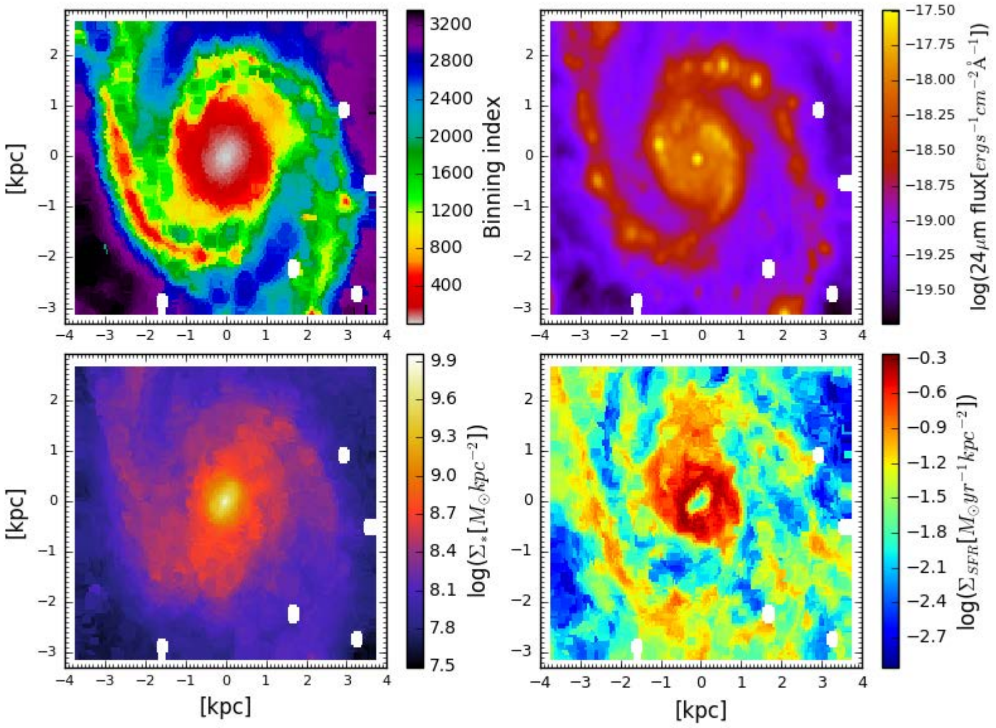

Figure A.4: Pixel-to-pixel SED fitting result for the M51 galaxy. Top left, top right, bottom left, and bottom right panels show pixel binning result, 24μm flux map, Σ_* map, and $\Sigma_{\rm SFR}$ map, respectively. This figure is taken from Abdurro'uf and Akiyama (2017).

line compared to the results from the other methods. The resulted $\log(\mathrm{SFR_{fit}}/\mathrm{SFR_{24\mu m}})$ distribution using our method has scatter (σ) of 0.40 dex and mean value (μ) of -0.31 dex.

A.4 Comparison of the integrated SFR and M_* with the MPA-JHU and 3D-HST catalogs

In order to check reliability of the SFR and M_* from our pixel-to-pixel SED fitting method, in addition to the tests described in the previous sections, we also compare the integrated SFR and M_* from the pixel-to-pixel SED fitting with those taken from the MPA-JHU (for galaxies in the $z \sim 0$ sample) and the 3D-HST (for galaxies in the $z \sim 1$ sample) catalogs. Fig. A.6 shows comparison between the integrated SFR (bottom left panel) and M_* (bottom right panel) derived using the pixel-to-pixel SED fitting ($\mathrm{SFR_{ptpSEDfit}}$) and those taken from the MPA-JHU catalog. The integrated SFR and M_* of a galaxy are derived by summing up of the SFR and m_* of pixels that belong to the galaxy. It is shown by the figure that there are discrepancies between the integrated SFR and M_* from our method with those taken from the MPA-JHU catalog. The integrated SFR from the MPA-JHU catalog is estimated using the H_α emission of the spectrum from central region of the galaxy i.e. within the SDSS fiber diameter (3″) and then extrapolated using resolved color information to

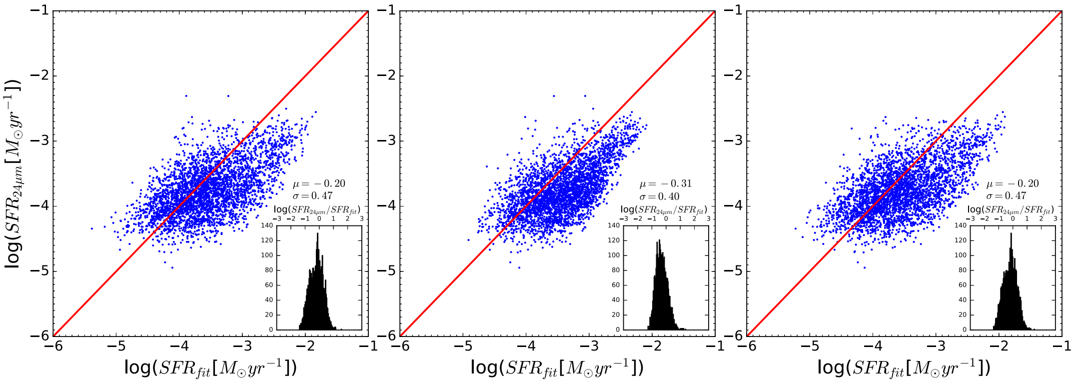

Figure A.5: Comparison among the $\mathrm{SFR}_{24\mu\mathrm{m}}$ versus $\mathrm{SFR}_{\mathrm{fit}}$ from three SED fitting methods: maximum likelihood or χ^2 minimization (left panel), Bayesian SED fitting with likelihood in the form of the Student's t distribution with $\nu = 3$ (middle panel), and Bayesian SED fitting with likelihood in the form of the Gaussian distribution ($(P\theta|X) \propto \exp(-\chi^2/2)$; right panel). This figure is taken from Abdurro'uf and Akiyama (2017).

estimate the total SFR (Brinchmann et al. 2004). The integrated M_* from the MPA-JHU catalog is derived by fitting the integrated (i.e. aperture) FUV-z photometric SED with a set of model SEDs (Salim et al. 2007). Considering the difference in methodology used in estimating the total SFR and M_*, it is possible that one of the cause of the discrepancy is the aperture bias. In order to escape from the effect of the aperture bias, we compare the total SFR and M_* within a diameter of $3''$ from the galactic center derived using our method with the total SFR and M_* within fiber aperture taken from the MPA-JHU catalog. Those comparisons are shown in the top panel. By matching the aperture size, the estimation of the SFR and M_* from our method and those from MPA-JHU catalog are in broad agreement.

Fig. A.7 shows comparisons of the integrated SFR (left panel) and M_* (right panel) of the galaxies in the $z \sim 1$ sample from those derived using the pixel-to-pixel SED fitting and those taken from the 3D-HST catalog. The integrated SFR from the 3D-HST catalog is derived using combination of the UV and IR luminosities (Whitaker et al. 2014) and the integrated M_* from the catalog is derived using $0.3 - 8\mu$m SED fitting with the FAST code (Kriek et al. 2009). The left panel shows that the integrated SFR derived using our method ($\mathrm{SFR}_{\mathrm{ptpSEDfit}}$, which is the sum of the SFR of galaxy's pixels) is broadly consistent with the integrated SFR from the 3D-HST catalog ($\mathrm{SFR}_{\mathrm{UV+IR}}$). The histogram in the inset shows the distribution of the $\log(\mathrm{SFR}_{\mathrm{UV+IR}}/\mathrm{SFR}_{\mathrm{ptpSEDfit}})$, which has mean ($\mu$) and standard deviation (σ) of 0.031 and 0.48 dex, respectively. In order to investigate the causes of the scatter in the $\mathrm{SFR}_{\mathrm{UV+IR}}$ versus $\mathrm{SFR}_{\mathrm{ptpSEDfit}}$, we check the effect of the dust extinction in the sample galaxies using the ratio of $\log(\mathrm{SFR}_{\mathrm{UV}}/\mathrm{SFR}_{\mathrm{UV+IR}})$ ($\mathrm{SFR}_{\mathrm{UV}}$ and $\mathrm{SFR}_{\mathrm{IR}}$ are taken from the 3D-HST catalog), which is expected to be inversely proportional to the amount of dust extinction. The $\log(\mathrm{SFR}_{\mathrm{UV}}/\mathrm{SFR}_{\mathrm{UV+IR}})$ ratio is represented by the color-coding. It is suggested by the figure that there is a systematic dependence of the scatter on the amount of dust extinction, such that the $\mathrm{SFR}_{\mathrm{ptpSEDfit}}$ is systematically lower for galaxies with large dust extinction. The large offset is

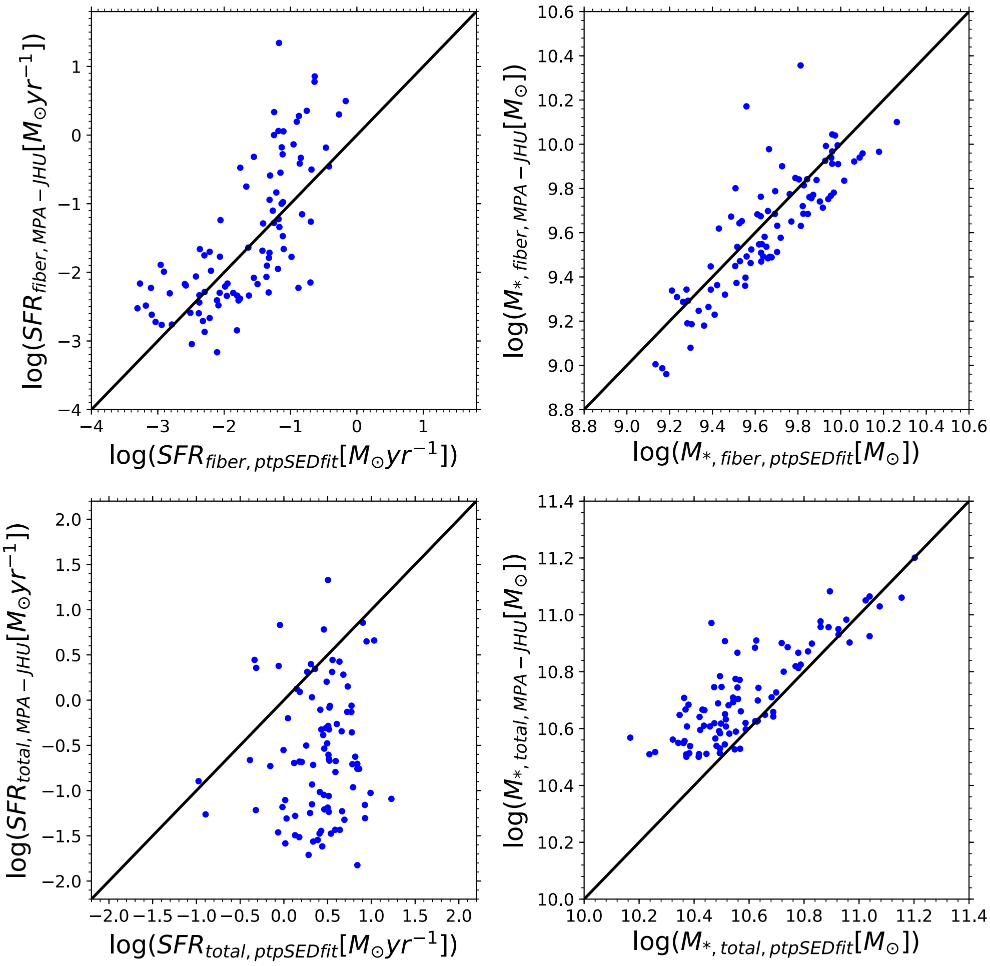

Figure A.6: Comparison of the integrated SFR and M_* of the galaxies in the $z \sim 0$ sample between those derived using the pixel-to-pixel SED fitting and those taken from the MPA-JHU catalog. In the top left and top right panels, total SFR and M_* within fiber diameter ($3''$) are used for the comparison, while in the bottom left and bottom right panels, total SFR and M_* over galaxy region are used for the comparison.

only observed among a few galaxies in the sample and we expect their effects on the analysis of the statistical sample can be minor. Moreover, there seem to be no mixing among the galaxy groups (z1-ΔMS1, z1-ΔMS2, and z1-ΔMS3 as represented by the different symbols), such that on average $\mathrm{SFR}_{\text{z1-}\Delta\text{MS1}} > \mathrm{SFR}_{\text{z1-}\Delta\text{MS2}} > \mathrm{SFR}_{\text{z1-}\Delta\text{MS3}}$ in both $\mathrm{SFR}_{\mathrm{ptpSEDfit}}$ and $\mathrm{SFR}_{\mathrm{UV+IR}}$.

Right panel in the Fig. A.7 shows comparison between the integrated M_* derived using the pixel-to-pixel SED fitting method ($M_{*,\mathrm{ptpSEDfit}}$) and that from the 3D-HST catalog ($M_{*,\text{3D-HST}}$). It is shown by the figure that there is a discrepancy between the $M_{*,\mathrm{ptpSEDfit}}$ and $M_{*,\text{3D-HST}}$. Part of the causes of the discrepancy in the integrated M_* and possibly also the discrepancy in the integrated SFR (as mentioned above) is a difference in photometry. Fig. A.8 shows comparisons between total fluxes calculated by summing up fluxes of the galaxy's pixels (this work) and the integrated fluxes

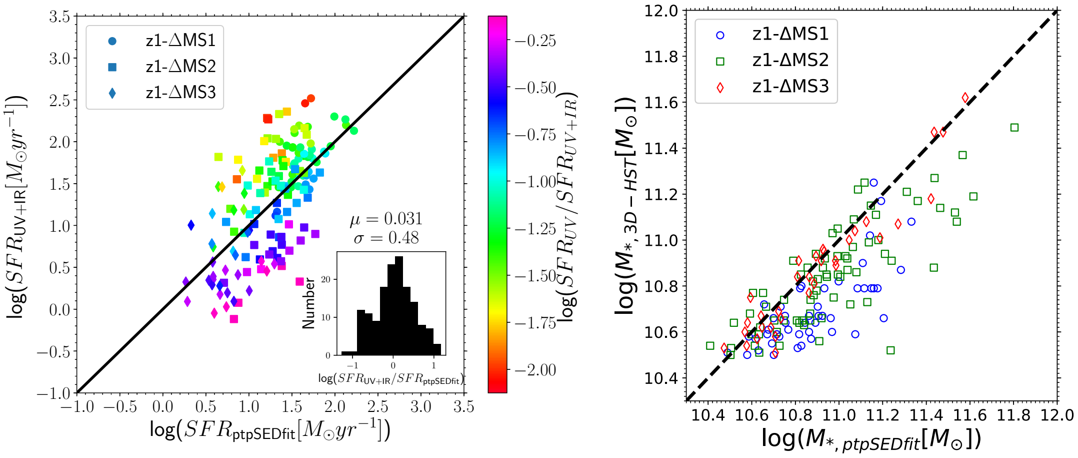

Figure A.7: Comparison of the integrated SFR (left panel) and M_* (right panel) of the galaxies in the $z \sim 1$ sample between those derived using the pixel-to-pixel SED fitting and those taken from the 3D-HST catalog. This figure is adopted from Abdurro'uf and Akiyama (2018).

taken from the 3D-HST catalog. It is shown by the figure that there is a discrepancy in the total flux especially for the bands in the shorter wavelength. The photometry of the 3D-HST is based on 0.7 arcsec aperture (calculated using `SExtractor`) which then extrapolated using surface brightness profile in F160W band (see Skelton et al. 2014). Given the extended and clumpy feature of the galaxy structure in the rest-frame UV bands, this extrapolation could lead to an underestimation of the total fluxes in the shorter wavelength bands. The discrepancy of total fluxes in the shorter wavelength bands make discrepancies in color and normalization of the SED and could lead to the discrepancy in M_* and SFR.

Other possible contributor to the discrepancy in M_* is a potential underestimation of the M_* derived using the global SED fitting compared to that derived using the spatially resolved SED fitting, even if there is no discrepancy in the photometric SED, as observed by previous researchers, e.g. Sorba and Sawicki (2015) and Sorba and Sawicki (2018). Fig. A.9 shows comparison between the integrated M_* derived using the pixel-to-pixel SED fitting ($M_{*,\rm ptpSEDfit(spatially\text{-}resolved)}$, which is obtained by summing up m_* of galaxy's pixels) and that derived using the global SED fitting ($M_{*,\rm spatially\text{-}unresolved}$). For the later, the same Bayesian SED fitting method, as one adopted in the pixel-to-pixel SED fitting is applied to the integrated SEDs of the sample galaxies. As shown by the figure, the $M_{*,\rm ptpSEDfit(spatially\text{-}resolved)}$ is systematically higher than the $M_{*,\rm spatially\text{-}unresolved}$.

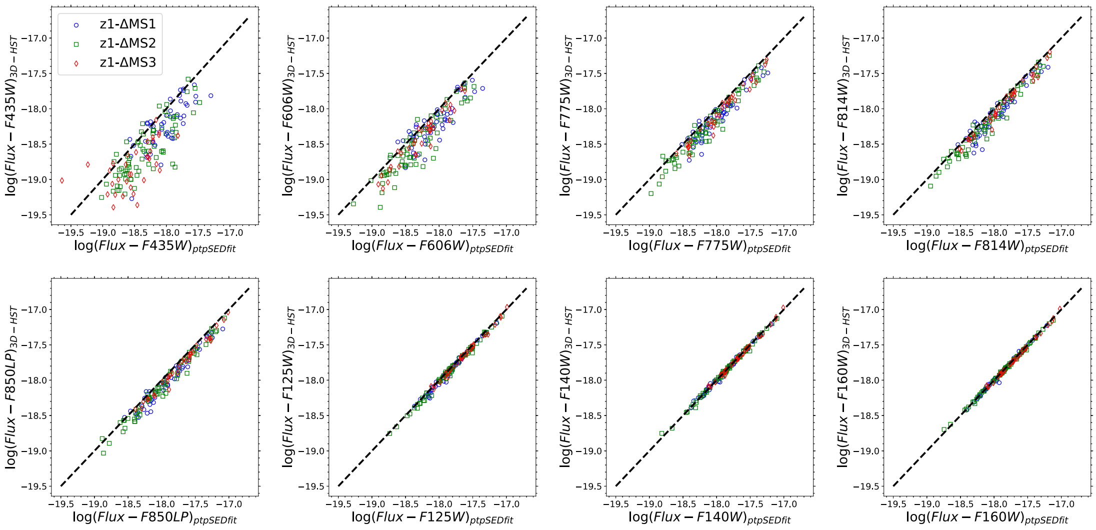

Figure A.8: Comparisons of integrated fluxes in the 8 bands of CANDELS+ 3D-HST between those derived by summing up fluxes of galaxy's pixels (this work; x axis in each panel) and those taken from the 3D-HST catalog (which is derived through aperture photometry; y axis in each panel). Blue circles, green squares, and red diamonds represent z1-ΔMS1, z1-ΔMS2, and z1-ΔMS3 sub-samples, respectively. This figure is taken from Abdurro'uf and Akiyama (2018).

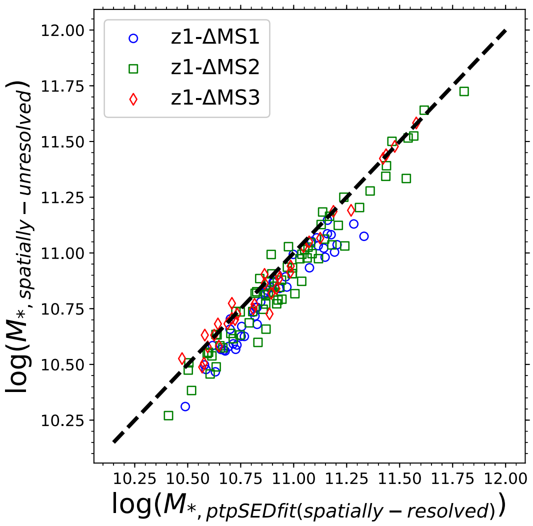

Figure A.9: Comparison between the integrated M_* derived using the pixel-to-pixel SED fitting ($M_{*,\mathrm{ptpSEDfit(spatially\text{-}resolved)}}$) and that derived using the global SED fitting ($M_{*,\mathrm{spatially\text{-}unresolved}}$). Blue circles, green squares, and red diamonds represent z1-ΔMS1, z1-ΔMS2, and z1-ΔMS3 galaxies, respectively. This figure is taken from Abdurro'uf and Akiyama (2018).

Appendix B

Integrated and spatially resolved UVJ diagram

B.1 Integrated and spatially resolved UVJ diagram for galaxies in the $z \sim 1$ sample

In order to examine whether quiescent sub-sample galaxies in the $z \sim 1$ sample (i.e. z1-ΔMS3) are indeed quiescent galaxies and not mistaken for red colors of possibly dusty star-forming galaxies, we estimate the rest-frame U, V, and J magnitudes of the $z \sim 1$ sample galaxies to locate their positions on the $U - V$ versus $V - J$ plane (i.e. UVJ diagram). We estimate the rest-frame U, V, and J magnitudes of a galaxy based on the best-fitting model spectrum of the galaxy's integrated SED (sum of fluxes of galaxy's pixels) which is obtained from the χ^2 minimization fitting. Top panel of Fig. B.1 shows positions of the z1-ΔMS1, z1-ΔMS2, and z1-ΔMS3 galaxies on the UVJ diagram. Upper left 'box' indicated by the solid line is a selection criteria for quiescent galaxies by Williams et al. (2009). Dusty star-forming galaxies are expected to reside in the upper right region in the UVJ diagram. It is shown by the figure that majority of the z1-ΔMS3 galaxies fall within the selection criteria thereby confirm that they are indeed quiescent galaxies which are dominated by old stellar population.

In order to check the reliability of the centrally quiescent properties of the z1-ΔMS2 and z1-ΔMS3 galaxies as indicated in Fig. 5.6, we also check distribution of the pixels (i.e. sub-galactic regions) that belong to the $z \sim 1$ sample galaxies on the UVJ diagram. In order to estimate the U, V, and J magnitudes of each galaxy's pixel, first we perform SED fitting with χ^2 minimization method to each SED of a galaxy's bin (i.e. collection of pixels) to obtain best-fitting model spectrum of the bin's SED. Based on the best-fitting model spectrum of the bin's SED, U, V, and J magnitudes of the bin are estimated. The magnitudes of the bin are then shared by pixels that belong to the bin, such that all pixels in the bin have the same magnitudes. Fig. B.2 shows the distribution of the

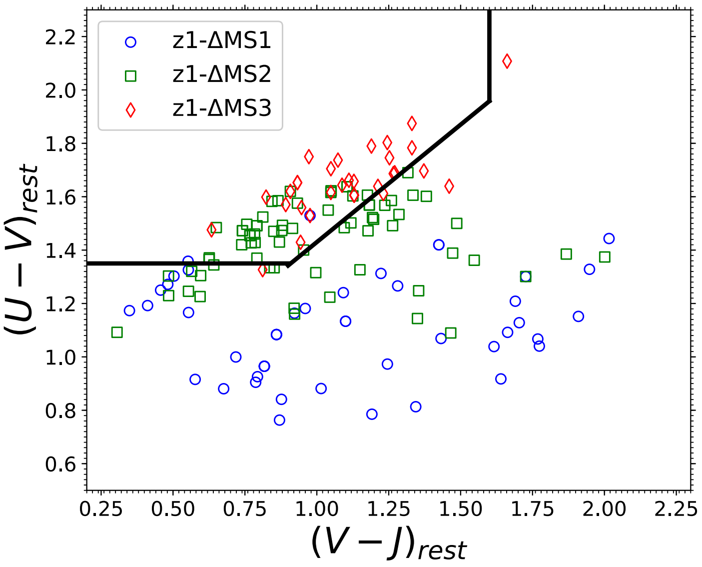

Figure B.1: Integrated $U-V$ versus $V-J$ (i.e. UVJ diagram) of the galaxies in the $z\sim1$ sample. Upper left "box" represents selection criteria for quiescent galaxies by Williams et al. (2009). Blue circles, green squares, and red diamonds represent z1-ΔMS1, z1-ΔMS2, and z1-ΔMS3 sub-samples, respectively.

pixels on the UVJ diagram, i.e. spatially resolved UVJ diagram. In the figure, left panel, middle panel, and right panel show the spatially resolved UVJ diagram for the z1-ΔMS1, z1-ΔMS2, and z1-ΔMS3 galaxies, respectively. In order to check a radial dependence of the spatially resolved UVJ diagram, we divide region in each galaxy into three: *central* ($r\leqslant2$ kpc), *middle* ($2<r\leqslant8$ kpc), and *outskirt* ($r>8$ kpc). In each panel of the figure, blue circles, green squares, and red stars represent *central*, *middle*, and *outskirt* regions, respectively.

It is shown in the Fig. B.2 that the central regions of the z1-ΔMS2 and z1-ΔMS3 galaxies are less star-forming (i.e. quiescent systems that dominated by old stellar population) compared to their middle and outskirt regions as majority of the central pixels in those galaxies are shifted toward the selection criteria of the quiescent galaxies (a "box" in upper left side). However, we notice that some central pixels of the z1-ΔMS2 and z1-ΔMS3 galaxies fall into the dusty star-forming locus. Majority of the central pixels of the z1-ΔMS1 are star-forming regions similar as their middle and outskirt pixels, confirming their flat sSFR(r) radial profile.

B.2 Integrated and spatially resolved UVJ diagram for galaxies in the $z\sim0$ sample

In the similar way as we done for the $z\sim1$ sample, we also estimate distribution of the $z\sim0$ sample galaxies on the UVJ diagram. The integrated U, V, and J magnitudes of a galaxy in the $z\sim0$

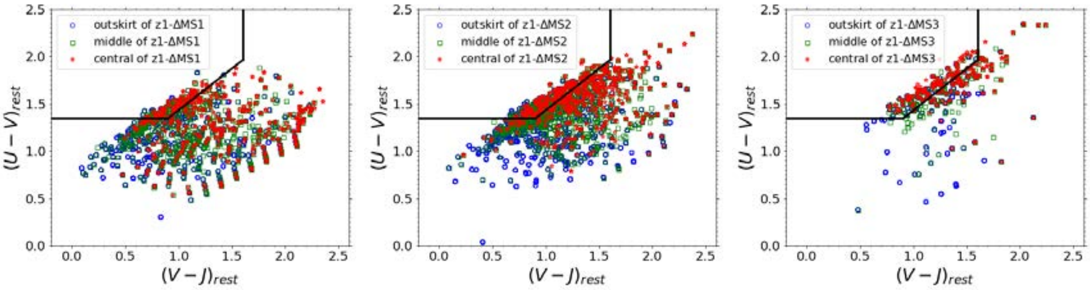

Figure B.2: Distributons of pixels associated with the z1-ΔMS1 (left panel), z1-ΔMS2 (middle panel), and z1-ΔMS3 (right panel) on the UVJ diagram. Red stars, green squares, and blue circles in each panel represent pixels located in the central ($r \leqslant 2$ kpc), middle ($2 < r \leqslant 8$ kpc), and outskirt ($r > 8$ kpc) regions. Upper left "box" in each panel represents selection criteria for quiescent galaxies by Williams et al. (2009).

sample are estimated using the same method as we used for the $z \sim 1$ sample galaxies (as described in previous section). Fig. B.3 shows distribution of the $z \sim 0$ sample galaxies on the UVJ diagram. The z0-ΔMS1, z0-ΔMS2, and z0-ΔMS3 sub-samples are shown with blue circles, green squares, and red diamonds, respectively. It is shown from this figure that the z0-ΔMS1 galaxies, which reside above +0.3 dex from the global SFMS, are mostly located in the bottom left side where star-forming galaxies are expected to reside on the UVJ diagram, while majority of the z0-ΔMS3 galaxies are located within the selection criteria for quiescent galaxies by Williams et al. (2009) which is drawn as a 'box' in the top left side. The z0-ΔMS2 galaxies are located in an intermediate between the star-forming and quiescent locus. This figure suggests that the z0-ΔMS1 galaxies are star-forming galaxies and the z0-ΔMS3 galaxies are quiescent galaxies.

In order to check the reliability of the centrally suppressed sSFR found for all the $z \sim 0$ sample galaxies as suggested by Fig. 4.11, we estimate the U, V, and J magnitudes of all pixels associated with the galaxies and locate their positions on the UVJ diagram. The U, V, and J magnitudes of a galaxy's pixel are estimated using the same method as we used to estimate the U, V, and J magnitudes of a pixel that belong to a galaxy in the $z \sim 1$ sample, which is described in the previous section. Fig. B.4 shows distributions of pixels that belong to the z0-ΔMS1 (left panel), z0-ΔMS2 (middle panel), and z0-ΔMS3 (right panel) on the UVJ diagram. In each panel, blue circles, green squares, and red stars represent pixels located in the *central* ($r \leqslant 5$ kpc), *middle* ($5 < r \leqslant 20$ kpc), and *outskirt* ($r > 20$ kpc) regions, respectively. It is shown from this figure that the central regions are less star-forming than the middle and outskirt regions for all galaxies in the three sub-samples as majority of the central pixels are shifted toward the selection criteria of quiescent galaxies (drawn as a 'box' in the top left side of each panel). It is also shown from this figure that for z0-ΔMS2 and z0-ΔMS3 galaxies, pixels in all the three regions are shifted toward the selection criteria for quiescent galaxies indicating a growing central quiescent regions as we go to galaxies with lower global sSFR.

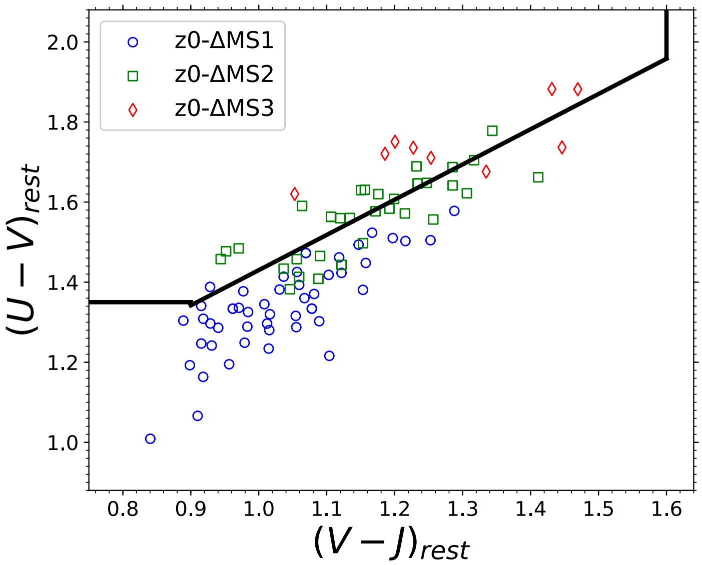

Figure B.3: Integrated $U - V$ versus $V - J$ diagram (i.e. UVJ diagram) of galaxies in the $z \sim 0$ sample. Upper left "box" represents selection criteria for quiescent galaxies by Williams et al. (2009). Blue circles, green squares, and red diamonds represent z0-ΔMS1, z0-ΔMS2, and z0-ΔMS3 sub-samples, respectively.

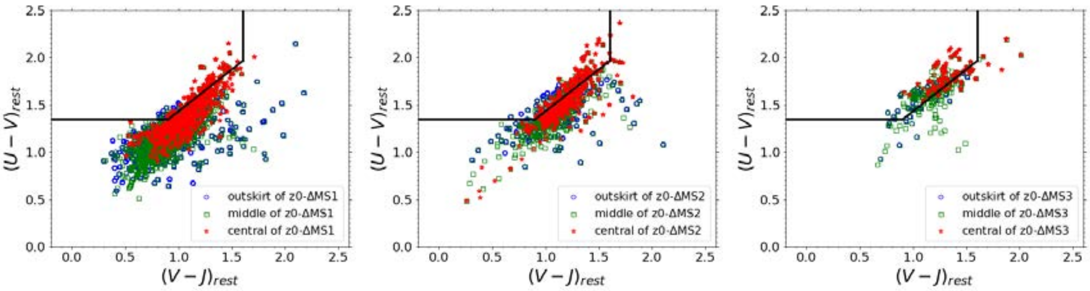

Figure B.4: Distributons of pixels associated with the z0-ΔMS1 (left panel), z0-ΔMS2 (middle panel), and z0-ΔMS3 (right panel) on the UVJ diagram. Red stars, green squares, and blue circles in each panel represent pixels located in the central ($r \leqslant 5$ kpc), middle ($5 < r \leqslant 20$ kpc), and outskirt ($r > 20$ kpc) regions. Upper left "box" in each panel represents selection criteria for quiescent galaxies by Williams et al. (2009).

Bibliography

Abdurro'uf and M. Akiyama. Understanding the scatter in the spatially resolved star formation main sequence of local massive spiral galaxies. MNRAS, 469:2806–2820, August 2017. doi: 10.1093/mnras/stx936.

Abdurro'uf and M. Akiyama. Evolution of spatially resolved star formation main sequence and surface density profiles in massive disc galaxies at $0 \lesssim z \lesssim 1$: inside-out stellar mass buildup and quenching. MNRAS, 479:5083–5100, October 2018. doi: 10.1093/mnras/sty1771.

R. G. Abraham, R. S. Ellis, A. C. Fabian, N. R. Tanvir, and K. Glazebrook. The star formation history of the Hubble sequence: spatially resolved colour distributions of intermediate-redshift galaxies in the Hubble Deep Field. MNRAS, 303:641–658, March 1999. doi: 10.1046/j.1365-8711.1999.02059.x.

L. E. Abramson, D. D. Kelson, A. Dressler, B. Poggianti, M. D. Gladders, A. Oemler, Jr., and B. Vulcani. The Mass-independence of Specific Star Formation Rates in Galactic Disks. ApJ, 785:L36, April 2014. doi: 10.1088/2041-8205/785/2/L36.

V. Acquaviva, E. Gawiser, and L. Guaita. Spectral Energy Distribution Fitting with Markov Chain Monte Carlo: Methodology and Application to z = 3.1 Lyα-emitting Galaxies. ApJ, 737:47, August 2011. doi: 10.1088/0004-637X/737/2/47.

C. P. Ahn, R. Alexandroff, C. Allende Prieto, F. Anders, S. F. Anderson, T. Anderton, B. H. Andrews, É. Aubourg, S. Bailey, F. A. Bastien, and et al. The Tenth Data Release of the Sloan Digital Sky Survey: First Spectroscopic Data from the SDSS-III Apache Point Observatory Galactic Evolution Experiment. ApJS, 211:17, April 2014. doi: 10.1088/0067-0049/211/2/17.

E. Athanassoula. The existence and shapes of dust lanes in galactic bars. MNRAS, 259:345–364, November 1992. doi: 10.1093/mnras/259.2.345.

I. K. Baldry, K. Glazebrook, J. Brinkmann, Ž. Ivezić, R. H. Lupton, R. C. Nichol, and A. S. Szalay. Quantifying the Bimodal Color-Magnitude Distribution of Galaxies. ApJ, 600:681–694, January 2004. doi: 10.1086/380092.

F. Belfiore, R. Maiolino, K. Bundy, K. Masters, M. Bershady, G. A. Oyarzún, L. Lin, M. Cano-Diaz, D. Wake, A. Spindler, D. Thomas, J. R. Brownstein, N. Drory, and R. Yan. SDSS IV MaNGA - sSFR profiles and the slow quenching of discs in green valley galaxies. MNRAS, 477:3014–3029, July 2018. doi: 10.1093/mnras/sty768.

E. Bertin and S. Arnouts. SExtractor: Software for source extraction. A&AS, 117:393–404, June 1996. doi: 10.1051/aas:1996164.

Y. Birnboim and A. Dekel. Virial shocks in galactic haloes? MNRAS, 345:349–364, October 2003. doi: 10.1046/j.1365-8711.2003.06955.x.

M. R. Blanton, D. W. Hogg, N. A. Bahcall, I. K. Baldry, J. Brinkmann, I. Csabai, D. Eisenstein, M. Fukugita, J. E. Gunn, Ž. Ivezić, D. Q. Lamb, R. H. Lupton, J. Loveday, J. A. Munn, R. C. Nichol, S. Okamura, D. J. Schlegel, K. Shimasaku, M. A. Strauss, M. S. Vogeley, and D. H.

Weinberg. The Broadband Optical Properties of Galaxies with Redshifts 0.02<z<0.22. ApJ, 594: 186–207, September 2003. doi: 10.1086/375528.

G. B. Brammer, P. G. van Dokkum, and P. Coppi. EAZY: A Fast, Public Photometric Redshift Code. ApJ, 686:1503-1513, October 2008. doi: 10.1086/591786.

G. B. Brammer, P. G. van Dokkum, M. Franx, M. Fumagalli, S. Patel, H.-W. Rix, R. E. Skelton, M. Kriek, E. Nelson, K. B. Schmidt, R. Bezanson, E. da Cunha, D. K. Erb, X. Fan, N. Förster Schreiber, G. D. Illingworth, I. Labbé, J. Leja, B. Lundgren, D. Magee, D. Marchesini, P. McCarthy, I. Momcheva, A. Muzzin, R. Quadri, C. C. Steidel, T. Tal, D. Wake, K. E. Whitaker, and A. Williams. 3D-HST: A Wide-field Grism Spectroscopic Survey with the Hubble Space Telescope. ApJS, 200:13, June 2012. doi: 10.1088/0067-0049/200/2/13.

M. Brightman, M. Baloković, M. Koss, D. M. Alexander, A. Annuar, H. Earnshaw, P. Gandhi, F. A. Harrison, A. E. Hornschemeier, B. Lehmer, M. C. Powell, A. Ptak, B. Rangelov, T. P. Roberts, D. Stern, D. J. Walton, and A. Zezas. A long hard-X-ray look at the dual active galactic nuclei of M51 with NuSTAR. ArXiv e-prints, May 2018.

J. Brinchmann, S. Charlot, S. D. M. White, C. Tremonti, G. Kauffmann, T. Heckman, and J. Brinkmann. The physical properties of star-forming galaxies in the low-redshift Universe. MNRAS, 351:1151–1179, July 2004. doi: 10.1111/j.1365-2966.2004.07881.x.

G. Bruzual and S. Charlot. Stellar population synthesis at the resolution of 2003. MNRAS, 344: 1000–1028, October 2003. doi: 10.1046/j.1365-8711.2003.06897.x.

J. J. Bryant, M. S. Owers, A. S. G. Robotham, S. M. Croom, S. P. Driver, M. J. Drinkwater, N. P. F. Lorente, L. Cortese, N. Scott, M. Colless, A. Schaefer, E. N. Taylor, I. S. Konstantopoulos, J. T. Allen, I. Baldry, L. Barnes, A. E. Bauer, J. Bland-Hawthorn, J. V. Bloom, A. M. Brooks, S. Brough, G. Cecil, W. Couch, D. Croton, R. Davies, S. Ellis, L. M. R. Fogarty, C. Foster, K. Glazebrook, M. Goodwin, A. Green, M. L. Gunawardhana, E. Hampton, I.-T. Ho, A. M. Hopkins, L. Kewley, J. S. Lawrence, S. G. Leon-Saval, S. Leslie, R. McElroy, G. Lewis, J. Liske, Á. R. López-Sánchez, S. Mahajan, A. M. Medling, N. Metcalfe, M. Meyer, J. Mould, D. Obreschkow, S. O'Toole, M. Pracy, S. N. Richards, T. Shanks, R. Sharp, S. M. Sweet, A. D. Thomas, C. Tonini, and C. J. Walcher. The SAMI Galaxy Survey: instrument specification and target selection. MNRAS, 447:2857–2879, March 2015. doi: 10.1093/mnras/stu2635.

K. Bundy, M. A. Bershady, D. R. Law, R. Yan, N. Drory, N. MacDonald, D. A. Wake, B. Cherinka, J. R. Sánchez-Gallego, A.-M. Weijmans, D. Thomas, C. Tremonti, K. Masters, L. Coccato, A. M. Diamond-Stanic, A. Aragón-Salamanca, V. Avila-Reese, C. Badenes, J. Falcón-Barroso, F. Belfiore, D. Bizyaev, G. A. Blanc, J. Bland-Hawthorn, M. R. Blanton, J. R. Brownstein, N. Byler, M. Cappellari, C. Conroy, A. A. Dutton, E. Emsellem, J. Etherington, P. M. Frinchaboy, H. Fu, J. E. Gunn, P. Harding, E. J. Johnston, G. Kauffmann, K. Kinemuchi, M. A. Klaene, J. H. Knapen, A. Leauthaud, C. Li, L. Lin, R. Maiolino, V. Malanushenko, E. Malanushenko, S. Mao, C. Maraston, R. M. McDermid, M. R. Merrifield, R. C. Nichol, D. Oravetz, K. Pan, J. K. Parejko, S. F. Sanchez, D. Schlegel, A. Simmons, O. Steele, M. Steinmetz, K. Thanjavur, B. A. Thompson, J. L. Tinker, R. C. E. van den Bosch, K. B. Westfall, D. Wilkinson, S. Wright, T. Xiao, and K. Zhang. Overview of the SDSS-IV MaNGA Survey: Mapping nearby Galaxies at Apache Point Observatory. ApJ, 798:7, January 2015. doi: 10.1088/0004-637X/798/1/7.

D. Calzetti, L. Armus, R. C. Bohlin, A. L. Kinney, J. Koornneef, and T. Storchi-Bergmann. The Dust Content and Opacity of Actively Star-forming Galaxies. ApJ, 533:682–695, April 2000. doi: 10.1086/308692.

M. Cano-Díaz, S. F. Sánchez, S. Zibetti, Y. Ascasibar, J. Bland-Hawthorn, B. Ziegler, R. M. González Delgado, C. J. Walcher, R. García-Benito, D. Mast, M. A. Mendoza-Pérez, J. Falcón-Barroso, L. Galbany, B. Husemann, C. Kehrig, R. A. Marino, P. Sánchez-Blázquez, C. López-Cobá, Á. R. López-Sánchez, and J. M. Vilchez. Spatially Resolved Star Formation Main Sequence of Galaxies in the CALIFA Survey. ApJ, 821:L26, April 2016. doi: 10.3847/2041-8205/821/2/L26.

M. Cappellari and Y. Copin. Adaptive spatial binning of integral-field spectroscopic data using Voronoi tessellations. MNRAS, 342:345–354, June 2003. doi: 10.1046/j.1365-8711.2003.06541.x.

J. A. Cardelli, G. C. Clayton, and J. S. Mathis. The relationship between infrared, optical, and ultraviolet extinction. ApJ, 345:245–256, October 1989. doi: 10.1086/167900.

D. Ceverino, A. Klypin, E. S. Klimek, S. Trujillo-Gomez, C. W. Churchill, J. Primack, and A. Dekel. Radiative feedback and the low efficiency of galaxy formation in low-mass haloes at high redshift. MNRAS, 442:1545–1559, August 2014. doi: 10.1093/mnras/stu956.

G. Chabrier. Galactic Stellar and Substellar Initial Mass Function. PASP, 115:763–795, July 2003. doi: 10.1086/376392.

E. Cheung, E. Athanassoula, K. L. Masters, R. C. Nichol, A. Bosma, E. F. Bell, S. M. Faber, D. C. Koo, C. Lintott, T. Melvin, K. Schawinski, R. A. Skibba, and K. W. Willett. Galaxy Zoo: Observing Secular Evolution through Bars. ApJ, 779:162, December 2013. doi: 10.1088/0004-637X/779/2/162.

J. Chevallard and S. Charlot. Modelling and interpreting spectral energy distributions of galaxies with BEAGLE. MNRAS, 462:1415–1443, October 2016. doi: 10.1093/mnras/stw1756.

C. Chiappini, F. Matteucci, and R. Gratton. The Chemical Evolution of the Galaxy: The Two-Infall Model. ApJ, 477:765–780, March 1997. doi: 10.1086/303726.

S. Cole, C. G. Lacey, C. M. Baugh, and C. S. Frenk. Hierarchical galaxy formation. MNRAS, 319: 168–204, November 2000. doi: 10.1046/j.1365-8711.2000.03879.x.

G. Consolandi, G. Gavazzi, M. Fumagalli, M. Dotti, and M. Fossati. Robust automatic photometry of local galaxies from SDSS. Dissecting the color magnitude relation with color profiles. A&A, 591:A38, June 2016. doi: 10.1051/0004-6361/201527618.

L. L. Cowie, A. Songaila, E. M. Hu, and J. G. Cohen. New Insight on Galaxy Formation and Evolution From Keck Spectroscopy of the Hawaii Deep Fields. AJ, 112:839, September 1996. doi: 10.1086/118058.

E. da Cunha, S. Charlot, and D. Elbaz. A simple model to interpret the ultraviolet, optical and infrared emission from galaxies. MNRAS, 388:1595–1617, August 2008. doi: 10.1111/j.1365-2966.2008.13535.x.

G. de Vaucouleurs. Recherches sur les Nebuleuses Extragalactiques. Annales d'Astrophysique, 11: 247, January 1948.

A. Dekel and Y. Birnboim. Galaxy bimodality due to cold flows and shock heating. MNRAS, 368: 2–20, May 2006. doi: 10.1111/j.1365-2966.2006.10145.x.

A. Dekel and N. Mandelker. An analytic solution for the minimal bathtub toy model: challenges in the star formation history of high-z galaxies. MNRAS, 444:2071–2084, November 2014. doi: 10.1093/mnras/stu1427.

A. Dekel, A. Zolotov, D. Tweed, M. Cacciato, D. Ceverino, and J. R. Primack. Toy models for galaxy formation versus simulations. MNRAS, 435:999–1019, October 2013. doi: 10.1093/mnras/stt1338.

D. Elbaz, E. Daddi, D. Le Borgne, M. Dickinson, D. M. Alexander, R.-R. Chary, J.-L. Starck, W. N. Brandt, M. Kitzbichler, E. MacDonald, M. Nonino, P. Popesso, D. Stern, and E. Vanzella. The reversal of the star formation-density relation in the distant universe. A&A, 468:33–48, June 2007. doi: 10.1051/0004-6361:20077525.

A. C. Fabian. Observational Evidence of Active Galactic Nuclei Feedback. ARA&A, 50:455–489, September 2012. doi: 10.1146/annurev-astro-081811-125521.

C.-A. Faucher-Giguère, D. Kereš, and C.-P. Ma. The baryonic assembly of dark matter haloes. MNRAS, 417:2982–2999, November 2011. doi: 10.1111/j.1365-2966.2011.19457.x.

C. Firmani and V. Avila-Reese. Disc galaxy evolution models in a hierarchical formation scenario: structure and dynamics. MNRAS, 315:457–472, July 2000. doi: 10.1046/j.1365-8711.2000.03338.x.

N. M. Förster Schreiber, R. Genzel, N. Bouché, G. Cresci, R. Davies, P. Buschkamp, K. Shapiro, L. J. Tacconi, E. K. S. Hicks, S. Genel, A. E. Shapley, D. K. Erb, C. C. Steidel, D. Lutz, F. Eisenhauer, S. Gillessen, A. Sternberg, A. Renzini, A. Cimatti, E. Daddi, J. Kurk, S. Lilly, X. Kong, M. D. Lehnert, N. Nesvadba, A. Verma, H. McCracken, N. Arimoto, M. Mignoli, and M. Onodera. The SINS Survey: SINFONI Integral Field Spectroscopy of z ~ 2 Star-forming Galaxies. ApJ, 706: 1364–1428, December 2009. doi: 10.1088/0004-637X/706/2/1364.

G. Gavazzi, G. Consolandi, M. Dotti, R. Fanali, M. Fossati, M. Fumagalli, E. Viscardi, G. Savorgnan, A. Boselli, L. Gutiérrez, H. Hernández Toledo, R. Giovanelli, and M. P. Haynes. Hα3: an Hα imaging survey of HI selected galaxies from ALFALFA. VI. The role of bars in quenching star formation from z = 3 to the present epoch. A&A, 580:A116, August 2015. doi: 10.1051/0004-6361/201425351.

R. Genzel, N. M. Förster Schreiber, P. Lang, S. Tacchella, L. J. Tacconi, S. Wuyts, K. Bandara, A. Burkert, P. Buschkamp, C. M. Carollo, G. Cresci, R. Davies, F. Eisenhauer, E. K. S. Hicks, J. Kurk, S. J. Lilly, D. Lutz, C. Mancini, T. Naab, S. Newman, Y. Peng, A. Renzini, K. Shapiro Griffin, A. Sternberg, D. Vergani, E. Wisnioski, E. Wuyts, and G. Zamorani. The SINS/zC-SINF Survey of z ~ 2 Galaxy Kinematics: Evidence for Gravitational Quenching. ApJ, 785:75, April 2014. doi: 10.1088/0004-637X/785/1/75.

R. M. González Delgado, R. Cid Fernandes, E. Pérez, R. García-Benito, R. López Fernández, E. A. D. Lacerda, C. Cortijo-Ferrero, A. L. de Amorim, N. Vale Asari, S. F. Sánchez, C. J. Walcher, L. Wisotzki, D. Mast, J. Alves, Y. Ascasibar, J. Bland-Hawthorn, L. Galbany, R. C. Kennicutt, I. Márquez, J. Masegosa, M. Mollá, P. Sánchez-Blázquez, and J. M. Vílchez. Star formation along the Hubble sequence. Radial structure of the star formation of CALIFA galaxies. A&A, 590:A44, May 2016. doi: 10.1051/0004-6361/201628174.

N. A. Grogin, D. D. Kocevski, S. M. Faber, H. C. Ferguson, A. M. Koekemoer, A. G. Riess, V. Acquaviva, D. M. Alexander, O. Almaini, M. L. N. Ashby, M. Barden, E. F. Bell, F. Bournaud, T. M. Brown, K. I. Caputi, S. Casertano, P. Cassata, M. Castellano, P. Challis, R.-R. Chary, E. Cheung, M. Cirasuolo, C. J. Conselice, A. Roshan Cooray, D. J. Croton, E. Daddi, T. Dahlen, R. Davé, D. F. de Mello, A. Dekel, M. Dickinson, T. Dolch, J. L. Donley, J. S. Dunlop, A. A. Dutton, D. Elbaz, G. G. Fazio, A. V. Filippenko, S. L. Finkelstein, A. Fontana, J. P. Gardner, P. M. Garnavich, E. Gawiser, M. Giavalisco, A. Grazian, Y. Guo, N. P. Hathi, B. Häussler, P. F. Hopkins, J.-S. Huang, K.-H. Huang, S. W. Jha, J. S. Kartaltepe, R. P. Kirshner, D. C. Koo, K. Lai, K.-S. Lee, W. Li, J. M. Lotz, R. A. Lucas, P. Madau, P. J. McCarthy, E. J. McGrath, D. H. McIntosh, R. J. McLure, B. Mobasher, L. A. Moustakas, M. Mozena, K. Nandra, J. A. Newman, S.-M. Niemi, K. G. Noeske, C. J. Papovich, L. Pentericci, A. Pope, J. R. Primack, A. Rajan, S. Ravindranath, N. A. Reddy, A. Renzini, H.-W. Rix, A. R. Robaina, S. A. Rodney, D. J. Rosario, P. Rosati, S. Salimbeni, C. Scarlata, B. Siana, L. Simard, J. Smidt, R. S. Somerville, H. Spinrad, A. N. Straughn, L.-G. Strolger, O. Telford, H. I. Teplitz, J. R. Trump, A. van der Wel, C. Villforth, R. H. Wechsler, B. J. Weiner, T. Wiklind, V. Wild, G. Wilson, S. Wuyts, H.-J. Yan, and M. S. Yun. CANDELS: The Cosmic Assembly Near-infrared Deep Extragalactic Legacy Survey. ApJS, 197:35, December 2011. doi: 10.1088/0067-0049/197/2/35.

Y. Han and Z. Han. BayeSED: A General Approach to Fitting the Spectral Energy Distribution of Galaxies. ApJS, 215:2, November 2014. doi: 10.1088/0067-0049/215/1/2.

A. M. Hopkins. On the Evolution of Star-forming Galaxies. ApJ, 615:209–221, November 2004. doi: 10.1086/424032.

A. M. Hopkins and J. F. Beacom. On the Normalization of the Cosmic Star Formation History. ApJ, 651:142–154, November 2006. doi: 10.1086/506610.

P. F. Hopkins, L. Hernquist, T. J. Cox, T. Di Matteo, B. Robertson, and V. Springel. A Unified, Merger-driven Model of the Origin of Starbursts, Quasars, the Cosmic X-Ray Background, Supermassive Black Holes, and Galaxy Spheroids. ApJS, 163:1–49, March 2006. doi: 10.1086/499298.

P. F. Hopkins, T. J. Cox, D. Kereš, and L. Hernquist. A Cosmological Framework for the Co-Evolution of Quasars, Supermassive Black Holes, and Elliptical Galaxies. II. Formation of Red Ellipticals. ApJS, 175:390-422, April 2008. doi: 10.1086/524363.

B. C. Hsieh, L. Lin, J. H. Lin, H. A. Pan, C. H. Hsu, S. F. Sánchez, M. Cano-Díaz, K. Zhang, R. Yan, J. K. Barrera-Ballesteros, M. Boquien, R. Riffel, J. Brownstein, I. Cruz-González, A. Hagen, H. Ibarra, K. Pan, D. Bizyaev, D. Oravetz, and A. Simmons. SDSS-IV MaNGA: Spatially Resolved Star Formation Main Sequence and LI(N)ER Sequence. ApJ, 851:L24, December 2017. doi: 10.3847/2041-8213/aa9d80.

E. P. Hubble. Extragalactic nebulae. ApJ, 64, December 1926. doi: 10.1086/143018.

E. P. Hubble. Realm of the Nebulae. 1936.

L. K. Hunt and M. A. Malkan. Morphology of the 12 Micron Seyfert Galaxies. I. Hubble Types, Axial Ratios, Bars, and Rings. ApJ, 516:660–671, May 1999. doi: 10.1086/307150.

H. J. Ibarra-Medel, S. F. Sánchez, V. Avila-Reese, H. M. Hernández-Toledo, J. J. González, N. Drory, K. Bundy, D. Bizyaev, M. Cano-Díaz, E. Malanushenko, K. Pan, A. Roman-Lopes, and D. Thomas. SDSS IV MaNGA: the global and local stellar mass assemby histories of galaxies. MNRAS, 463:2799–2818, December 2016. doi: 10.1093/mnras/stw2126.

S. Jogee, N. Scoville, and J. D. P. Kenney. The Central Region of Barred Galaxies: Molecular Environment, Starbursts, and Secular Evolution. ApJ, 630:837–863, September 2005. doi: 10.1086/432106.

T. Jones, R. Ellis, E. Jullo, and J. Richard. Measurement of a Metallicity Gradient in a z = 2 Galaxy: Implications for Inside-out Assembly Histories. ApJ, 725:L176–L180, December 2010. doi: 10.1088/2041-8205/725/2/L176.

S. Juneau, K. Glazebrook, D. Crampton, P. J. McCarthy, S. Savaglio, R. Abraham, R. G. Carlberg, H.-W. Chen, D. Le Borgne, R. O. Marzke, K. Roth, I. Jørgensen, I. Hook, and R. Murowinski. Cosmic Star Formation History and Its Dependence on Galaxy Stellar Mass. ApJ, 619:L135–L138, February 2005. doi: 10.1086/427937.

G. Kauffmann. Disc galaxies at z=0 and at high redshift: an explanation of the observed evolution of damped Lyalpha absorption systems. MNRAS, 281:475–486, July 1996. doi: 10.1093/mnras/281.2.475.

G. Kauffmann, T. M. Heckman, C. Tremonti, J. Brinchmann, S. Charlot, S. D. M. White, S. E. Ridgway, J. Brinkmann, M. Fukugita, P. B. Hall, Ž. Ivezić, G. T. Richards, and D. P. Schneider. The host galaxies of active galactic nuclei. MNRAS, 346:1055–1077, December 2003a. doi: 10.1111/j.1365-2966.2003.07154.x.

G. Kauffmann, T. M. Heckman, S. D. M. White, S. Charlot, C. Tremonti, J. Brinchmann, G. Bruzual, E. W. Peng, M. Seibert, M. Bernardi, M. Blanton, J. Brinkmann, F. Castander, I. Csábai, M. Fukugita, Z. Ivezic, J. A. Munn, R. C. Nichol, N. Padmanabhan, A. R. Thakar, D. H. Weinberg, and D. York. Stellar masses and star formation histories for 10^5 galaxies from the Sloan Digital Sky Survey. MNRAS, 341:33–53, May 2003b. doi: 10.1046/j.1365-8711.2003.06291.x.

R. C. Kennicutt, Jr., L. Armus, G. Bendo, D. Calzetti, D. A. Dale, B. T. Draine, C. W. Engelbracht, K. D. Gordon, A. D. Grauer, G. Helou, D. J. Hollenbach, T. H. Jarrett, L. J. Kewley, C. Leitherer, A. Li, S. Malhotra, M. W. Regan, G. H. Rieke, M. J. Rieke, H. Roussel, J.-D. T. Smith, M. D. Thornley, and F. Walter. SINGS: The SIRTF Nearby Galaxies Survey. PASP, 115:928–952, August 2003. doi: 10.1086/376941.

A. M. Koekemoer, S. M. Faber, H. C. Ferguson, N. A. Grogin, D. D. Kocevski, D. C. Koo, K. Lai, J. M. Lotz, R. A. Lucas, E. J. McGrath, S. Ogaz, A. Rajan, A. G. Riess, S. A. Rodney, L. Strolger, S. Casertano, M. Castellano, T. Dahlen, M. Dickinson, T. Dolch, A. Fontana, M. Giavalisco, A. Grazian, Y. Guo, N. P. Hathi, K.-H. Huang, A. van der Wel, H.-J. Yan, V. Acquaviva, D. M. Alexander, O. Almaini, M. L. N. Ashby, M. Barden, E. F. Bell, F. Bournaud, T. M. Brown, K. I. Caputi, P. Cassata, P. J. Challis, R.-R. Chary, E. Cheung, M. Cirasuolo, C. J. Conselice, A. Roshan Cooray, D. J. Croton, E. Daddi, R. Davé, D. F. de Mello, L. de Ravel, A. Dekel, J. L. Donley, J. S. Dunlop, A. A. Dutton, D. Elbaz, G. G. Fazio, A. V. Filippenko, S. L. Finkelstein, C. Frazer, J. P. Gardner, P. M. Garnavich, E. Gawiser, R. Gruetzbauch, W. G. Hartley, B. Häussler, J. Herrington, P. F. Hopkins, J.-S. Huang, S. W. Jha, A. Johnson, J. S. Kartaltepe, A. A. Khostovan, R. P. Kirshner, C. Lani, K.-S. Lee, W. Li, P. Madau, P. J. McCarthy, D. H. McIntosh, R. J. McLure, C. McPartland, B. Mobasher, H. Moreira, A. Mortlock, L. A. Moustakas, M. Mozena, K. Nandra, J. A. Newman, J. L. Nielsen, S. Niemi, K. G. Noeske, C. J. Papovich, L. Pentericci, A. Pope, J. R. Primack, S. Ravindranath, N. A. Reddy, A. Renzini, H.-W. Rix, A. R. Robaina, D. J. Rosario, P. Rosati, S. Salimbeni, C. Scarlata, B. Siana, L. Simard, J. Smidt, D. Snyder, R. S. Somerville, H. Spinrad, A. N. Straughn, O. Telford, H. I. Teplitz, J. R. Trump, C. Vargas, C. Villforth, C. R. Wagner, P. Wandro, R. H. Wechsler, B. J. Weiner, T. Wiklind, V. Wild, G. Wilson, S. Wuyts, and M. S. Yun. CANDELS: The Cosmic Assembly Near-infrared Deep Extragalactic Legacy Survey-The Hubble Space Telescope Observations, Imaging Data Products, and Mosaics. ApJS, 197:36, December 2011. doi: 10.1088/0067-0049/197/2/36.

M. Kriek, P. G. van Dokkum, I. Labbé, M. Franx, G. D. Illingworth, D. Marchesini, and R. F. Quadri. An Ultra-Deep Near-Infrared Spectrum of a Compact Quiescent Galaxy at z = 2.2. ApJ, 700:221–231, July 2009. doi: 10.1088/0004-637X/700/1/221.

E. Laurikainen, H. Salo, and R. Buta. Comparison of Bar Strengths and Fractions of Bars in Active and Nonactive Galaxies. ApJ, 607:103–124, May 2004. doi: 10.1086/383462.

A. K. Leroy, F. Walter, F. Bigiel, A. Usero, A. Weiss, E. Brinks, W. J. G. de Blok, R. C. Kennicutt, K.-F. Schuster, C. Kramer, H. W. Wiesemeyer, and H. Roussel. Heracles: The HERA CO Line Extragalactic Survey. AJ, 137:4670–4696, June 2009. doi: 10.1088/0004-6256/137/6/4670.

S. J. Lilly, O. Le Fevre, F. Hammer, and D. Crampton. The Canada-France Redshift Survey: The Luminosity Density and Star Formation History of the Universe to Z approximately 1. ApJ, 460: L1, March 1996. doi: 10.1086/309975.

L. Lin, F. Belfiore, H.-A. Pan, M. S. Bothwell, P.-Y. Hsieh, S. Huang, T. Xiao, S. F. Sánchez, B.-C. Hsieh, K. Masters, S. Ramya, J.-H. Lin, C.-H. Hsu, C. Li, R. Maiolino, K. Bundy, D. Bizyaev, N. Drory, H. Ibarra-Medel, I. Lacerna, T. Haines, R. Smethurst, D. V. Stark, and D. Thomas. SDSS-IV MaNGA-resolved Star Formation and Molecular Gas Properties of Green Valley Galaxies: A First Look with ALMA and MaNGA. ApJ, 851:18, December 2017. doi: 10.3847/1538-4357/aa96ae.

C. J. Lintott, K. Schawinski, A. Slosar, K. Land, S. Bamford, D. Thomas, M. J. Raddick, R. C. Nichol, A. Szalay, D. Andreescu, P. Murray, and J. Vandenberg. Galaxy Zoo: morphologies derived from visual inspection of galaxies from the Sloan Digital Sky Survey. MNRAS, 389: 1179–1189, September 2008. doi: 10.1111/j.1365-2966.2008.13689.x.

Q. Liu, E. Wang, Z. Lin, Y. Gao, H. Liu, B. Berhane Teklu, and X. Kong. Elevation or Suppression? The Resolved Star Formation Main Sequence of Galaxies with Two Different Assembly Modes. ApJ, 857:17, April 2018. doi: 10.3847/1538-4357/aab3d5.

B. Luo, W. N. Brandt, Y. Q. Xue, B. Lehmer, D. M. Alexander, F. E. Bauer, F. Vito, G. Yang, A. R. Basu-Zych, A. Comastri, R. Gilli, Q.-S. Gu, A. E. Hornschemeier, A. Koekemoer, T. Liu, V. Mainieri, M. Paolillo, P. Ranalli, P. Rosati, D. P. Schneider, O. Shemmer, I. Smail, M. Sun, P. Tozzi, C. Vignali, and J.-X. Wang. The Chandra Deep Field-South Survey: 7 Ms Source Catalogs. ApJS, 228:2, January 2017. doi: 10.3847/1538-4365/228/1/2.

P. Madau. Radiative transfer in a clumpy universe: The colors of high-redshift galaxies. ApJ, 441: 18–27, March 1995. doi: 10.1086/175332.

P. Madau and M. Dickinson. Cosmic Star-Formation History. ARA&A, 52:415–486, August 2014. doi: 10.1146/annurev-astro-081811-125615.

G. E. Magdis, M. Bureau, J. P. Stott, A. Tiley, A. M. Swinbank, R. Bower, A. J. Bunker, M. Jarvis, H. Johnson, and R. Sharples. KROSS: mapping the Hα emission across the star formation sequence at $z \approx 1$. MNRAS, 456:4533–4541, March 2016. doi: 10.1093/mnras/stv2931.

K. Makishima, T. Ohashi, H. Kondo, G. G. C. Palumbo, and G. Trinchieri. X-ray spectrum of the spiral galaxy M51 (NGC 5194). ApJ, 365:159–163, December 1990. doi: 10.1086/169465.

A. Maragkoudakis, A. Zezas, M. L. N. Ashby, and S. P. Willner. The sub-galactic and nuclear main sequences for local star-forming galaxies. MNRAS, 466:1192–1204, April 2017. doi: 10.1093/mnras/stw3180.

M. Martig, F. Bournaud, R. Teyssier, and A. Dekel. Morphological Quenching of Star Formation: Making Early-Type Galaxies Red. ApJ, 707:250–267, December 2009. doi: 10.1088/0004-637X/707/1/250.

E. E. Martínez-García, G. Bruzual, G. Magris C., and R. A. González-Lópezlira. The resolved star formation history of M51a through successive Bayesian marginalization. MNRAS, 474:1862–1872, February 2018. doi: 10.1093/mnras/stx2801.

A. M. Medling, L. Cortese, S. M. Croom, A. W. Green, B. Groves, E. Hampton, I.-T. Ho, L. J. M. Davies, L. J. Kewley, A. J. Moffett, A. L. Schaefer, E. Taylor, T. Zafar, K. Bekki, J. Bland-Hawthorn, J. V. Bloom, S. Brough, J. J. Bryant, B. Catinella, G. Cecil, M. Colless, W. J. Couch, M. J. Drinkwater, S. P. Driver, C. Federrath, C. Foster, G. Goldstein, M. Goodwin, A. Hopkins, J. S. Lawrence, S. K. Leslie, G. F. Lewis, N. P. F. Lorente, M. S. Owers, R. McDermid, S. N. Richards, R. Sharp, N. Scott, S. M. Sweet, D. S. Taranu, E. Tescari, C. Tonini, J. van de Sande, C. J. Walcher, and A. Wright. The SAMI Galaxy Survey: spatially resolving the main sequence of star formation. MNRAS, 475:5194–5214, April 2018. doi: 10.1093/mnras/sty127.

T. Morishita, T. Ichikawa, M. Noguchi, M. Akiyama, S. G. Patel, M. Kajisawa, and T. Obata. From Diversity to Dichotomy, and Quenching: Milky-Way-like and Massive Galaxy Progenitors at 0.5 < z <3.0. ApJ, 805:34, May 2015. doi: 10.1088/0004-637X/805/1/34.

P. Morrissey, T. Conrow, T. A. Barlow, T. Small, M. Seibert, T. K. Wyder, T. Budavári, S. Arnouts, P. G. Friedman, K. Forster, D. C. Martin, S. G. Neff, D. Schiminovich, L. Bianchi, J. Donas, T. M. Heckman, Y.-W. Lee, B. F. Madore, B. Milliard, R. M. Rich, A. S. Szalay, B. Y. Welsh, and S. K. Yi. The Calibration and Data Products of GALEX. ApJS, 173:682–697, December 2007. doi: 10.1086/520512.

N. Murray, E. Quataert, and T. A. Thompson. On the Maximum Luminosity of Galaxies and Their Central Black Holes: Feedback from Momentum-driven Winds. ApJ, 618:569–585, January 2005. doi: 10.1086/426067.

E. J. Nelson, P. G. van Dokkum, G. Brammer, N. Förster Schreiber, M. Franx, M. Fumagalli, S. Patel, H.-W. Rix, R. E. Skelton, R. Bezanson, E. Da Cunha, M. Kriek, I. Labbe, B. Lundgren, R. Quadri, and K. B. Schmidt. Spatially Resolved Hα Maps and Sizes of 57 Strongly Star-forming Galaxies at z ˜ 1 from 3D-HST: Evidence for Rapid Inside-out Assembly of Disk Galaxies. ApJ, 747:L28, March 2012. doi: 10.1088/2041-8205/747/2/L28.

E. J. Nelson, P. G. van Dokkum, N. M. Förster Schreiber, M. Franx, G. B. Brammer, I. G. Momcheva, S. Wuyts, K. E. Whitaker, R. E. Skelton, M. Fumagalli, C. C. Hayward, M. Kriek, I. Labbé, J. Leja, H.-W. Rix, L. J. Tacconi, A. van der Wel, F. C. van den Bosch, P. A. Oesch, C. Dickey, and J. Ulf Lange. Where Stars Form: Inside-out Growth and Coherent Star Formation from HST Hα Maps of 3200 Galaxies across the Main Sequence at $0.7 < z < 1.5$. ApJ, 828:27, September 2016a. doi: 10.3847/0004-637X/828/1/27.

E. J. Nelson, P. G. van Dokkum, I. G. Momcheva, G. B. Brammer, S. Wuyts, M. Franx, N. M. Förster Schreiber, K. E. Whitaker, and R. E. Skelton. Spatially Resolved Dust Maps from Balmer Decrements in Galaxies at z ˜ 1.4. ApJ, 817:L9, January 2016b. doi: 10.3847/2041-8205/817/1/L9.

K. G. Noeske, B. J. Weiner, S. M. Faber, C. Papovich, D. C. Koo, R. S. Somerville, K. Bundy, C. J. Conselice, J. A. Newman, D. Schiminovich, E. Le Floc'h, A. L. Coil, G. H. Rieke, J. M. Lotz, J. R. Primack, P. Barmby, M. C. Cooper, M. Davis, R. S. Ellis, G. G. Fazio, P. Guhathakurta, J. Huang, S. A. Kassin, D. C. Martin, A. C. Phillips, R. M. Rich, T. A. Small, C. N. A. Willmer, and G. Wilson. Star Formation in AEGIS Field Galaxies since z=1.1: The Dominance of Gradually Declining Star Formation, and the Main Sequence of Star-forming Galaxies. ApJ, 660:L43–L46, May 2007. doi: 10.1086/517926.

S. Noll, D. Burgarella, E. Giovannoli, V. Buat, D. Marcillac, and J. C. Muñoz-Mateos. Analysis of galaxy spectral energy distributions from far-UV to far-IR with CIGALE: studying a SINGS test sample. A&A, 507:1793–1813, December 2009. doi: 10.1051/0004-6361/200912497.

S. E. Nuza, C. Chiappini, C. Scannapieco, I. Minchev, M. Martig, and T. C. Junqueira. How does the stellar disk of the Milky Way get its gas? ArXiv e-prints, May 2018.

Y.-j. Peng and R. Maiolino. From haloes to Galaxies - I. The dynamics of the gas regulator model and the implied cosmic sSFR history. MNRAS, 443:3643–3664, October 2014. doi: 10.1093/mnras/stu1288.

Y.-j. Peng, S. J. Lilly, K. Kovač, M. Bolzonella, L. Pozzetti, A. Renzini, G. Zamorani, O. Ilbert, C. Knobel, A. Iovino, C. Maier, O. Cucciati, L. Tasca, C. M. Carollo, J. Silverman, P. Kampczyk, L. de Ravel, D. Sanders, N. Scoville, T. Contini, V. Mainieri, M. Scodeggio, J.-P. Kneib, O. Le Fèvre, S. Bardelli, A. Bongiorno, K. Caputi, G. Coppa, S. de la Torre, P. Franzetti, B. Garilli, F. Lamareille, J.-F. Le Borgne, V. Le Brun, M. Mignoli, E. Perez Montero, R. Pello, E. Ricciardelli, M. Tanaka, L. Tresse, D. Vergani, N. Welikala, E. Zucca, P. Oesch, U. Abbas, L. Barnes, R. Bordoloi, D. Bottini, A. Cappi, P. Cassata, A. Cimatti, M. Fumana, G. Hasinger, A. Koekemoer, A. Leauthaud, D. Maccagni, C. Marinoni, H. McCracken, P. Memeo, B. Meneux, P. Nair, C. Porciani, V. Presotto, and R. Scaramella. Mass and Environment as Drivers of Galaxy Evolution in SDSS and zCOSMOS and the Origin of the Schechter Function. ApJ, 721:193–221, September 2010. doi: 10.1088/0004-637X/721/1/193.

E. Pérez, R. Cid Fernandes, R. M. González Delgado, R. García-Benito, S. F. Sánchez, B. Husemann, D. Mast, J. R. Rodón, D. Kupko, N. Backsmann, A. L. de Amorim, G. van de Ven, J. Walcher, L. Wisotzki, C. Cortijo-Ferrero, and CALIFA Collaboration. The Evolution of Galaxies Resolved in Space and Time: A View of Inside-out Growth from the CALIFA Survey. ApJ, 764:L1, February 2013. doi: 10.1088/2041-8205/764/1/L1.

M. Querejeta, E. Schinnerer, S. García-Burillo, F. Bigiel, G. A. Blanc, D. Colombo, A. Hughes, K. Kreckel, A. K. Leroy, S. E. Meidt, D. S. Meier, J. Pety, and K. Sliwa. AGN feedback in the nucleus of M 51. A&A, 593:A118, October 2016. doi: 10.1051/0004-6361/201628674.

A. Renzini and Y.-j. Peng. An Objective Definition for the Main Sequence of Star-forming Galaxies. ApJ, 801:L29, March 2015. doi: 10.1088/2041-8205/801/2/L29.

G. H. Rieke, A. Alonso-Herrero, B. J. Weiner, P. G. Pérez-González, M. Blaylock, J. L. Donley, and D. Marcillac. Determining Star Formation Rates for Infrared Galaxies. ApJ, 692:556–573, February 2009. doi: 10.1088/0004-637X/692/1/556.

G. Rodighiero, E. Daddi, I. Baronchelli, A. Cimatti, A. Renzini, H. Aussel, P. Popesso, D. Lutz, P. Andreani, S. Berta, A. Cava, D. Elbaz, A. Feltre, A. Fontana, N. M. Förster Schreiber, A. Franceschini, R. Genzel, A. Grazian, C. Gruppioni, O. Ilbert, E. Le Floch, G. Magdis, M. Magliocchetti, B. Magnelli, R. Maiolino, H. McCracken, R. Nordon, A. Poglitsch, P. Santini, F. Pozzi, L. Riguccini, L. J. Tacconi, S. Wuyts, and G. Zamorani. The Lesser Role of Starbursts in Star Formation at z = 2. ApJ, 739:L40, October 2011. doi: 10.1088/2041-8205/739/2/L40.

E. Rovilos, I. Georgantopoulos, A. Akylas, J. Aird, D. M. Alexander, A. Comastri, A. Del Moro, P. Gandhi, A. Georgakakis, C. M. Harrison, and J. R. Mullaney. A wide search for obscured active galactic nuclei using XMM-Newton and WISE. MNRAS, 438:494–512, February 2014. doi: 10.1093/mnras/stt2228.

S. Salim, R. M. Rich, S. Charlot, J. Brinchmann, B. D. Johnson, D. Schiminovich, M. Seibert, R. Mallery, T. M. Heckman, K. Forster, P. G. Friedman, D. C. Martin, P. Morrissey, S. G. Neff, T. Small, T. K. Wyder, L. Bianchi, J. Donas, Y.-W. Lee, B. F. Madore, B. Milliard, A. S. Szalay, B. Y. Welsh, and S. K. Yi. UV Star Formation Rates in the Local Universe. ApJS, 173:267–292, December 2007. doi: 10.1086/519218.

S. F. Sánchez, R. C. Kennicutt, A. Gil de Paz, G. van de Ven, J. M. Vílchez, L. Wisotzki, C. J. Walcher, D. Mast, J. A. L. Aguerri, S. Albiol-Pérez, A. Alonso-Herrero, J. Alves, J. Bakos, T. Bartáková, J. Bland-Hawthorn, A. Boselli, D. J. Bomans, A. Castillo-Morales, C. Cortijo-Ferrero, A. de Lorenzo-Cáceres, A. Del Olmo, R.-J. Dettmar, A. Díaz, S. Ellis, J. Falcón-Barroso, H. Flores, A. Gallazzi, B. García-Lorenzo, R. González Delgado, N. Gruel, T. Haines, C. Hao, B. Husemann, J. Iglésias-Páramo, K. Jahnke, B. Johnson, B. Jungwiert, V. Kalinova, C. Kehrig, D. Kupko, Á. R. López-Sánchez, M. Lyubenova, R. A. Marino, E. Mármol-Queraltó, I. Márquez, J. Masegosa, S. Meidt, J. Mendez-Abreu, A. Monreal-Ibero, C. Montijo, A. M. Mourão, G. Palacios-Navarro, P. Papaderos, A. Pasquali, R. Peletier, E. Pérez, I. Pérez, A. Quirrenbach, M. Relaño, F. F. Rosales-Ortega, M. M. Roth, T. Ruiz-Lara, P. Sánchez-Blázquez, C. Sengupta, R. Singh, V. Stanishev, S. C. Trager, A. Vazdekis, K. Viironen, V. Wild, S. Zibetti, and B. Ziegler. CALIFA, the Calar Alto Legacy Integral Field Area survey. I. Survey presentation. A&A, 538:A8, February 2012. doi: 10.1051/0004-6361/201117353.

D. B. Sanders, B. T. Soifer, J. H. Elias, B. F. Madore, K. Matthews, G. Neugebauer, and N. Z. Scoville. Ultraluminous infrared galaxies and the origin of quasars. ApJ, 325:74–91, February 1988. doi: 10.1086/165983.

M. T. Sargent, M. Béthermin, E. Daddi, and D. Elbaz. The Contribution of Starbursts and Normal Galaxies to Infrared Luminosity Functions at z < 2. ApJ, 747:L31, March 2012. doi: 10.1088/2041-8205/747/2/L31.

K. Schawinski, S. Khochfar, S. Kaviraj, S. K. Yi, A. Boselli, T. Barlow, T. Conrow, K. Forster, P. G. Friedman, D. C. Martin, P. Morrissey, S. Neff, D. Schiminovich, M. Seibert, T. Small, T. K. Wyder, L. Bianchi, J. Donas, T. Heckman, Y.-W. Lee, B. Madore, B. Milliard, R. M. Rich, and A. Szalay. Suppression of star formation in early-type galaxies by feedback from supermassive black holes. Nature, 442:888–891, August 2006. doi: 10.1038/nature04934.

K. Schawinski, C. M. Urry, B. D. Simmons, L. Fortson, S. Kaviraj, W. C. Keel, C. J. Lintott, K. L. Masters, R. C. Nichol, M. Sarzi, R. Skibba, E. Treister, K. W. Willett, O. I. Wong, and S. K. Yi. The green valley is a red herring: Galaxy Zoo reveals two evolutionary pathways towards quenching of star formation in early- and late-type galaxies. MNRAS, 440:889–907, May 2014. doi: 10.1093/mnras/stu327.

M. J. Seaton. Interstellar extinction in the UV. MNRAS, 187:73P–76P, June 1979. doi: 10.1093/mnras/187.1.73P.

P. Serra, A. Amblard, P. Temi, D. Burgarella, E. Giovannoli, V. Buat, S. Noll, and S. Im. CIGALEMC: Galaxy Parameter Estimation Using a Markov Chain Monte Carlo Approach with CIGALE. ApJ, 740:22, October 2011. doi: 10.1088/0004-637X/740/1/22.

J. L. Sérsic. Influence of the atmospheric and instrumental dispersion on the brightness distribution in a galaxy. Boletin de la Asociacion Argentina de Astronomia La Plata Argentina, 6:41, 1963.

J. Silk and M. J. Rees. Quasars and galaxy formation. A&A, 331:L1–L4, March 1998.

R. E. Skelton, K. E. Whitaker, I. G. Momcheva, G. B. Brammer, P. G. van Dokkum, I. Labbé, M. Franx, A. van der Wel, R. Bezanson, E. Da Cunha, M. Fumagalli, N. Förster Schreiber, M. Kriek, J. Leja, B. F. Lundgren, D. Magee, D. Marchesini, M. V. Maseda, E. J. Nelson, P. Oesch, C. Pacifici, S. G. Patel, S. Price, H.-W. Rix, T. Tal, D. A. Wake, and S. Wuyts. 3D-HST WFC3-selected Photometric Catalogs in the Five CANDELS/3D-HST Fields: Photometry, Photometric Redshifts, and Stellar Masses. ApJS, 214:24, October 2014. doi: 10.1088/0067-0049/214/2/24.

R. Sorba and M. Sawicki. Missing stellar mass in SED fitting: spatially unresolved photometry can underestimate galaxy masses. MNRAS, 452:235–245, September 2015. doi: 10.1093/mnras/stv1235.

R. Sorba and M. Sawicki. Spatially unresolved SED fitting can underestimate galaxy masses: a solution to the missing mass problem. MNRAS, 476:1532–1547, May 2018. doi: 10.1093/mnras/sty186.

J. S. Speagle, C. L. Steinhardt, P. L. Capak, and J. D. Silverman. A Highly Consistent Framework for the Evolution of the Star-Forming "Main Sequence" from z ˜ 0-6. ApJS, 214:15, October 2014. doi: 10.1088/0067-0049/214/2/15.

D. Spinoso, S. Bonoli, M. Dotti, L. Mayer, P. Madau, and J. Bellovary. Bar-driven evolution and quenching of spiral galaxies in cosmological simulations. MNRAS, 465:3729–3740, March 2017. doi: 10.1093/mnras/stw2934.

V. Springel, T. Di Matteo, and L. Hernquist. Modelling feedback from stars and black holes in galaxy mergers. MNRAS, 361:776–794, August 2005. doi: 10.1111/j.1365-2966.2005.09238.x.

J. P. Stott, A. M. Swinbank, H. L. Johnson, A. Tiley, G. Magdis, R. Bower, A. J. Bunker, M. Bureau, C. M. Harrison, M. J. Jarvis, R. Sharples, I. Smail, D. Sobral, P. Best, and M. Cirasuolo. The KMOS Redshift One Spectroscopic Survey (KROSS): dynamical properties, gas and dark matter fractions of typical $z \sim 1$ star-forming galaxies. MNRAS, 457:1888–1904, April 2016. doi: 10.1093/mnras/stw129.

I. Strateva, Ž. Ivezić, G. R. Knapp, V. K. Narayanan, M. A. Strauss, J. E. Gunn, R. H. Lupton, D. Schlegel, N. A. Bahcall, J. Brinkmann, R. J. Brunner, T. Budavári, I. Csabai, F. J. Castander, M. Doi, M. Fukugita, Z. Győry, M. Hamabe, G. Hennessy, T. Ichikawa, P. Z. Kunszt, D. Q. Lamb, T. A. McKay, S. Okamura, J. Racusin, M. Sekiguchi, D. P. Schneider, K. Shimasaku, and D. York. Color Separation of Galaxy Types in the Sloan Digital Sky Survey Imaging Data. AJ, 122:1861–1874, October 2001. doi: 10.1086/323301.

M. J. Stringer and A. J. Benson. The formation of galaxy discs in a hierarchical universe. MNRAS, 382:641–651, December 2007. doi: 10.1111/j.1365-2966.2007.12469.x.

S. Tacchella, C. M. Carollo, A. Renzini, N. M. F. Schreiber, P. Lang, S. Wuyts, G. Cresci, A. Dekel, R. Genzel, S. J. Lilly, C. Mancini, S. Newman, M. Onodera, A. Shapley, L. Tacconi, J. Woo, and G. Zamorani. Evidence for mature bulges and an inside-out quenching phase 3 billion years after the Big Bang. Science, 348:314–317, April 2015. doi: 10.1126/science.1261094.

S. Tacchella, A. Dekel, C. M. Carollo, D. Ceverino, C. DeGraf, S. Lapiner, N. Mandelker, and J. R. Primack. Evolution of density profiles in high-z galaxies: compaction and quenching inside-out. MNRAS, 458:242–263, May 2016a. doi: 10.1093/mnras/stw303.

S. Tacchella, A. Dekel, C. M. Carollo, D. Ceverino, C. DeGraf, S. Lapiner, N. Mandelker, and R. Primack Joel. The confinement of star-forming galaxies into a main sequence through episodes of gas compaction, depletion and replenishment. MNRAS, 457:2790–2813, April 2016b. doi: 10.1093/mnras/stw131.

S. Tacchella, C. M. Carollo, N. M. Forster Schreiber, A. Renzini, A. Dekel, R. Genzel, P. Lang, S. J. Lilly, C. Mancini, M. Onodera, L. J. Tacconi, S. Wuyts, and G. Zamorani. Dust attenuation, bulge formation and inside-out cessation of star-formation in Star-Forming Main Sequence galaxies at $z \sim 2$. ArXiv e-prints, April 2017.

S. Tacchella, C. M. Carollo, N. M. Förster Schreiber, A. Renzini, A. Dekel, R. Genzel, P. Lang, S. J. Lilly, C. Mancini, M. Onodera, L. J. Tacconi, S. Wuyts, and G. Zamorani. Dust Attenuation, Bulge Formation, and Inside-out Quenching of Star Formation in Star-forming Main Sequence Galaxies at $z \sim 2$. ApJ, 859:56, May 2018. doi: 10.3847/1538-4357/aabf8b.

K.-i. Tadaki, R. Genzel, T. Kodama, S. Wuyts, E. Wisnioski, N. M. Förster Schreiber, A. Burkert, P. Lang, L. J. Tacconi, D. Lutz, S. Belli, R. I. Davies, B. Hatsukade, M. Hayashi, R. Herrera-Camus, S. Ikarashi, S. Inoue, K. Kohno, Y. Koyama, J. T. Mendel, K. Nakanishi, R. Shimakawa, T. L. Suzuki, Y. Tamura, I. Tanaka, H. Übler, and D. J. Wilman. Bulge-forming Galaxies with an Extended Rotating Disk at z ˜ 2. ApJ, 834:135, January 2017. doi: 10.3847/1538-4357/834/2/135.

T. Treu, K. B. Schmidt, G. B. Brammer, B. Vulcani, X. Wang, M. Bradač, M. Dijkstra, A. Dressler, A. Fontana, R. Gavazzi, A. L. Henry, A. Hoag, K.-H. Huang, T. A. Jones, P. L. Kelly, M. A. Malkan, C. Mason, L. Pentericci, B. Poggianti, M. Stiavelli, M. Trenti, and A. von der Linden. The Grism Lens-Amplified Survey from Space (GLASS). I. Survey Overview and First Data Release. ApJ, 812:114, October 2015. doi: 10.1088/0004-637X/812/2/114.

F. C. van den Bosch. The impact of cooling and feedback on disc galaxies. MNRAS, 332:456–472, May 2002. doi: 10.1046/j.1365-8711.2002.05328.x.

P. G. van Dokkum, K. E. Whitaker, G. Brammer, M. Franx, M. Kriek, I. Labbé, D. Marchesini, R. Quadri, R. Bezanson, G. D. Illingworth, A. Muzzin, G. Rudnick, T. Tal, and D. Wake. The Growth of Massive Galaxies Since z = 2. ApJ, 709:1018–1041, February 2010. doi: 10.1088/0004-637X/709/2/1018.

F. Walter, E. Brinks, W. J. G. de Blok, F. Bigiel, R. C. Kennicutt, Jr., M. D. Thornley, and A. Leroy. THINGS: The H I Nearby Galaxy Survey. AJ, 136:2563–2647, December 2008. doi: 10.1088/0004-6256/136/6/2563.

X. Wang, T. A. Jones, T. Treu, T. Morishita, L. E. Abramson, G. B. Brammer, K.-H. Huang, M. A. Malkan, K. B. Schmidt, A. Fontana, C. Grillo, A. L. Henry, W. Karman, P. L. Kelly, C. A. Mason, A. Mercurio, P. Rosati, K. Sharon, M. Trenti, and B. Vulcani. The Grism Lens-amplified Survey from Space (GLASS). X. Sub-kiloparsec Resolution Gas-phase Metallicity Maps at Cosmic Noon behind the Hubble Frontier Fields Cluster MACS1149.6+2223. ApJ, 837:89, March 2017. doi: 10.3847/1538-4357/aa603c.

N. Welikala, A. J. Connolly, A. M. Hopkins, R. Scranton, and A. Conti. Spatially Resolved Galaxy Star Formation and Its Environmental Dependence. I. ApJ, 677:970–984, April 2008. doi: 10.1086/527666.

K. E. Whitaker, P. G. van Dokkum, G. Brammer, and M. Franx. The Star Formation Mass Sequence Out to z = 2.5. ApJ, 754:L29, August 2012. doi: 10.1088/2041-8205/754/2/L29.

K. E. Whitaker, M. Franx, J. Leja, P. G. van Dokkum, A. Henry, R. E. Skelton, M. Fumagalli, I. G. Momcheva, G. B. Brammer, I. Labbé, E. J. Nelson, and J. R. Rigby. Constraining the Low-mass Slope of the Star Formation Sequence at 0.5 < z < 2.5. ApJ, 795:104, November 2014. doi: 10.1088/0004-637X/795/2/104.

S. D. M. White and M. J. Rees. Core condensation in heavy halos - A two-stage theory for galaxy formation and clustering. MNRAS, 183:341–358, May 1978. doi: 10.1093/mnras/183.3.341.

R. J. Williams, R. F. Quadri, M. Franx, P. van Dokkum, and I. Labbé. Detection of Quiescent Galaxies in a Bicolor Sequence from Z = 0-2. ApJ, 691:1879–1895, February 2009. doi: 10.1088/0004-637X/691/2/1879.

E. Wisnioski, N. M. Förster Schreiber, S. Wuyts, E. Wuyts, K. Bandara, D. Wilman, R. Genzel, R. Bender, R. Davies, M. Fossati, P. Lang, J. T. Mendel, A. Beifiori, G. Brammer, J. Chan, M. Fabricius, Y. Fudamoto, S. Kulkarni, J. Kurk, D. Lutz, E. J. Nelson, I. Momcheva, D. Rosario, R. Saglia, S. Seitz, L. J. Tacconi, and P. G. van Dokkum. The KMOS^{3D} Survey: Design, First Results, and the Evolution of Galaxy Kinematics from 0.7 <= z <= 2.7. ApJ, 799:209, February 2015. doi: 10.1088/0004-637X/799/2/209.

S. Wuyts, N. M. Förster Schreiber, A. van der Wel, B. Magnelli, Y. Guo, R. Genzel, D. Lutz, H. Aussel, G. Barro, S. Berta, A. Cava, J. Graciá-Carpio, N. P. Hathi, K.-H. Huang, D. D. Kocevski, A. M. Koekemoer, K.-S. Lee, E. Le Floc'h, E. J. McGrath, R. Nordon, P. Popesso, F. Pozzi, L. Riguccini, G. Rodighiero, A. Saintonge, and L. Tacconi. Galaxy Structure and Mode of Star Formation in the SFR-Mass Plane from z ˜ 2.5 to z ˜ 0.1. ApJ, 742:96, December 2011. doi: 10.1088/0004-637X/742/2/96.

S. Wuyts, N. M. Förster Schreiber, R. Genzel, Y. Guo, G. Barro, E. F. Bell, A. Dekel, S. M. Faber, H. C. Ferguson, M. Giavalisco, N. A. Grogin, N. P. Hathi, K.-H. Huang, D. D. Kocevski, A. M. Koekemoer, D. C. Koo, J. Lotz, D. Lutz, E. McGrath, J. A. Newman, D. Rosario, A. Saintonge, L. J. Tacconi, B. J. Weiner, and A. van der Wel. Smooth(er) Stellar Mass Maps in CANDELS: Constraints on the Longevity of Clumps in High-redshift Star-forming Galaxies. ApJ, 753:114, July 2012. doi: 10.1088/0004-637X/753/2/114.

S. Wuyts, N. M. Förster Schreiber, E. J. Nelson, P. G. van Dokkum, G. Brammer, Y.-Y. Chang, S. M. Faber, H. C. Ferguson, M. Franx, M. Fumagalli, R. Genzel, N. A. Grogin, D. D. Kocevski, A. M. Koekemoer, B. Lundgren, D. Lutz, E. J. McGrath, I. Momcheva, D. Rosario, R. E. Skelton, L. J. Tacconi, A. van der Wel, and K. E. Whitaker. A CANDELS-3D-HST synergy: Resolved Star Formation Patterns at 0.7 ¡ z ¡ 1.5. ApJ, 779:135, December 2013. doi: 10.1088/0004-637X/779/2/135.

G. Yang, C.-T. J. Chen, F. Vito, W. N. Brandt, D. M. Alexander, B. Luo, M. Y. Sun, Y. Q. Xue, F. E. Bauer, A. M. Koekemoer, B. D. Lehmer, T. Liu, D. P. Schneider, O. Shemmer, J. R. Trump, C. Vignali, and J.-X. Wang. Black Hole Growth Is Mainly Linked to Host-galaxy Stellar Mass Rather Than Star Formation Rate. ApJ, 842:72, June 2017. doi: 10.3847/1538-4357/aa7564.

S. Zibetti, S. Charlot, and H.-W. Rix. Resolved stellar mass maps of galaxies - I. Method and implications for global mass estimates. MNRAS, 400:1181–1198, December 2009. doi: 10.1111/j.1365-2966.2009.15528.x.

A. Zolotov, A. Dekel, N. Mandelker, D. Tweed, S. Inoue, C. DeGraf, D. Ceverino, J. R. Primack, G. Barro, and S. M. Faber. Compaction and quenching of high-z galaxies in cosmological simulations: blue and red nuggets. MNRAS, 450:2327–2353, July 2015. doi: 10.1093/mnras/stv740.